University of Sheffield

Department of Mechanical Engineering

PhD Thesis

Mechanical Engineering Department

HYBRID MULTI-LASER POWDER BED FUSION

Halil Emre **CAGLAR**

May 2024

Supervisor: Prof Kamran MUMTAZ

Thesis submitted to the Department of Mechanical Engineering, the University of Sheffield in partial fulfilment of the requirements for the degree of PhD

Declaration of Originality

I, Halil Emre CAGLAR, hereby declare that the work presented in this thesis is entirely my own. All sources and materials used have been appropriately acknowledged and referenced in accordance with the prescribed copyright guidelines.

I certify that:

1. This work has been written by me and is based on my original research.
2. Where I have used the published work of others, this has always been clearly acknowledged.
3. Where I have quoted from the work of others, the source is always given. Such quotations are distinguished from my own work.
4. This thesis has not been submitted for any other degree or professional qualification.
5. I have followed all ethical guidelines for research and writing in my field of study as well as the ethical use of AI.
6. The research data, including samples, have been collected and analysed by me and any assistance received in the process has been fully disclosed and acknowledged.

I understand that failure to comply with these statements may result in allegations of academic misconduct. The responsibility for this thesis and the views expressed in it rests solely with me and not with the institution to which it is submitted.

Date: 15/05/2024

Halil E. CAGLAR

Abstract

In Laser Powder Bed Fusion (LPBF) systems, both single fibre systems and multi-laser systems are currently at the forefront of industry and academic research. Among the multi-laser approaches, Diode Area Melting (DAM) stands out as a novel alternative to conventional single-fibre LPBF systems. DAM offers the advantage of processing metal powder feedstock with a low cooling rate, courtesy of its short-wavelength, low-power diode lasers. However, the system is challenged by its lack of precision processing capabilities. In contrast, single fibre LPBF is renowned for its ability to process metals with high precision, owing to its high-power laser and high velocity scanning capabilities. Yet, these systems suffer from a deficiency in high cooling rates and microstructure control. This thesis introduces a groundbreaking Hybrid Laser Powder Bed Fusion (HLPBF) system, which combines two distinct laser processing methods to explore their effects on microstructure control. Firstly, a HLPBF system was developed, comprising a traversing DAM laser head equipped with an array of nine 450 nm (4W each) diode lasers alongside a conventional 200W single fibre LPBF and galvo-scanning head operating at a wavelength of 1064 nm. Subsequently, single fibre LPBF and DAM systems were individually tested to establish a literature background for hybrid processing, including parameter maps (based on normalised energy density), side and top surface roughness, heat-affected zones, cross-sectional densities, and microstructure investigations. During the investigations with the 450 nm DAM, a new phenomenon termed the 'crescent effect' was identified and added to the literature. This effect explains the wide, slow-moving melt pool's impact on the solidified sample. The hybrid processing phase commenced with the processing of Ti6Al4V feedstock utilizing both laser types within a single sample for the first time. A specific scanning strategy delineated separate laser processing regions within the same sample, including an overlap where both lasers interacted to fuse the feedstock and bridge the two regions. The regions melted by the fibre laser experienced significantly higher cooling rates (~10^7 °C/s) compared to DAM regions (~600 °C/s), resulting in finer microstructures characterized by acicular α´/α phases. In contrast, DAM regions exhibited larger α+β grains with parent β grain sizes approximately 13 times larger than those in the fibre

laser-melted zone. In addition to its microstructural spatial tailoring capabilities, this investigation of the hybrid laser system also illuminates variations in the laser-induced heat-affected zone, surface roughness, and mechanical properties across DAM, single fibre LPBF, and overlap regions within fabricated Ti6Al4V samples.

Acknowledgements

I want to take a moment to express my heartfelt gratitude to my wife Gamze Caglar, then my supervisor Prof Kamran Mumtaz, my mentors, Dr Tugrul Gulenc, Dr Ashfaq Khan, Dr Yunus Emre Cogurcu, Dr Busra Karas, Dr Mohammed Alsaddah, and my parents for their unwavering support throughout my PhD journey, especially during the challenging period of COVID-19. I cannot thank them enough for being there for me during this difficult time, not only for my doctoral studies but also for any kind of work or endeavour. The challenges I faced were substantial.

I want to express my sincere appreciation to the Turkish Government for the generous scholarship they awarded me. Their support provided me with the priceless opportunity to pursue my education abroad without any financial difficulties. It has been a true privilege and a significant factor in my academic career.

I appreciate everyone's support during this time.

Cheers!

Halil E. CAGLAR

Table of Contents

List of Figures

List of Tables

List of Abbreviations

3DP	3d Printing
AM	Additive Manufacturing
AOR	Angle Of Repose
BCC	Body Centred Cubic
BPP	Beam Parameter Product
CAD	Computer Aided Design
DAM	Diode Area Melting
DED	Directed Energy Deposition
DLPC	Diode Laser Power Controller
DLTC	Diode Laser Temperature Controller
EBM	Electron Beam Melting
FGM	Functionally Graded Materials
FLM	Fibre Laser Melting
FLU	Fibre Laser Unit
HCP	Hexagonal Closed Packed
HIP	Hot Isostatic Pressing
HLPBF	Hybrid Laser Powder Bed Fusion
HPDL	High Power Diode Lasers
LAM	Laser Additive Manufacturing
LED	Linear Energy Density
LMD	Laser Metal Deposition
LPBF	Laser Powder Bed Fusion
MAM	Metal Additive Manufacturing
MHGC	Multi-Laser Head Gantry Controller
NED	Normalised Energy Density
NIR	Near Infrared
PBF	Powder Bed Fusion
PDF	Powder Diffraction File
PPC	Powder Pistons Controller
PSD	Particle Size Distribution
RSW	Residual Stress in Term of Warpage
RQ(s)	Research Question(s)
SED	Surface Energy Density
SLM	Selective Laser Melting
SLS	Selective Laser Sintering
SSR	Side Surface Roughness
TEC	Thermo-Electric Cooler
TEM	Transverse Mode
VED	Volumetric Energy Density

Publications

Conference Paper:

Caglar H., Liang A., Mumtaz K., 2023, MULTIPLE 450 nm DIODE LASER PROCESSING OF TI6AL4V POWDER, Solid Freeform Fabrication 2023: Proceedings of the 34th Annual International Additive Manufacturing Conference, Reviewed Paper, Accessed: https://utw10945.utweb.utexas.edu/2023-table-contents , at 25/01/2024.

Journal Paper:

Caglar H., Liang A., Groom K., Mumtaz K., 2024, Multi-Laser Powder Bed Fusion of Ti6Al4V: Diode Area Melting Utilizing Low-Power 450nm Diode Lasers, J. Mater. Process. Technol. 118303. https://doi.org/10.1016/j.jmatprotec.2024.118303

Submitted Paper to "Additive Manufacturing Journal":

Caglar H., Aydin A., Gulenc I.T., Groom K., Mumtaz K., 2024. "Hybrid Powder Bed Fusion: Dual-laser coupling using multi-laser 450 nm diode area melting and 1064 nm fiber laser powder bed fusion for in-situ microstructural spatial tailoring of Ti6Al4V". 14/05/2024.

1. Introduction

1.1 Background

In Laser Powder Bed Fusion (LPBF) systems, both single fibre systems and multi-laser systems are currently at the forefront of industry and academic research. Single-fibre LPBF is widely used in the aerospace, automotive, and healthcare industries to produce high-density components [1–3]. Single fibre LPBF has the advantage of creating customized, geometrically efficient structures with minimal material waste by melting thin layers of metallic feedstock (such as Ti6Al4V) [1,4,5]. These conventional industrial-type high power (>100W) near-infrared (NIR) fibre lasers use a highly focused laser beam (40-100 µm spot diameter) with a galvanometer (galvo) scanner that can reach high scanning speeds (up to 7000 mm/s) and build rates [6–9]. This processing methodology, employing a highly fast-moving laser spot, leads to a reduced heat-affected zone (HAZ) [10,11] and paves the way for the production of high-resolution samples [12,13].

Diode Area Melting (DAM), an alternative to conventional LPBF, was developed by investigators at The University of Sheffield [14]. The system integrates multiple low-power (~4.5W) short wavelength (450-808 nm) fibre coupled diode lasers into a laser head that traverses on a gantry system across the powder bed. The diode lasers are individually addressable so that each laser can be switched on/off whilst traversing across the powder bed to create net-shape components [14–16] see Figure 1.1-(A). Each focused laser has a spot size of lower than 100 µm at the substrate. Within the laser head, two or more linear arrays of fibres can be tightly packed at a pitch between 75-150 µm to allow suitable beam overlap at the substrate [8,17]. The diode laser operates at higher efficiency compared to fiber lasers. Consequently, the metal feedstock can be melted more effectively due to the inherently higher laser-absorptivity levels associated with shorter wavelengths. Previous DAM research [9] with Ti6Al4V powder showed that 808 nm diode laser has the laser absorptivity of by 14% when compared to a 1064 nm (NIR) laser, followed by a further 25% with the use of a 450 nm laser (Figure 1.1-(B)).

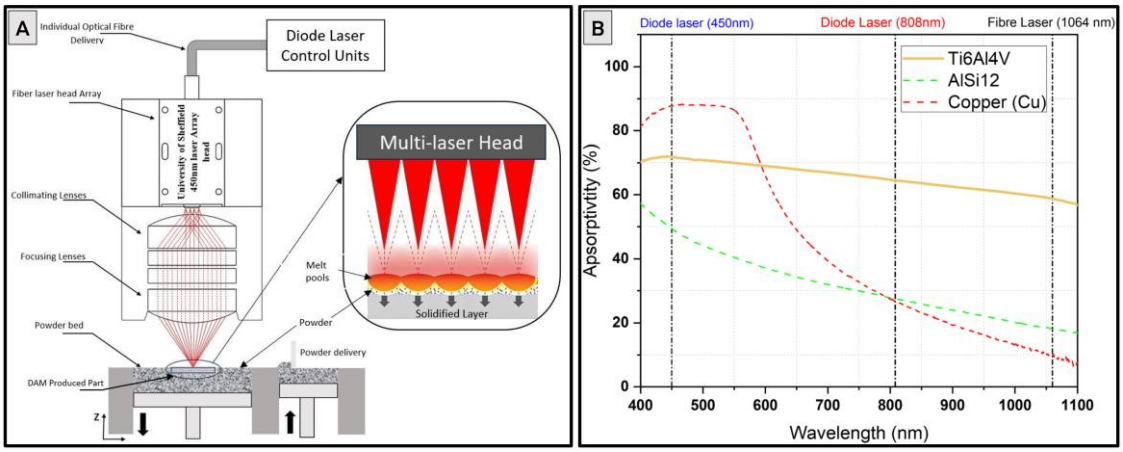

Figure 1.1 – (A) - Operational schematic illustration for DAM, (B) - material's absorptivity percentages at various wavelengths (Alsaddah et al.[9])

1.2 Limitations of Single Fibre LPBF and DAM

Although single-fibre LPBF systems have undergone extensive study over the past decade, LPBF still faces several limitations that need to be addressed. These include post-processing requirements arising from its high cooling rate processing (can be as high as 10^7 ℃/s), challenges in achieving in-situ microstructure control, scalability issues, and the low radiation emissivity of metal powder due to the high wavelength of the laser (>1060 nm) [2,6,18–21]. Conversely, the DAM process operates at a speed measured in mm/min, which is notably slower than conventional single-fibre laser PBF systems that operate at mm/s. This considerable reduction in scanning speed leads to a decrease in cooling rate (can be as low as 600 ℃/s). Still, an increase in the heat-affected zone within the produced part, consequently resulting in high side surface roughness on the samples. Such issues are typically alleviated in single-fibre laser systems owing to their high-resolution lasers and faster scan speeds [8,9,14–16]. As a result, the side surface roughness of the sample is assumed to increase, but the fibre laser processing samples have a tendency to have lower side surface roughness [22–24]. Additionally, the density of samples produced by the DAM process is not satisfactory for use in future case studies [8]. The literature [8,9,14–16,25] claims that the productivity rate can be increased by increasing the number of lasers, but only ten lasers within two arrays on a Ti6Al4V powder have been examined. There is no evidence of the laser-powder interactions with

more than five lasers within an array. Furthermore, in-situ microstructure control is limited due to the high scanning speed range in single-fibre laser PBF systems.

The motivation for this research stems from the potential of a dual laser coupling hybrid processing approach to enhance the processing capabilities of LPBF significantly. By integrating two distinct laser processing systems into one (Hybrid LPBF or HLPBF), this approach may promise to address key challenges faced by current LPBF techniques. Specifically, it may present an opportunity to control hardness across different sections of a sample and explore new avenues for microstructural tailoring within a single part, all without the need for post-processing interventions.

1.3 Aim of the Research

This research aims to investigate the feasibility of integrating two distinct laser processing systems into a single LPBF setup (HLPBF) to address specific challenges associated with each individual system (such as side surface roughness observed in DAM and the effect of the cooling rate differences on hybrid LPBF produced parts) and ultimately achieve spatial microstructure tailoring with Ti6Al4V feedstock. It is important to emphasise that the HLPBF system developed for this study is not intended to replace or be directly compared with established industrial systems.

1.3.1 Objectives

- Designing a bespoke, air-tight and light-tight hybrid laser PBF build chamber to house both a single fibre laser and a multi-laser head, complete with appropriate motion mechanisms and electronics.
- Assess the scientific reliability of 1064 nm fibre laser equipment and novel 450 nm DAM system using data from existing literature and comparing densification, hardness and microstructure of samples.
- Develop an innovative parameter map for Ti6Al4V using the 450 nm DAM system via normalised energy density.

- ❖ Investigate new scanning strategies inherent to the HLPBF system and undertake comprehensive microstructural analysis of multi-layer hybrid Ti6Al4V samples, particularly at the interfaces between the two laser types.
- ❖ Identify system limitations in order to suggest improvements for future work and assess the impact of these limitations on the samples produced.

1.3.2 Research Questions (RQs)

The RQs of this study are as follows:

RQ1. Will the customised system and its components prove to be sufficiently reliable for conducting scientific studies?

RQ2. Are there distinct interactions between multi-diode lasers and Ti6Al4V powder similar to those observed in single-fibre laser processing?

RQ3. Can the multi-laser 450 nm DAM system effectively produce high-density Ti6Al4V samples?

RQ4. Will the hybrid samples be successfully fused together using different lasing technologies?

RQ5. Is it possible to effectively control the microstructure in situ by leveraging the varying cooling rates of different systems within a sample?

1.3.3 Novelty Contributions

This thesis presents three primary novelty contributions to the literature.

1. A novel LPBF system (HLPBF) was developed using a single fibre laser and multi-diode lasers within a single-build chamber.
2. A new laser-powder interaction phenomenon called the "crescent effect" was identified. This effect is characterised by increased solidification of the melt pool in an array of lasers, influenced by Marangoni flow, heat transfer dynamics and recoil pressure.
3. The size of the parental β-grains in the DAM processed section in the hybrid samples was observed to be almost 13 times larger than in the fibre laser

processed sections. It showcases that hybrid processing has the ability to tailor the microstructure within a single process.

The technical contribution focuses on analysing densification through an incremental normalised density approach rather than examining one factor at a time.

1.4 Thesis Outline

The chapters of this thesis are listed in Table 1-1.

Table 1-1 - Detailed Breakdown of Thesis Chapters with Defined Scope for Each Area

Chapter No	***Chapter Name***	***Scope of the Chapter***
1	Introduction	Novelty statement, aim, and objectives of this research will be revealed. The research questions will be reviewed in the conclusion chapter.
2	Literature Review	A detailed overview of the scientific principles behind LPBF, reviewing key studies to set the groundwork for this research's focused exploration.
3	Experimental Methodology	Details the experimental equipment, variable control, and data analysis methods used to ensure the replicability and reliability of the results with a 'Bespoke Hybrid Laser Powder Bed Fusion (HLPBF) System Development' section.
4	Optimising Parameters for Ti6Al4V Using Fibre Laser Equipment in HLPBF Process	Validates the fibre laser processing, revealing new findings on Ti6Al4V's microstructure and hardness at a 60 µm layer height, and informs optimal parameters for hybrid laser processing.
5	Multi-laser PBF with Ti6Al4V via Use of 450 nm Diode Area Melting (DAM) System	Explores 450 nm DAM processing to melt Ti6Al4V powder, creating high-density samples and developing a new parameter map linking normalised energy density with microstructural changes.
6	Hybrid Laser Powder Bed Fusion (HLPBF)	Investigates hybrid laser processing by integrating optimal parameters from earlier chapters, uniquely focusing on using varied laser systems for microstructural control and investigation, examining scanning orders, side surface roughness, and mechanical assessments.
7	Conclusion and Future Work Suggestions	Highlighting the research objectives and suggesting further research topics.
8	References	Used references from scientific resources.

2. Literature Review

2.1 Introduction

This literature review examines the current landscape of additive manufacturing, particularly emphasising laser beam additive manufacturing for metals. The review investigates various LPBF processing technologies, focusing on single and multiple-fibre LPBF and novel DAM systems. The need to integrate these distinct laser systems into a hybrid LPBF is underscored by exploring state-of-the-art advancements and identifying existing gaps in the literature. This integration aims to address the limitations of each system and leverage their combined strengths for enhanced microstructural control of Ti6Al4V samples. Additionally, critical LPBF variables that influence processing outcomes are discussed, providing a comprehensive context for understanding the potential of HLPBF in advancing additive manufacturing technologies.

2.2 Metal Additive Manufacturing (MAM)

Additive manufacturing (AM), a contemporary and widespread manufacturing method, is primarily used for modelling, prototyping, end-use components, and tooling [18–20]. The ISO ASTM 52910:2017(E) standard defines AM as a process in which materials are sequentially added in layers according to a 3D CAD model, as opposed to subtractive and formative manufacturing techniques [26]. The process involves creating a design, converting it to ".STL" format, slicing it into a specified number of layers using various software, and finally sending it to a AM machine for printing or deposition [27], as shown in Figure 2.1.

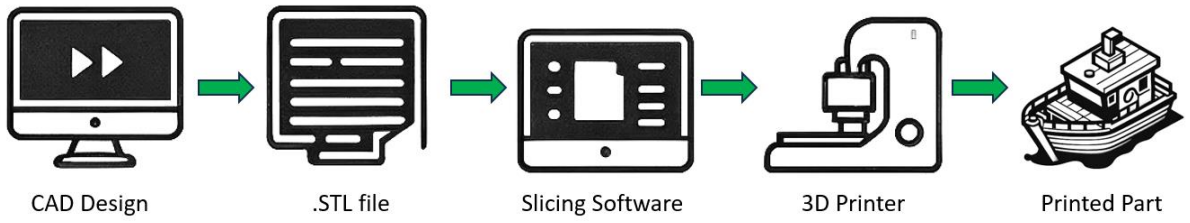

Figure 2.1 - Fundamental Process Diagram for Additive Manufacturing (AM)

According to ASTM 52900:2015 [28], AM can be categorised into seven main methods: Material Extrusion, Powder Bed Fusion (PBF), VAT Photopolymerisation, Material Jetting,

Binder Jetting, Sheet Lamination and Directed Energy Deposition (DED). The short summary is given for categorisation of AM in Figure 2.2.

CATEGORIES	TECHNOLOGIES	PRINTED "INK"	POWER SOURCE	STRENGTHS / DOWNSIDES
Material Extrusion	Fused Deposition Modeling (FDM)	Thermoplastics, Ceramic slurries, Metal pastes	Thermal Energy	• Inexpensive extrusion machine • Multi-material printing • Limited part resolution • Poor surface finish
	Contour Crafting			
Powder Bed Fusion	Selective Laser Sintering (SLS)	Polyamides /Polymer	High-powered Laser Beam	• High Accuracy and Details • Fully dense parts • High specific strength & stiffness • Powder handling & recycling • Support and anchor structure • Fully dense parts • High specific strength and stiffness
	Direct Metal Laser Sintering (DMLS)	Atomized metal powder (17-4 PH stainless steel, cobalt chromium, titanium Ti6Al-4V), ceramic powder		
	Selective Laser Melting (SLM)			
	Electron Beam Melting (EBM)		Electron Beam	
Vat Photopolymerization	Stereolithography (SLA)	Photopolymer, Ceramics (alumina, zirconia, PZT)	Ultraviolet Laser	• High building speed • Good part resolution • Overcuring, scanned line shape • High cost for supplies and materials
Material Jetting	Polyjet / Inkjet Printing	Photopolymer, Wax	Thermal Energy / Photocuring	• Multi-material printing • High surface finish • Low-strength material
Binder Jetting	Indirect Inkjet Printing (Binder 3DP)	Polymer Powder (Plaster, Resin), Ceramic powder, Metal powder	Thermal Energy	• Full-color objects printing • Require infiltration during post-processing • Wide material selection • High porosites on finished parts
Sheet Lamination	Laminated Object Manufacturing (LOM)	Plastic Film, Metallic Sheet, Ceramic Tape	Laser Beam	• High surface finish • Low material, machine, process cost • Decubing issues
Directed Energy Deposition	Laser Engineered Net Shaping (LENS) Electronic Beam Welding (EBW)	Molten metal powder	Laser Beam	• Repair of damaged / worn parts • Functionally graded material printing • Require post-processing machine

Figure 2.2 - Categorisation of Additive Manufacturing: Analysing Technologies, Feedstocks, Power Sources, and Their Advantages/Disadvantages [28,29]

In the field of metal AM (MAM) industry, PBF and DED techniques are predominantly employed [26,28,30–33]. These techniques utilise either laser or electron beams as the primary source of thermal energy for material fusion. To gain a comprehensive understanding of the inherent limitations and advantages of various MAM systems relative to each other, it is imperative to first grasp their fundamental operational principles. The key systems in focus include Electron Beam Melting (EBM), DED, and LPBF.

EBM operates by focusing a high-energy electron beam in a vacuum to fuse metal powder particles in a bed. This process builds parts layer-by-layer by melting the powder according to the cross-sectional geometry defined by a digital model [2,6]. DED works by feeding metal powder or wire into a focused laser beam or arc that is scanned across a substrate, melting and depositing the material to form a high-density layer. This process is typically used for

repair, coating, or manufacturing large parts [2,6]. LPBF, uses a high-power laser beam to selectively melt and fuse metal powder particles in a powder bed. The process occurs under a shield gas to prevent oxidation and builds parts layer-by-layer directly from 3D CAD data [34,35].

The most common metal powder among these three technologies (EBM,DED,LPBF) that uses can be said to be Ti6Al4V. Ti6Al4V is a crucial alloy known for its strong mechanical properties and distinctive microstructural characteristics when processed using these technologies, particularly in the biomedical, aerospace, and automotive industries compared to traditional manufacturing methods [1–4].

2.2.1 Brief Introduction of the Metallurgical Attributes of Ti6Al4V

Ti6Al4V is comprised of two primary phases: alpha (HCP-α) and beta (BCC-β) (Figure 2.3). The α phase can manifest in several forms, including α martensite (α'), which is produced from the β phase through rapid cooling (Figure 2.4-A) [36].

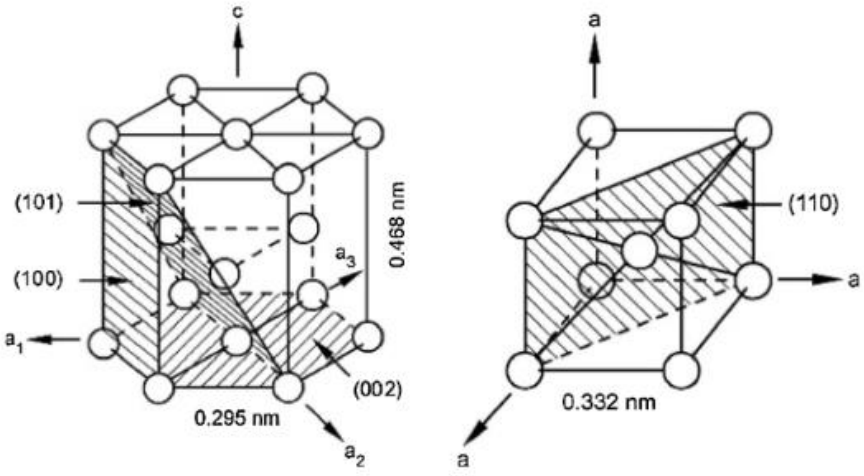

Figure 2.3 - Unit cell of HCP α-phase (left) and BCC β-phase (right) [37,38]

In Ti6Al4V, aluminium serves to stabilize the α-phase, enhancing properties such as creep resistance and strength at elevated temperatures. Conversely, vanadium stabilizes the β-phase, which is essential for improving ductility and formability at higher temperatures and influences the transformation temperatures between the alpha and beta phases. The alloy is notably reactive to oxygen and nitrogen, elements that stabilize the α-phase but at the cost of reduced ductility. Carbon and tin also stabilize the α-phase; however, high carbon content can lead to increased brittleness. Other elements like molybdenum, which enhances

formability and ductility, niobium, which boosts corrosion resistance, chromium, which contributes to hardenability and strength, and iron, often an impurity that impacts stability and mechanical properties, are significant β-phase stabilizers [38]. Most machines used in MAM, such as those operating under LPBF maintain a residual oxygen concentration of approximately 1000 ppm (<0.1% O_2), or a vacuum in EBM, or use argon purging in a closed environment for DED. Oxygen, highly soluble in the α-phase (up to 14.2 wt%, as illustrated in Figure 2.4-B), is known to stabilise this phase [37,39].

The presence of vanadium, which has smaller lattice parameters, causes the titanium lattice to contract. The melting point of Ti6Al4V is between 1604°C and 1666°C. The martensitic phase, although chemically similar to the β-phase, has a hexagonal pseudo-compact crystal structure which results in high residual stresses [37,38]. The martensitic transformation begins (M_S) and ends (M_E) at 780°C and 650°C, respectively (Figure 2.4-A). Above the β-transus temperature of 980 °C, the lattice structure is BCC with a parameter of 3.192 Å [40].

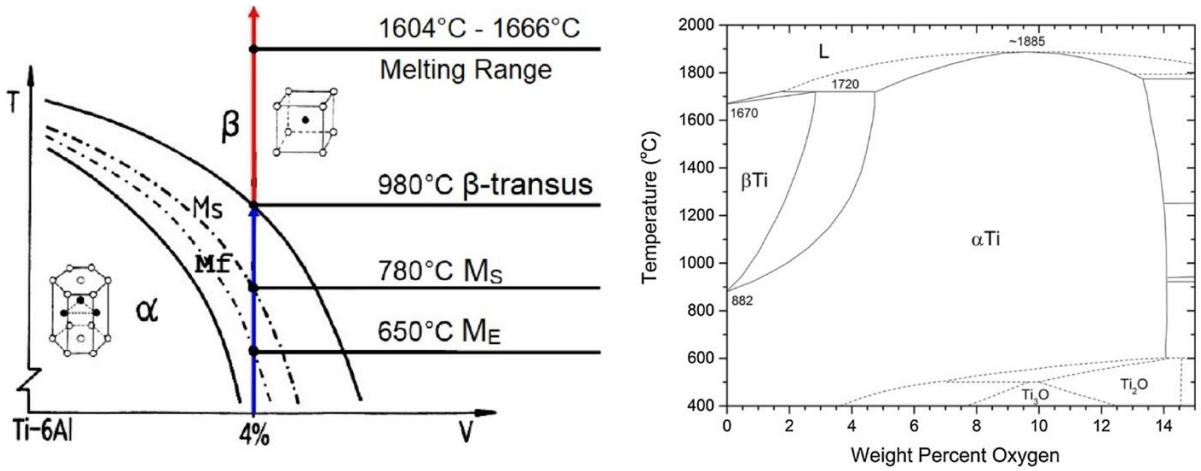

Figure 2.4 - (A) Schematic pseudo-binary diagram of Ti6Al4V, (B) Titanium-oxygen phase diagram [37].

2.2.2 Microstructure Control of Ti6Al4V

Cooling rate or solidification rate defines the structure type of the solidified material [39,41]. Efficient control of the microstructure, optimization of mechanical functionality, and management of residual stress in manufactured components depend heavily on the cooling rate [36,42]. EBM and LPBF distinctly influence the alloy's microstructure due to differing thermal behaviors. EBM, operating at temperatures often above the β-transus temperature, results in a lamellar α+β structure [43] with slower cooling rates (10^3–10^5 °C/s [44]), producing

coarse, columnar grains that enhance fatigue resistance but may increase defect formation [36]. Conversely, fibre LPBF's much higher cooling rates (up to 10^7 °C/s) produces an α martensite structure or fine α lath [43,45] promoting increased hardness and strength, with a tendency to form finer, basket-weave type structures [46,47]. These rapid cooling rates in LPBF prevent the formation of larger β grains [48], optimizing the material for high-performance applications, whereas EBM's slower rates allow for more extensive grain growth, impacting dimensional stability and mechanical properties differently [48,49]. In general, as-built LPBF Ti6Al4V has higher tensile strength, lower ductility and higher hardness, whereas post-heat treatment typically results in lower tensile strength, higher ductility and lower hardness [2,10,50,51]. Generally, the direction of the sub-grain structure line up parallel to the build direction which it can be find out with EBSD analyses for both technology produced samples [52–54].

Laser power, scanning speed, hatch distance, layer height, laser-powder energy absorptivity, effective spot size, material conductivity, and powder bed temperature are critical LPBF parameters that influence the cooling rate. The distribution of temperature across the powder bed and the minimum temperature within it are pivotal, as they determine the microstructure that results from varying solidification rates. Understanding the effects of these cooling rates requires precise control of energy densities. For instance, the minimum energy density needed to melt the powder typically results in the highest cooling rate, whereas applying the highest possible energy density without triggering keyhole phenomena (assuming all other parameters are held constant) leads to a different cooling behaviour [2,41,52,53,55–57]. These effects and their implications on microstructure will be further detailed in subsequent sections of this study.

The key strategy to control the microstructure is to vary the energy density during multi-layer fabrication, which in turn affects the phase composition and mechanical properties of the resulting material. At lower energy densities, the material experiences heating effects from adjacent scan lines, leading to partial transformation. At higher energy densities, the material remains completely martensitic due to the higher cooling rates and lack of adequate heating [39,58]. Alsaddah *et al.* [9] found that the DAM system's cooling rate can be as slow as 600-750 °C/s via 450 nm, making it one of the slowest cooling rates achievable among other LPBF systems. They also stated in another research [8] that the α lath

size was relatively larger than that of a fibre LPBF system due to the slow cooling rate of 808 nm DAM.

2.2.3 Main Advantages of MAM systems

The primary advantages of EBM stem from its high energy density, which facilitates the easy processing of powdered metals [2]. The system operates at elevated temperatures (typically around 700°C) [44], reducing residual stresses and enhancing material properties, which often eliminates the need for extensive heat treatment [35,59–62]. EBM also excels in manufacturing complex geometries without the need for support structures and efficiently uses materials, allowing for the recycling of unused powder [63]. Microstructural control can be done due to low cooling rate however it is limited.

DED's advantages include its capacity to add material to existing components for repairs or modifications [2], its efficient material usage with minimal waste, and its ability to fabricate functionally graded materials (FGM), and this system is well-suited for large-scale applications and is known for its rapid prototyping and production capabilities [2,18,64,65].

LPBF is renowned for its high precision and excellent control over microstructural properties [35]. It can produce intricate, finely detailed geometries and is compatible with a wide range of materials, including high-performance alloys [66,67]. LPBF systems also deliver strong mechanical properties and dense parts [68], with relatively quick build times for complex designs [6,69,70]. LPBF also allows the use of recyclable powders and often results in improved mechanical properties following heat treatment processes [71,72].

2.2.4 Main Limitations of MAM systems

The limitations of EBM include a relatively coarse surface texture, fewer material choices compared to other MAM systems, and the requirement for a vacuum environment that can escalate operating expenses. The process also features a slower preheating phase and achieves less precise resolution due to the large beam diameter (greater than 200 µm) [2,27,64,65,73].

DED faces challenges such as lower resolution and less accuracy relative to powder bed techniques, variability in achieving uniform properties throughout the build, and a reliance on operator expertise for maintaining quality. Additionally, it struggles to achieve smooth

surface finishes and is limited in its capacity to create complex internal features [3,18,20,27,48,64,65,73–76].

LPBF's main drawbacks include its vulnerability to thermal stresses and deformation [77,78], the necessity for support structures that necessitate further post-processing , and restrictions on the size of parts due to the dimensions of the build chamber [23,79]. However, the most important aspect is the lack of ability to control microstructure due to high cooling rate [2,41,80]. Challenges also arise from handling and safety concerns associated with fine powder particles [3], an inert gas cost and operational regulations and effect on the powder bed [1,21]. Mass production is also limited by process speed, equipment cost and maintenance, work envelope size, therefore, scalability is poor [81–83]. In contrast to DED, LPBF faces challenges in producing FGM, bimetallic or multi-materials, largely due to its powder delivery systems [75].

The current trend in processing technologies is increasingly focused on LPBF due to its unique advantages that surpass those of other technologies. Moreover, the inherent challenges of LPBF can be mitigated through system modifications or innovative approaches to processing methodologies, given that LPBF is relatively the newest among these systems. The prevailing trend aims to enhance microstructural properties, essentially controlling solidification rates [9,36,41,47,80,84]. Consequently, LPBF has the potential to achieve superior mechanical properties compared to EBM and can relatively maintain faster build rates than DED without sacrificing its inherent benefits [48,85,86]. To overcome the specific challenges associated with LPBF, it is essential to thoroughly investigate the current state-of-the-art processing technologies especially that can melt complex metal alloys such as Ti6Al4V.

2.3 LPBF Processing Technologies

The primary goal of LPBF systems is to completely melt the metal powders layer by layer, in contrast to the sintering process often used with polymers, thereby achieving near full density in the final product [3,87]. The systems generally consist of build and reservoir plates. Upon completion of each layer, the build plate descends, and a new layer of powder is evenly distributed over the bed using a powder delivery system, which can be a hopper, recoater, razor blade or feed cartridge [88]. The laser then scans and melts the new layer of powder, and this cycle is repeated until the entire geometry is constructed (Figure 2.5 - [89])

[27]. LPBF systems can be broadly categorized into two types: single and multiple laser configurations. Currently, these configurations can include systems such as single fibre lasers, multi-fibre lasers, single diode lasers, multiple diode laser setups.

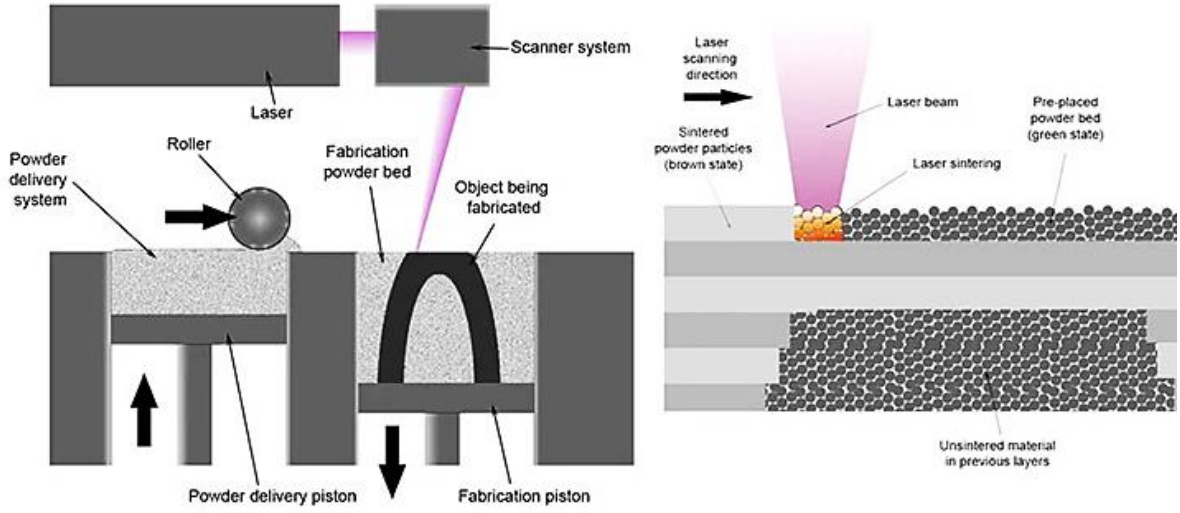

Figure 2.5 – Single Fibre LPBF Operational Mechanics Diagram [89]

2.3.1 Single and Multi-Fibre Laser Systems

The most common industrial system equivalent is fibre laser systems in LPBF industry[90]. Fibre LPBF is widely regarded as a promising AM technology for manufacturing metals, particularly in the aerospace, automotive and healthcare sectors, due to its appeal to researchers and developers [27,91]. These LPBF machines have typically been powered by a single solid-state fibre delivered laser with a galvanometer mirror (generally up to 7000 mm/s) [92], laser delivery system with generally being in the wavelength range of 950-1070 nm (infrared (IR) lasers)[93,94]. This processing methodology, employing a highly fast moving laser spot leads to a reduced HAZ [10,11] and paves the way for the production of high-resolution samples [12,13]. However, the fast moving laser spot generates a rapid solidification of the melt pool with cooling rates that can reach 10^7 °C/s [14,95,96]. By varying key parameters such as laser power, scan speed, hatch distance and layer height, LPBF allows the mechanical properties (including ultimate tensile strength and hardness), surface quality of manufactured parts to be tailored [97–99].

For enhanced scalability, numerous researchers have explored systems equipped with either dual or quad fibre lasers. While these systems operate on the same principles as the single fibre laser setups, the key difference lies in the impact of multiple lasers, which

significantly increase productivity and build rates. Metelkova *et al.* [100] carried out research aimed at improving the quality of inclined face surfaces in LPBF using a dual-laser setup (Figure 2.6). This setup involved the sequential use of a 500 W continuous wave fibre laser with a 60 µm focal spot, followed by a 50 W nanosecond pulse wave laser with a 50 µm focal spot. A single scanner system permits alternating use of either continuous wave (CW) or pulsed wave (PW) lasers. This dual-laser strategy notably enhanced the surface quality of inclined surfaces. The method involved selective powder removal followed by a remelting step, which substantially improved the surface finish. However, there was no demonstrated effect on the microstructure of maraging steel M789, nor were any phenomena related to the dual laser approach observed in the laser powder interaction.

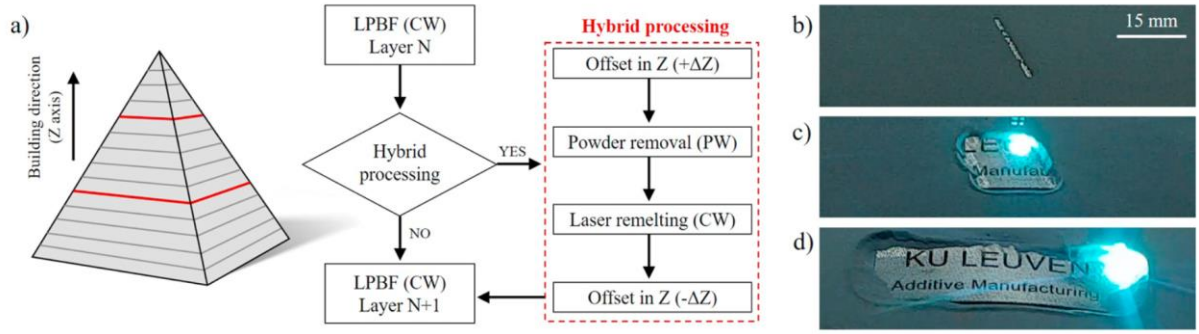

Figure 2.6 - Metelkova et al.'s system proposal [100]

Heeling and Wegener [101] investigated multi-fibre LPBF strategies using a second, larger beam (as a heating power) to spread the heat of the melt pool over a larger area while focusing on the same area (Figure 2.7). They found that solidification time was increased, and smoother surface roughness was achieved. In addition, they claimed that a higher scanning speed can be achieved without losing the densification quality of the 316L stainless steel parts, so high productivity rates can be achieved. However, the no direct correlation for cooling rate and microstructural effect of using multiple lasers were shown.

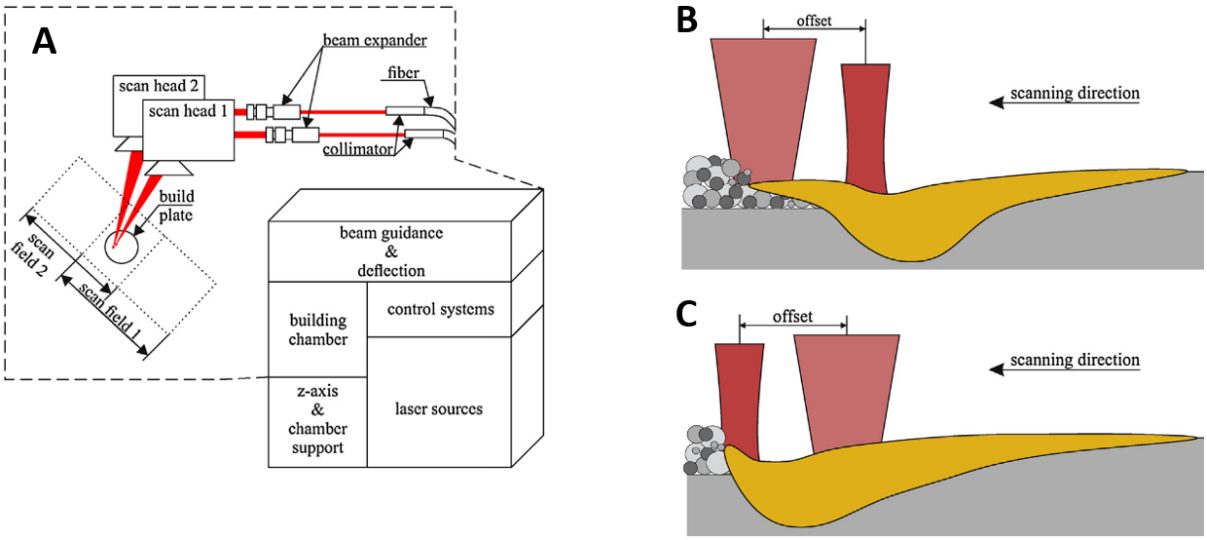

Figure 2.7 - Heeling and Wegener's (A) system schematic, (B) and (C) processing schematics [101]

Tsai *et al.* [102] conducted research regarding multi-spot scanning strategies with a bespoke LPBF system (Figure 2.8). The implementation of a synchronised three-spot scanning strategy, with adjustable characteristics, resulted in a significant improvement in surface roughness of 3.2 µm. Furthermore, this approach resulted in a 38.1% reduction in scanning time compared to traditional single-spot LPBF, significantly enhancing the overall build rate and efficiency of the LPBF process. Despite these improvements, there is a lack of evidence on how this approach impacts the microstructure compared to single fibre laser systems. While such strategies are suggested to increase penetration depth, they could also alter the cooling rate, potentially affecting the residual stresses in the as-built parts.

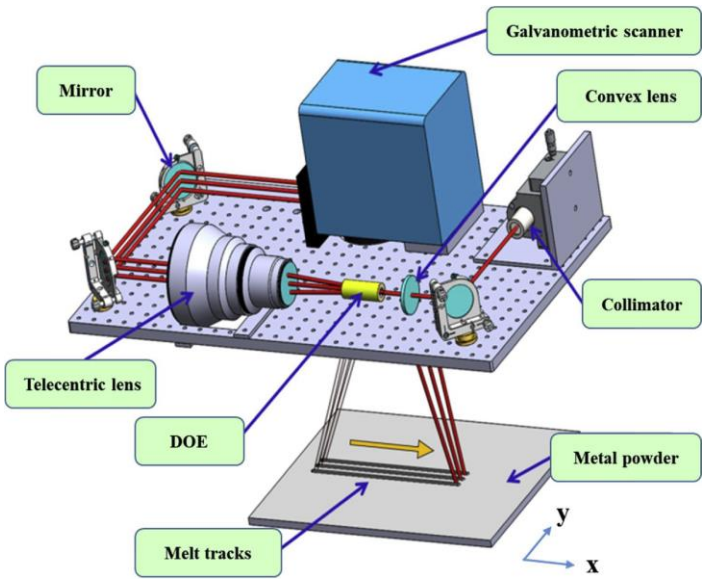

Figure 2.8 - Tsai et al.'s system schematic [200]

Zhang *et al.* [103] conducted a comparative study of LPBF using both single and multi-laser setups, focusing on a quadrant technology (Figure 2.9). They showed that under optimal processing parameters, samples in four distinct, separate quadrants could reach a high density of about 99.93%. In contrast, overlapping samples, where the laser paths intersected, had a slightly lower density of 99.88%. Larger melt pools with some pores at the bottom were observed in these overlap areas, creating a distinct boundary. It was also noted that the proportion of grains oriented in the $\{100\}_{\beta}$ direction was more pronounced in the overlap areas than in the isolated areas, a phenomenon attributed to the exposure to multiple laser beams. The microstructure analysis revealed that lath sizes in the overlap areas were larger than those in sections processed by a single laser. However, there was no observed impact on the cooling rate or residual stress related to the quadrant approach. Moreover, the type of the lasers was the same.

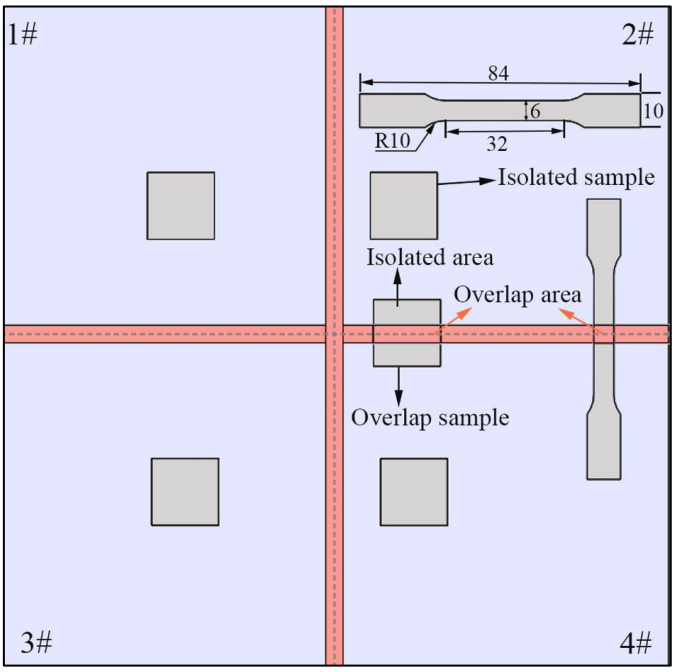

Figure 2.9 - Zhang et al.'s processing schematic [103]

Wei *et al.* [104] also used a quadrant LPBF method to study the laser-Ti6Al4V powder interactions (Figure 2.10). Their results showed that the overlap region could reach near full density whether the scan paths of the two corresponding lasers were identical or different. They also noted that if the two lasers scan the overlap region simultaneously and their points of incidence coincide, there could be significant formation of keyhole defects. In terms of microstructure, all overlap regions exhibited an acicular martensite structure similar to that

found in materials produced by single fibre LPBF. In addition, they emphasised that to ensure consistent performance of large Ti6Al4V components produced by multi-Laser PBF, it is critical to prevent the overlap of different laser incident points in the overlap region similar to Yin *et al.*'s findings [105]. This strategy is shown to be a key to avoiding the formation of defects and maintaining the integrity of the material's microstructure and hardness. These results are in close agreement with those of Li *et al.* [106] who also reported similar results in their study, which they provided insights into the identification of parent grain direction and size, adding another dimension to the understanding of microstructural evolution in parts produced by multi-laser PBF techniques. However, there was no observed impact on the cooling rate or grain size differences related to the quadrant approach. Moreover, the type of the lasers was the same.

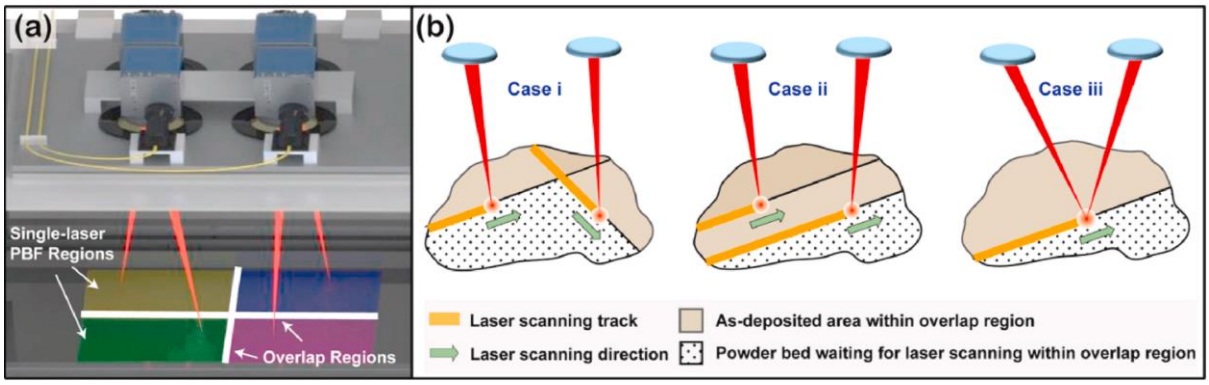

Figure 2.10 - Wei et al.'s (a) system and (b) processing schematics [104]

Zhang *et al.* [107] investigated the effect of scanning strategies of multi-laser PBF on temperature, residual stress, and deformation (Figure 2.11). The study revealed that increasing the number of laser beams in multi-fibre LPBF reduces both the magnitude and average residual stress distribution compared to single fibre LPBF manufacturing. As the number of laser beams increases, there is more heat input at any one time, leading to a slower loss of energy by conduction, convection, or radiation. These results in a lower temperature gradient and slower cooling rate, showed resulting in a reduction in residual stress and deflection. However, no microstructural examination was done to reveal the effect of the number of lasers effect on the melt pool. Again, the type of the lasers was the same.

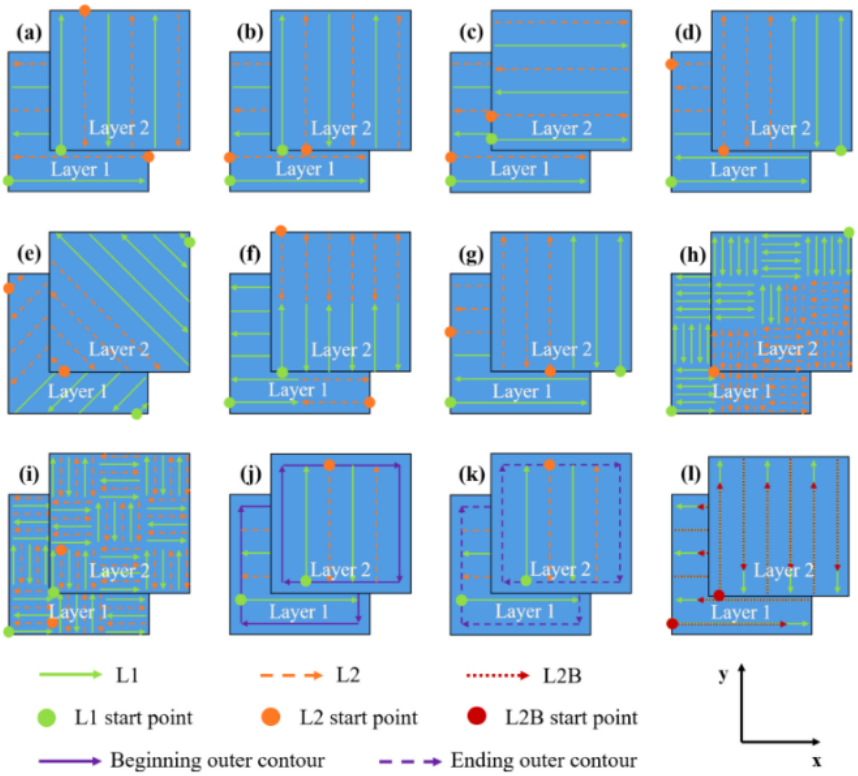

Figure 2.11 - Zhang et al.'s processing schematics [107]

As for single and multi-fibre LPBF, there are not without their systematic drawbacks. First and foremost, the scalability is very poor as maximum quad fibre lasers are available on the market [108]. The low wall-plug efficiency of laser systems in commercial facilities increases both operating and capital costs [74,109]. Other limitations include the need for improvements in machine speed, resolution and power consumption, and the need for careful planning of part orientation due to the constraints of the powder delivery system trajectory [81]. Additionally, quad laser systems do not fully overlap, with the four lasers focusing on a single point only in limited areas, typically no more than roughly 10% of the overall powder bed and primarily at the center. This limitation makes multiple fibre laser systems less feasible for overlap processing, leading to scant research on the microstructural effects within the overlap regions.

Other problems include gas pores, keyhole pores, insufficient fusion, melt pool instability, overlap failure, and the need for post-processing can be classified as microstructure related drawbacks. [8,110–113]. The process often encounters residual stresses due to high cooling rate, requiring well-defined parameters prior to initiation or post-processing is inevitable [77,78]. The complexity of the process is influenced by several factors,

such as the surface tension of the melt pool [114], the chemical composition of the material and its absorptivity due to wide wavelength [115].

2.3.2 Single and Multi-Diode Laser Systems

As opposed to fibre laser LPBF systems, short wavelength (405 - 808 nm) diode laser(s) has been using for an alternative LPBF approach till to date. Diode Area Melting (DAM), an alternative to conventional LPBF was developed by investigators at The University of Sheffield[14]. Arredondo *et al.*[14] introduced a DAM system to improve the productivity rate and process efficiency of single laser LPBF systems using low power, short wavelength, individually addressable 808 nm diode lasers (Figure 2.12). They achieved density close to 80% in a multi-layer 17-4 PH stainless steel part. Later, they [16] studied the melt pool dynamics and thermal properties of DAM over 316L stainless steel. They stated that the DAM process has the potential to reduce residual stress build-up compared to single fibre LPBF due to its specific laser scanning strategy and lower temperature gradients. However, a high layer height was used, and there was no indication of any microstructural investigation being conducted.

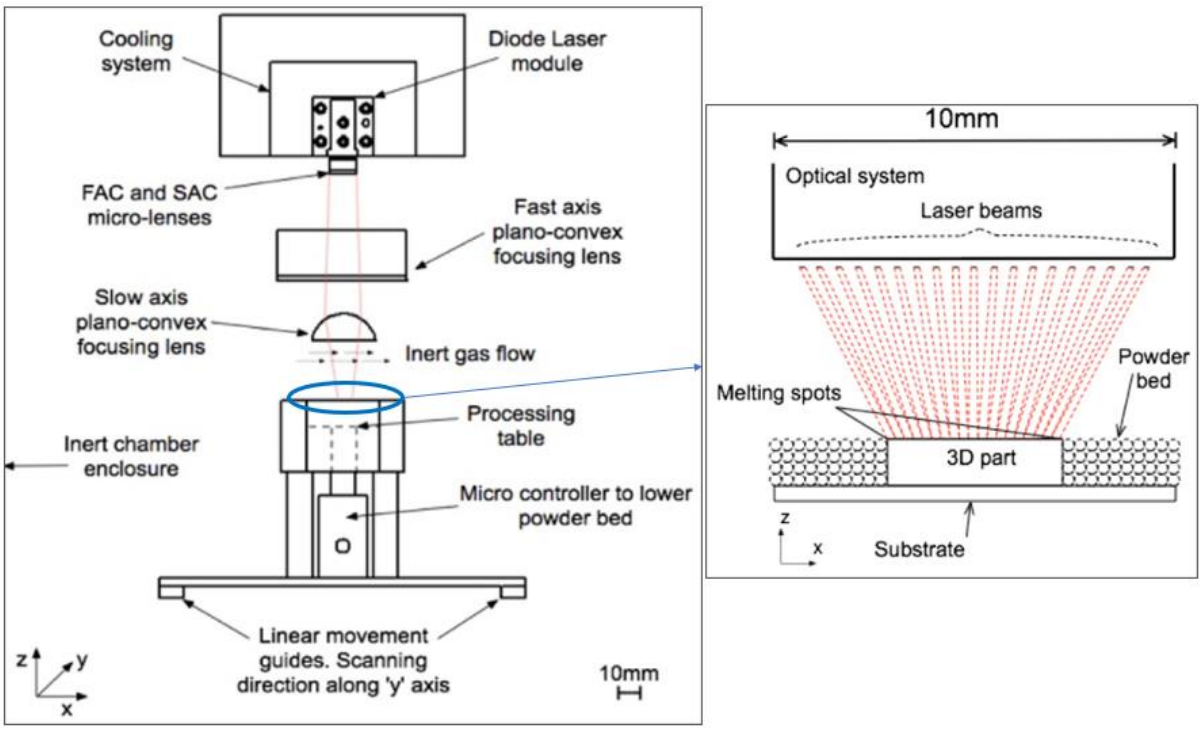

Figure 2.12 - Arredondo et al.'s system schematics [16]

Another system [8] integrates multiple low power (~4.5W) short wavelength (450-808 nm) fiber coupled diode lasers into a laser head that traverse on a gantry system across the powder bed. The diode lasers individually addressable so that each laser can be switched on/off whilst traversing across the powder bed to create net-shape components [14–16] see Figure 2.13. Each focused laser has a spot size of approximately 100 µm at the substrate. Within the laser head two or more linear arrays of fibers can be tightly packed at a pitch between 75-150 µm to allow suitable beam overlap at the substrate [8]. The diode laser operates at higher efficiency compared to fiber lasers. Consequently, the metal feedstock can be melted more effectively due to the inherently higher laser-absorptivity levels associated with shorter wavelengths.

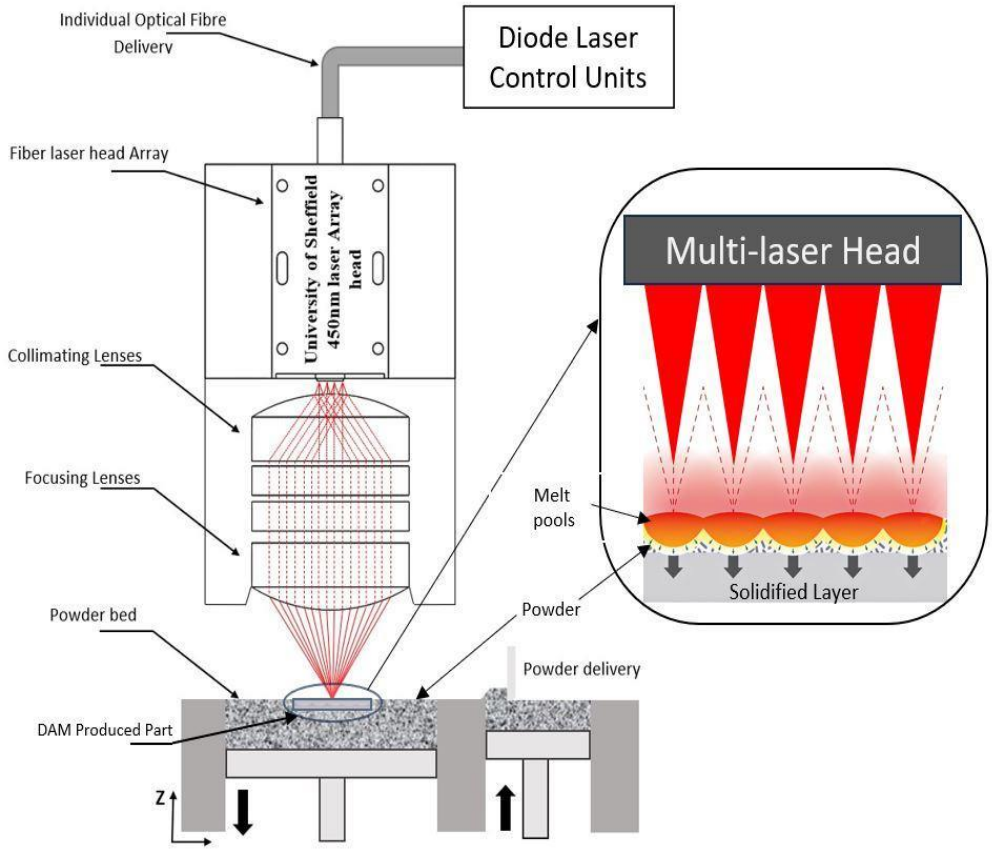

Figure 2.13 - Visual Diagrams of DAM System Components [8], Featuring Detailed Illustration of Melt Pool and Surrounding Laser Spot Configurations

Previous DAM research [9] with Ti6Al4V powder showed that 808 nm diode laser has the laser absorptivity of by 14% when compared to a 1064 nm (NIR) laser, followed by a further 25% with the use of a 450 nm laser. Due to the use of low powers DAM, the scanning speed of the laser head is much lower than traditional high power fiber galvo-scanning PBF-

LB, resulting in a much lower cooling rate, ~ 600 ℃/s when using a 4W 450 nm diode laser [9]. Subsequently, in another study, Alsaddah *et al.*[8] found that martensitic decomposition occurred in certain sections of as-built Ti6Al4V samples with an 808 nm diode laser head within the DAM system (Figure 2.14). Despite DAM's high scalability potential (potentially thousands of lasers within a laser head), the slower DAM scanning speeds create a larger HAZ, reduced resolution capability and rougher size surface roughness compared to conventional PBF-LB systems. In terms of microstructural findings, their research identified the presence of the β phase, however, the system was unable to produce fully dense parts.

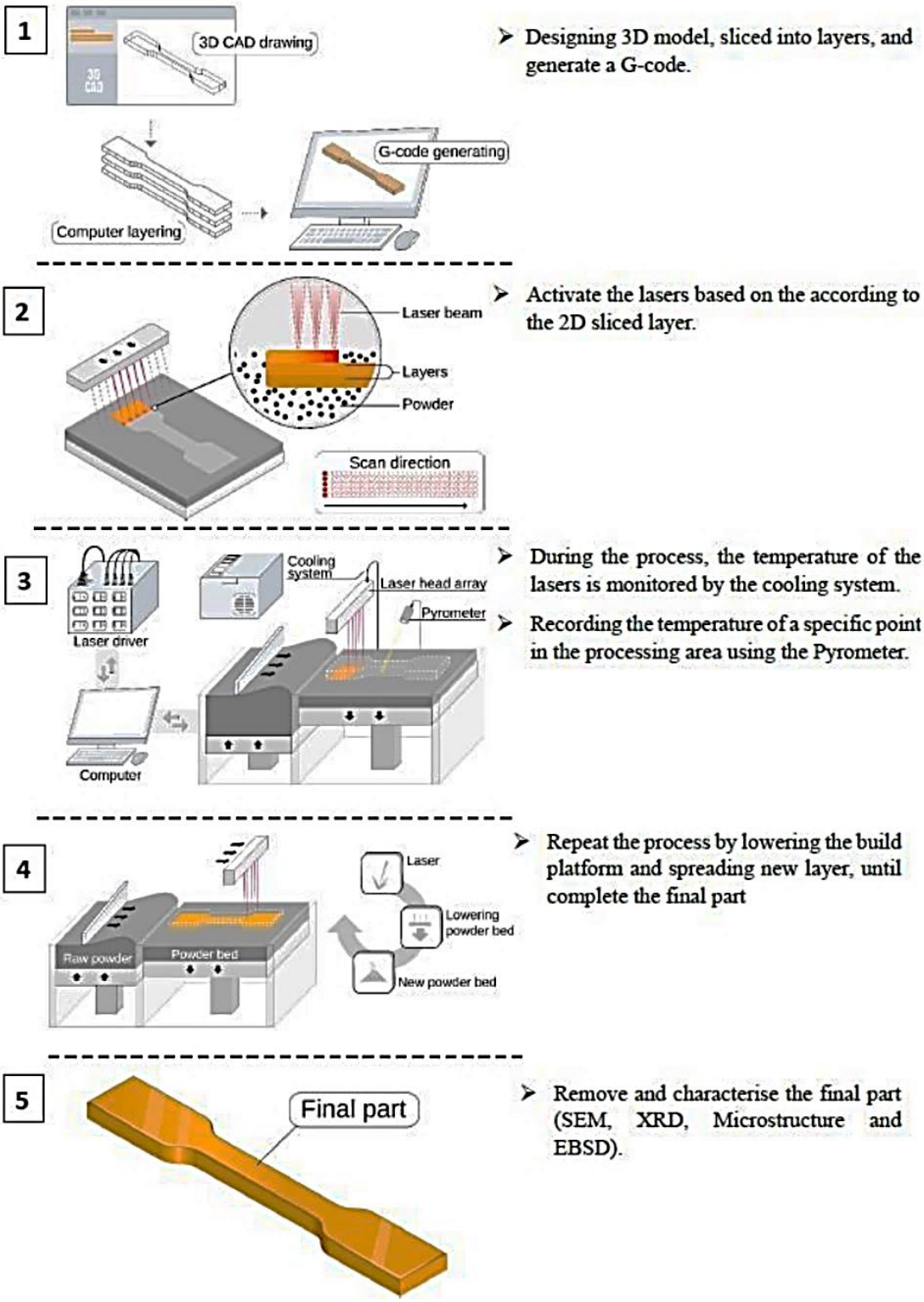

Figure 2.14 - Alsaddah et al's system schematics [116]

Karp *et al.* [117] demonstrated area melting using an array of 16 individually addressable fibre-coupled diode lasers with a combined laser power of 60W (Figure 2.15). The arrangement of the lasers in an array enabled them to produce wide melt pool tracks using gantry motion mechanisms. They achieved a density of over 99% in cobalt-chromium

(CoCr) wall samples. In addition, they found that this multi-diode laser technique using an array configuration has the potential to significantly increase the build rate in LPBF processes as suggested by the previously stated literature. However, the study did not show any significant effect on understanding the microstructural behaviour of the material, with neither microstructural characteristics nor cooling rates being thoroughly examined. Moreover, only a single type of laser was used, and the structures created were simple walls rather than complex MAM samples.

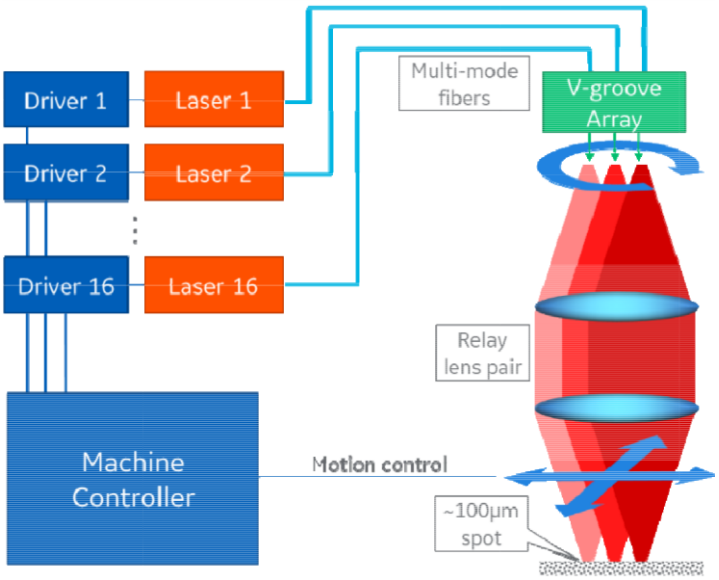

Figure 2.15 - Karp et al.'s system schematic [117]

Payne [118] undertook research focusing on the use of multiple diode lasers in PBF (Figure 2.16). He used an array of seven diode lasers, similar to the DAM system, to investigate the overall build quality of the system and the effect of beam quality on the samples. Payne noted that while the system showed promise for scalability, the use of pulsed-mode lasers in these multi-laser setups had drawbacks. He also pointed out that increasing the number of lasers beyond a certain point would lead to a significant increase in power consumption in the future. However, the study did not show any AM parts produced by this method.

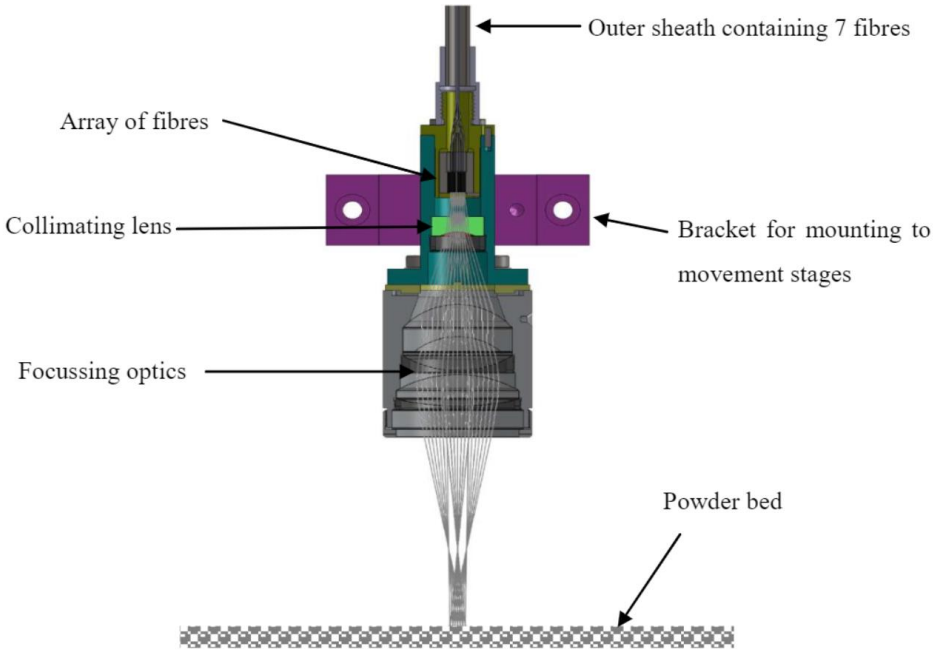

Figure 2.16 - Payne's system schematic [89]

Several key advantages of a novel area melting approach, which can be summarised in a simplified way, have been outlined by Arredondo *et al.*'s research [14–16]. Instead of using solid-state IR fibre lasers directed by galvo mirrors, this approach uses an array of individual short-wavelength diode lasers. This change results in a faster process, a smaller main power source, reduced costs and a more compact system. Unlike the fixed spot size of fibre lasers and their optical components, this technology offers an adjustable spot size, allowing larger areas to be melted without compromising the laser's maximum energy distribution. In addition, these diode lasers have a high wall-plug efficiency of 50-80% [119,120], which is significantly higher than the approximate 20% efficiency of fibre lasers [109,121]. Another advantage is the ability to perform optical preheating, which is both more efficient and faster for heating specific areas. In addition, the diode lasers are replaceable, increasing the long-term compatibility and sustainability of the system [14].

Despite its advantages, area melting approach presents several challenges. Key among these are design constraints and a lack of research into the integration of multiple lasers into a single array. The behaviour of the melt pool in DAM is particularly complex, and there's a significant heat-affected zone around the edges of the geometry, which can extend up to 1000 µm [8]. Compared to fibre LPBF, DAM operates at a lower scan speed due to its 3-axis gantry laser scanning system. In addition, managing the individually addressable diode lasers in DAM is not straightforward, largely due to limitations in existing software. The large area

covered by the laser also results in a wavy surface finish, as it creates wider melt pools than those typically seen in single laser SLM systems. This can affect the overall quality and consistency of the final product.

In order to fully understand LPBF variables and their effects on the sample quality and microstructure, it is crucial to examine deeper into the effects of LPBF variables and understand how they manifest as different phenomena. This detailed analysis will help not only in contrasting fibre and diode laser systems, but also in addressing questions of what kind of system is necessary to overcome for which phenomena for system development and commenting the results for hybrid processing.

2.4 LPBF Variables

To successfully achieve desired geometries with LPBF, it is crucial to understand the various process variables. These include factors related to the laser (i.e. power and wavelength), scanning (i.e. speed and strategy), powder characteristics (i.e. particle size and distribution), environmental conditions within the build chamber, and other relevant aspects. A detailed examination of these factors will be provided later to enhance understanding of their impact on the LPBF process and the quality of the final parts (Figure 2.17).

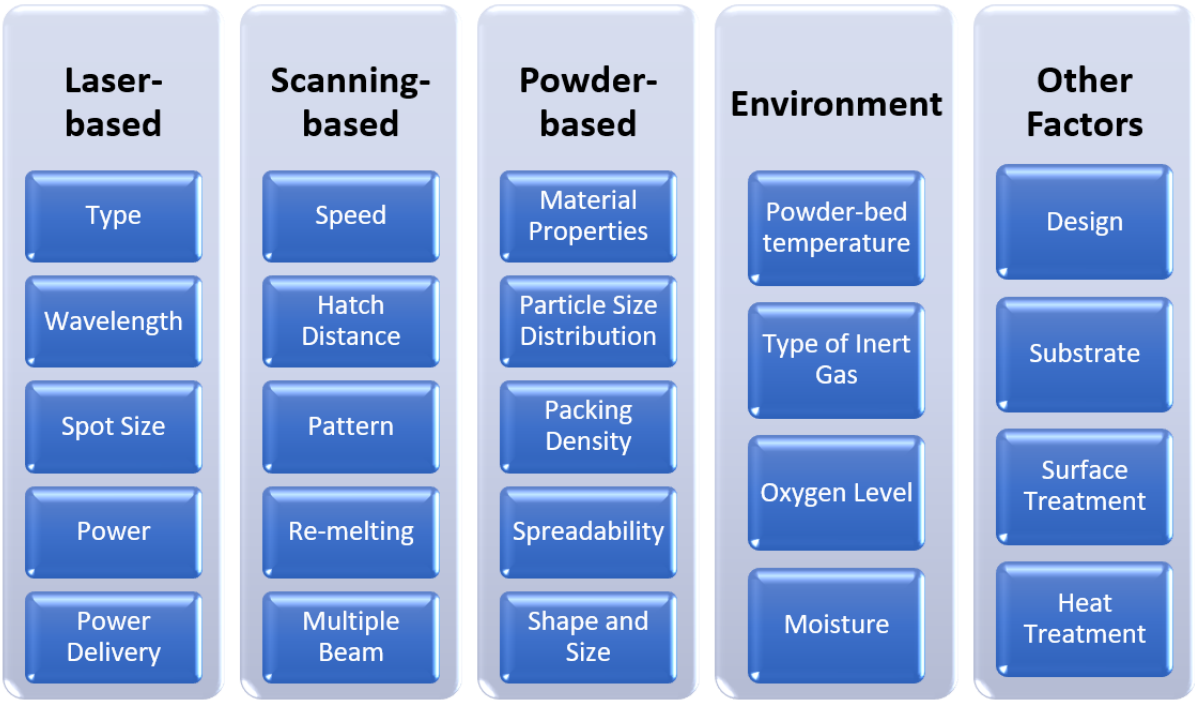

Figure 2.17 - Categorizing Key Variables in LPBF Technology

2.4.1 Laser-based effects

In LPBF, common laser types include solid-state lasers such as Nd:YAG fibre lasers, Yb-doped fibre lasers and fibre-coupled diode lasers which they had been chosen over CO_2 because of its high wavelength (around 10.2 µm for CO_2 lasers [116]) [122]. These are categorised based on parameters such as wall plug efficiency, output power, beam quality, wavelength, system robustness, maintenance cycles, lifetime and investment cost [3,99,122]. The laser beam distribution, or beam profile, is critical and varies with the type of laser [123]. Continuous lasers emit a steady beam that maintains constant power, while pulsed lasers emit beams in short bursts, allowing precise control over heat-input and minimizing thermal damage. Pulsed lasers are advantageous in applications requiring fine detail or where heat-sensitive materials are involved, as they prevent material warping and reduce the heat-affected zone. However, capital cost of these lasers are higher than that of a continuous wave version [124,125].

Lasers, which are essentially monochromatic, operate at a specific wavelength [126] and cannot focus light to a single point due to the wave-like behaviour of light, known as diffraction [127]. The precision of a laser's output is improved by the beam parameter product (BPP), which is influenced by the wavelength [122]. The smaller the BPP, the greater the energy distribution within the beam. The diffraction limit, referred to as "λ/π", defines the minimum BPP achievable, which can only be achieved with a Gaussian beam Figure 2.18. For simplicity, the beam quality factor (M^2) is used for classification, calculated as "BPP/diffraction limit", where a Gaussian beam typically scores 1 [128]. The Gaussian beam is a theoretical shape [129] with symmetrical cross-sections at the beam waist (w_z) (Figure 2.18-A-C), where the intensity peaks in the centre and decreases towards the edges [123,127,128]. It exhibits the 'fundamental' transverse mode (TEM_{00}), which is induced by inserting a circular aperture into the laser cavity, a technique demonstrated in Figure 2.18-C. The M^2 value for TEM_{00} is close to 1 in many lasers, but increases with the presence of multiple transverse modes [123,130,131].

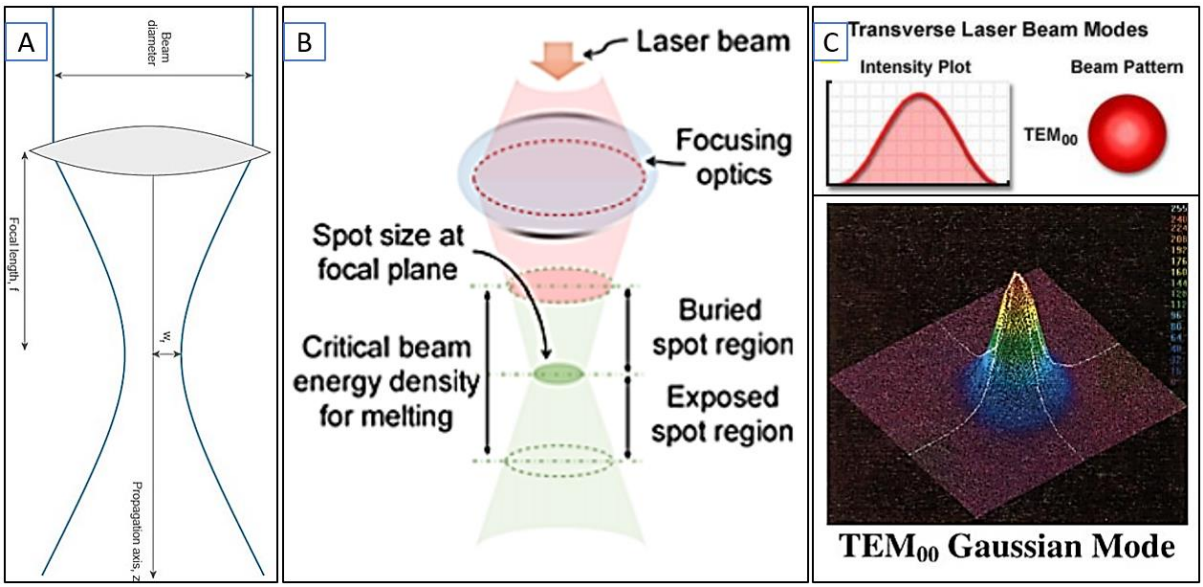

Figure 2.18 - (A) Diagram of Laser Beam Profile [132], (B) Depiction of Beam Post-Focusing Optics and Spot Size [133], (C) TEM_{00} Gaussian Mode Beam Distribution[127,134]

The beam waist will define the spot size of the laser and also the distance to the plane that the waist occur which is known as focal length (Figure 2.18-A-B). Spot size is a crucial parameter for energy transfer from photons to the powder bed. For instance, if the spot size is narrow a higher energy density can be achieved in the focal plane compared to large spot sizes, such as Nd:YAG and CO_2 lasers, respectively.

Power needs to be increased for a melting point to create a melt pool, and also energy densities needs be at a specific ratio so that scanning speed might also alternate accordingly to power. In general, there are two power delivery systems: continuous and pulsed power delivery [124]. Pulsed lasers can emit the laser in a very specific short time fixed repetition band, thus, the intensity of the laser will be tremendously higher than the continuous lasers because the peak power is much higher than the continuous one [124], but it will create high cooling rates which therefore affects the materials microstructure and even creates residual stresses [91,135].

2.4.2 Scanning-based effects

The scanning speed in LPBF plays a critical role in determining the energy density, with an increase in speed typically resulting in a decrease in energy density. Such changes can contribute to phenomena such as balling, warping and poor wetting during the manufacturing process [1]. Laser scanning strategies significantly influence structural integrity by affecting

the melt pool shape, cooling rates, and thermal gradients, which collectively determine the microstructure, residual stresses, and mechanical properties of the final part [55,136].

Another critical parameter that can be adjusted in the LPBF software prior to starting the process can be said that it is the hatch distance. This strategy is used to ensure overlap between scanned tracks, considering the intensity distribution of the beam. The energy distribution within the beam in LPBF is typically divided into two levels: Full Width Half Maximum (FWHM) and $1/e^2$ (equivalent to 13.5%) (see Figure 2.19). Depending on whether $1/e^2$ or FWHM is selected as the beam distribution factor, the hatch distance should be carefully calculated to match the selected beam spot size [123,127,128,137–139].

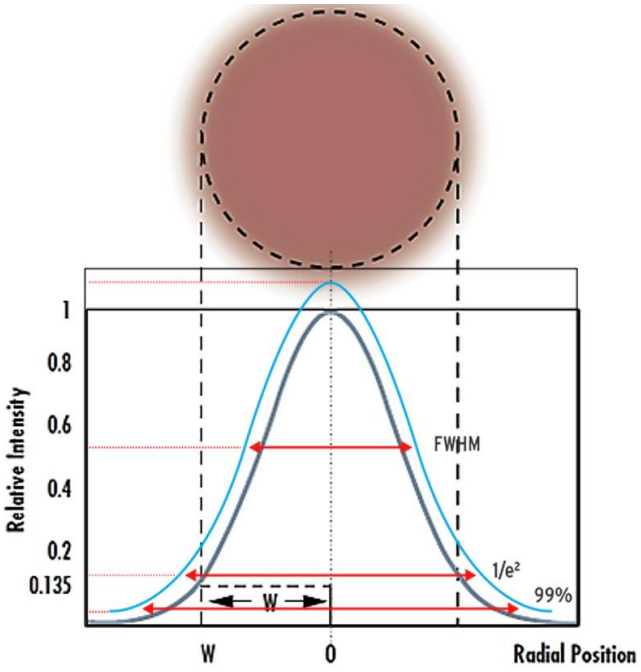

Figure 2.19 - Beam Distribution Factors [138]

It is often misunderstood that the terms 'build strategy' and 'scanning strategy' are interchangeable in additive manufacturing, when in fact they refer to different aspects. Build strategy refers to the choice of material, the morphology of the particles and the orientation of the design within the powder bed. In contrast, the scanning strategy involves decisions about laser power, speed and the pattern created by the movement of the laser [118]. The choice of scanning strategy can significantly affect various properties of the final product, such as temperature gradient [77], residual stresses [136,140,141], microstructure [142], melt pool boundaries [11,140] and densification [143]. Commonly used scanning patterns include line or unidirectional, island (also known as bidirectional), alternating layer, spiral scanning (which

can be either out-in or in-out) and checkerboard strategy [90]. These patterns, which play a crucial role in determining the quality and characteristics of the final print, are shown in Figure 2.20.

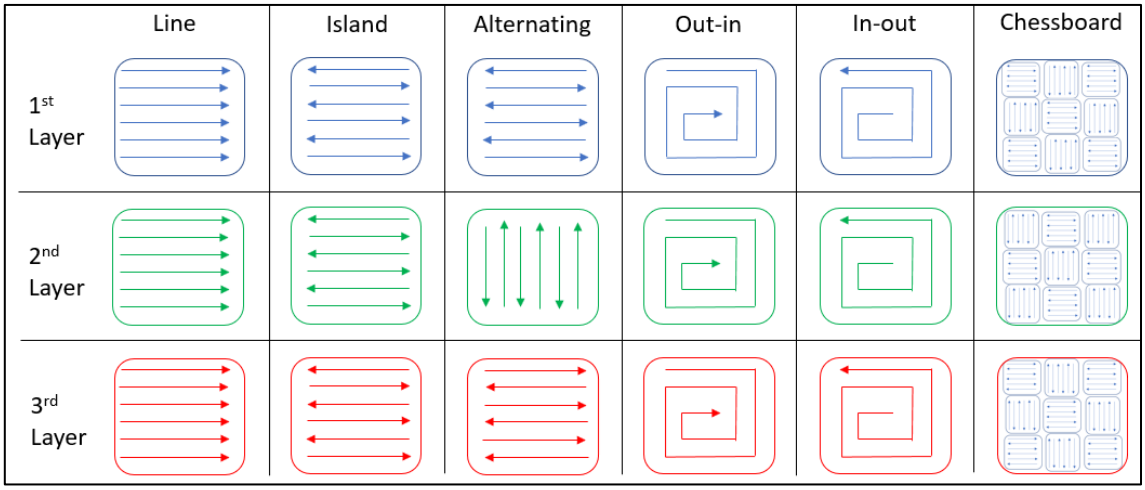

Figure 2.20 - Consolidated Summary of Various Scanning Strategy Patterns

The rescanning or remelting technique is used to increase relative density and surface smoothness while reducing thermal stress in materials [144–146]. This technique can be integrated with various scanning strategies, including adjustments in scanning speed [147], laser power [148] and preheating methods [144]. Rescanning plays a key role in altering the microstructure of materials as a result of the additional energy input either to solidified layers or by re-melting the layers [145,149,150]. These microstructural changes subsequently influence the mechanical properties of the produced specimens in accordance with the Hall-Petch relationship [36,145,151].

Another innovative development in this area is the multiple beam strategy, which aims to increase the build rate efficiency of the machine [116]. In LPBF, increasing the number of lasers in the build chamber can be achieved either by focusing all the lasers on the same spot [117] or by positioning them adjacent to each other. The latter approach creates a larger laser irradiated area while scanning the area perpendicular to laser array, a characteristic feature of DAM systems [116,152].

2.4.3 Powder-based effects

LPBF utilises powder as the primary material for deposition. The powder's characteristics are intrinsically linked to both metallurgical properties, such as flaws, grain

structure, grain growth, and solidification [5], and mechanical properties, including hardness, tensile strength, and yield strength [153,154]. Vock *et al.* [153] classified these properties into three groups: (1) powder properties, which include morphology, particle size distribution (PSD), impurities, chemical composition, moisture content, intrinsic density, and bulk material physical properties; (2) bulk powder behaviour, which encompasses flowability, powder packing, and powder physical properties; and (3) in-process effects, such as rakeability, bed-preheat temperature, and beam-powder interaction effectiveness. Additional categories have been added to the aforementioned groups in further studies [88,155–157], including spreadability. However, this section will not cover powder-bed temperature as it is not a system requirement for DAM systems.

Vock *et al.*[153] summarised that the morphology of particles, including their shape and structural relationships, was a complex subject that influences various aspects such as the thermal conductivity of the bed, laser absorption, and flowability. The chemistry of the powder has an impact. High oxygen levels can cause increased oxidation, affecting the material's melting behaviour and potentially compromising mechanical properties like ductility and strength. Lower oxygen content is preferred to minimise these effects and maintain the integrity of the metal's characteristics during and after processing. The size of the particles affects the spacing between neighbouring particles; coarser particles result in greater porosity within the bulk powder. If particles were too small (<10 µm), van der Waals forces become dominant over gravity, leading to agglomeration. Furthermore, smaller particles increase the total surface area, which can cause a rise in melt pool temperature due to enhanced laser absorption. In terms of shape, particles with higher sphericity generally have better flowability and therefore a higher packing density. Conversely, less spherical particles tend to interlock due to their edges, reducing flowability and creating uneven packing density across the bed, which could potentially lead to fusion issues or porosity.

Particle Size Distribution (PSD) is a critical factor in additive manufacturing. A well-balanced PSD can minimize porosity in the bed. A wider PSD results in lower internal stress, surface roughness, porosity, and distortion [5,154,158]. Additionally, powder beds with a broad PSD range exhibit higher thermal conductivity and reflectivity compared to those with a narrower PSD [27]. A lower PSD can also prevent segregation [159] and enhance flowability

[160]. Variations in PSD can affect not only the processing parameters of a part but also the rate of occurrence of physical phenomena.

Various powder properties such as shape, size and surface roughness affect the homogeneity of the powder bed layer in PBF [154,156,161]. A study [158] examined the influence of spreading velocity, layer thickness and powder morphology on layer uniformity, particularly for metal powders used in PBF. The study found that the texture and sphericity of the powders play a crucial role in determining the spreader velocity. This velocity is essential for maintaining a uniform powder bed. Moreover, the type of powder wipe blade used can vary depending on the material selected.

A study indicated that the use of finer particles resulted in components with less dimensional accuracy compared to coarser particles due to their lower flowability [162]. Furthermore, irregular shapes and roughness of particles [163] can adversely affect the spread characteristics and packing density of the powder bed. This can result in inhomogeneity and irregularities on the powder bed surface, therefore, manufactured part microstructural and mechanical properties [164]. Powder flowability is often linked to the angle of repose (AOR), with a consensus that a smaller AOR indicates better flowability, therefore, spreadability (Figure 2.21) [88,97,113,157].

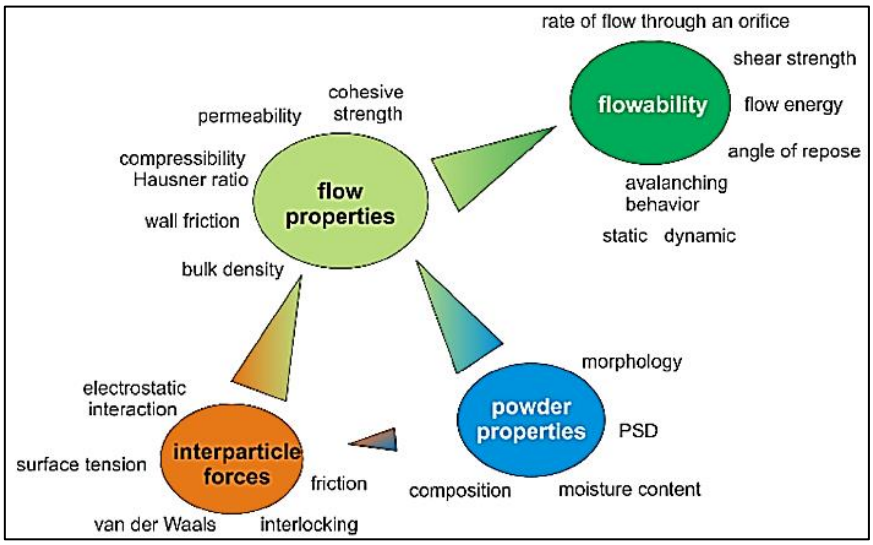

Figure 2.21 – Powder Properties summary illustrated by Vock et al.[153]

2.4.4 Environment-based effects

In LPBF systems, a high temperature gradient during the solidification phase leads to the formation of residual stress in the final product as discussed earlier [78]. To address the issue of high temperature gradients, elevated powder-bed assemblies (such as diode surface heating [165]) have been proposed as a solution. Furthermore, the DAM system has the potential for optical preheating by defocusing the lasers, which could increase the temperature of the raw powder and decrease the cooling rate, therefore, residual stress might decrease, and some mechanical properties can be improved such as ductility. However, there is a lack of research specifically investigating this optical preheating system in DAM.

It is crucial to maintain an inert environment to prevent metal oxidation or other chemical reactions that could adversely affect the metallurgical and mechanical properties of the final product. Therefore, the type of inert gas used should be carefully selected based on the material being processed [76]. The inert chamber may also be a vacuum chamber, making the oxygen level a consideration in either scenario. Moreover, it mentioned in section *2.4.3.* that moisture content has an impact on powder flowability. Specifically, higher levels of moisture can result in reduced flow due to powder agglomeration [88,153].

2.4.5 Other Factors

Designing for LPBF presents unique challenges for designers, requiring a different approach compared to subtractive manufacturing [7]. Factors such as overhang features and orientation must be carefully considered to minimize build time, save material, reduce post-processing material removal, and decrease surface contact between supports and the part [166]. The ISO/ASTM 52911-1:2019 standard for LPBF provides fundamental guidelines for part design and orientation before the deposition process [26].

Post-processing methods are commonly used in LPBF. These methods include surface treatments to improve roughness and heat treatment techniques for stress relief, achieving a more uniform microstructure and enhanced ductility [12,68,69,167]. HIP differs significantly from conventional post-processing heat treatments in that it combines high temperatures with isostatic pressure applied uniformly in all directions. HIP is used to reduce cracks and porosity, enhance phase stability, leading to improved mechanical properties such as

toughness and fatigue resistance compared to those achieved through conventional heat treatments that primarily rely on thermal cycles to alter the microstructure [69].

Substrate design is a critical aspect that affects wetting capability and sample removability. High residual stress may cause cracking between the sample and the support structure, even during the removal process [77,78]. Therefore, substrate design presents challenges that require potential solutions to overcome these difficulties [8,9].

2.5 Energy Density: Combination of LPBF Variables

Linear Energy Density (LED), Surface Energy Density (SED) and Volumetric Energy Density (VED) represent energy densities in one, two and three dimensions respectively. In LPBF, the consideration of different process parameters is crucial, as they individually influence the characteristics of the final product [1]. However, general rule of thumb is tend to focus on only one or two of these parameters. The primary parameters in LPBF - laser power, scan speed, hatch distance, and layer height - collectively contribute to the VED used in the process. VED is commonly used as a benchmark for optimising these parameters, as it provides a holistic view by incorporating all four key factors [1,27,52,53,55–57,168–172].

It was explained by Guo *et al.* [171] that the variation in laser absorption, especially at a constant input energy density, significantly influenced the melt pool variation. This absorption variation was attributed to the different effects of laser power and scan speed on the development of the deepening zone during melt pool solidification. It was found that the rate of energy absorption changes, leading to changes in the melt pool, even when the VED level remains constant. Specifically, at a constant VED level, an increase in energy absorption was observed when both laser power and scan speed were increased simultaneously. When very high energy density is applied, especially to alloys containing elements with low melting temperatures, there can be several detrimental effects. The excessive energy input can lead to overheating, resulting in the evaporation of low melting point elements, which alters the chemical composition of the alloy. This can cause issues like increased porosity, formation of undesirable phases, and a decrease in mechanical properties. Additionally, high energy density can lead to a larger heat-affected zone, which can exacerbate residual stresses and distortion in the final part [52,56,173].

Although VED can be explanatory in many aspects, it was found that VED does not explain melt pool physics and prediction of laser-powder interactions well enough [173,174]. Thomas *et al.* [57] compiled a comprehensive analysis of the factors influencing the microstructure of parts produced by LPBF and created a normalised energy density (NED-E_0^*). Beam quality, focusing, wavelength (therefore, surface absorptivity (coupling coefficient-*A*)), PSD (the authors assumed PSD of 0.67 and provided an explanation), scanning strategy, oxygen levels within the chamber, the specific heat capacity of the powder (C_p), single laser beam radius (r_b), thermal conductivity, diffusivity, material density, and its melting temperature (T_M), powder-bed temperature (T_0), layer height (l) and its normalised version (l^*), hatch distance (h) and its normalised version (h^*), laser power (q) and its normalised version (q^*), and scanning speed (v) and its normalised version (v^*) were among the parameters under consideration. This research demonstrated that parameter dimensionless groups provide a broader explanation than VED. The E^* equation is the amount of energy needed to increase the local temperature of the powder bed to the melting temperature of the metal during one scan. Equation 1 (Eq.1) shows the final version after iterations with the influenced parameters of the E^* equation (Figure 2.22-A), including all other parameter integrations, as stated by Thomas *et al.*[57].

$$E^* = \frac{q^*}{(v^* l^*)} = \left[\frac{Aq}{(2vlr_b)}\right]\left[\frac{1}{0.67C_p(T_m - T_0)}\right] \qquad Eq.1$$

Alsaddah *et al.* [8,9] conducted a study on the NED regions of Ti6Al4V processed using 808 nm DAM, and 808 nm and 450 nm single diode lasers (Figure 2.22-B). They used E_0^* to represent the constant levels of NEDs required to raise the melt pool temperature above the melting point by scanning several times. This was calculated by multiplying E^* by $1/h^*$. In their study, the researchers made a significant modification by adjusting the beam radius to account for the elliptical shape of the spot that resulted from the activation of multiple beams. This adjustment resulted in a modified beam length along the scanning direction, which they referred to as $2r_m$. Consequently, they developed a new equation (Eq.2), which served as a modification of Eq.1, replacing r_b. They also adjusted h^* as shown in Eq.3.

$$2r_m = (n * 2r_b) + ((n-1) * d_g) \qquad Eq.2$$

$$h^* = h/r_m \qquad Eq.3$$

Where n represents the number of active adjacent lasers and d_g is the distance between diode lasers. Consequently, an understanding of all types of energy densities is critical to the establishment of a relationship between LPBF variables and laser-powder interactions.

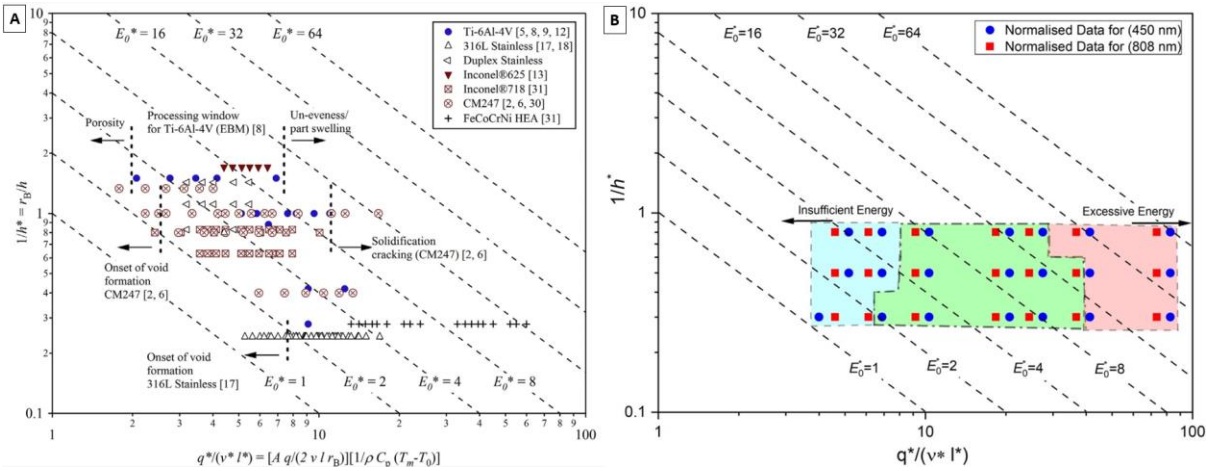

Figure 2.22 - Normalised Energy Density Representation (A) with Literature Data by Thomas et al.[57] (B) by Alsaddah et al.[9]

2.6 Laser-Powder Interaction During LPBF Process

The physical phenomena in LPBF arise from the interactions between the laser and powder, governed by both adjustable (laser power, scanning speed, hatch distance, scanning strategy, spreadability, and PSD (prior to selecting the material for experiments)) and fixed (system and environment related) parameters. These interactions and their resulting phenomena are illustrated in Figure 2.23-B [175].

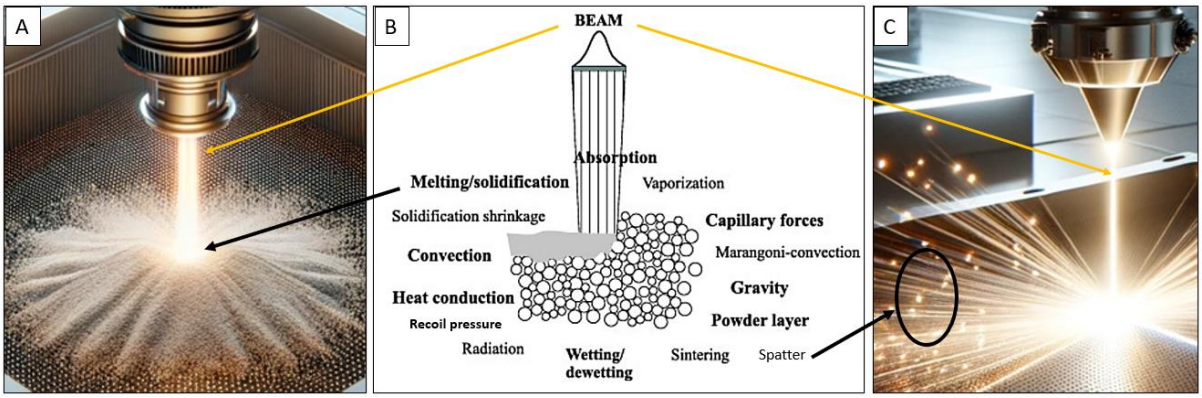

Figure 2.23 - (A), (C) Conceptual Visualizations of AI-Enhanced LPBF, (B) Overview of Physical Phenomena within LPBF Process[175]

2.6.1 Absorptivity

If the surface irregularities of a powder particle are smaller than the wavelength of the laser, the surface of the particle becomes specular, or in other words, it exhibits high reflectivity (the sum of reflectivity and absorptivity equals to 1) [176–178]. On the other hand, a shorter wavelength can result in higher beam resolution and improved focus quality due to the optical diffraction limit, and increased photon energy, respectively [128,178]. The absorptivity can depend on many factors for metal powders such as packing density of the powder, particle size distribution, thermal conductivity of the material, and layer height [176,179,180]. Furthermore, a higher PSD increases absorptivity. This is due to the reflection of light among the powder particles (Q_c), which converts some photon energy to heat, raising the overall temperature of the powder bed and consequently enhancing the absorptivity of the metal powders (Figure 2.24) [116,160].

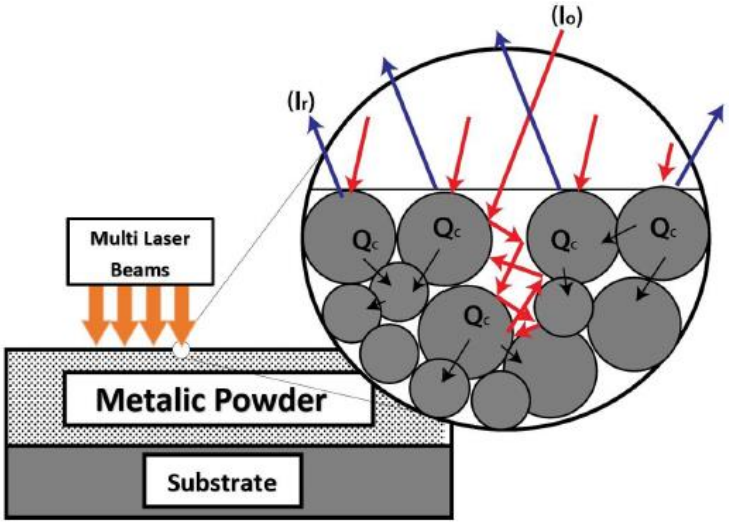

Figure 2.24 - Schematic Illustration of In-Situ Powder Absorption and Reflection: 'I_r' for Reflected Beam, 'I_o' as Laser Radiation, and 'Q_c' Representing Conducted Heat [116]

If the metal powder has low absorptivity, it may reflect light and cause incomplete melting if the laser power is insufficient [8,9,126]. A recent study [9] has demonstrated that employing diode lasers with shorter wavelengths can markedly enhance the absorptivity of metal powders. For instance, utilizing an 808 nm diode laser on the titanium alloy Ti6Al4V can boost its absorptivity by approximately 13% in comparison to a 1064 nm laser. Moreover, the application of 450 nm lasers on Ti6Al4V was observed to increase absorption by an additional 11% over the 808 nm diode lasers, underscoring the efficiency of shorter wavelengths in

augmenting energy absorption during laser processing experiments. (These data are shown in Figure 2.25).

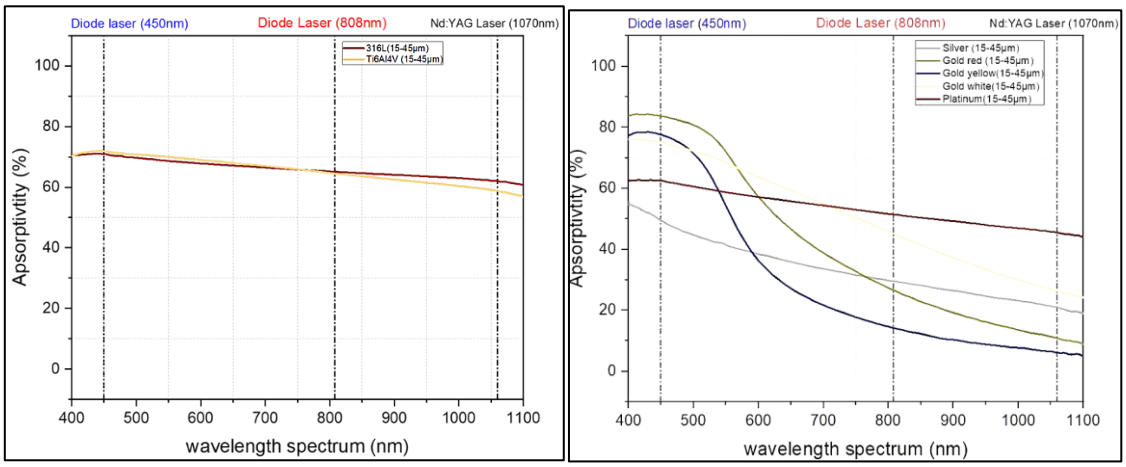

Figure 2.25 - Absorption Rates of Different Metals at Different Wavelengths

2.6.2 Marangoni Convection

To understand phenomena such as balling or wetting in LPBF, it is essential to understand the Marangoni flow and its influencing factors. Mass transfer within the melt pool is primarily driven by thermocapillary forces, commonly referred to as Marangoni flow or convection. The Marangoni effect is related to the surface tension gradient, which behaves as follows: first, in metals, surface tension generally increases with increasing heat input [181]. Second, due to the distribution of the laser beam, the heat input typically decreases from the centre of the melt pool towards its edges. Thirdly, the recoil pressure acts to push the melt pool downwards as the air immediately above the pool becomes extremely hot and expands. The combination of these factors results in two dominant types of melt pool motion [114,182,183], as shown in Figure 2.26. The dynamic viscosity of the melt pool must be carefully balanced; if it is too high (resulting in inward flow), balling may occur, whereas if it is too low (resulting in outward flow), the pool may not spread or penetrate effectively, affecting wetting [80,114,184]. Melting pool dynamics include several factors, such as melting pool heat conduction and convection, mass transfer, laser beam/powder interaction, and melt pool-powder-substrate relationships. The melt pool temperature and temperature gradient are directly related to the laser power. Conversely, these factors are inversely related to the scan speed. As far as the dimensions of the melt pool are concerned, an increase in energy density results in expansion in almost all directions [5,113,185].

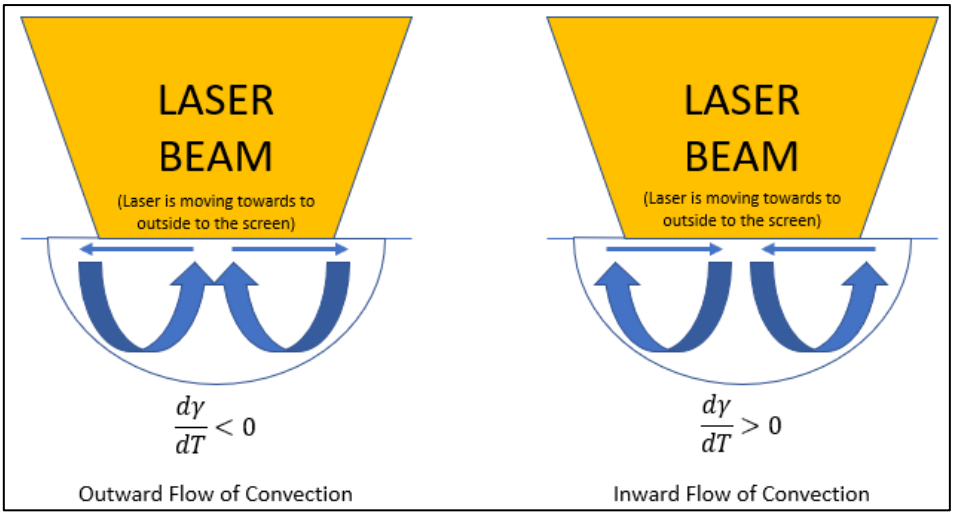

Figure 2.26 - Marangoni Flow's Directions Schematic

2.6.3 Balling

Balling occurs due to insufficient wetting of the underlying layer by the powder, coupled with the extremely high surface tension and low viscosity of the melt pool [186]. The term 'balling' is derived from the spherical shape of the solidified metal. This phenomenon is attributed to capillary instability, which causes the melt line to break into spherical shapes due to the high surface tension within the pool [186,187]. This can lead to increased surface roughness, porosity, and lack of fusion in the final part. Balling is indicative of low energy density in the process, suggesting that a combination of factors such as laser power, scan speed and layer height can influence these results [111,186–188]. By increasing the energy density, balling effect can be eliminated, however, each MAM system may behave differently.

2.6.4 Wetting

Wetting refers to the ability of the melt pool to adhere to a solid surface, in this case a layer in the AM process. The contact angle plays a key role in determining the extent of fusion to a substrate or layer and the likelihood of balling [189,190]. An increased contact angle, as shown in Figure 2.27, is associated with the occurrence of balling on the surface. Improving the wetting properties of the melt pool can be achieved by applying high energy density and by increasing the temperature of the powder [113,187,189].

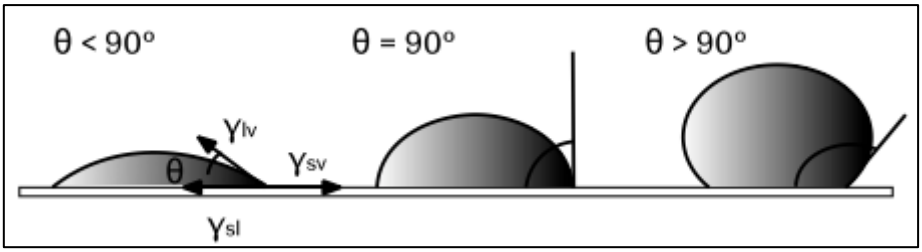

Figure 2.27 - Examples of Contact Angles: A Visual Representation [189]

2.6.5 Spattering and Vaporization of the Powders

Spattering occurs when particles in the vicinity of the laser spot are violently ejected, a process known as "spattering", while some are dragged to other areas of the powder bed, leading to a clearing around the laser-melted track, known as "denudation" [191,192]. The powder bed may be disturbed in a number of ways, including balling, porosity, inclusion and surface roughness. The detailed process involves several stages: first, as the metal vapour begins to be ejected, particles in and around the powder bed are blown up and drawn towards the vapour [193]. As the vapour moves, it continues to entrain particles from the powder layer, resulting in denudation zones near the scan path [194–198]. The scanning speed has been found to have the most detrimental impact on spattering (with an increase, spattering increases significantly), and three types of spattering introduced to the literature (Figure 2.28): droplet spatter, metallic jet, powder spatter [196].

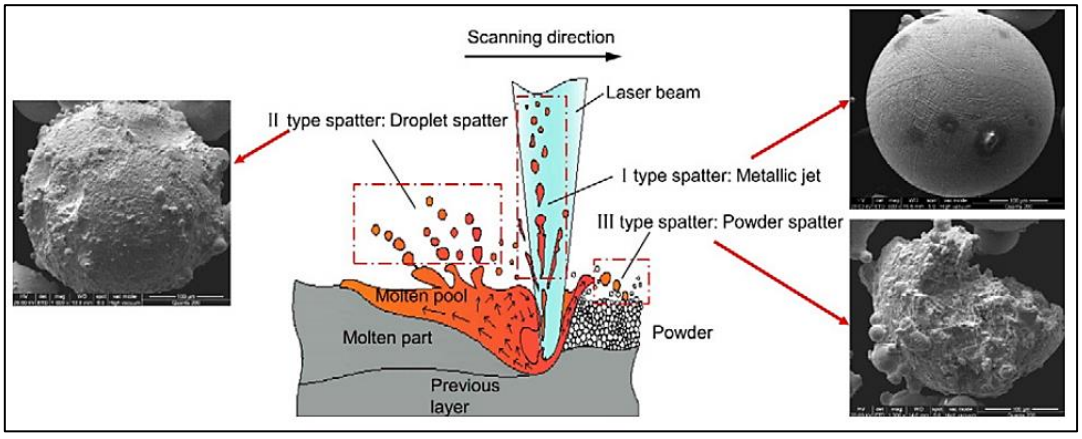

Figure 2.28 - Illustration of the three types of spattering [196]

2.6.6 Keyhole

In LPBF, keyhole porosity is a significant problem that can affect the fatigue life of components. Keyhole porosity can occur not only in unstable keyhole regimes, but also in transient keyhole regimes created by high laser power-velocity conditions that cause rapid

radial keyhole fluctuations [199]. This phenomenon can lead to the formation of a bubble in the melt pool. This bubble can be trapped by the solidification front and form a pore. These keyhole pores remaining in the final part can act as stress concentrators and sites for crack initiation and growth, adversely affecting the mechanical properties of the final part. Generally, lowering the power will eliminate the keyhole issue [80,199–202]. The dynamics of keyhole pore formation is also influenced by factors such as recoil pressure, surface tension, Marangoni convection, gravity, drag, buoyancy and thermocapillary forces [202]. Keyhole collapse often results from a combination of these factors, leading to bubble formation and subsequent porosity (Figure 2.29).

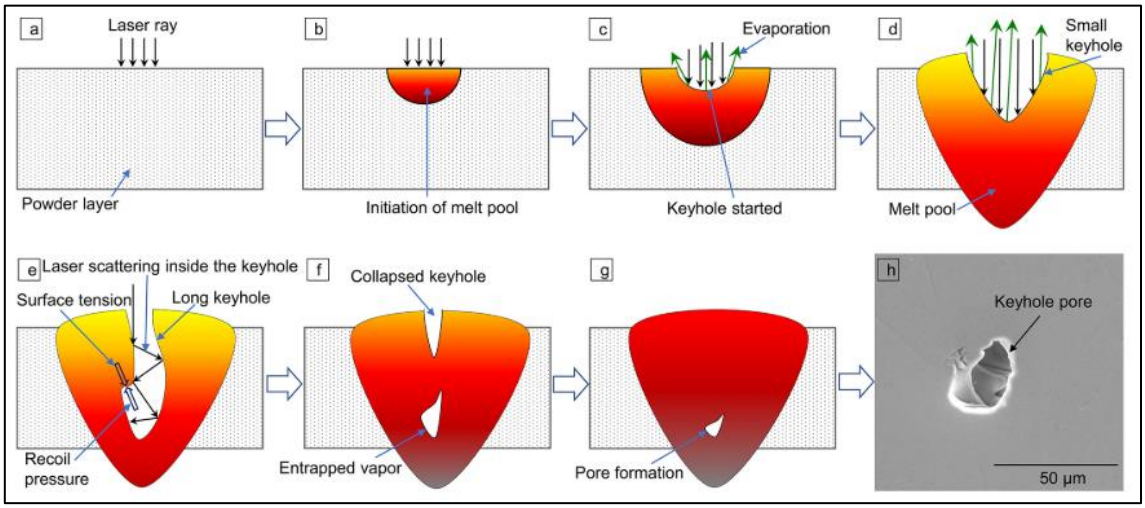

Figure 2.29 - Keyhole Phenomenon Illustration [202]

2.6.7 Porosity or Densification

Porosity is characterised by the presence of voids within the overall volume in the final part of a LPBF process. Several factors contribute to this porosity, including an unbalanced energy density (low energy density may cause high air porosity to the insufficient penetration, high energy density may create keyhole porosity), a narrow PSD, powder morphology and the occurrence of balling [99,186,203]. Other contributing factors include a high layer height, an excessively wide hatch distance, lower absorption rates due to wavelength [9], the presence of oxides, a low heat transfer coefficient within the powder bed, or insufficient energy density [1,170,204]. Melt pool instability, keyhole porosity and insufficient overlap can also lead to increased porosity. Porosity is a significant factor influencing surface roughness, cracking susceptibility, mechanical strength, fatigue resistance and overall density of the final part [170,205–207]. Adjustments to process parameters and the application of rescanning

(remelting) strategies are potential solutions to improve porosity issue via increasing density [150].

2.6.8 Residual Stress, Distortion, Delamination

In LPBF, residual stresses are mainly due to the large thermal gradients and rapid cooling rates inherent in the process especially with the single fibre LPBF processing [80,136,141,144]. As metal parts are manufactured, these stresses can cause distortion that can lead to failure during or after manufacturing and can cause parts to fall outside of acceptable tolerances. The distribution and magnitude of residual stresses in LPBF parts are highly anisotropic and variable, depending on process parameters, material properties and part geometry [78]. One direct method of controlling residual fields in LPBF has been to change the scanning pattern of the laser, where rotating patterns and the island scan method have been found to reduce anisotropy in parts [77,208]. In addition, the thermal conductivity of materials plays a significant role in controlling the magnitude of RS developed as if it has high conductivity, RS may be lower than that of a low conductivity material [80]. It was suggested that thermal material properties have a more dominant influence on RS development during PBF processing than mechanical properties, although an increase in tensile strength and yield strength showed a weak correlation with residual stress [10,77,136,146]. Pre-heating the solidified layer was shown to reduce residual stress [165] as well as heat treatment methods to eliminate residual stresses such as HIP or annealing [12,209,210]. The geometrical distortion defects in the production process, as detailed by Kruth *et al.* [211] and illustrated in Figure 2.30, arise from the thermal cycles involved in spreading cold powders onto a previously heated layer or processing without preheating the powder bed, where the thermal conductivity and coefficient of expansion of the powder are critical. In addition, increasing surface tension leads to elastic deformation at the top surface, while the bottom surface undergoes buckling or plastic deformation during solidification. Delamination, the separation of layers after solidification, occurs due to insufficient melting resulting in lack of fusion, and is primarily caused by residual stresses, poor wetting of the melt pool, insufficient energy density and, most importantly, the thickness of the layers involved [212].

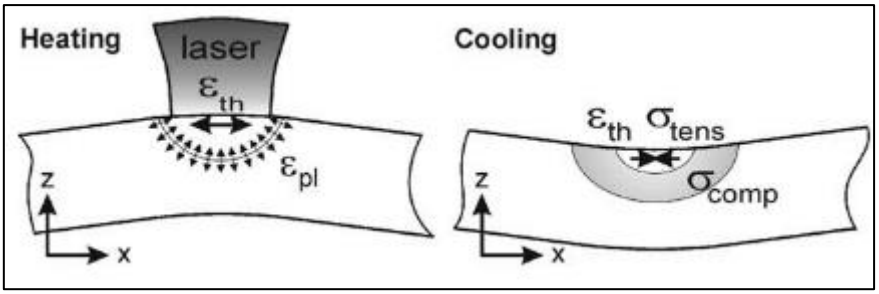

Figure 2.30 - Illustration of the Distortion [16]

2.7 State-of-the-Art and Literature Gaps

The most closest study for a hybrid lasing strategy was done by Gong *et al.* [95]. However, they investigated hybrid laser AM by combining LPBF and DED techniques on AlSi10Mg alloy (Figure 2.31). In their research, they observed that the top 200 µm of the LPBF region underwent in-situ annealing due to the sequential high laser energy input from the DED process, changing the distribution morphology of the parts. In particular, the microstructure in the lower 30 µm of the DED region was found to be significantly finer than in other areas of the DED zone. This finer microstructure was attributed to greater undercooling at the bottom of the melt pools due to the heat sink effect of the LPBF substrate. As the DED process progressed, the heat input to the substrate was greater than in the LPBF process, resulting in heat accumulation. This led to a slower cooling rate of the melt track, thereby stabilising the thermal environment of the melt pool. As a result, the microstructure in the subsequent layers formed by DED remained stable. In addition, the study revealed a marked change in the microstructural morphology around the LPBF/DED interface zone, with the distribution of major elements showing significant variations. The higher heat input of the DED process had an influence on the solidification process and the distribution of the elements, which resulted in clear differences in the microstructure between the LPBF and the DED zones. On of the limitation is that the process involved transferring the sample between various deposition methods, utilizing different MAM technologies. Another limitation of this method is that it cannot be used to produce materials that are prone to oxidation or flammability, as the sample needs to be removed in order to proceed.

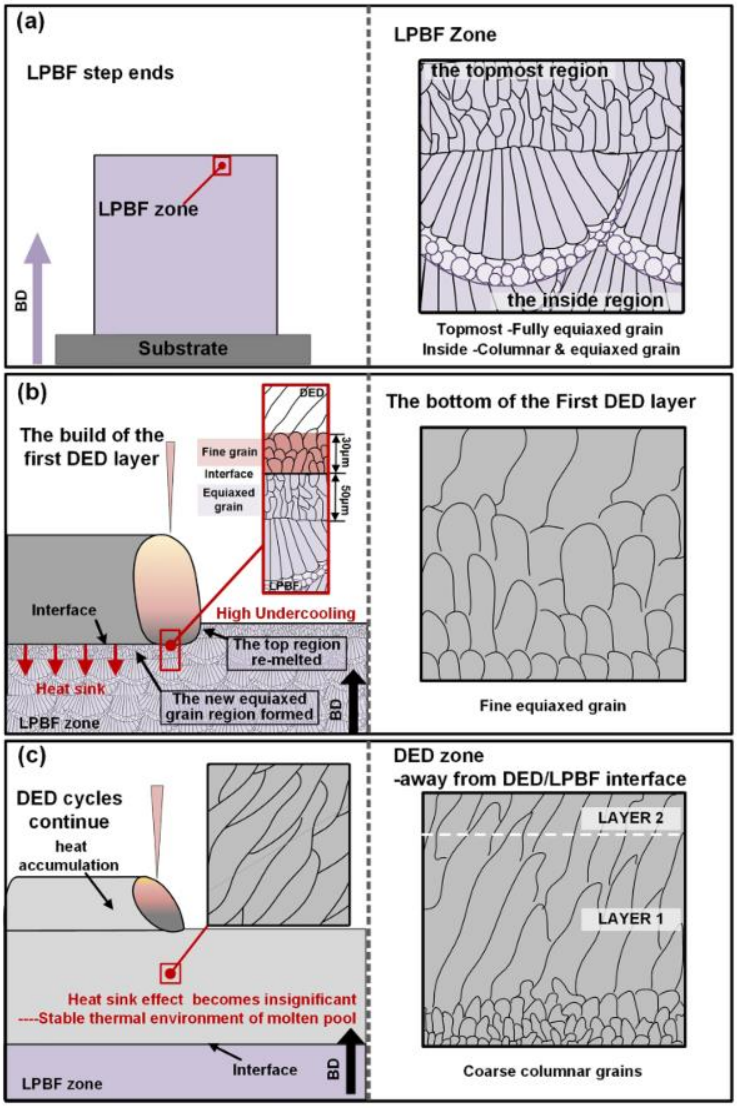

Figure 2.31 - Gong et al.'s hybrid laser system schematics [95]

Based on the literature review, several gaps have been identified that need to be addressed:

1. Microstructural control in both single and multi-fibre LPBF systems is limited due to high cooling rates, typically necessitating post-process heat treatment to achieve desired properties.

2. While the double array 808 nm DAM system allows for microstructure tailoring, the side surface roughness impedes the transition to near-net or net shape processing.

3. Recommendations for enhancing the 450 nm DAM system's efficiency have been made; however, no studies have implemented a multi-diode laser approach for producing LPBF parts. Previous DAM research used an 808 nm system with 50W total power, focusing solely on the effects on Ti6Al4V microstructure.

4. There is a lack of research on the effects of multiple 450 nm beams within a single diode laser array on the Ti6Al4V powder bed.

5. Differences in cooling rates and their impact on microstructure have been explored through combined LPBF and DED processes, yet they still require post-processing.
6. A hybrid laser powder bed fusion process, combining single-fibre and multi-diode LPBF systems, has not been investigated, which could potentially allow for precise microstructure control without compromising the quality.
7. The impact of overlapping different lasing technologies on the microstructure of Ti6Al4V samples remains unexplored.
8. Studies on LPBF variables indicate the necessity for a novel, bespoke LPBF system to address the limitations of existing fibre and diode laser systems and to minimize laser-powder interaction phenomena.

These gaps highlight the need for a new system design, specifically tailored to explore these unaddressed areas. This bespoke system would be crucial for delving into the identified gaps, designed with the sole purpose of advancing research in this field without exceeding its intended capabilities.

3. Experimental Methodology

3.1 Introduction

The methodology chapter encompasses a system development segment aimed at elucidating the construction of the HLPBF system, offering detailed insights into the components used and their integration Furthermore, this chapter thoroughly investigates the materials utilised in the experiments, providing detailed descriptions of the multi-laser head of the DAM system and the fibre laser equipment (FLM). It comprehensively analyses the lasers utilised, the test equipment employed, and the recorded measurement process. The section also examines a comprehensive discussion of the reliability of the test results and the equations employed in the thesis.

3.2 Bespoke Hybrid Laser Powder Bed Fusion (HLPBF) System Development

The HLPBF system represents an advanced manufacturing technique that employs two distinct types of LPBF technology in order to fabricate metal parts of high quality. These technologies are FLM and DAM respectively. The HLPBF system schematic and proposed operational schematics are shown in Figure 3.1. In order to fully integrate these two systems, several modifications will be necessary. These modifications will involve the selection of the most suitable FLM equipment, the redefinition of the DAM system to be compatible with 450 nm diode lasers, the implementation of a gantry system for the multi-laser head (MHGC), a diode laser power controller (DLPC), and a diode laser temperature controller (DLTC). Subsequently, a fully enclosed processing chamber needs to be created to accommodate the wiper blade (selection was made based on [88]), reservoir, and build piston controller, as well as the vacuum motor and air knife for argon circulation. The hierarchical operating procedure of the HLPBF system is explained in Figure 3.2. All the designed components were created using Fusion360 software.

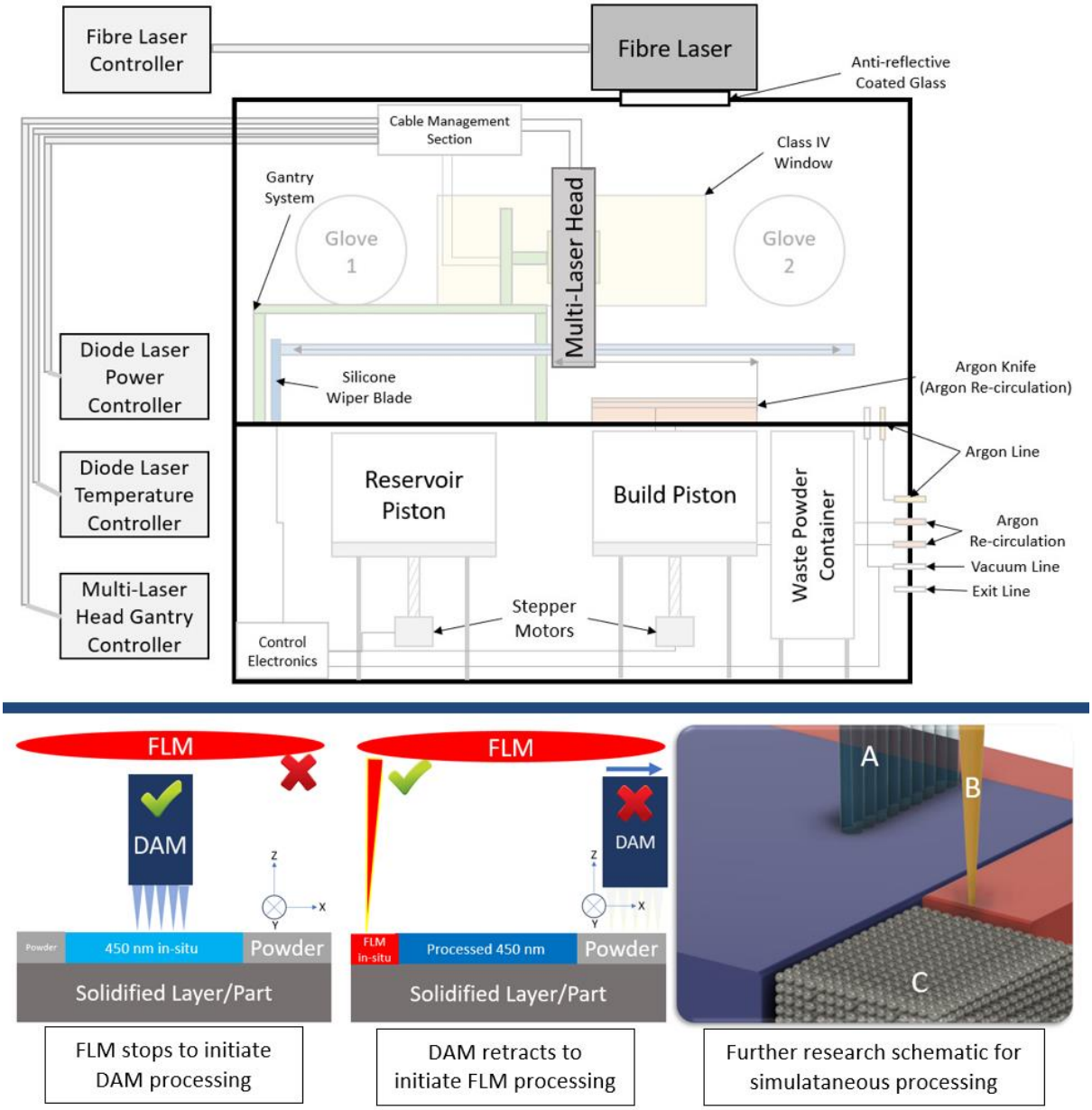

Figure 3.1 - Schematic Diagrams of the HLPBF Assembly and Operational Procedure

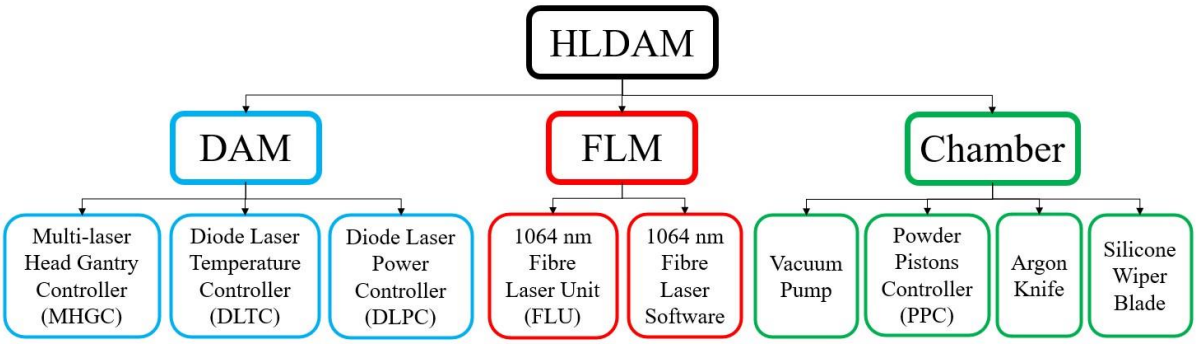

Figure 3.2 - Comprehensive Hierarchical Listing of Components in the HLPBF System

3.2.1 Selection of a Similar Industrial-Type FLM System

According to the available data in academic literature and market research, it has been established that a high-precision FLM system typically operates within the wavelength range of 1060 nm to 1070 nm [1,96], employing a galvanometer scanner to optimize operational speed. In alignment with this, a 1064 nm fibre laser was specifically selected to configure the high-precision segment of the HLPBF system, drawing from the inventory of the mechanical engineering department at the University of Sheffield. The detailed specifications of this laser can be found in Table 3-2.

To ensure precise focusing, a final focus lens with a diameter of 16 cm exhibiting f-θ type characteristics was chosen for the laser. The dimensions of the powder-bed area were determined by this critical choice. The laser operates within a square-shaped operating window measuring 200 mm by 200 mm. The fibre laser unit (FLU) consists of a fibre laser temperature and power control module, a PC dedicated to operating the fibre laser with its associated software, and a 1064 nm fibre laser incorporating an integrated galvanometer scanner, as illustrated in Figure 3.3

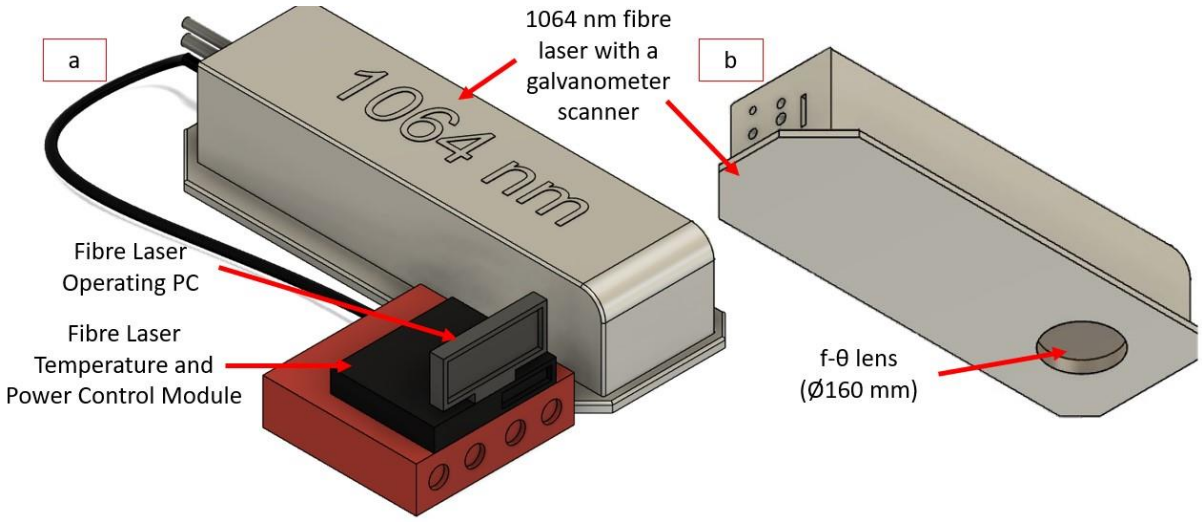

Figure 3.3 – Design and Functionality of the Fibre Laser Unit (FLU): (a) Schematic of the 1064 nm Fibre Laser, (b) Illustrated Bottom View of an f-ϑ Lens

The Thinklaser SLM 2.0 software, designed for fibre laser applications, possesses the capability to consolidate multiple parameters into a singular parameter map, thereby covering the entire laser area. This unique functionality allows for the generation of up to 100 distinct samples with varying parameter settings. Operating on the "mm/s" unit, this system

is inherently optimized for high-speed operation, facilitated by the integration of galvanometer mirrors within the system. The adjustable parameters encompass hatch distance, scanning strategies (excluding chess and alternating chess patterns), power adjustments ranging from 20W to 200W, focal length adjustments (±30 mm), overlap strategies, and dwell time.

3.2.2 Development of a DAM System Tailored for 450 nm Compatibility

In order to enable compatibility with 450 nm studies, a novel multi-laser head was employed in this experiment (Figure 3.4). This custom-made multi-laser head was specifically designed to accommodate 50 diode laser fibres in a single array. The decision to utilize a single array was driven by the desire to reduce both the manufacturing cost and time associated with the head. The laser head has the capacity to produce an optical power output of 250W, with a maximum power of 5W per diode laser installed. The positioning of the lasers, spaced 127 µm apart from each other (Figure 3.4-e), was determined based on previous studies [8,9,14–16]. The gantry system of the multi-laser head covers a scanning area of 30 mm by 80 mm. The focal length of the designated lenses was set at 60±3 mm, due to the placement of the collimating and focusing lenses inside the multi-laser head. Unfortunately, the manufacturer has not disclosed the specific placement dimensions of these lenses, citing copyright concerns. However, it is known that the multi-laser head comprises a total of four lenses, including two collimator lenses and two focusing lenses. Notably, the final focusing lens does not have any anti-reflection material. The primary function of a collimator lens is to gather beams from various directions and redirect them in a perpendicular direction towards the exit surface of the lens. Conversely, a focusing lens is primarily responsible for collecting

straight beams and focusing them onto a single spot. The accompanying image provides an illustrative representation of the multi-laser head's primary schematics.

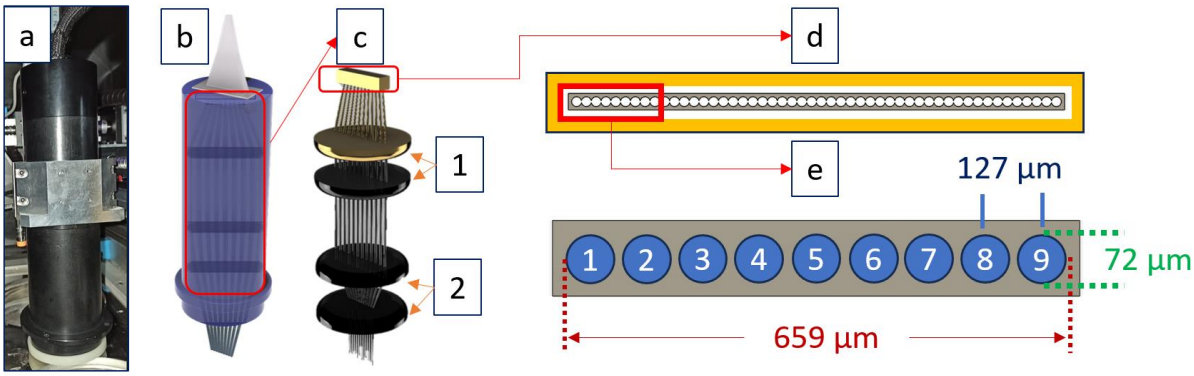

Figure 3.4 - Multi-laser Head Specification. (a) Real image view. (b) 3D illustration. (c) Inside optics. (d)Multi-laser head diode pitch schematics. (e) The 9-lasers used in this study with the FWHM laser irradiated area dimensions.

To activate the lasers during the manufacturing process, three distinct units were developed to ensure precise control and enhanced customizability: the Movement and Heat Gantry Control (MHGC) unit, the Diode Laser Temperature Control (DLTC) unit, and the Diode Laser Power Control (DLPC) unit.

The first component of the HLPBF system is the MHGC unit (Figure 3.5), which is manufactured by U-Mot Technologies in China. This unit is not custom-made and consists of various features such as four threaded rails for three-axis movement (1X-2Y-1Z), a g-code control screen for code overwriting, a holder for the multi-laser head, and limit switches. It is capable of supporting a multi-laser head weighing 3 kg and retracting it towards the reservoir after the completion of the 450 nm processing. This retraction creates space for the fibre laser unit to carry out the processing in the designated area. Proficiency in G-code is necessary to operate the 450 nm system. In order to execute the desired geometry with specific scanning strategies and hatch distance values, an open-source software called Pronterface was used to activate the g-codes during experiments.

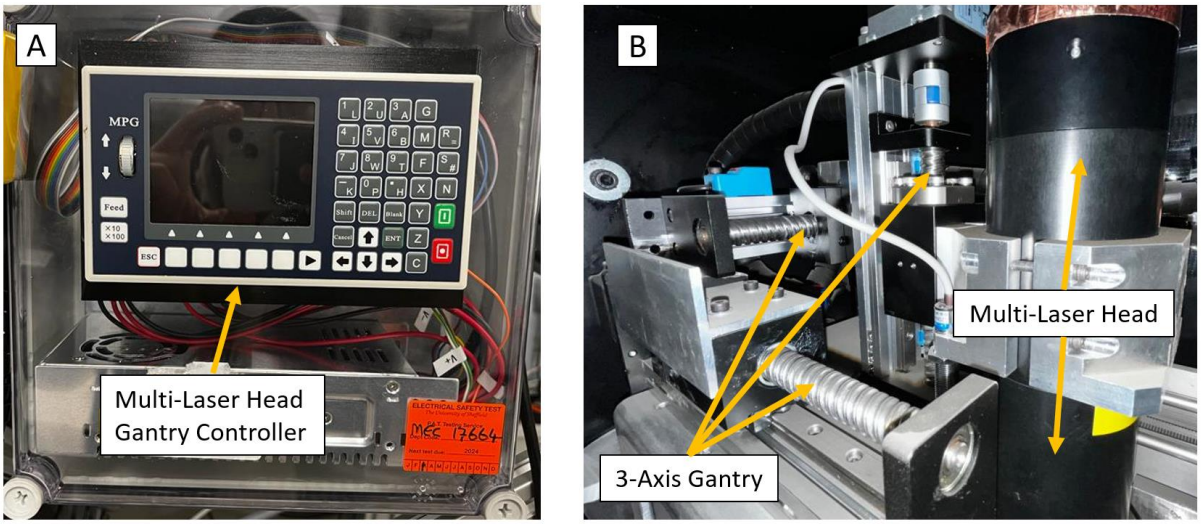

Figure 3.5 - (A) Detailed Look at the MHGC Module, (B) Implementation of MHGC with an Integrated Multi-Laser Head

The second unit, known as DLTC (Figure 3.6), was designed to maintain the optimal operating temperature for the diode lasers. It utilizes Peltier cooling modules (also known as Thermoelectric coolers or TECs) and consists of six 35W TEC modules positioned between an aluminium cooling block with thermal fins and a 10 mm thick copper plate. Each TEC is connected to a Voltcraft ETC-200+ temperature controller, with the operating temperature limits set between 15-20°C. An aluminium double-diode laser lock was developed to secure the lasers to the copper plate, allowing the DLTC unit to cool 12 lasers simultaneously during the processing.

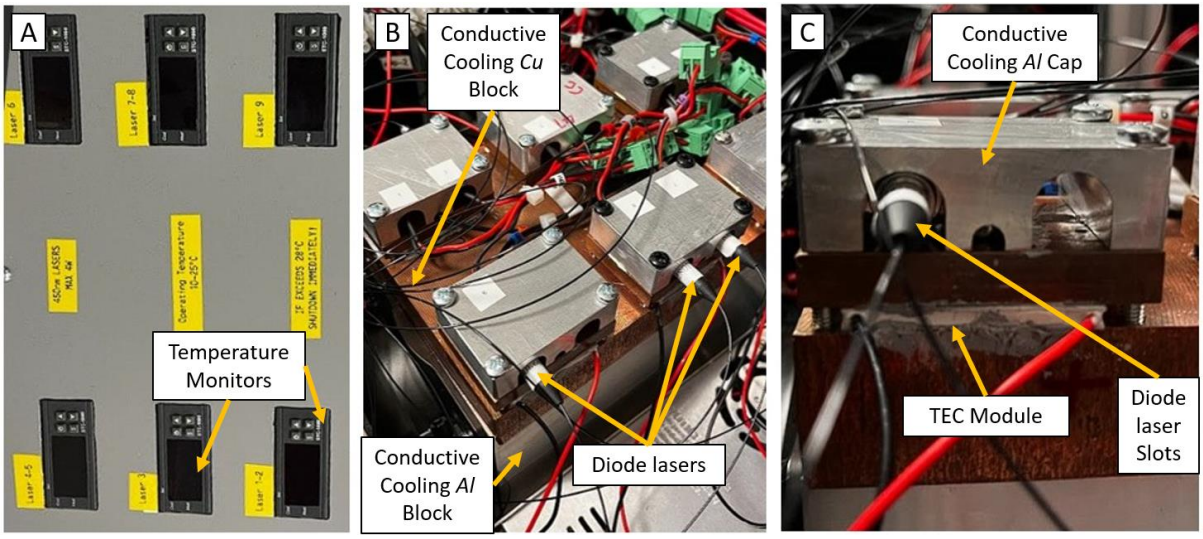

Figure 3.6 - (A) Top View of DLTC System, (B) Internal Structure of DLTC Featuring Multi-Laser Holders for Up to 12 Diodes, (C) Detailed Close-Up of a Peltier Module

Lastly, the DLPC unit, depicted in Figure 3.7, was designed to simultaneously operate nine lasers. It utilizes nine DPS5005 modules to ensure a constant and stable supply of current and voltage. Maintaining a consistent and non-fluctuating amperage supply is crucial to maintain the optical quality of the diode lasers. An image illustrating the assembly of the MHGC, DLTC, and DLPC units is provided for reference.

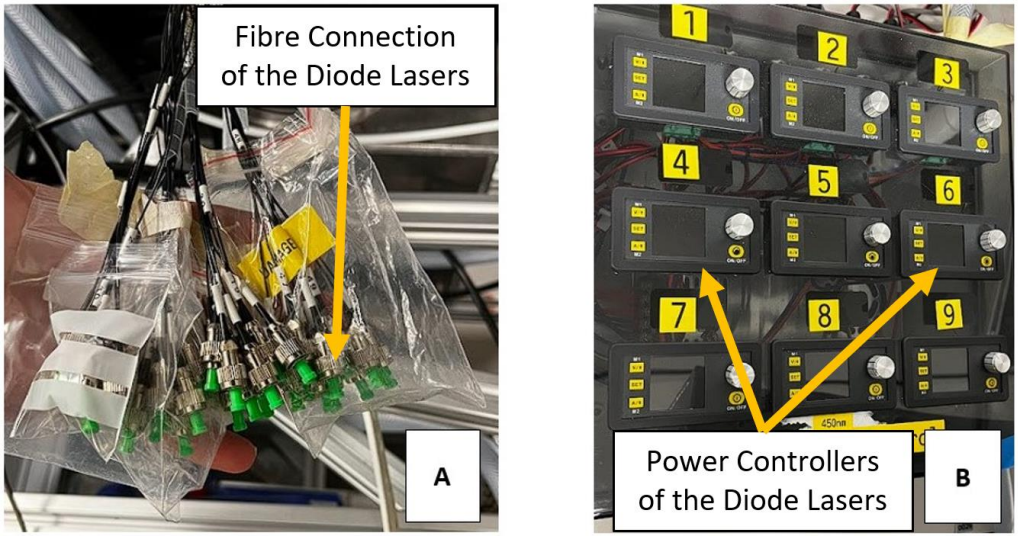

Figure 3.7 - (A) Schematic of Fibre Connections in the System, (B) Overview of the DLPC Module

3.2.3 Closed Airtight and Laser-Lighttight Chamber

During the initial phase of designing the HLPBF system, the focus was on the lower section. This approach was driven by the need to carefully position key components such as electronics, piston control mechanisms, argon knife, air pump for circulation, and vacuum lines. The dimensions and structure of the build piston and gantry unit were taken into consideration during this stage of development. Figure 3.8-A-B provides a visual representation of the design for the lower part of the system.

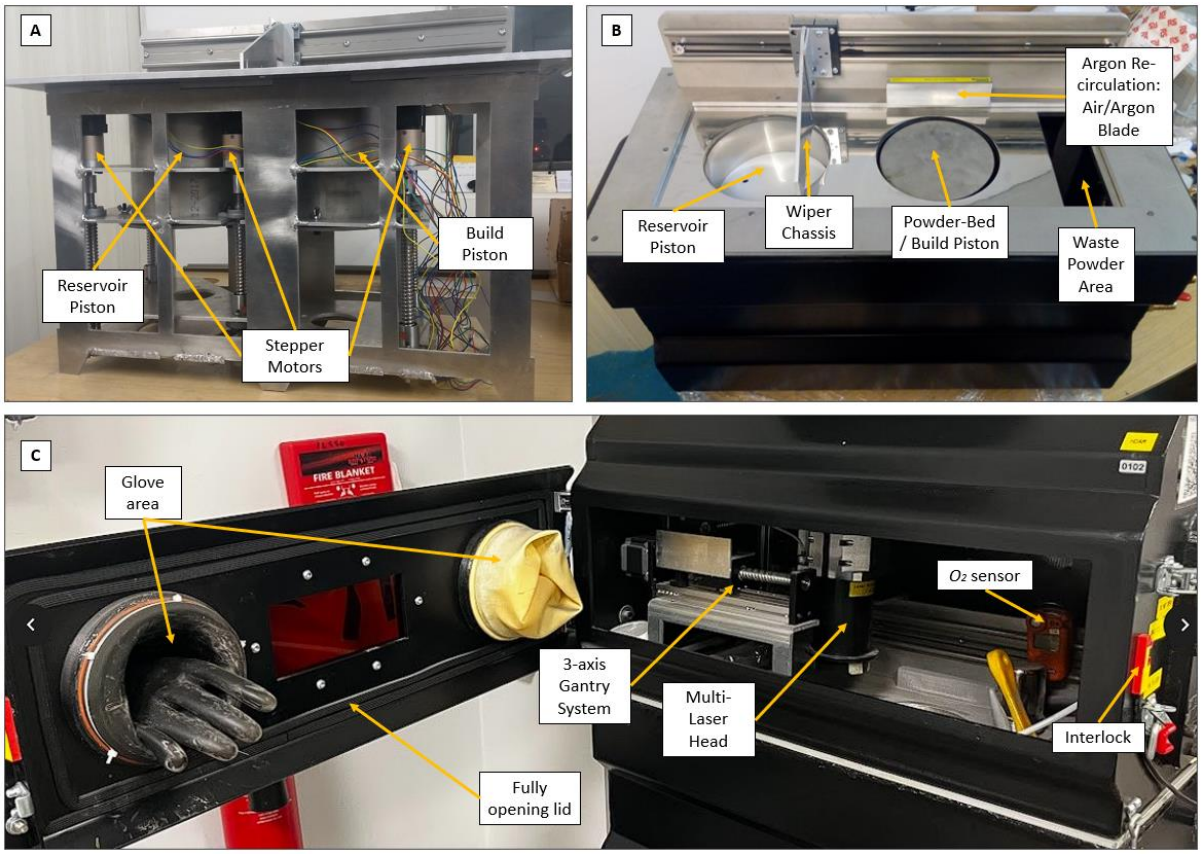

Figure 3.8 – (A) Interior of HLPBF's Bottom Part, (B) Powder-Bed Top View Photo(C) Authentic Footage of the System's Lid

The lid of the system was designed using Fusion360 software, with the main consideration being the effective positioning of the multi-laser head while maintaining focus for both the fibre laser and diode lasers. One notable challenge was the height of the multi-laser unit with attached cables, as it had to be accommodated within the limited bending angle of the diode laser fibres (restricted to 40 degrees). Additionally, a specific door design was implemented, which includes two hand gloves integrated into the door (Figure 3.8-C). Furthermore, a Class 4 laser protective window was incorporated into the door, allowing observation of the process and enabling the use of a thermal camera to investigate the melt pool.

The focal length of the multi-laser head was set to 60 mm from the bottom part, while the height of the multi-laser unit was 300 mm. The total height required, including the cables, was 450 mm, which precisely matched the focal length of the fibre laser. Consequently, the fibre laser was relocated to the right-hand side of the system. Furthermore, in order to prevent exceeding the bending limit, a cable escape system was devised adjacent to the galvo entrance circle. This design incorporated several bending curves due to the system's

requirement to sustain a vacuum pressure of at least -1 bar. The entire system was carefully designed to be airtight laser light-tight. After evacuating the air, argon was introduced to create an inert environment. To withstand the negative pressure, an aluminium sheet with a thickness of 4 mm was chosen as the suitable material. This decision was made based on the observation that a 1 mm thick sheet did not meet the required airtight criteria. The system's controller hardware was based on Arduino, with software utilizing Marlin (Open source). The HLPBF system's chassis and electronics were manufactured by a third-party company (WeDo3DPrinting Ltd. - Figure 3.9).

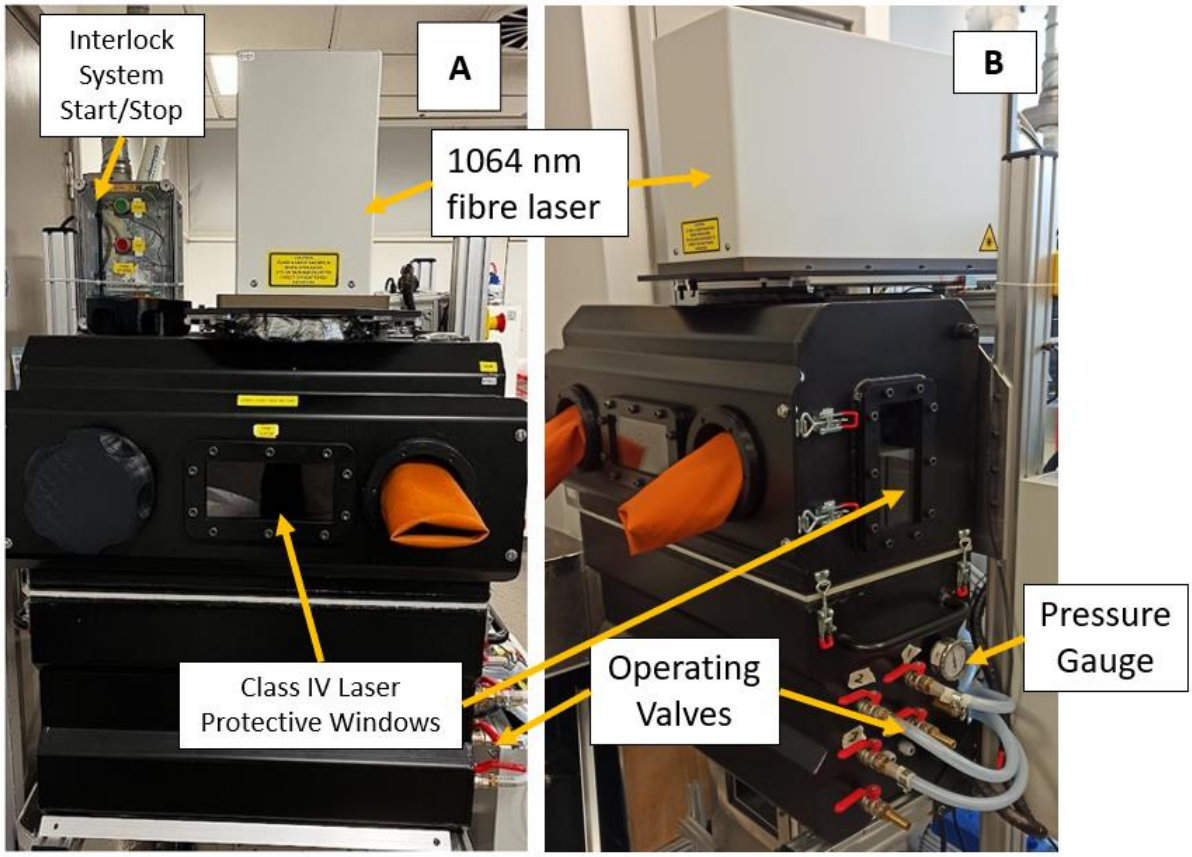

Figure 3.9- Authentic Visual Documentation of the Assembled HLPBF System

3.2.4 Ensuring Data Reliability and Integrity

The accuracy and reliability of data obtained from the HLPBF system heavily depend on its thorough calibration. For example, when the operator commands the piston to "Move up the build piston by 50 µm," the actual movement of the piston typically falls within the range of 48 to 52 µm. This variation is influenced by two primary factors. Firstly, environmental conditions such as temperature fluctuations can affect thermal expansion, subsequently impacting the frictional force and the accuracy of the piston's movement.

Secondly, the presence of fine particles lodged between the pistons and the board can disrupt smooth movement due to increased friction. The temperature distribution of the powder bed during the process further contributes to this effect. To mitigate these challenges, a manual height measuring tool (micrometre stand gauge) is utilized before each deposition cycle to ensure precise positioning. Additionally, a thorough cleaning of the system is conducted after each shutdown to address potential issues arising from powder residues. Furthermore, the HLPBF system incorporates a separation between the galvanometer scanner controller and the electronic control module for the multi-laser head gantry system. However, this separation can sometimes lead to misalignment among the lasers, impacting the contour and infill. To counteract this issue, an alignment laser embedded in the fibre laser is employed for realignment. Lastly, regular maintenance of the test equipment is essential to ensure precise and reliable results. Standard Operating Procedures (SOPs) and a comprehensive maintenance schedule have been established to guide and uphold the necessary maintenance protocols.

3.2.5 System Limitations

The limitations of the new system are defined by its scanning speed range of DAM, cooling system, oxygen exposure, pre-heating, and current productivity rate. The multi-laser head has a scanning speed range of 10-1000 mm/min (0.17 to 16.7 mm/s) due to the gantry system. Possible improvements include the addition of a galvanometer scanner or a robotic arm, which would enable the laser head to tilt and rotate. Secondly, the cooling system could be extended and upgraded to support up to 50 lasers, which is a significant increase from the current nine. It is important to note that although the DAM system is designed to minimize oxygen exposure, there is still a possibility of O_2 entering during argon circulation. This could lead to oxidation of the powder bed or built samples. To address interlayer fusion concerns, preheating the powder bed may be necessary, but it also poses a risk of heat-related damage to the closely positioned multi-laser head due to its focal length to the build plate. The study's findings suggest that the current productivity rate of the DAM system is approximately 0.104 cm^3/hr with 9 lasers. To increase productivity, possible solutions include increasing the number of lasers to create larger melt pools and reducing the number of scans per layer, increasing the scanning speed with more powerful lasers, or using pre-heating techniques with 2D laser arrays.

3.3 Material Specifications

The study employed gas-atomised Ti-6Al-4V Grade 23 from Carpenter Additive as the feedstock. Material is always handled in an inert environment. This material is also known as Ti.Gr.23, CL 41 TI ELI, Ti6Al4VELI, and Ti6Al4V ELI-0406. The material has a particle size distribution that ranges from 15-45 µm, with over 90% of the particles being spherical in shape [213]. Figure 3.10 provides a cumulative percentage plot of the material's PSD and a scanning electron microscope image, a and b, respectively. Table 3-1**Error! Reference source not found.** provides further specifications for this material. The powder packing density was taken as 0.66 according to the calculations from graph and literature [214].

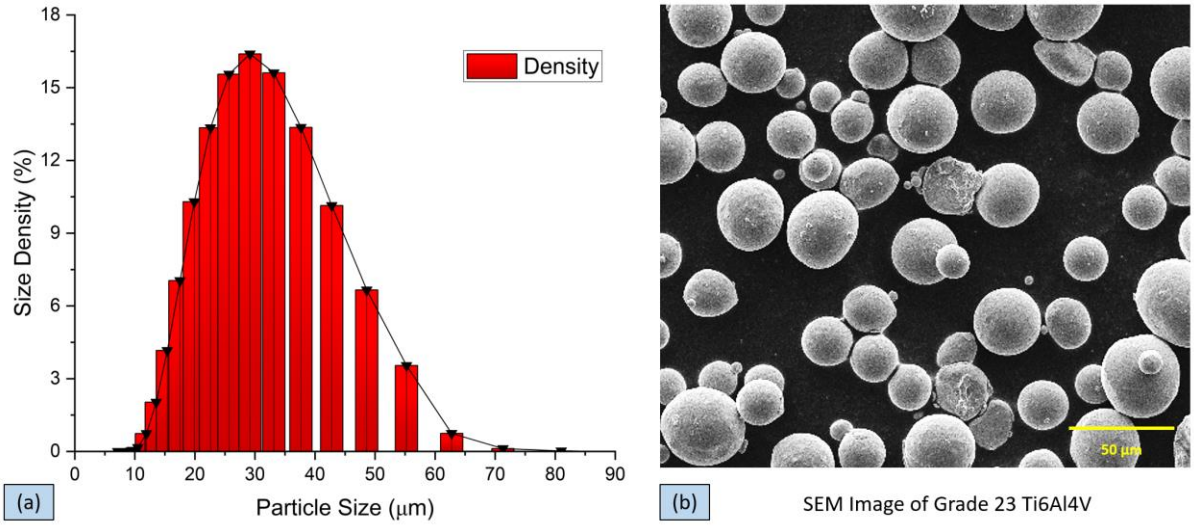

Figure 3.10 - Characterization of Grade 23 Ti-6Al-4V: (a) Detailed Particle Size Distribution, and (b) SEM Visualization of Raw Powder

Table 3-1 - Specifications and Properties of Ti-6Al-4V Grade 23 Alloy

Chemical Composition [215]

Element	Ti	Al	V	Fe	O	C	N	H	Y
wt%	Balance	5.5-6.5	3.5-4.5	0.24	0.132	0.08	0.03	0.0122	0.005

3.4 Lasers and their Characteristics

This section will comprehensively analyse various laser classifications, power variations, temperature-induced effects, and fundamental attributes that define laser beams.

3.4.1 Laser Types

This study employed three different laser sources: a 1064 nm fibre laser, a 3W diode laser, and a 4.5W diode laser. The laser names were abbreviated for ease of reference in the

research. The specifications of each laser are provided in Table 3-2**Error! Reference source not found.** to facilitate comparison in subsequent chapters. The 1064 nm fibre laser was used to verify the system reliability with literature and in the hybrid laser experiments. The 3W diode lasers were exclusively used in Chapter 5. The 4.5W diode lasers were used in the Chapter 5 and 6. The 1064 nm fibre laser operates in 'mm/s' unit perimeter, while the DAM system operates in 'mm/min'. The operating velocity limit for the 1064 nm fibre laser is between 100 mm/s and 3000 mm/s, and for the DAM system, it is between 10 mm/min and 1000 mm/min. All lasers are classified as continuous wavelength.

Table 3-2- Technical Specifications of 1064 nm and 450 nm Lasers

Brand Names	SPI 200W Fibre Laser	Beijing Reful Co. RH450-3-105-FC/PC	Beijing Reful Co. RH450-45-105-FC/PC
Shortened Versions	1064 nm Fibre	3W Diodes	4.5W Diodes
Number of Lasers Used	1	6	9
Max. Power (W)	200	18 (3 x 6)	40.5 (4.5 x 9)
Beam quality (M^2)	0.98	0.945	0.945
Wavelength (nm)	1064	450	450
Wavelength Shift with Temperature (nm)	±3	±5	±5
Spot Size at $1/e^2$ (µm)	Ø100	Ø88	Ø72
Focal Length (mm)	450 ± 30	60 ± 1	60 ± 1

The system units were not changed during this investigation due to the complexity of scientific conversions, as this would make the systems incomparable with the literature. For example, the increments in the FLM systems are generally between 50-100 mm/s, which equates to around 3000-6000 mm/min. Therefore, one single increment for the FLM experiments is almost triple the size of the whole DAM operating limit, which is a maximum of 1000 mm/min.

3.4.2 Multi-laser Head Specifications

In this experiment, a new multi-laser head was used for 450 nm studies (Figure 3.4). The specifications of the multi-laser head are discussed in *section 4.2*. The effects of only the transverse scanning orientation were investigated in this research. The multi-laser head was never lowered below its own focused distance during the experiments. This was to prevent the multi-laser head from heated/molten powder's temperature from reaching as high as 1900°C. Therefore, it is possible that the lenses of the multi-laser head were damaged, which could have affected the reliability of the results. All defocusing experiments or measurements were conducted by moving the multi-laser in the up (+Z) direction, which is opposite to the substrate's build direction.

3.4.3 Laser Power and Temperature Distribution

The power losses of the 1064 nm fibre laser were measured by Thinklaser prior to delivery/assembly of the laser system. The power meter was placed at a focused point 45 cm away and defocusing adjustments were made using Thinklaser software. The measured power test data after 30 seconds of continuous laser energy applied to the power meter is shown in Table 3-3. It was concluded that the average output power loss at the base plate was approximately ±3%. The temperature at which the readings were taken was 20°C, which is the average temperature set for laser cooling in the software used by the company.

Table 3-3 - Evaluation of Power Output in the 1064 nm Fibre Laser System

Power Test (W)	50	100	150	200
Readings taken at base plate, after Scan Head and Sacrificial Window (W)	47.1	96.5	145.6	194.6
Final Output Acceptance Power (±3%)				

The optical output power of the laser was measured after 1 metre of fibre and multi-laser head loss using an optical power meter (Thorlabs PM100D-S142C) with a 30-second dwell time. Measurements were taken at different amp settings (0.5, 1.5, 2.5, 3.5 Amps). The average maximum optical output per laser was found to be 2.94W for 3W diodes and 4.33W for 4.5W diodes. The power losses through the fibre were calculated to be approximately 2% and 3.8%, respectively. The loss of the multi-laser head was calculated to be around 3% using both the fibre optical output and the focused output. To ensure scientific and comparable

results, the power was adjusted to 2.85W with the installation of 3W diodes and 4W with the installation of 4.5W diodes. The summary of the power dataset can be seen in the Table 3-4.

Table 3-4 - *Analysis of Power Output in 450 nm Diode Laser Systems*

Tested Laser\Output	Fibre Output (W)	Fibre Loss (%)	Focused Output (W)	Multi-laser Head Loss (%)
3W Diodes	2.94	2.0	2.85	3.06
4.5W Diodes	4.33	3.8	4.20	3.00

During the experiment, it was observed that the operating temperature of the diode laser had a significant impact on the optical power output. As a result, a small calibration experiment was conducted to determine the optimal operating temperature for the diode laser. The experiment was conducted within a temperature range of 0 to 30°C with 5°C increments, as the maximum operating temperature limit for the diode lasers is 30°C. All lasers were set to their maximum power output. The lasers were defocused by approximately 10 mm from the focal point in the opposite direction to the substrate (moved upwards). Power data was collected with a 30-second dwell time and averaged for output. Six lasers were used in 3W diodes, and nine lasers were used in 4.5W diodes. Based on experimental results, the diode laser temperature needs to be above 20°C to deliver the designated power. Therefore, the laser cooling temperature module was set to operate between 20 and 28°C. The experimental data output is presented in Figure 3.11.

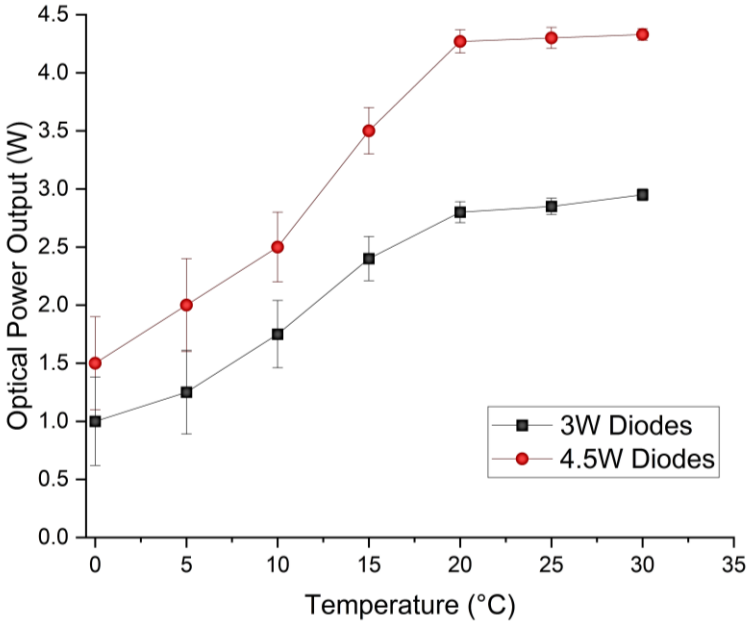

Figure 3.11 - Analysis of Optical Power Output in Relation to Operating Temperatures of Lasers

3.4.4 Laser Beam Characteristics

The Thinklaser company measured the beam quality of the 1064 nm fibre laser using a Spiricon SP620U Camera and the software BeamGage. According to the setup procedure, the spot size and beam quality matched the industry standard SLM systems. The claimed spot size was set in the Thinklaser Software as a circular 100 µm Gaussian beam shape with an M^2 value of 0.98. The size and shape of the diode lasers were measured using a NanoScan2sPryo/9/5 profilometer scanning slit and NanoScan software (Figure 3.12).

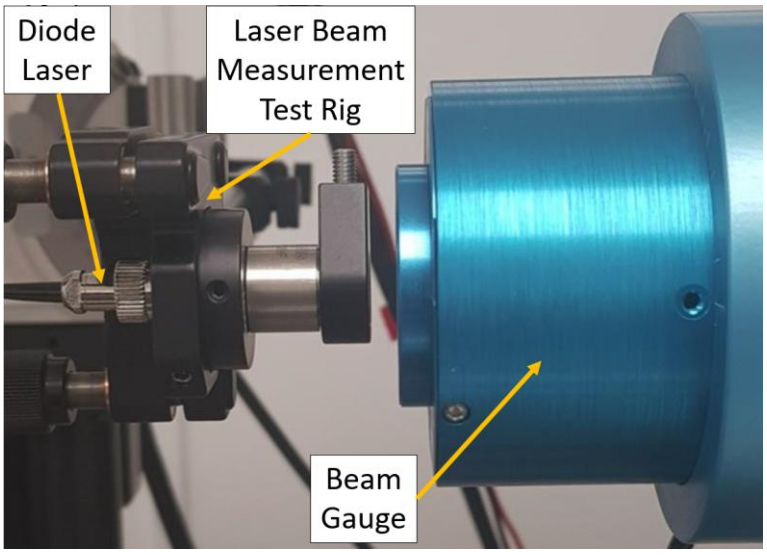

Figure 3.12 - Laser Beam Measurement Operation

The lasers were focused at the top of the scanning slit, and the laser power was set to 0.5A for 3W diodes and 0.7A for 4.5W diodes (approximately 1W per laser (±0.1)) during the scanning process. The resulting each specific laser measurement was a single spot size was observed to be 72 x 72 ±1 µm and 659 µm in width with nine adjacent lasers at the Full Width at Half Maximum (FWHM) (Figure 3.13). It is important to acknowledge that the area irradiated by the nine-laser setup appeared non-uniform and elliptical. This irregularity may be explained by beam reflection caused by the laser head or laser fibre, especially since there was no back reflection protective mirror or glass for the multi-laser head. As a result, the measurement process was probably disturbed by the reflection of the laser beam. Consequently, for all calculations and assumptions, the width of the laser spot was taken as 72 µm. average M^2 was measured to be around 0.945 for both diode laser types. Figure 3.13 displays the laser beam profiles and spot sizes.

Laser Orientation	Laser's version	50% Width X	13.5% Width X	X-plane View	Y-Plane View	3D View
1	3W	68 µm	89 µm	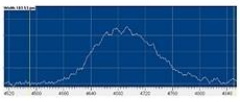	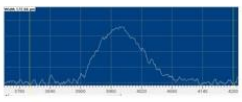	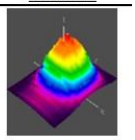
1-4	3W	274 µm	303 µm	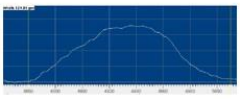	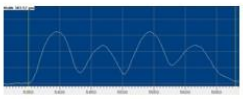	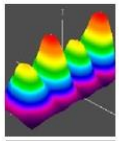
1	4.5W	52 µm	72 µm	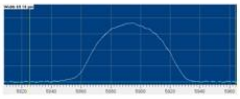	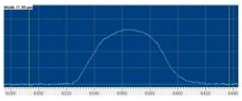	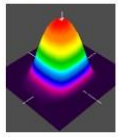
1-6	4.5W	430 µm	466 µm	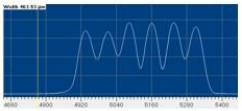	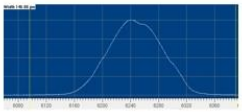	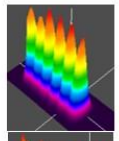
1-9	4.5W	659 µm	688 µm	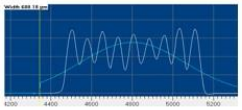	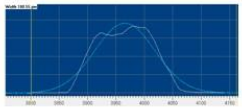	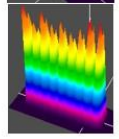

Figure 3.13 - Analysis and Results from Laser Beam Profiling Tests with respect to their orientation, version, 50% width, 13.5% width, X-plane view, Y-plane view, and 3D view

3.5 Substrate Creation

To enable damage-free sample removal and reduce the residual stress, a substrate made of stainless steel 316L with holes was created, following the approach used in Alsaddah's studies [8,9]. The processing area was designed to be 40 x 40 mm² out of a 66 x 66 mm² substrate perimeter (Figure 3.14). To prevent warpage due to thermal gradient changes

during the process, the substrate was fixed to the powder bed piston using four M4 holes. Preliminary studies have shown that the new substrate design allows for a nearly damage-free sample removal procedure. However, the first layers exhibit a non-uniform texture due to holes in the substrate. Some particles move towards the holes due to recoil pressure during the process, resulting in a non-uniform solidified layer. It was observed that layer deposition became more uniform after the 5th to 7th layer, depending on the parameters. As a result, the experiments were scheduled to begin after the 15th layer.

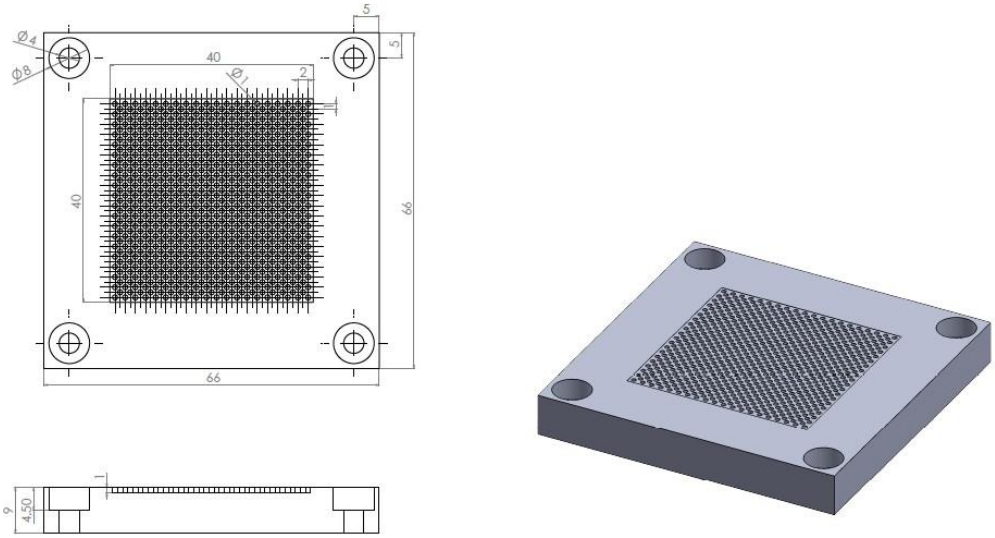

Figure 3.14 - Technical Blueprint of Substrate Design

3.6 Analysis Procedure and Equipment

To monitor surface temperature during the process, a Hamamatsu ORCA-Flash4.0 V3 digital CMOS thermal camera was utilized. The camera was set up at a 30-degree angle and positioned 41 cm away from the target area. X-ray Diffraction (XRD) analyses were performed using PANalytical Aeris hardware. The scans commenced at a start angle of 30° and concluded at 80°, with a step size of 0.022° 2θ, each lasting 10 minutes. Surface roughness (R_a) measurements were conducted using an Alicona Infinite Focus microscope. Mean R_a values were obtained from five distinct measurements across different line patterns. The average R_a values were calculated using the embedded Eq.14 in the Alicona Infinite Focus software, where Z(x) represents the profile height function, and '*L'* denotes the evaluation length.

Density measurement of the samples was evaluated through cross-sectional examination using a Nikon Light Optical Microscope (LOM or OM). The samples were hot mounted, and the sample preparation involved grinding using abrasives from 320 grit up to

4000 grit, followed by polishing with a 0.06 µm colloidal silica (CS10) suspension mixed with 10% hydrogen peroxide. The detailed preparation procedures are outlined in Table 3-5. Image processing required for the analysis was carried out using ImageJ software. The procedure involved converting the images to 8-bit binary colour coding, followed by a transformation into black and white. In the processed images, black regions represented porosity or voids, whereas white regions indicated the solidified Ti6Al4V material. The density of the samples was quantified by measuring the ratio of white pixels (representing solidified material) to black pixels (indicating porosity or voids).

Table 3-5 - Step-by-Step Procedure for Preparing Samples

Grid	***Time (min)***	***Base (rpm)***	***Head (rpm)***	***Force (N)***	***Rotation***	***Solution***
240 or 320	01:00	303	60	28	Contra	Water
400 or 600	01:30	303	60	22	Contra	Water
800	02:00 / 2	303	60	18	Contra	Water
1200	02:00 / 2	252	60	15	Comp	Water
2500	02:00 / 2	198	60	13	Comp	Water
4000	05:00 / 2	151	60	9	Comp	CS10%
Polish cloth 1	5:00–10:00	151	60	19	Contra	CS10%
Polish cloth 2	20:00	177	60	17	Comp	Water

The microstructure of the surface was imaged using Oxford Instruments Tescan Vega 3 Scanning Electron Microscopy (SEM) in both Secondary Electrons (SE) and Back-scattering Electron (BSE) modes. The beam intensity was set to 10 and HV was set to 15 kV for both SE and BSE modes. The fixed spot size was 72.3 nm. In addition, the equipment was fitted with Energy-dispersive X-ray spectroscopy (EDXS or EDS or EDX) sensors to perform the elemental mapping procedure. The elemental mapping was carried out using AZtec 4.3 acquisition software.

EBSD analysis was conducted using the JEOL-7900F Schottky Field Emission Scanning Electron Microscope to examine crystallography. The data acquisition area was set to 300 x 220 µm. Areas with higher magnification (>600x zoom) were scanned using a step size of 150

nm, while those with lower magnification (≤ 400x zoom) employed a step size of 400 nm, ensuring detailed and comprehensive imaging. An area of 506000 μm^2 was scanned for hybrid samples. EBSD scan was performed on YZ plane Figure 3.16-A and all figures named according to axes in this figure. Parent β grains were reconstructed according to Burgers orientation relationship ($\{0111\}_\alpha // \{110\}_\beta$ and $\langle 11\bar{2}0\rangle_\alpha // \langle 111\rangle_\beta$). Aztec Crystal was used for pole figures (PF, using an equal area projection, marked with a half-width of 10 degrees, and scaled in multiples of random density), inverse PF (IPF) mapping, parent β grain reconstruction, and grain size analyses. One EBSD scan covers 2.2 mm × 0.23 mm area in size. The misorientation limit was set to 10° to identify different grains.

The Vickers hardness tests were performed using a Mitutoyo Indenter, applying a 500 g load with a 15-second dwell time. A total of 15 measurements were conducted horizontally on a per polished sample and three along the build direction. Nano-hardness and reduced modulus were assessed using the Micro Materials NanoTest Vantage instrument. Nano-indentation was carried out on a 3x3 grid (9 points) utilizing an open-loop trapezoidal method during both the loading and unloading phases, incorporating a 5-second pause at the peak load of 100 mN. Various loads were tested—50 mN, 100 mN, 200 mN, and 400 mN—with 100 mN ultimately selected as the most suitable for direct comparison between FLM and DAM samples within a scientific context.

3.7 Parameter Tests

The samples were manufactured using the HLPBF system. All single tracks were 20 mm in length, and each single layer sample was created with dimensions of 5 x 6 mm to distinguish start and stop positions in OM or SEM images. The parameters were entered into Thinklaser software for the 1064 nm fibre laser and Pronterface software for the 450 nm multi-laser head, as described in the G-codes. To enhance layer uniformity, powder was spread onto the substrate using a silicone-based wiper.

Experiments for solely FLM (discussed in Chapter 4) and solely DAM (discussed in Chapter 5) began with single tracks to investigate melt pool behaviour. This was followed by single layer processing to explore the relationships between energy density, surface roughness, and melt pool shape. Multi-layer fabrication experiments were then carried out using optimum parameters selected through a full-factorial approach, focusing on normalised

energy density. For hybrid sample experiments, an exclusively multi-layer fabrication approach was adopted with the optimum parameters from earlier experiments. Initially, an overlap study determined the extent to which FLM and DAM could fully fuse together in a sample. Subsequently, a study on scanning strategy order was conducted to assess the impact of processing sequence. After the manufacturing process was completed, all samples underwent comprehensive analysis, including density assessments, SEM, top and side surface roughness measurements, XRD, EDS, EBSD, and both micro-hardness and nano-indentation tests.

The multi-laser head's gantry system has an operational speed range of 10 to 1000 mm/min (0.17 mm/s to 16.7 mm/s). To ensure a controlled environment, the build chamber was vacuumed until the oxygen content dropped below 0.09% (as measured by an O_2 sensor embedded in the DAM system). Argon gas was then introduced and continuously purged just above the powder bed throughout the experiment to supplement the environment without disturbing or causing the raw powders to scatter. The reason for this was the focal distance of the multi-laser head, which was 60 mm ± 3 mm. To protect the multi-laser head from fumes and prevent material oxidation, a circulation system was used, similar to DED systems [95]. The scanning process employed a single strategy that overlapped multiple tracks (Figure 3.15). Throughout the scanning process, the multi-laser head remained stationary and did not tilt or rotate. The lasers remained active throughout the experiments, resulting in the creation of high energy density sections at the sideways locations due to the head's fixed orientation. As a result, areas 1 mm from the edge were disregarded in top surface or cross-sectional examinations. No additional heating sources were used, including optical preheating or powder bed heating, and the studies were conducted at a laboratory temperature of 20°C.

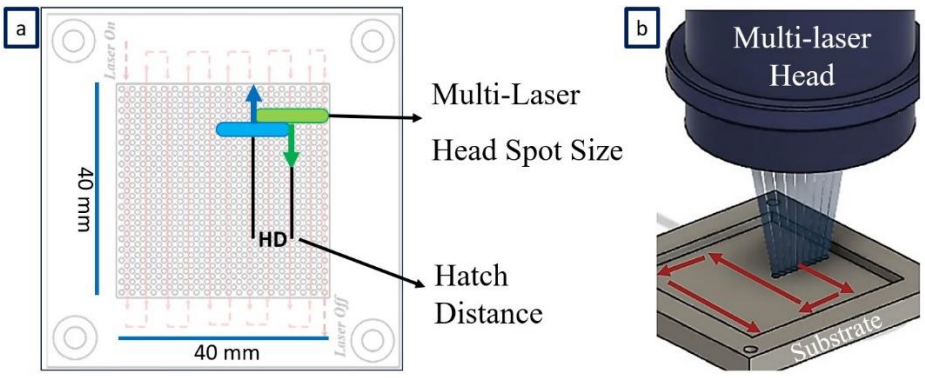

Figure 3.15 - (a) Visual Depiction of the Utilised Substrate Emphasising the DAM Scanning Strategy, (b) Three-Dimensional Representation of the In-Situ DAM Process with an In-Depth Scanning Methodology

Minitab Software was used for beginning of 450 nm DAM experiments to understand the first laser-powder phenomenon types which was a two-factorial setup, as direct correlation studies were conducted each time. The power was fixed at 2.85W for the 3W diode setup and 4W for the 4.5W diode setup, resulting in a total output of around 17W (using 6 lasers) and 36W (using 9 lasers), respectively. Initially, wide-range single-track studies were conducted to determine the optimal region for Ti6Al4V on 450 nm DAM. A study was conducted on a single layer to determine the hatch distance using the optimal parameters. Subsequently, a range of NED was created based on the optimum parameters used in layer height studies. For study consistency, three samples were produced for each parameter set. Sample coding was used, such as 150ss700hd60lh9E^*, which refers to a scanning speed of 150 mm/min, a hatch distance of 700 µm, a layer height of 60 µm, and E^* equal to 9. Figure 3.16-A illustrates the build direction and sample planes based on the cutting sections. Additionally, Figure 3.16-B displays the scanning strategies used for processing the hybrid sample. The arrows indicate the laser's scanning movement, and the distance between them represents the hatch distance.

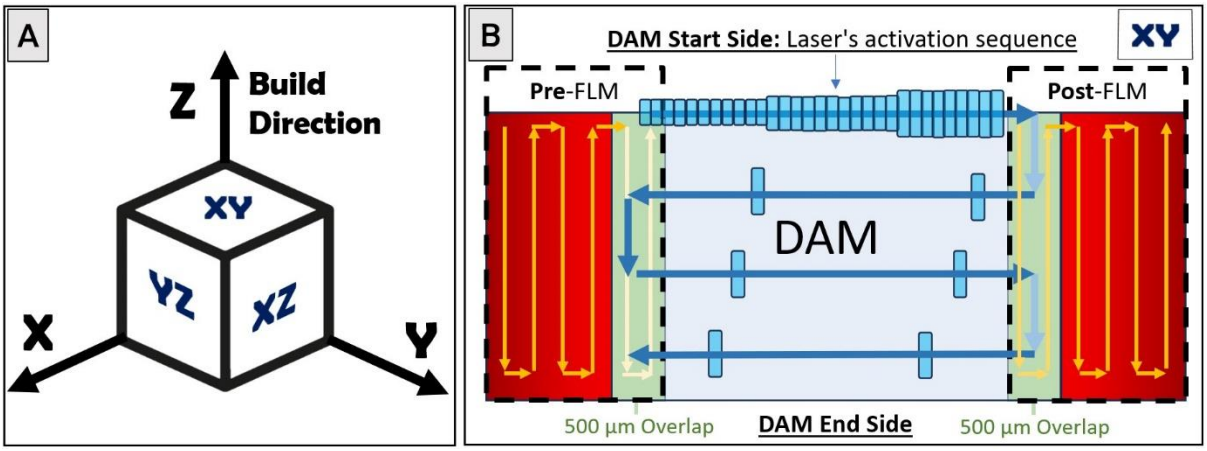

Figure 3.16 - (A) Diagram Illustrating Plane Nomenclature and Build Orientation, (B) Layout of Hybrid Laser Processing with Indicated Laser Pathways with The Overlap Area Shown in Green.

3.8 Equations

This research utilised only the volumetric and revised normalised energy density equations for DAM, namely VED (Equation 1) and NED (Equation 2). The fixed parameters for NED can be found in Table 3-6.

Table 3-6 - Detailed Enumeration of Parameters for Calculating Normalised Energy Density

T_m (K)[213]	1877	**r_B (m) (3W Diodes)**	$2.45*10^{-4}$
T_0 (K)	300	**r_B (m) (4.5W Diodes)**	$3.30*10^{-4}$
ρ (kg/m^3)[9]	4430	**A (%)[9] @ 450 nm**	0.72
α (m^2/s)[9]	$6.7*10^{-6}$	**A (%)[9] @ 1064 nm**	0.58
λ (W/m.K)[8]	32.00	**C_p** (J/kg.K)[9]	526

Where *A* is absorptivity, ρ is density of the material, C_p is specific heat capacity, T_m is melting temperature, T_0 is ambient temperature, λ thermal conductivity, α thermal diffusivity, and r_B is calculated entire laser spot radius.

$$E_{SED} = \frac{P}{SS.HD}\ (J/mm^2)$$ Eq.4 [174]

$$E_{VED} = \frac{P}{SS.HD.LH}\ (J/mm^3)$$ Eq.5 [1]

$$E_0^* = \frac{q^*}{v^*.l^*.h^*} = \frac{[A.P/(2.SS.LH.HD)]}{[\rho.C_p.(T_m - T_0)]}$$ Eq.6 [214]

$$q^* = \frac{A.P}{[r_B.\lambda(T_m - T_0)]}$$ Eq.7 [214]

$$h^* = \frac{HD}{r_m}$$ Eq.8 [214]

$$l^* = LH/r_m$$ Eq.9 [214]

$$v^* = \frac{SS.r_B}{\alpha}$$ Eq.10 [214]

$$\lambda = 14.307 + (0.0181\ x\ T_m) - (6\ x\ 10^{-6}T_m^2)$$ Eq.11 [9]

$$2r_m = (n * 2r_b) + \Big((n-1) * d_g\Big)$$ Eq.12 [8]

$$\frac{1}{E_r} = \frac{1-\epsilon_i^2}{E_i} + \frac{1-\epsilon_s^2}{E_s}$$ Eq.13 [8]

$$R_a = (\frac{1}{L}) \int_0^L |Z(x)|dx$$ Eq.14 [216]

$$Overlap\ Percentage\ (\%) = \frac{(Melt\ Pool\ Width - HD)}{Melt\ Pool\ Width} * 100$$ Eq.15

Where *SS* is scanning speed, *HD* is hatch distance, *LH* is layer height, *P* is power, q^* is normalised power ratio, r_s is single diode spot size radius, *n* is the number of adjacent lasers installed, d_g is the seperation distance between lasers, l^* is normalised layer height ratio, v^* is normalised scanning speed ratio. Eq. 3, 4, 5, 6, 7 and 8 have been used in Eq.5. For Young's modulus calculations, Eq.12 was used in the nanoindentation sections. Where Poisson's ratio of indenter ϵ_i=0.07, Elastic modulus of the indenter E_s=1140 GPa, Poisson's ratio of Ti6Al4V $\epsilon_s = 0.342$. Moreover, Eq.14 used to calculate the average surface roughness measurement calculation by Alicona software. Where *L* is the length of the *Z(x)* is the profile height function, and *L* is the evaluation length. For the overlap percentage calculation for hatch distance studies the Eq.15 was used for determination.

4. Optimising Parameters for Ti6Al4V Using Fibre Laser Equipment in HLPBF Process

4.1 Introduction

This chapter demonstrates the reliability of the 1064 nm fibre laser FLM system, equipped within the HLPBF system, by comparing it with conventional LPBF machines. This approach ensures the comparability of the system for scientific research. New investigations were conducted to contribute to the existing literature, focusing on 60 µm layer height processing capabilities. The analysis includes the correlation between top surface roughness and residual stress concerning warpage measurements, the introduction of NED into FLM parameter sets, and assessments of nano-indentation hardness. The study found that the FLM equipment can produce structures with 99.3% density at a 60 µm layer height. The findings related to microstructure, hardness, and elongation modulus were consistent with existing literature. Furthermore, these results paved the way for aligning the parameters to be compatible with a DAM system for hybrid processing.

4.2 Development of a Parameter Map Aligned with Literature-Derived Data

Initially, an extensive range of parameter maps was developed to determine the system's ability to melt Ti6Al4V alloy. The range was determined by the specifications of the FLM system. In the initial phase, 110 different trials were carried out using a single track. These parameters were then refined to 12, using literature data and visual inspection of the powder bed, but this phase focused on single-layer studies only. Finally, the set of parameters was further reduced to four, specifically for multi-layer studies.

In these studies, data from the literature were predominantly in VED [1,174], with only a few reports in [57]. Singla *et al.* [217] conducted a literature review comparing Ti6Al4V studies, which informed the selection of suitable parameters for this research. These parameters were chosen considering the capabilities of the system [1,6,18,20,217,218]: a spot size of 100 µm, a maximum optical power of 200 W, a minimum layer thickness of 50 µm and a scan velocity range between 100 and 3000 mm/s. Based on these criteria derived from the literature, **Error! Reference source not found.** was compiled for the final parameter

optimisation comparison specific to the HLPBF system. This table is used to evaluate the single-track results and determine their consistency with the results reported in the literature. Notably, the literature also has several data gaps, such as powder bed temperature, substrate element and material thermal conductivity. For ease of comparison, the data sets from the existing literature have been presented in both VED and NED formats. However, NED can only be used after multilayer studies where the known variables are entered into an equation.

Table 4-1- Aggregated Dataset Extracted from Literature References

Test Code	L1	L2	L3	L4	L5
Power (W)	120	170	175	95	150
Scanning Speed (mm/s)	1200	1250	1029	900	667
Hatch Distance (µm)	40	100	120	77	90
Layer Height (µm)	50	30	60	25	50
VED (J/mm^3)	**50**	**45.3**	**23.6**	**54.8**	**50**
Reference	[219]	[98,220,221]	[50]	[222]	[223]

4.2.1 Single Track and Single Layer Studies

In the single-track studies, a layer height of 1000 µm was used to evaluate the continuity of the tracks over a sample length of 20 mm. Of the tests carried out, 110 tracks were made, as shown in Figure 4.1. This chart categorises the tracks according to the problems encountered, such as balling, discontinuity, warping, cracking, or partial sintering.

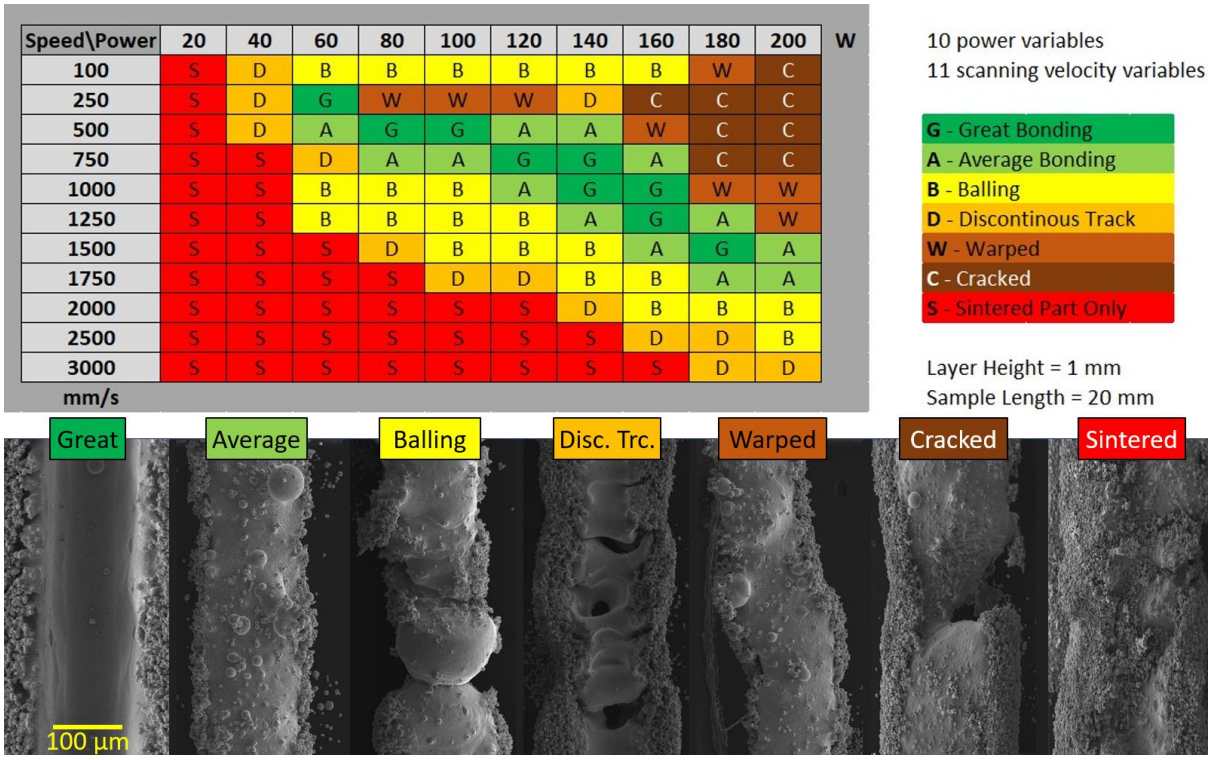

Figure 4.1 - Broad-Spectrum Parameter Mapping to Identify System Constraints and Laser-Powder Interaction Effects

Figure 4.1 facilitates the refinement of the ideal bond zone, which is, in essence, similar to increasing the resolution of a particular area of an image. The set of data is narrowed down in order to find the optimum parameter. Particularly for good bonds, it can be observed that an increase in speed leads initially to balling, followed by a break in the continuity of the sample, and finally to sintering. In addition, once well-bonded specimens have been achieved, an increase in power at a fixed speed can result in material distortion and, in the most severe cases, cracking. The appearance of discontinuous tracks is often the result when balling phenomena are no longer apparent. Sintering is an indication of insufficient energy in the melt pool while cracking is generally happens with a highest energy or highest cooling rate. Thus, Figure 4.1 suggests a gradient of phenomena from high to low energy levels. These include solidification cracks, distortion or residual stress build-up, balling, optimum bonding, average bonding or high porosity bonding, followed by balling again, discontinuous tracks or melt pool disruption, and finally, regions of sintering characterised by unmelted areas.

It can also be observed that the good bond region closely matches the data set presented in **Error! Reference source not found.**. This is a promising development. Focusing only on the good and average bonding regions, the calculated range for the LED is between

0.09 and 0.24 J/mm. However, it is important to note that the data in **Error! Reference source not found.** is derived from samples built up to 30-50 µm layer height, which can impact melt pool dynamics. Consequently, the energy input required to melt the material effectively may vary. Factors such as the moisture content of the process material prior to processing, the specific grade of Ti6Al4V in use and laboratory conditions, among others, may also have an influence on the optimum energy density range.

For the second parameter map, the focus will be on data sets that include good and average bonded single tracks, while comparisons will be made with literature data (integrating Figure 4.1 and Table 4-1 as shown in Table 4-2) for single-layer studies. It is important to recognise that heat dissipation and thermal management within a single layer may differ from single-track studies, potentially resulting in different results. First, the optimal hatch distance representing the overlap of the laser spots, was determined through experiments with settings of 40-60-80 µm at 140W 750mm/s and 140W 1000mm/s. The 140W parameter was chosen on the basis that these samples had the least amount of surface defects. The dimensions of these samples were approximately 5x5 mm^2. A 200 µm layer height was used to evaluate the wetting capabilities at the first layer. Figure 4.2 clearly demonstrates that the densest parameter set was obtained with a 40 µm hatch distance, resulting in nearly 60% overlap relative to the spot size. This degree of overlap is notably significant, particularly in comparison to existing literature [1], and it is important to highlight that there was no heating of the powder bed during this experiment. Typically, a higher bed temperature would lead to increased depth of penetration. Therefore, for the single-layer studies, a hatch distance of 40 µm was selected. Although all samples exhibited a lack of fusion due to inadequate layer height for 100% penetration depth, they all demonstrated sufficient wetting to assess the impact of hatch distance and scanning speed on the top surface and wetting capabilities.

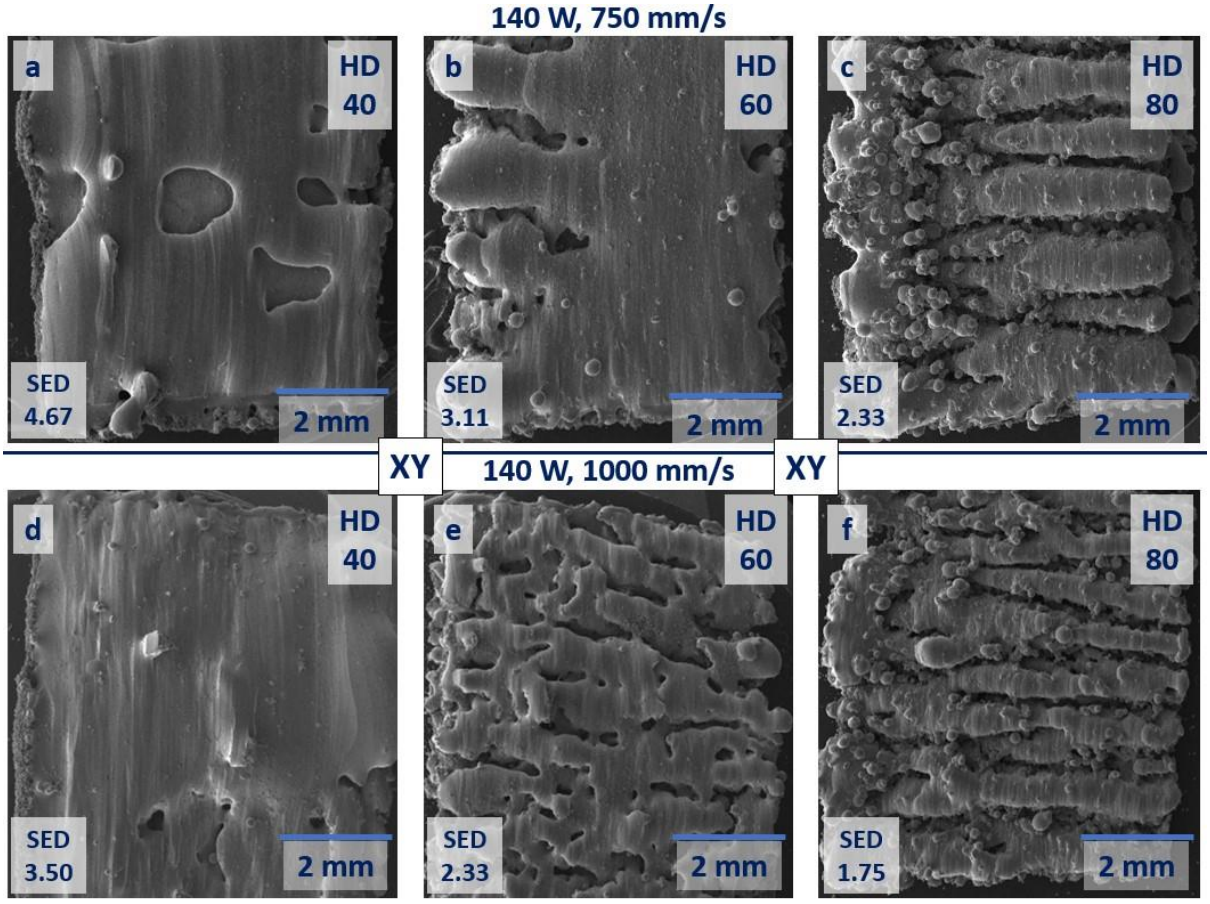

Figure 4.2 - Examination of Hatch Distances (a-40,b-60,c-80 µm) at 750 mm/s and (d-40, e-60, f-80 hatch distances) at 1000 mm/s, Including Surface Energy Density (SED) Measurements with 200 µm Layer Height under 140 W Power

In terms of wetting capability, assessed by substrate adhesion properties, it was observed that samples with a SED above 2.33 J/mm² were fully bonded to the substrate. Conversely, those with a SED below 2.33 J/mm² were unable to penetrate the 200 µm layer. This indicates that as the HD increases, the penetration depth or penetration power decreases accordingly.

The experiment was further refined to include 12 different sets of parameters, selected to closely match the data presented in Table 4-1 and Figure 4.1, thereby enhancing the resolution of the study. For these sets, three key metrics were measured and compared: top surface density (D_{top}), average top surface roughness in µm ($R_{a\text{-}top}$) and residual stress in terms of warpage (RSW), also measured in µm. The RSW was measured in a specific way after the samples had been detached from the substrate.

All of the results obtained from these measurements are shown in Table 4-2. The trends and patterns that can be discerned from these results are visually presented in Figure

4.2 and Figure 4.3 and provide a comprehensive overview of the effect of the various parameters on the quality of the samples in terms of density, surface roughness and residual stress. The most appropriate parameter sets for subsequent multi-layer studies can be determined from this comparative analysis.

Table 4-2 - Detailed Parameter Mapping Specifically Designed for Single-Layer Research

Test Code	S1	S2	S3	S4	S5	S6	S7	S8	S9	S10	S11	S12
P (W)	80	100	100	120	120	120	140	140	160	160	170	180
SS (mm/s)	500	500	700	700	900	1250	700	900	1100	1250	1250	1500
SED (J/mm^2)	4.0	5.0	3.6	4.3	3.3	2.4	5.0	3.9	3.6	3.2	3.4	3.0
Avg. D_{top} (%)	98.63	99.35	99.27	99.93	99.89	99.84	99.52	99.97	99.95	99.88	99.46	98.74
$R_{a\text{-}top}$ (µm)	2.012	2.103	3.188	2.857	4.066	4.574	4.721	3.887	3.951	5.798	4.201	8.407
RS-W (µm)	312	530	121	201	147	101	249	127	412	283	810	932

The data from Table 4-2 is visually interpreted using two primary graphs, as detailed in the study. These graphs focus on the representation of key parameters: density, average R_a and RSW are shown in Figure 4.2 and Figure 4.3, respectively. The RSW measurement was done via the cross-sectional image processing after removal from the substrate. This division into two distinct plots allows a clearer and more focused analysis of the effect of different parameters on these specific aspects of the samples.

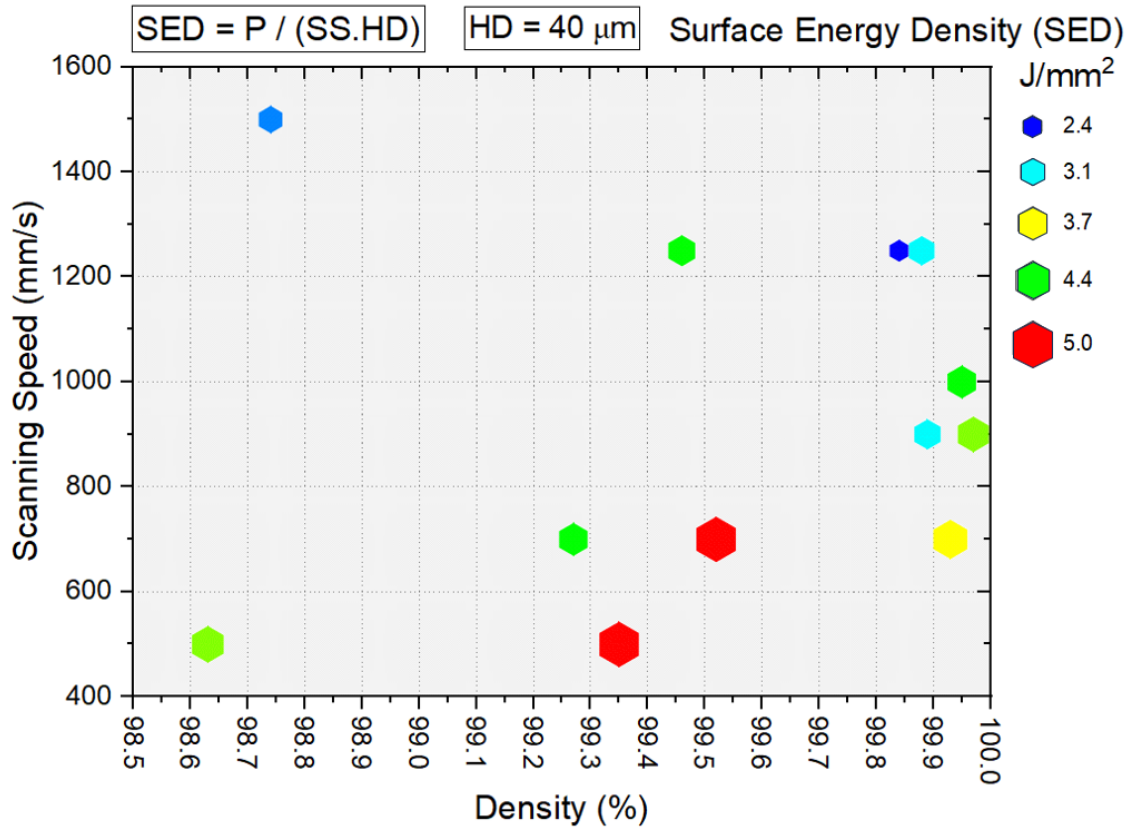

Figure 4.3 - Investigating Top Surface Density in Single Layer Studies: Mapping Scanning Speed Against LED for Power Determination (Uniform Colour Coding for Power Values). Power was shown as P, and scanning speed shown as SS.

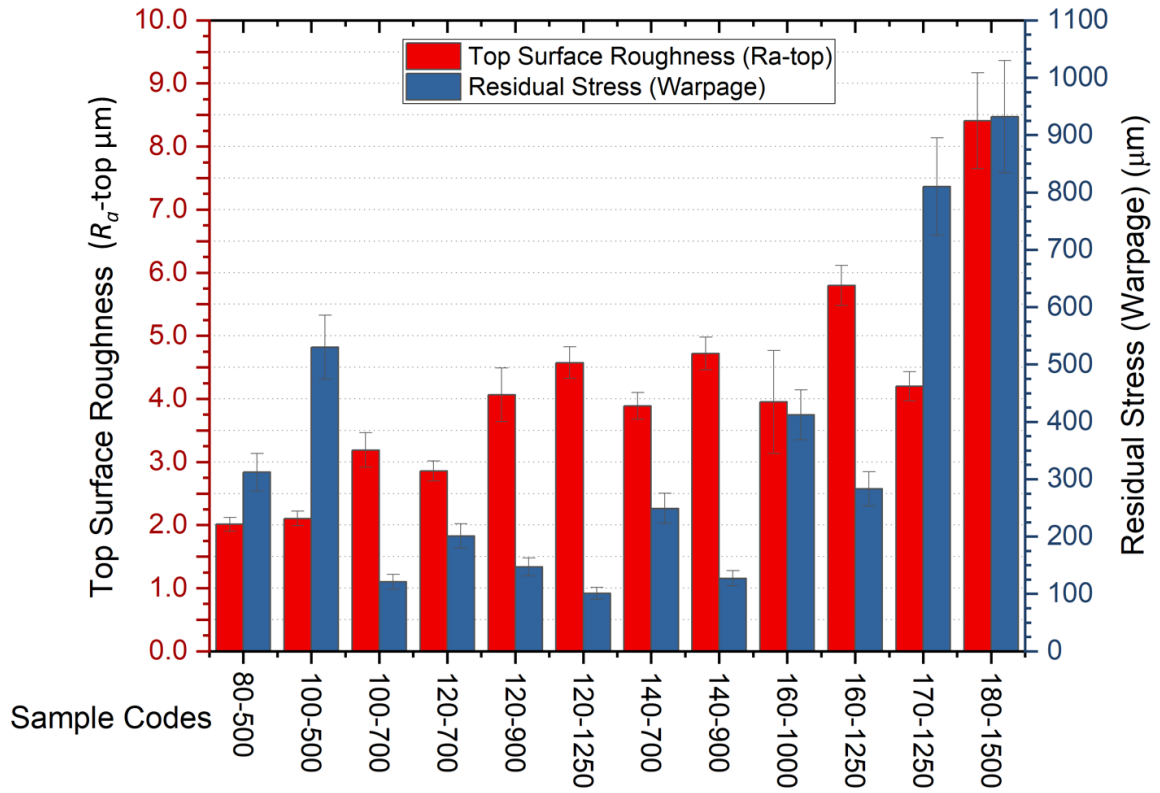

Figure 4.4 - Analysis of Top Surface Roughness Linked with Residual Stress (Indicated by Warpage) in Relation to Sample Codes Listed in Table 2

An interesting trend can be seen in Figure 4.3, where the density of the top surface increases with power up to 140W at constant speed. Beyond 140W, however, the density begins to decrease, indicating entry into the excessive power region of the parameter map. Conversely, Figure 4.4 shows that within the same power range, increasing the velocity tended to raise the average surface roughness, while decreasing the velocity tended to reduce it. However, this is accompanied by an increase in the RSW, which leads to a greater degree of distortion. Thus, the effects on the roughness of the top surface are found to be inversely proportional to the residual stress, regardless of the direction of the change in the SED.

Furthermore, a specific increase in power has a noticeable effect on RSW values, almost doubling them in terms of the distortion measurements. This may appear to be counter-intuitive, as RSW is typically directly proportional to the cooling rate. However, in this context, the cooling rate assumed only increases as the speed increases. In particular, the cooling rate probably remained above 10^5 °C/s at speeds of either 700 mm/s or 900 mm/s due to XRD readings as there was no sign of β phase. This classifies the speeds in this FLM experiment as being in the region of a high cooling rate, regardless of whether they are slow or fast [80]. As a result, the effect of the cooling rate on the RSW can be ignored for the results shown in Figure 4.4.

4.2.2 Multi-layer Fabrication

As the HLPBF system is designed to operate at relatively high layer heights in the range of 60 to 70 µm [8,9,14–16], it is necessary to increase the layer height to at least 60 µm for multi-layer fabrication in the DAM system. This approach is particularly significant as there are few studies dealing with high layer height [1,4,18,218,224–226] thus, these experiments will provide a valuable contribution to the field. Initially, the parameter set with the highest density (S8 from Table 4-2) was selected to explore and identify the optimal layer height. The dimensions of the samples were set at 5x5x5 mm^3.

The studies covered layer height from 120 µm down to 60 µm to evaluate aspects such as penetration status, different porosity levels, cross-sectional densification (%) (as shown in Figure 4.5-a-b-c) and the effect of spattering on the samples (quantified as particles/ms via thermal camera images in Figure 4.5-d-e-f). Table 4-3 shows the results of the layer height study using S8 parameters (140 W, 900 mm/s). It was observed that a layer height of only 60

µm could achieve near full density (>99.88%) with these parameters, implying that a minimum VED of 64 J/mm³ is required for fully dense parts. Figure 4.5 confirms the data from Table 4-3 and also illustrates additional spattering characteristics specific to this parameter set. These images serve as examples, with the main calculations being an average derived from a series of equivalent images of one-millisecond duration.

Table 4-3 - Investigative Review of Layer Height Studies Including Subsequent Analyses

LH (µm)	120	100	80	70	60
VED (J/mm³)	32.41	38.89	48.61	55.56	64.82
Penetration	Sintered powder between layers	Sintered powder between layers	powders can be spotted between layers	Near Full	Full
Porosity	High / Balling	High	Medium	Low	Near 0
Density (%)	96.37	97.90	98.72	99.11	99.88
Spatter (p/ms)	30-50	20-40	10-15	10-15	8-11

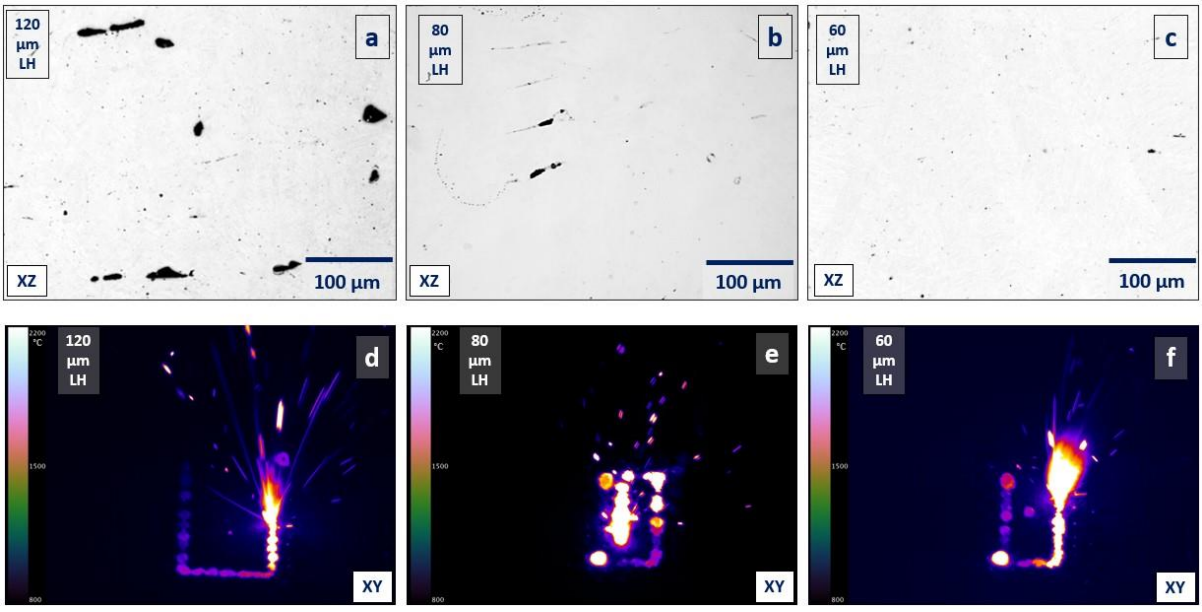

Figure 4.5 – Optical microscopy examination of the effect of the layer height on porosiys: cross-sections at 120 µm (a), 80 µm (b), 60 µm (c) layer heights, and thermal imaging for 120 µm (d), 80 µm (e), 60 µm (f) layer heights during the one of the layer processing of that of a sample.

Moreover, the study shows a significant reduction in spattering with a decrease in layer height, which can be attributed to the high recoil pressure experienced at greater layer height [196,225]. This is explained by the presence of more powder at higher layer height,

leading to more air being heated, expanding, and creating pressure. This increased pressure then propels both molten and non-melted heated particles away, resulting in spattering.

For further analysis, four specimens displaying high density, relatively low surface roughness and minimal distortion were selected, all processed with a 60 µm layer height, which gave the highest density. The primary aim is to recognise the least possible side surface roughness without compromising density, thereby ascertaining the most effective contour parameter for the HLPBF system. Shipley *et al.* [1] have pointed out that VED alone is not sufficient to assess or understand the densification of machined samples. Hence, both VED and NED[214] were calculated using the material and system specification tables for subsequent multi-layer studies. This method seeks to enhance the reproducibility of such studies, not just for this particular HLPBF system but for other FLM technology equipment as well. In recognition of the possibility of rapid variable changes during the process, including power fluctuations that affect NED values, this method is still a more accurate approach in terms of energy densities. Table 4-4 examines areas of excessive, optimum and insufficient energy based on just four sets of parameters.

Table 4-4 - Experimentation Details for Multi-Layer Fabrication: Focusing on 60 µm Layer Height and 40 µm Hatch Distance

Sample Code	**M1**	**M2**	**M3**	**M4**
Power (W)	100	120	140	160
Scanning Speed (mm/s)	500	700	900	1100
VED (J/mm^3)	83.33	71.43	64.81	60.61
NED (a.u.)	3.29	2.82	2.56	2.39

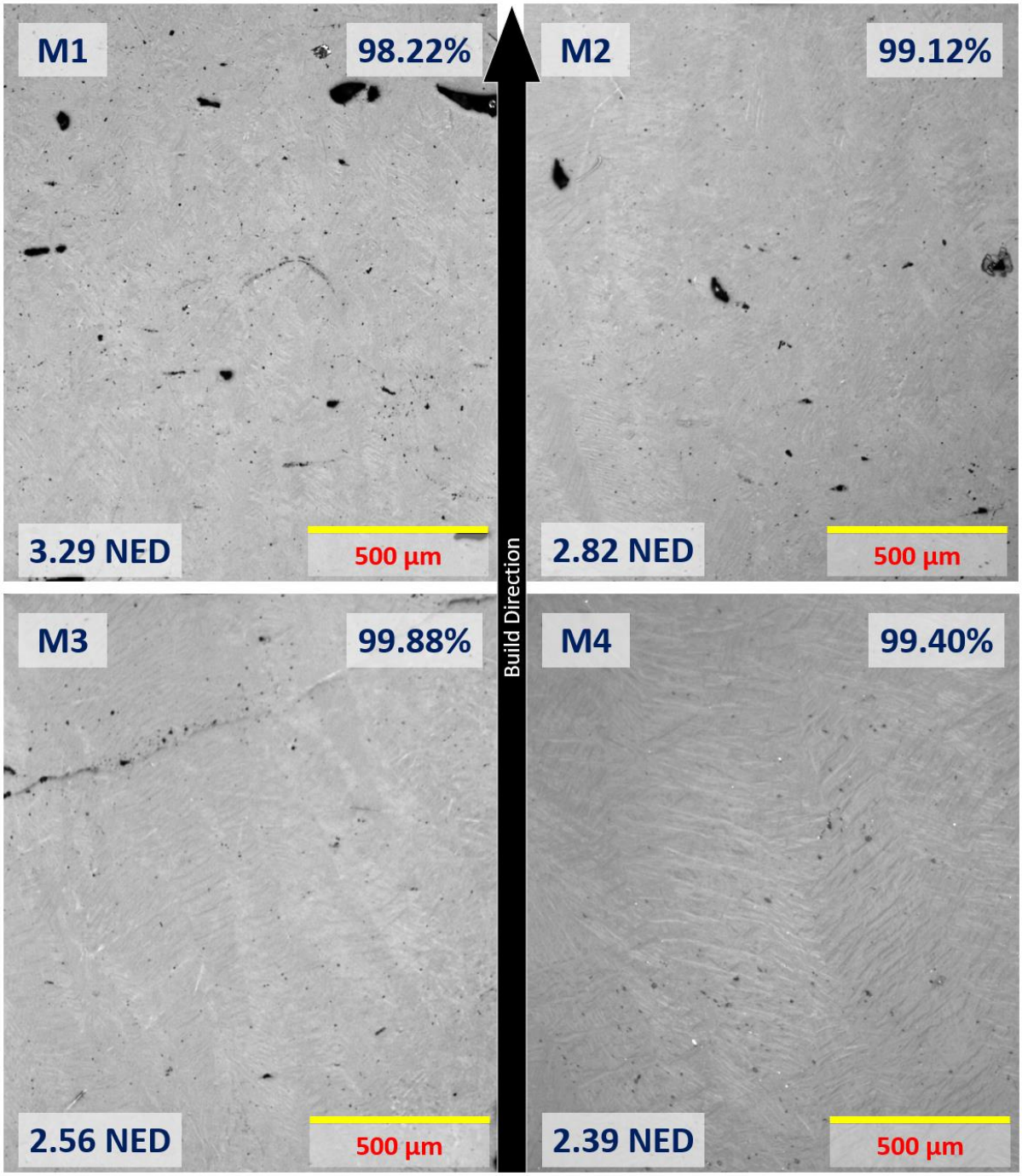

Figure 4.6 – OM examination of Density Analyses of Cross-Sections from Multi-Layer Samples in Table 4-4, Highlighting Normalised Energy Densities (NED)

In Figure 4.6, of the four tests carried out, the M3 parameter set achieved the highest density of 99.88%. This was in line with expectations. On the other hand, M1 was in an area of excess energy, which was indicated by a lower density and increased porosity. The main cause of this was insufficient solidification time, which resulted in the trapping of gas pores

[42,80]. Based on these results, either 2.39>OPT_{NED} (E_0)>2.73 or 70>OPT_{VED}>60 J/mm^3 can be identified as the optimum energy range.

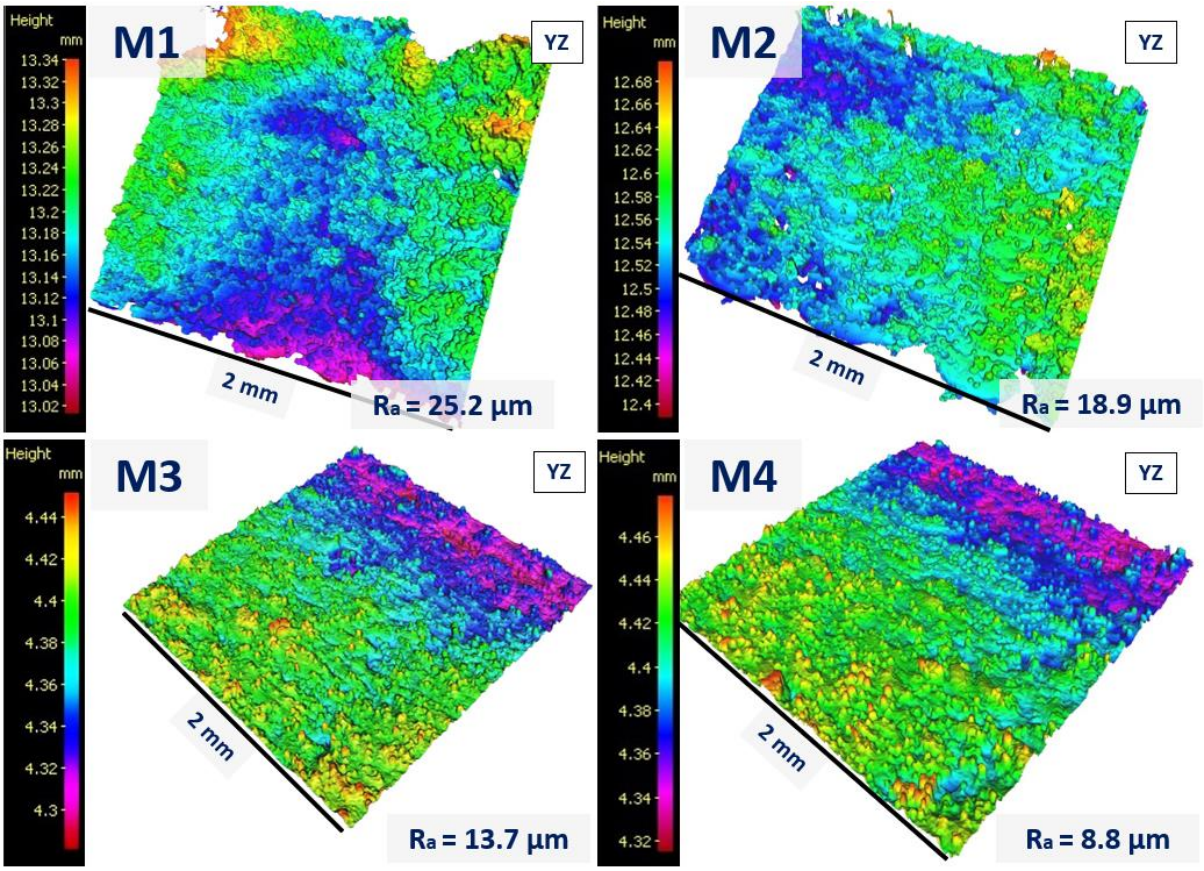

Figure 4.7 - Evaluating Side Surface Roughness Across Multi-Layer Studies Using Parameter Sets M1 to M4 as Listed in Table4- 4

Figure 4.7 investigates the side surface roughness (SSR) of four data cubes outlined in Table 4-4. The results, presented in Figure 4.8, indicate that an increase in NED, and therefore VED, results in an elevation in SSR. This tendency is primarily due to the heat dissipation characteristics of the powder particles surrounding the processed geometry. The higher energy per unit area results in a significant build-up of thermal energy, which in turn increases the temperature of the adjacent solidified tracks during the fabrication process [208]. Increased temperatures, often exceeding sintering temperatures, will affect the particles surrounding the geometry, resulting in a larger sintered area (in this case, HAZ) and consequently increased SSR.

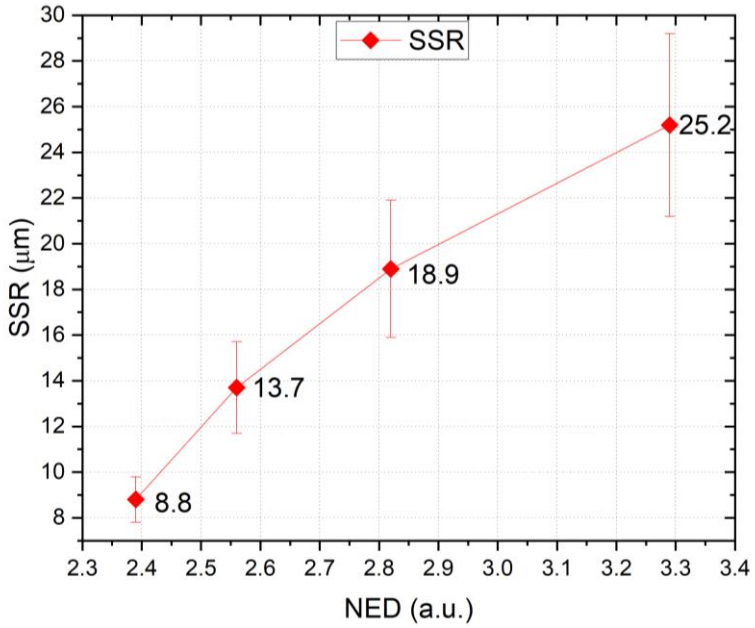

Figure 4.8 - Side Surface Roughness (SSR) Analysis: Correlating with Normalised Energy Density (NED) and Volumetric Energy Density (VED)

4.3 XRD and Microstructure Analyses

XRD patterns of 60 µm LH M3 parameter set samples were analysed to confirm the presence of α'/α and β structures in Ti6Al4V. ICDD PDF4+ maps were not filtered during pattern acquisition. The Powder Diffraction File (PDF) map (04-020-7055[227] and 00-044-1294 [228]) and several scientific sources ([145,229]) were used to identify the phases. Figure 4.9 shows a significant absence of β-phase diffraction peaks with a body-centred cubic (BCC) structure in the sample, probably due to a cooling rate in excess of 10^5 °C/s [145]. This discovery is in line with the patterns that have been seen in other research on the results of LPBF [59,61,145,217,229]. For Ti6Al4V, it has been found that cooling rates above 410°C/s result in the formation of fully martensitic hexagonal closed-packed (HCP) α' diffraction peaks only, this phenomenon is clearly shown in Figure 4.9 [36].

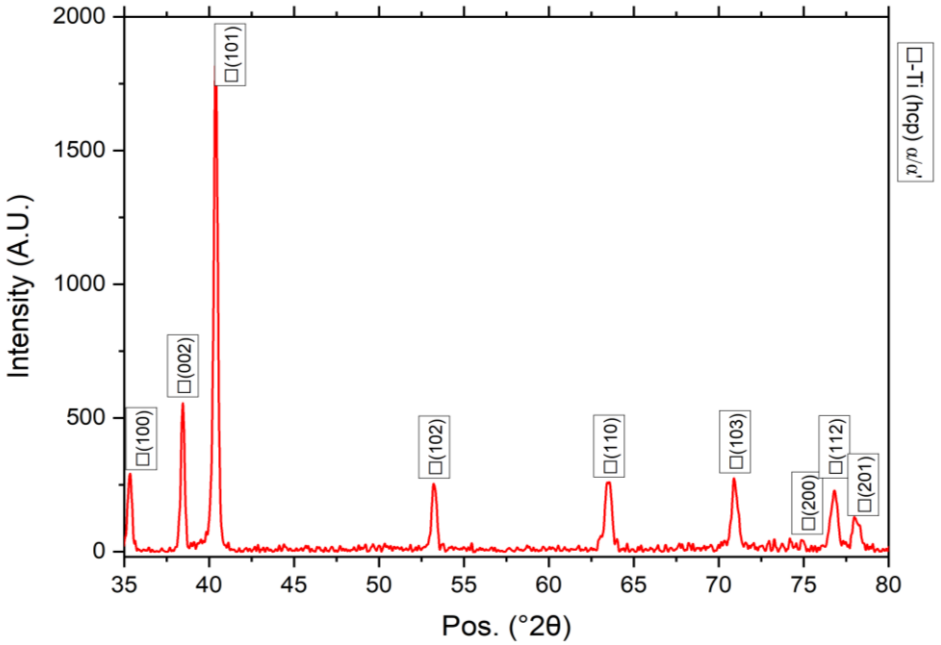

Figure 4.9 - Analysis of XRD Results for M3 Sample with Parameters: 140W, 900 mm/s, 40 µm Hatch Distance, and 60 µm Layer Height

Figure 4.10 shows cross-sectional microstructural images of samples M1 to M4, where the build direction is from bottom to top. Porosities decrease as the energy density decreases but resurface when the NED drops below 2.56. This phenomenon is due to both excess and inadequate energy densities [4]. All parameter settings exhibit the presence of fine lamellar α/α' structures in a basket weave pattern [48]. The transition from M1 to M4 causes these structures to take on a more needle-like shape, with a reduction in grain size, as cooling rates increase and affect the microstructural shape [50,222]. This change is linked to NED, as a decrease in NED due to increased speed results in higher cooling rates. Therefore, despite the increase in power input for each set of parameters, the influence of speed on microstructure is more significant than that of power.

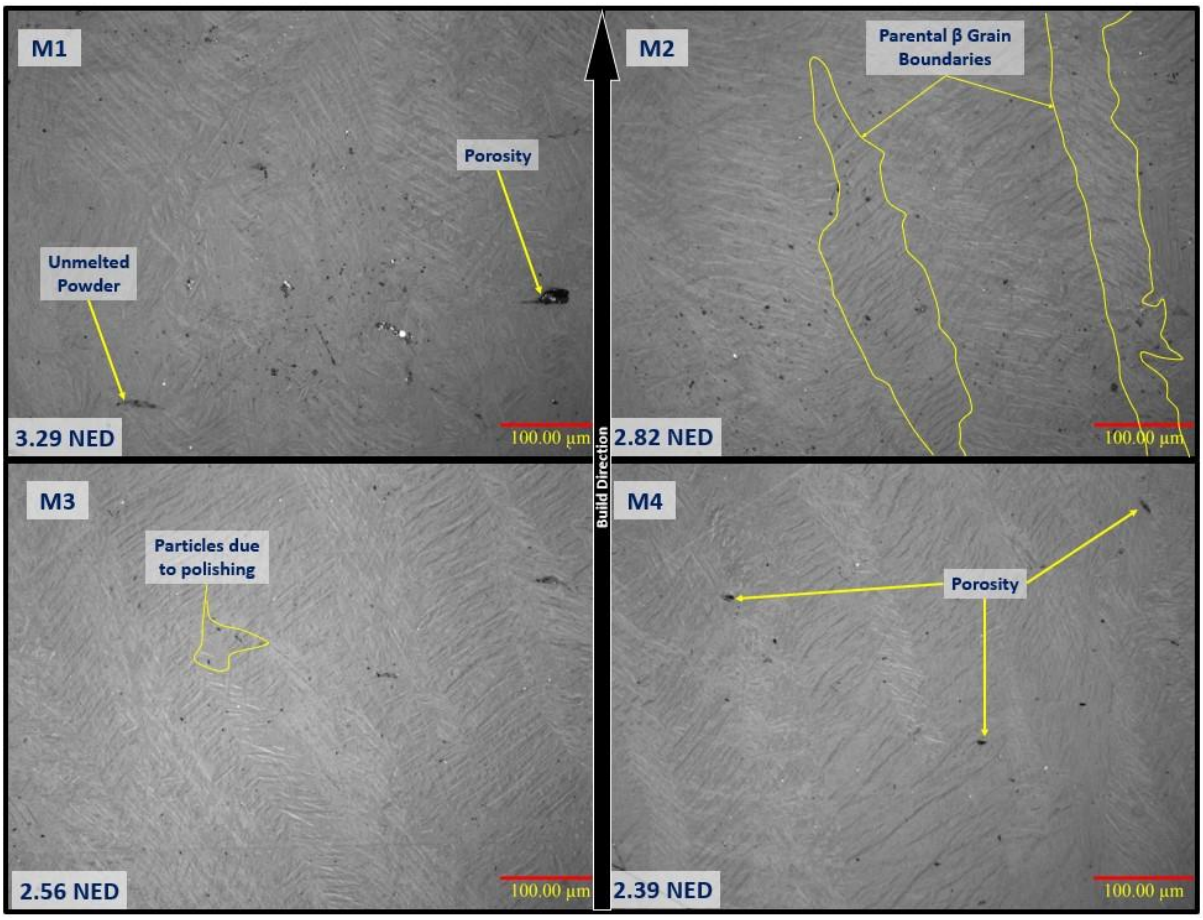

Figure 4.10 - Microstructural Analysis of M1, M2, M3, and M4 Parameter Sets: Optical Microscope Images at 20x Magnification

Figure 4.11 shows an enlarged view of M3 (as originally shown in Figure 4.10), which allows a closer examination of the microstructural properties of a high-density parameter set. As a result of the cooling rate employed, this magnified view reveals the existence of a basket-weave sorting microstructural orientation [38]. The lamellar α'/α structures mainly intersect at angles ranging from 30 to 60 degrees to the build direction. This pattern, clearly visible in the closely examined section of Figure 4.11 (indicated by blue markings), differs from a perpendicular arrangement. This provides essential insights into the microstructural dynamics under these particular manufacturing conditions [48].

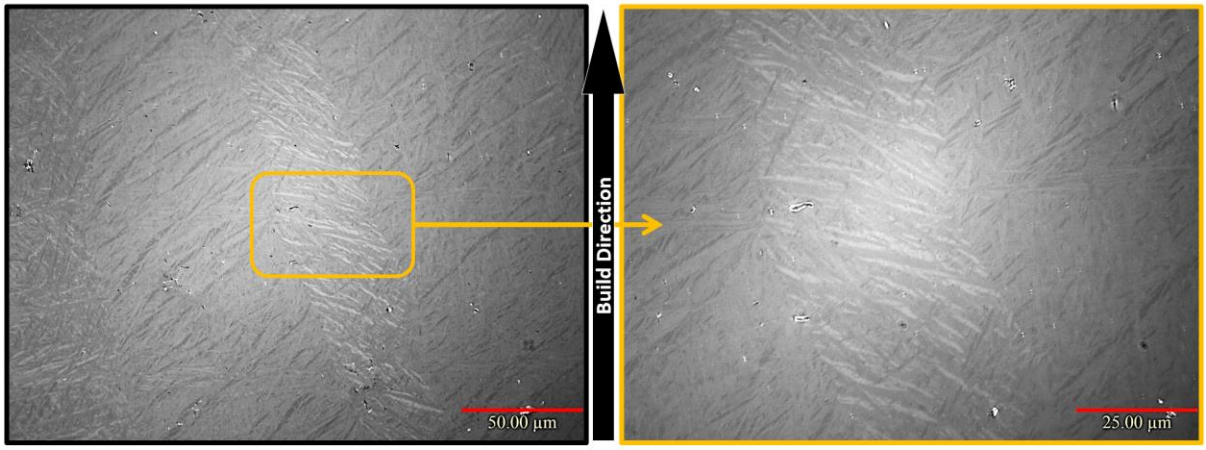

Figure 4.11 - Basket-Weave Microstructure of Ti6Al4V Examined Through M3 Parameter Set

Figure 4.12 shows that the EDS results are typical of the original powder material in terms of characteristic percentages. According to the research of Zhang *et al.* [230], "Al" has the highest tendency to evaporate among other elements present in Ti6Al4V, followed by "Ti" and "V". It was also noted that a significant decrease occurred in the "Al" composition as VED exceeded 126 J/mm^3, and the range below was between 6.13 and 6.33 in weight percentages. In this case, it can be concluded that the levels of "Al" and "Ti" are in a fairly optimal range with 6.17 and 89.27, respectively.

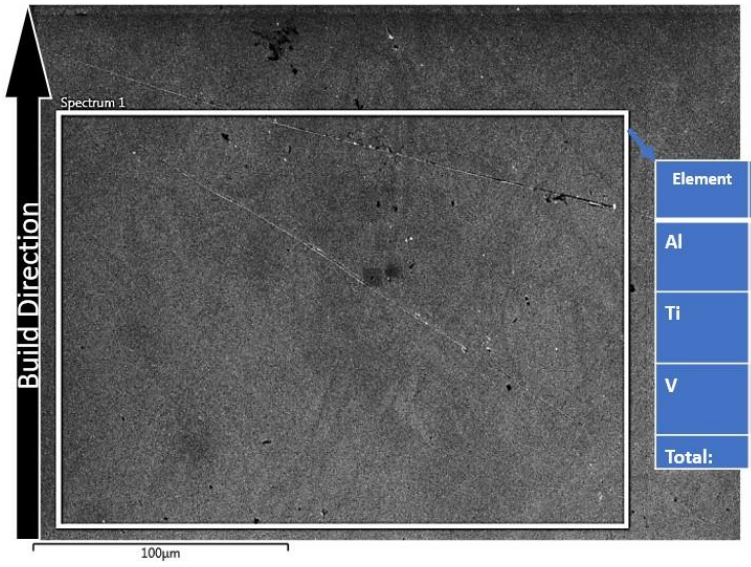

Element	Line Type	Apparent Concentration	k Ratio	Wt%	Wt% StDev
Al	K series	0.10	0.00069	**6.17**	0.08
Ti	K series	1.15	0.01149	**89.27**	0.27
V	K series	0.06	0.00057	**4.57**	0.27
Total:				**100.00**	

Figure 4.12 - M3 Sample Examination: Integration of EDX/EDS/EDXS Findings with SEM Imaging

4.4 Hardness Data

The Hall-Petch relationship suggests that a fine microstructure increases the hardness of the material, as reported in the literature [231,232]. The micro-hardness results for the as-

built Ti6Al4V samples, as presented in Figure 4.13, reveal that a reduction in energy density correlates with an increase in hardness, ranging from approximately 3 GPa to 4 GPa. This relationship between energy density and hardness is attributed to the cooling rate; as the cooling rate increases, the microstructure becomes more acicular, which enhances hardness. These results are consistent with findings reported in previous literature. [43]. Accurate hardness measurement can be challenging due to the large indentation area. Any air gap between the specimen and the hot-mounted bakelite structure can have a similar effect to that of a spring, reducing the measured hardness. A similar effect on the results can also be caused by a high level of porosity beneath the indentation surface, as this will add springiness to the material. Nano-indentation has a much smaller measurement scale of nanometres compared to the micrometres used in micro-hardness and is, therefore, expected to provide more accurate hardness measurements due to the much smaller impact area of the indenter compared to micro-hardness.

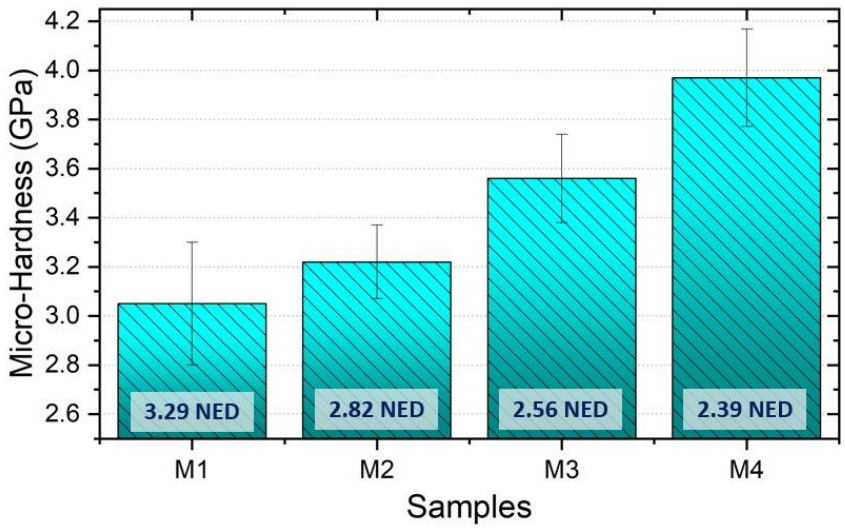

Figure 4.13 - Analysis of micro-hardness in M1, M2, M3, and M4 parameter set samples, including normalised energy density (NED) comparisons

Figure 4.14 presents the results of the nano-indentation hardness analyses for the as-built Ti6Al4V specimens, with M4 showing the highest hardness of the parameter sets tested. These results are consistent with the micro-indentation hardness data, although the nano-indentation values were significantly higher, presumably due to the shallower indentation depth. Nano-indentation appears to provide a more accurate measure of the hardness of certain phase structures, as it is unaffected by potential sub-surface processing or material

preparation defects, ensuring an accurate measurement of the hardness of, for instance, martensitic α'-structures. Variations in hardness can be accounted for by the indenter impacting different phases, such as α', α+β, or β, with α' exhibiting higher levels of hardness in most cases [33,42,54]. Additionally, the mean Young's modulus for the four samples was determined to be 142.375 GPa, with a tolerance of ±1.86 GPa. Furthermore, both Young's modulus and hardness showed a tendency to increase with decreasing energy density.

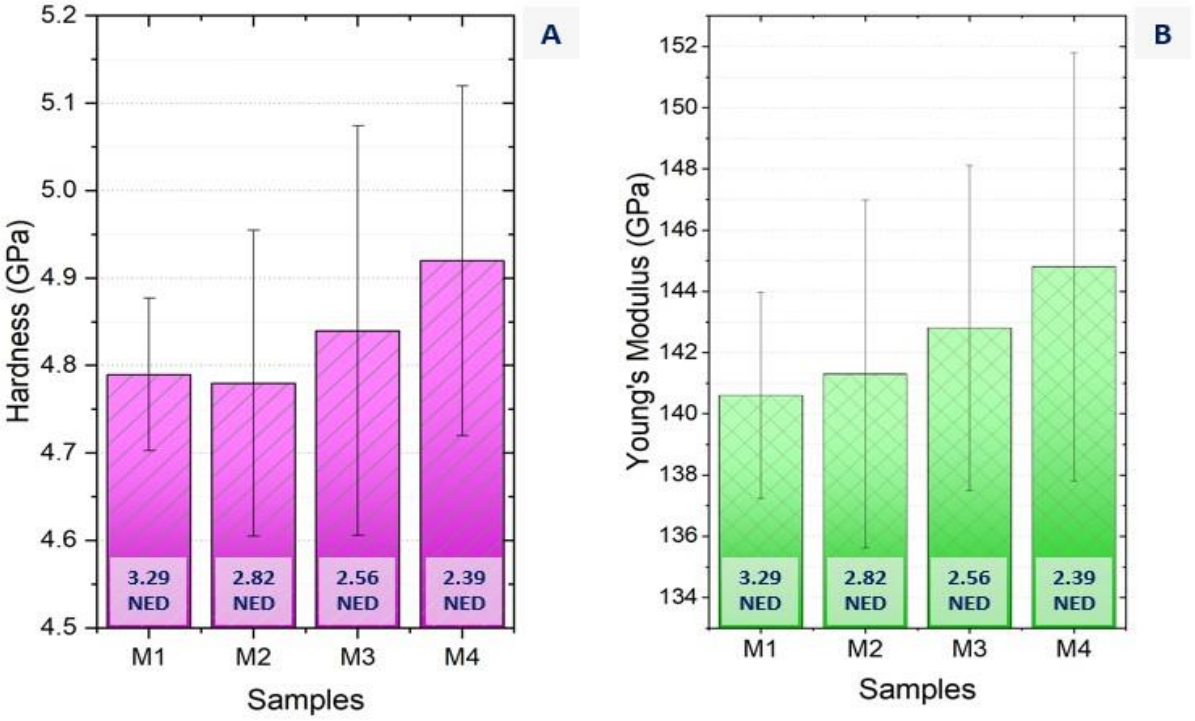

Figure 4.14 - Results of nano-indentation on M1, M2, M3, and M4 Sets: detailing (a) material hardness and (b) young's modulus metrics

Figure 4.15 displays a load and depth graph under a maximal load of 100 mN. It illustrates the reduced modulus of elasticity, calculated Young's modulus, and the hardness values across nine distinct matrix locations within the sample. Analysis of the hardness results indicates a correlation between increased hardness and a more refined microstructure, which is consistent with existing literature data [10,54,145,202,233,234].

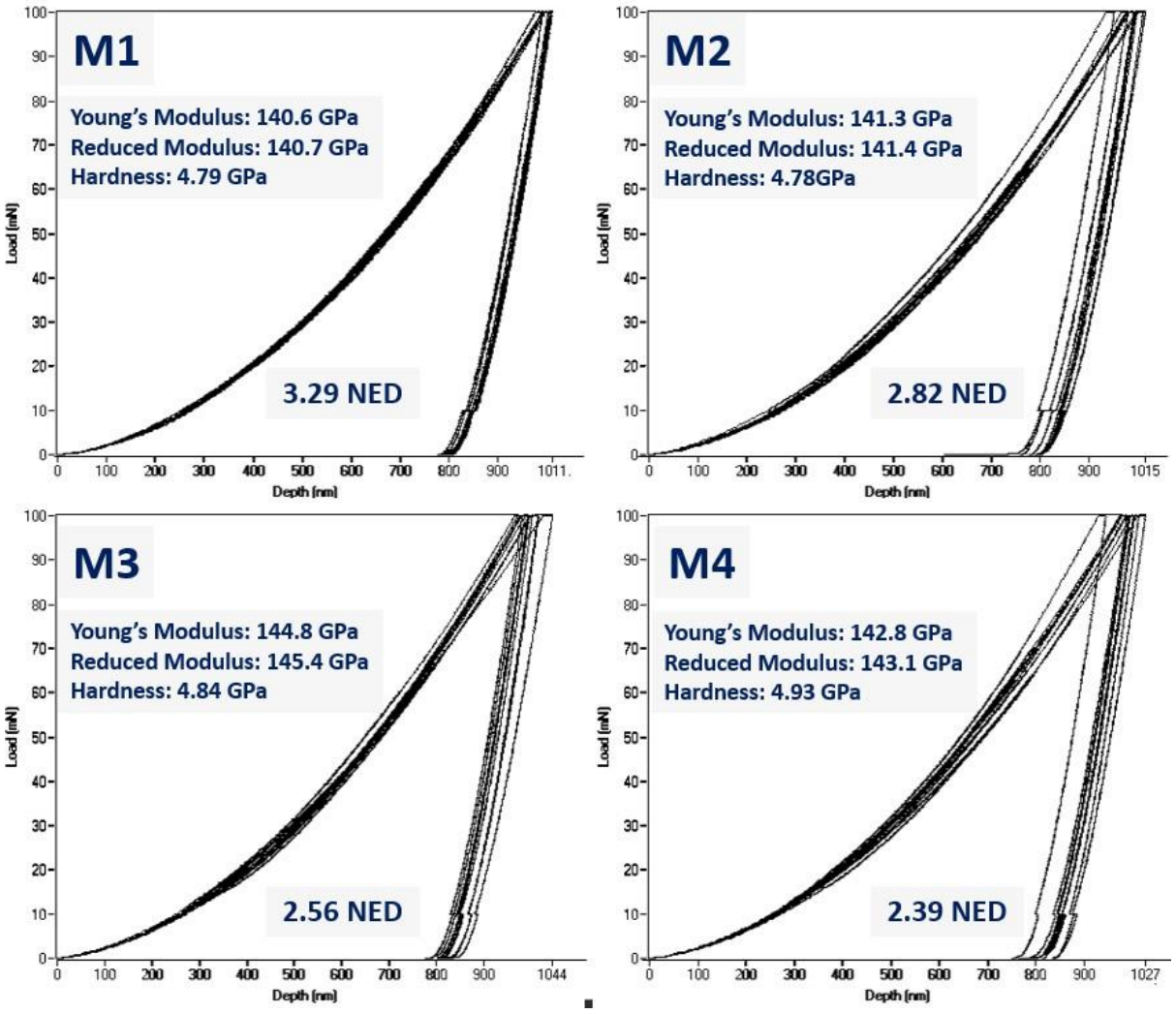

Figure 4.15 - Comparative Analysis Of Load-Depth Profiles In Nano-Indentation Across Different Parameter Sets With NED Correlation (Sample from Table4-4 M1,M2,M3,M4)

4.5 Conclusion

In this chapter, the reliability of the fibre laser equipment was assessed using Ti6Al4V powder in the bespoke HLPBF system. The evaluation began with single track studies to identify optimal parameters that define hatch distance for subsequent single layer studies. During these studies, the relationships between SED, top surface roughness, density, and warpage were explored. Following these findings, multi-layer studies were conducted using the optimized parameters from the single layer study. These investigations included spattering, cross-sectional density, side surface roughness correlated with normalized energy density, XRD, microstructural examination, EDS, and micro and nano-indentation analyses. Key findings of this chapter are:

- Decreasing layer height increases sample density and reduces spattering.

- High-density samples achieved in multilayer setups with 60 µm layer height, reaching peak densities of 99.88%.
- Reducing normalized energy density improved side surface roughness.
- Basket-weave structures were dominant under all experimental conditions.
- Data from micro and nano-indentation suggest that increasing normalized energy density decreases the cooling rate.
- No significant elemental evaporation was observed.
- Mechanical properties of Ti6Al4V parts produced by fibre laser melting align with literature: Young's modulus approximately 142 GPa, nanoindentation hardness around 4.85 GPa.
- The custom fibre laser in the HLPBF could produce high-density Ti6Al4V specimens with minimal defects.

5. Multi-laser PBF with Ti6Al4V via Use of 450 nm Diode Area Melting System

5.1 Introduction

This chapter examines the effect of the novel 450 nm DAM system on the powder bed, addressing a gap in the literature regarding the impact of single array multiple 450 nm diode lasers. A parameter mapping focused on NED values, with variations in layer height, scanning speed, and hatch distance analysed individually through a full factorial design for 4W study. Two power variants of the 450 nm diode laser, 2.8W and 4W, were utilised. The study found that the 2.8W power was insufficient to produce continuous, smooth melt pool tracks while increasing the power to 4W enabled the creation of melt pools wider than 1000 µm. However, this increase in melt pool width posed challenges in maintaining uniform melt pool penetration depths, affecting the achievement of high density in multi-layer parts. A new phenomenon, termed the 'Crescent Effect', was identified, highlighting the impact of wide melt pools on heat dynamics and solidification. Implementing a rescanning and offset strategy on each layer reduced average surface roughness, eliminated the Crescent Effect, increased density, and reduced hardness. A parameter map based on NED was developed. SEM examinations revealed coarser lamellar structures in the lower sections due to slower cooling rates, with finer martensite structures towards the top, resulting in a basket-weave microstructure throughout the sample. Overall, the 450 nm DAM system demonstrated that high-density parts can be achieved with a minimum 4W configuration at 60 µm layer height by implementing a rescanning strategy for hybrid laser processing.

5.2 Low Power (2.8W) Diode-Laser Power Studies

5.2.1 Power Experiments

Initially, the 3W lasers were calibrated for power studies, with settings adjusted to 1W, 2W, 2.5W and a maximum of 2.8W. The initial tests evaluated these power levels using a single laser. A scan speed of 50 mm/min was used over a track length of 20 mm. In contrast to conventional LPBF, which typically uses a layer height of about 40 µm [1], this study used thicker layers to determine the laser's penetration depth into the powder bed. A 1000 µm layer height was chosen to enable safe sample removal, allowing for cross-sectional analysis

of penetration and other phenomena. This was crucial in this novel study with low-power, adjacent multi-lasers where outcomes were uncertain [9]. The experimental results indicated that only the 2.8W power setting could achieve average melting, although this was accompanied by significant waviness on the top surface and lack of fusion. It was hypothesised that the heat dissipation characteristics would be significantly different in scenarios involving multi-laser setups as well as single and multi-layer studies. As a result of these observations and the limitations of the available settings, it was decided to continue with further experiments using the 2.8W setting as the default choice.

Insights into the width of the melt pool were obtained through measurements conducted under differing laser configurations. The experimentation began with the implementation of a single laser, followed by three lasers, and culminated in six lasers. Consistently, for each arrangement, the scanning speed was configured to 50 mm/min, and the power for each laser was sustained at 2.8W. This systematic approach facilitated a comparative analysis of the impact of laser count on the width of the melt pool and yielded valuable insights into the correlation between laser quantity, power, and the resulting characteristics of the melt pool. Figure 5.1 shows that as the number of lasers increases, the melt pool width increases along with its stability, and a direct correlation between laser usage and melt pool width can be observed. Furthermore, this correlation agrees with previously reported findings relating spot size to melt pool width [8].

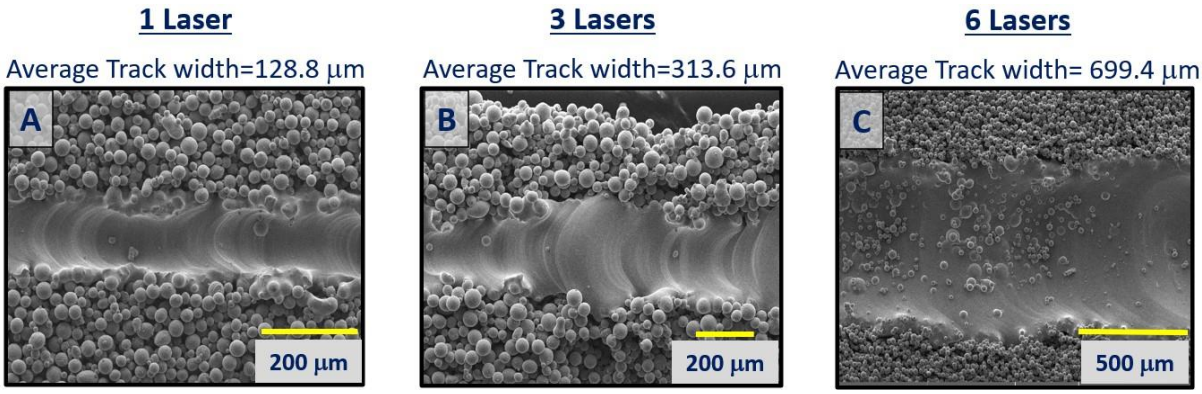

Figure 5.1 - Melt Pool Width Variability Across (A)-1, (B)-3, and (C)-6 Laser Configurations with Consistent 50 mm/min Scanning Speed and 2.8W Power

The experiment then progressed to using a six-diode array only (*section 3.2.3*). Consequently, the total power output was approximately 16.8 W (2.8 W per diode multiplied by six diodes) with reference to the study by Alsaddah *et al.* [9], which used a 3.5W single

laser with 100 µm layer height and achieved a melt pool temperature of approximately 1650°C at a scanning speed of up to 300 mm/min. Moreover, they defined hatch distance as 50-70% of melt pool width. Hence, it was assumed that a faster scanning speed than 300 mm/min would be ineffective in melting the powder. This presumption was based on single laser studies, which did not provide sufficient evidence of effective material melting with multi-laser settings.

To ensure a scientific and systematic approach to assessing the impact of various parameters at a 2.8W power setting, a randomized methodology was employed as the multi-450 nm diode lasers impact was unknown to be continued for full factorial approach like in the previous chapter. Using Minitab software, Table 5-1 was generated to design experiments based on a 2^2 Taguchi design. This design involves two factors—scanning speed and hatch distance—each set at two levels. The Taguchi method, renowned for its robustness in optimizing process parameters with a minimal number of experiments, facilitates the identification of the optimal settings by evaluating the effects of these two factors on the outcome in single-layer experiments. This structured approach allows for an efficient examination of the interaction between scanning speed and hatch for their influence on layer quality and dimensional accuracy.

Table 5-1 - Analysis of Literature-Derived Data Using Minitab Statistical Parameters

Sample Code	A	B	C	D
Parameters	SS10HD50	SS400HD400	SS400HD50	SS10HD400
SED (J/mm^2)	33.6	25.2	33.6	50.4

Figure 5.2 shows different results for each sample in the random study. Sample 'A' demonstrated predominantly void formations over more than half of its extent. Sample 'B' exhibited signs of sintering, indicating insufficient melting. Sample 'C' displayed void formations towards the end and sintering at the beginning. Sintering was happening due to a lack of energy required to melt the metal powder [226,235]. In terms of void formation, it occurs differently than the balling phenomenon. However, both of them are connected to each other. Both balling and void formation can be fixed by the increase in energy density. However, void formation requires more power [112,236], and balling requires less speed to achieve it [226,235]. Sample "D" presented sintering at the beginning with a gradual transition

to a more solidified state towards the end. As the SED increases, the problems associated with void formations are reduced, and the tracks allow for more efficient and thorough melting.

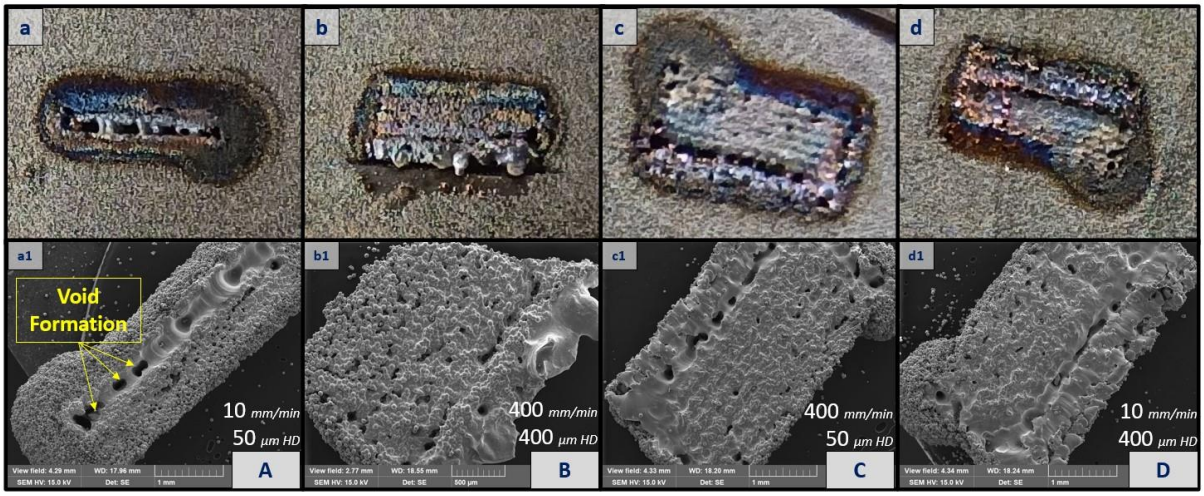

Figure 5.2 - Composite Display of On-Site Photographs (a-b-c-d) and SEM Images (a1-b1-c1-d1) of Literature-Derived Sample Set Featuring Identified Defects. HD stands for hatch distance in the pictures. a and a1, b and b1, c and c1, d and d1 are the same samples (dimensions can be compared within each other).

However, upon analysis, none of the parameter sets produced results that were promising. It was, therefore, decided to continue with further experiments, including laser pitch tests (also known as track tests due to the multi-laser system). This comprehensive approach aims to identify discrepancies with literature data [8,9] and thereby identify any system components that may not be performing as expected.

5.2.2 Diode Laser Pitch Experiments

This study segment examined the effect of diode laser spacing on melt pool quality and observed defects. The experiments were conducted with each diode laser at its maximum power of 2.8 W, a layer height of 1000 µm, a constant hatch distance of 500 µm, and a scanning speed of 50 mm/min. The aim was to assess the influence of track and hatch distances on large samples. A critical focus was on how varying cooling rates influenced laser operation and altered melt pool shapes, allowing for a detailed analysis of laser interactions and their effects on the microstructure and quality of the layers.

Figure 5.3 shows that of the configurations tested, only lasers one and two achieved satisfactory surface density. Furthermore, the combinations of diode number one with three, four, six and the 2-4-6 trio demonstrated that all lasers were working as intended, as

evidenced by the expected void formations. However, a problem arose with the pairing of diode lasers number one and five (highlighted in Figure 5.3-l), where laser number five was ineffective, as evidenced by its inability to achieve solidification, resulting in partial melting or mostly sintering. It is also important to note that some of the cracks observed during the study were not due to the process itself but occurred during the transfer of the samples to the SEM specimen holder. This observation is significant because the samples in question were not fully melted initially, nor was complete melting expected under the experimental conditions set. The cracks were, therefore, accidental, occurring during handling and do not necessarily reflect the inherent properties of the materials or the success of the melting process.

The knowledge gained from these observations led to the conclusion that this experimental approach was effective in identifying non-functioning lasers. However, despite the use of operational lasers, some instability in the melt pool dynamics was still evident, as shown in Figure 5.3-c-f-i-o-r. This instability required further investigation. To address this issue and gain a better understanding, diode number five, which was showing signs of ineffective operation, was replaced. With this modification, the study progressed to performing scanning speed experiments. The aim of these scanning speed experiments was to investigate melt pool behaviour in more detail and to assess the effect of varying scan speeds on melt pool quality and consistency, particularly with the updated laser configuration. This step was critical to refining the process and ensuring more reliable and consistent results in subsequent tests.

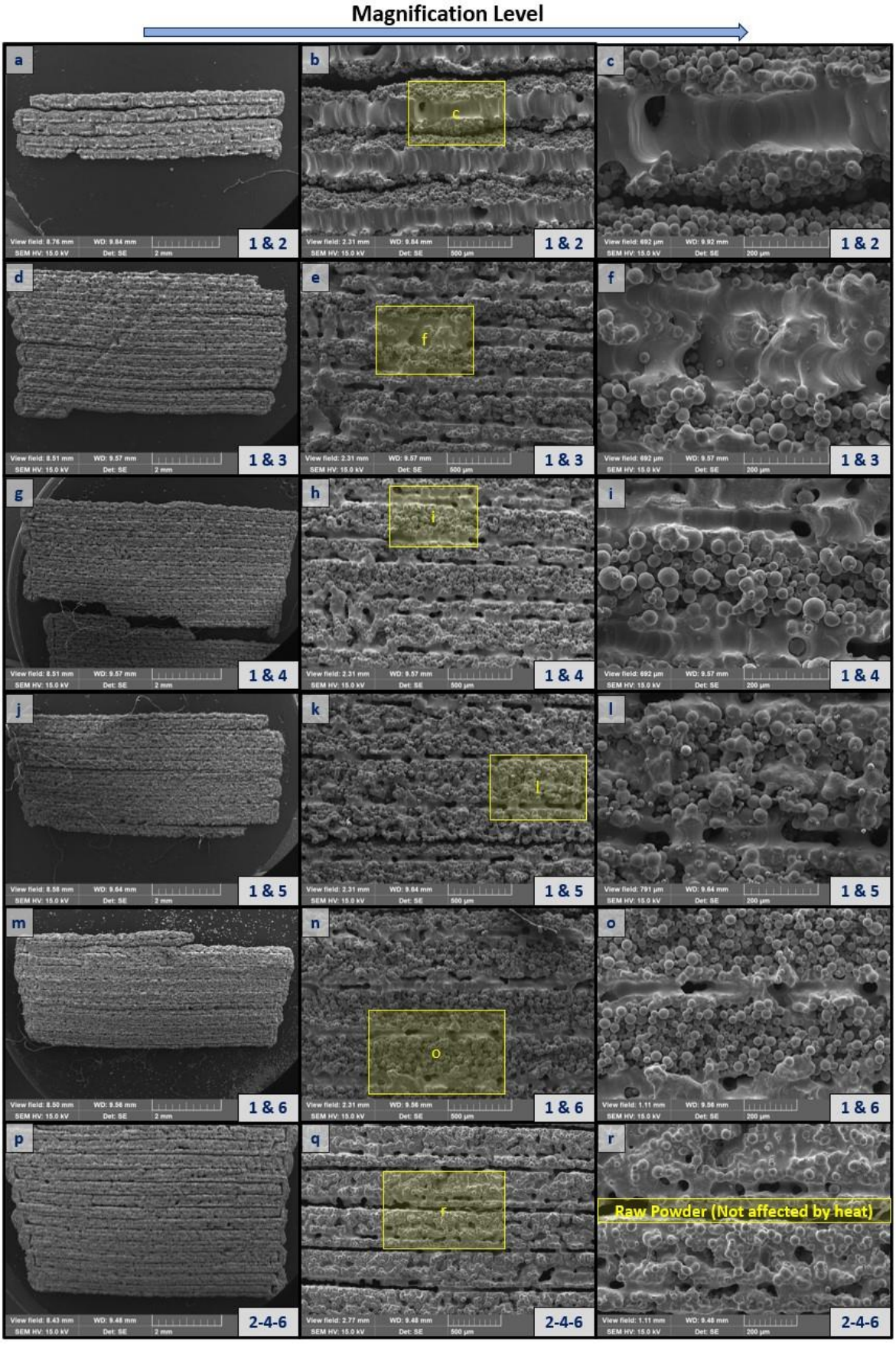

Figure 5.3 - SEM images from experiments assessing the effects of different diode laser pitch configurations. In the layout of the figure, each row depicts progressively higher magnifications from left to right for the same sample. The labels 1&2 (a-b-

c), 1&3 (d-e-f), 1&4 (g-h-i), 1&5 (j-k-l), 1&6 (m-n-o), and 2-4-6 (p-q-r) indicate the active lasers during deposition for each specific test. For all experiments, the hatch distance was consistently set at 500 µm, with each laser operating at a power of 2.8W, a scanning speed of 50 mm/min, and a layer height of 1000 µm.

Once the issue of non-functioning lasers had been addressed, it was decided to proceed with the scanning speed experiments. The primary objective of these experiments was to determine whether the speed data would be consistent with findings reported in the existing literature. This approach was particularly important to confirm that the previously observed discrepancies in the data were not simply due to the faulty lasers. By replacing the faulty lasers and performing scanning speed experiments, the aim was to isolate and understand the effect of scan speed on the results, thereby ensuring a more accurate and reliable assessment of system performance.

5.2.3 Scanning Speed Experiments

The scanning speed experiments were conducted to determine if the speed range was consistent with that reported in the literature and to understand the limitations of the system in this regard. The scanning speed settings tested were 10, 50, 100, 250, 500 and 1000 mm/min, with fixed parameters of 400 µm hatch distance, 1000 µm layer height and 16.8 W power. The results, as seen in the SEM images shown in Figure 5.4, varied across the different speeds.

At 10 mm/min, there was a high degree of void formation. It was also noted that a few lasers had malfunctioned (exploded) during this part of the experiment and were replaced for subsequent tests. This malfunction explained why the remainder of the sample at this speed (Figure 5.4-a) appeared sintered due to insufficient energy to melt the material properly. The sample processed at 50 mm/min experienced cracking, presumably due to extreme temperature gradients. At 100 mm/min, no void formations were observed, but the traces were inconsistently shaped, with some peaks resembling balling phenomena. Notably, this sample also cracked when removed from the unattached powder bed, suggesting incomplete melting and poor track attachment. Similar problems were encountered with the samples processed at 250, 500 and 1000 mm/min. These results indicate that while certain speeds resulted in better melting than others, none were entirely consistent with the expected results based on the literature, suggesting the need for further optimisation of the system parameters.

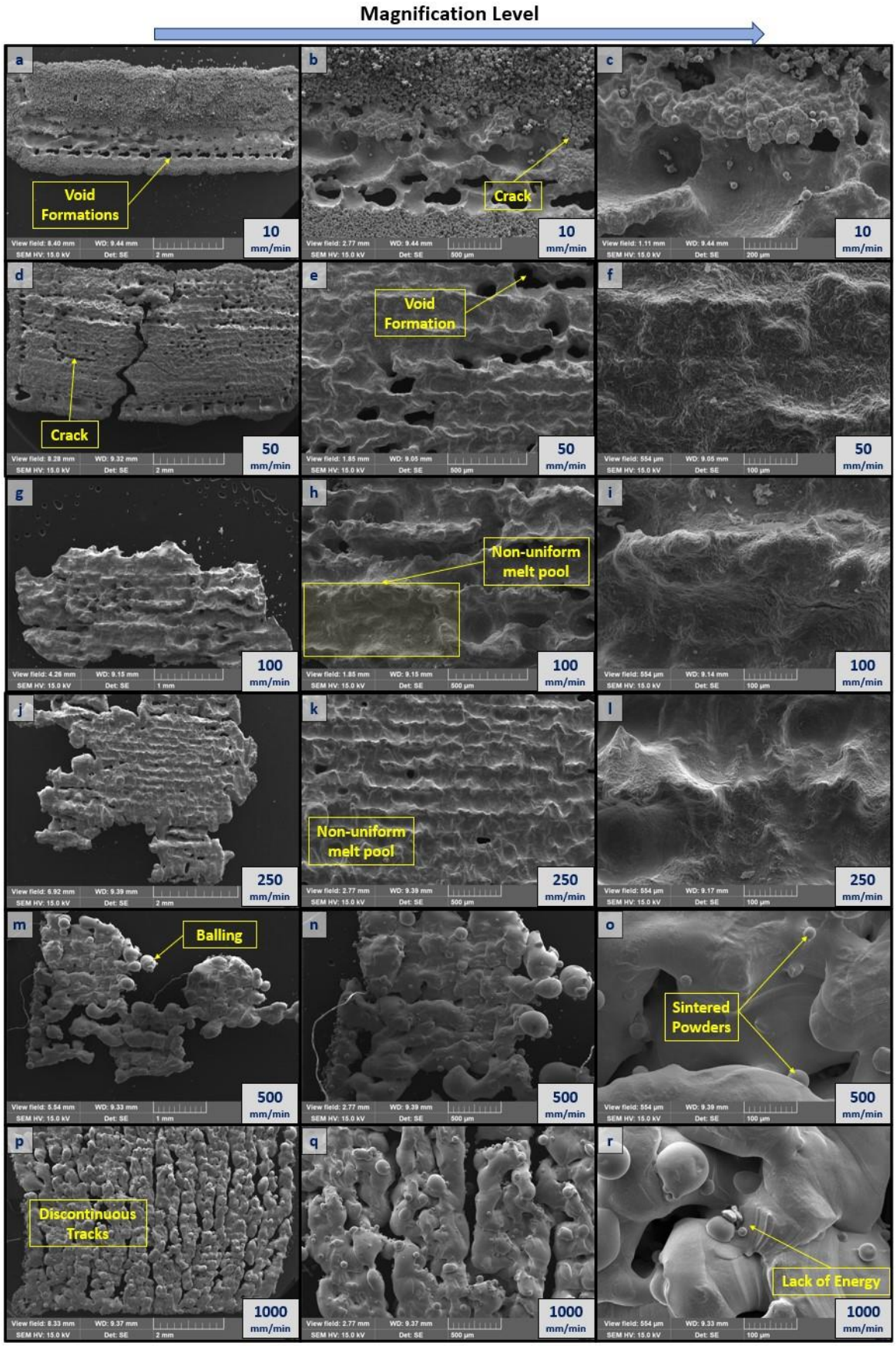

Figure 5.4 - SEM images from experiments assessing the effects of different scanning speed effect on solidified sample. In the layout of the figure, each row depicts progressively higher magnifications from left to right for the same sample.

Scanning speed with 10 mm/min (a-b-c), 50 mm/min (d-e-f), 100 mm/min (g-h-i), 250 mm/min (j-k-l), 500 mm/min (m-n-o), 1000 mm/min (p-q-r) is shown.

Based on previous experiments, a scanning speed of 50 mm/min was chosen for the hatch distance experiments because it consistently produced sufficient melt regions. This speed was selected to align with existing literature, ensuring that the results were comparable and could validate and corroborate existing research. The aim was to provide consistent and reliable data that contributes valuable insights to the field.

5.2.4 Hatch Distance Experiments

The hatch distance studies were performed to evaluate the system's melt track overlap within a range of 300-500 µm hatch distance, which is equivalent to 50-70% overlap, given that the spot size was approximately 475 µm wide. The parameters for these studies were set at increments that allowed meaningful comparison with literature data [8]. An increment of 100 µm was chosen for its effectiveness in detecting relevant hatch distance changes to fit one factor at a time approach.

For the experiments, hatch distances of 100, 200, 300, 400, and 500 µm were selected, with a fixed scanning speed of 50 mm/min, power setting of 16.8 W, and layer height of 1000 µm. The SEM images in Figure 5.5 revealed varying results: at 100 µm, the material surface was rough, resembling a burnt surface due to excessive energy input. At 200 µm, there was a slight improvement, though the quality was still poor. A 300 µm hatch distance showed improved track bonding in areas, while 400 and 500 µm distances exhibited increasing track separation. The results did not consistently align with literature, suggesting potential differences in system performance or experimental conditions and underscoring the need for further investigation and parameter optimisation.

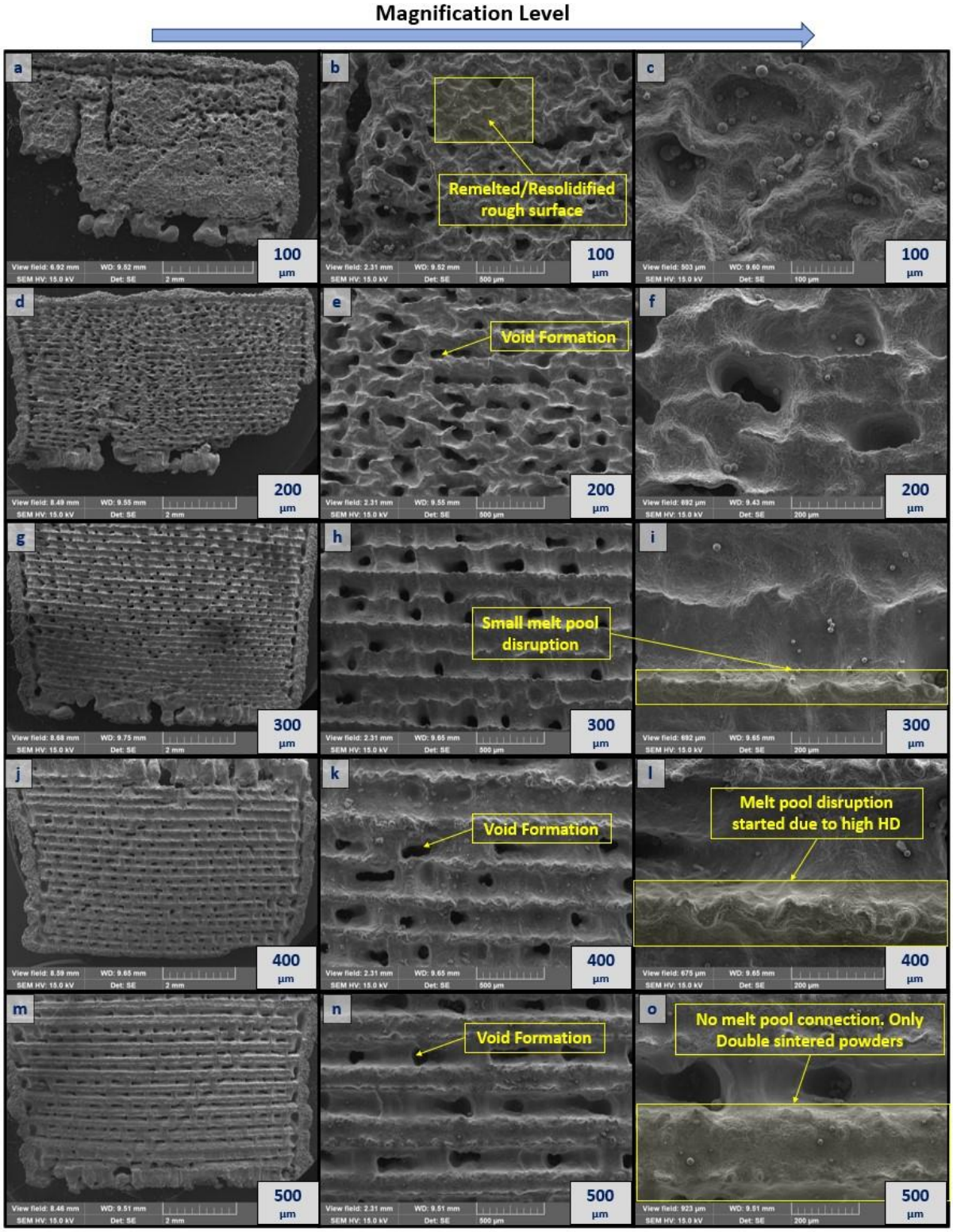

Figure 5.5 – SEM images from experiments assessing the effects of different hatch distance effect on solidified sample. In the layout of the figure, each row depicts progressively higher magnifications from left to right for the same sample. Hatch distance with 100 µm (a-b-c), 200 µm (d-e-f), 300 µm (g-h-i), 250 µm (j-k-l), 500 µm (m-n-o) is shown.

5.2.5 Optimal Parameters in Single Sample Experiments for Multi-Layer Studies

The aim of this section was to calculate VED and NED to analyse the behaviour of the melt pool under different energy input conditions. The focus was on assessing whether the tracks were properly connected to each other, the presence of any lack of fusion and potential distortions in the samples. A consistent parameter of 100 µm layer height, as reported in the literature [9], was maintained across all samples, each consisting of 50 layers. Based on the data derived from the literature, as shown in Table 5-2, new parameter sets were formulated to observe the effects associated with the corresponding VED and NED values.

Table 5-2 - 3W Multi-Layer Parameter Set Configurations

	A	B	C	D
Scanning Speed (mm/min)	200	300	100	50
Hatch Distance (µm)	200	100	300	400
VED (J/mm^3)	252	336	336	504
NED (E_0^*)	10.73	14.31	14.31	21.46

Figure 5.6 illustrates the results of the study using SEM images from samples A to D, representing a progression from lower to higher energy densities. In particular, the parameters for samples A and B, as detailed in Table 5-2, were chosen to demonstrate how parameters that did not work effectively in previous sections could alter the material behaviour in this context. As previously discussed, the cooling rate has a significant effect on this behaviour, with higher energy density correlating with lower cooling rates in terms of energy input per unit area.

Consequently, as the energy density increases in the order of A-B-C-D samples, a transition is observed from balling to almost fully melted sections on the top surface. It's important to note, however, that despite these variations in melting behaviour, none of the samples exhibited a surface quality sufficient to warrant further cross-sectional investigation. This underlines the complexity of achieving optimum surface conditions and highlights the need for further experimentation and parameter refinement.

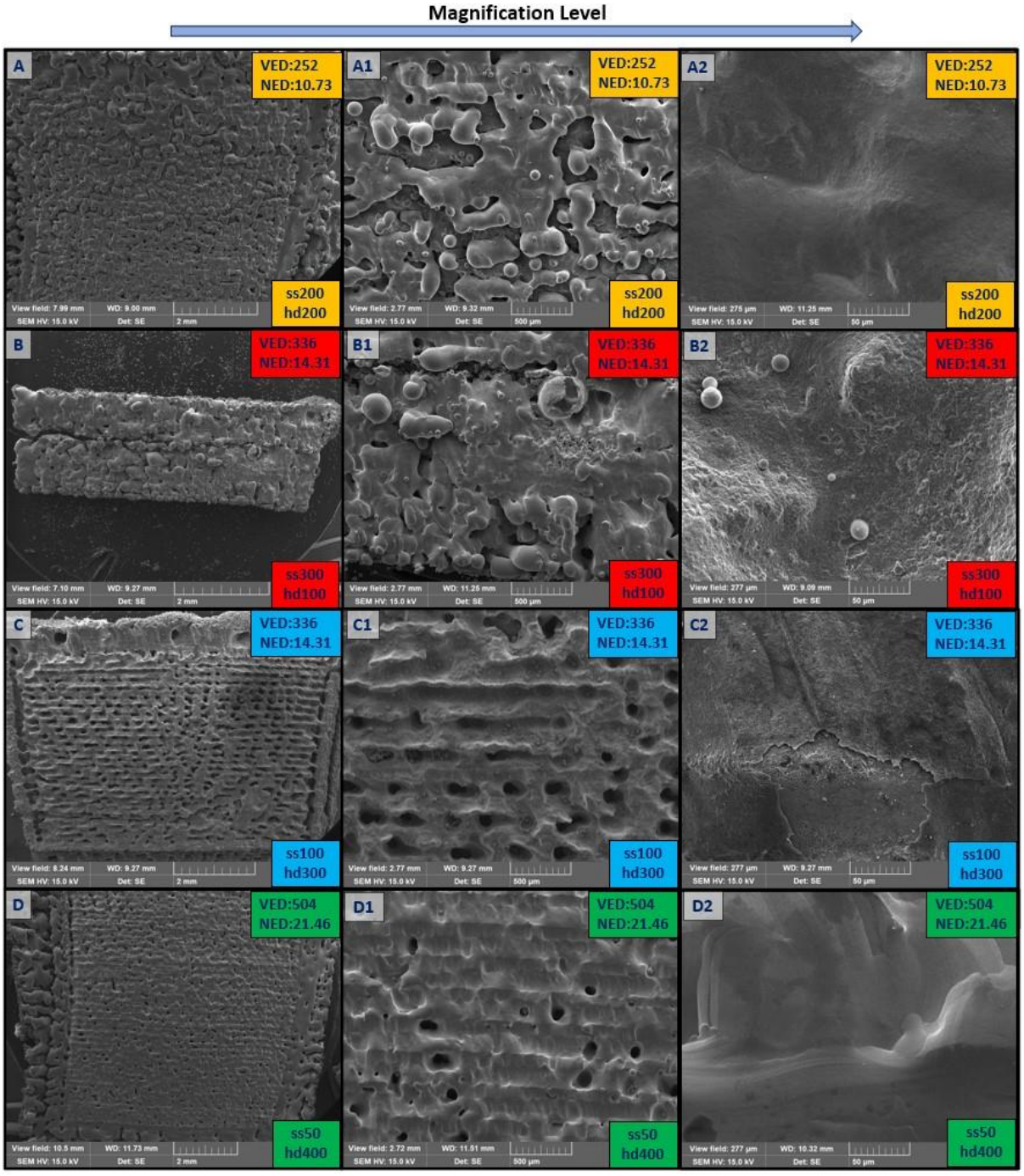

Figure 5.6 - Top Surface SEM Images from Multi-Layer Study Experiments from Table 5-2 based on VED and NED values in comparison via different effect of the dual parameter change, which these are scanning speed (ss) and hatch distance (hd). In the layout of the figure, each row depicts progressively higher magnifications from left to right for the same sample.

The observations from the experiments highlight that even with identical NED or VED values, the top surface quality of a sample can vary significantly. This is illustrated by the transition from lack of fusion to void formation surface defects observed from sample B to sample C (as shown in Figure 5.6- B and C). The influence of the scanning speed on the concurrent cooling rate and the influence of the hatch distance on the cooling rate of adjacent

tracks are both critical factors. However, these images suggest that scan speed has a more pronounced effect on melt pool continuity than hatch distance.

An interesting disparity is observed in the melt pool waviness across all samples, which differs from the expected results based on the literature. In particular, the 400 µm hatch distance melt pool showed inconsistent waviness within adjacent tracks. In particular, Figure 5.6-c shows more void formation surface defects compared to Figure 5.6-d, as sample C has a lower energy density than sample D (see Power Experiments section). Thus, the critical finding can be inferred that an increase in cooling rate (associated with low energy density) is more likely to result in void formation compared to scenarios with a low cooling rate.

Focused images (Figure 5.6-C2, D2) show that C2 contains a higher number of spattered particles than D2 due to its doubled velocity. In addition, C2 showed some surface cracking, whereas the fully melted areas of D2 appeared smoother. This could be related to the cooling rate, suggesting that a lower cooling rate improves the quality of the surface finish (in terms of reduced surface roughness).

A critical issue was the delamination of all samples with a 100 µm layer height, indicating a lack of fusion between the layers. In addition, the integrity of the samples was considered to be insufficient, as evidenced by the challenges encountered in removing them from the substrate. This lack of integrity and fusion issues highlight the need for further optimisation and adjustment of parameters in the experimental setup.

The study discovered a feedback loop in the laser system where increased heat led to more current draw, higher optical power, and elevated temperatures, often causing laser failure. This malfunction, potentially damaging laser components and affecting efficiency, was suspected of causing voids in samples. To resolve this, the research transitioned to 4.5W diode lasers, limiting power to 4W per laser for safety and adjusting the cooling system for improved efficiency. This shift from 3W to 4.5W lasers (in other words increasing the power), aimed at addressing issues like delamination and void formation, involved upgrading the cooling system to handle nine lasers with a total power of 36W. This adjustment aligned the system's efficiency with previous studies (50W with 808 nm with 2 arrays [8]), representing a significant development in the research.

5.3 High Power (4W) Diode-Laser Power Studies

Given the results of the low power (2.8W) study, which unveiled that the dynamics of the melt pool varied significantly with each combination of parameters, it became evident that a new dataset was necessary in order to generate a parameter map that is specific to the 450 nm multi-laser head. This approach acknowledges that the parameters for this particular setup should not be directly derived from existing literature [9] due to the distinct dynamics involved. Instead, they should be independently determined and subsequently compared to the results in the literature after analysis. A comprehensive investigation of single-track studies was initially conducted to ascertain the optimal region for Ti6Al4V processing. The parameters were then refined within the region that yielded complete melting. Then, layer height of 400 µm for hatch distance study was determined through a small preliminary experiment. The layer height was dropped from 1000 µm gradually till the penetration of the laser reached to optimal substrate adhesion and damage-free removal. Subsequently, a study focusing on a single-layer hatch distance was performed utilising the selected optimal parameters. A region known as "optimum NED" was subsequently established based on the optimal parameters employed in the layer height study. For the purpose of consistency of the experiment, three samples were fabricated for each parameter set. The aforementioned parameters are presented in Table 5-3.

Table 5-3 - Layout for Parameter Testing in the 4W Study. LH stands for layer height, HD stands for hatch distance, SS stands for scanning speed, NED stands for normalised energy density, and #L stands for number of layers

Expanded Single Track Parameters - 1				**Narrowed Single Track Parameters - 2**			
LH	1000	µm		**LH**	1000	µm	
SS	50, 100-1000	mm/min	100 inc.	**SS**	20-90	mm/min	10 inc.
Size	20	mm		**Size**	20	mm	
Hatch Distance Parameters - 3				**Layer Height Parameters - 4**			
LH	400	µm		**Area**	5 x 5	mm^2	
SS	50, 75	mm/min		**NED**	1-25		
HD	300-1200	µm	100 inc.	**LH**	400,200,100,60	µm	
Size	5x5	mm^2		**#L**	20	Layers	

5.3.1 Cooling rate vs Normalised Energy Density

To understand the effect of cooling rate on samples and parameters with this bespoke DAM system, it is necessary to investigate its importance. A high energy density can be created at slow scanning speed, short hatch distance, or a thin layer height, resulting in lower

cooling rates for almost all parameter conditions with higher E_0^*. Figure 5.7 illustrates the influence of scanning speed, hatch distance, layer height, and E_0^* on cooling rates. The correlation between cooling rates and E_0^* can be attributed to the HAZ that result from pre-heating the adjacent unmelted powder during the in-situ melting of a single track. Increasing the number of laser beam passes (short hatch distance or high number of overlaps) within a processing layer (in situ) gradually raises the temperature of neighbouring powders throughout the process. This reduction in melting temperature gradient (ΔT) for each subsequent pass results in a higher overall completed track temperature compared to the high hatch distance version of a specimen. This may prolong the solidification process and potentially impact the phase transition. The low cooling rate can also be attributed to the slow scanning speed and thin layer height (Figure 5.7-i). Slow scanning speed affects the temperature of adjacent raw powders similarly to hatch distance, while a thin layer height means there is less material available to melt and fuse the layer below (Figure 5.7-ii).

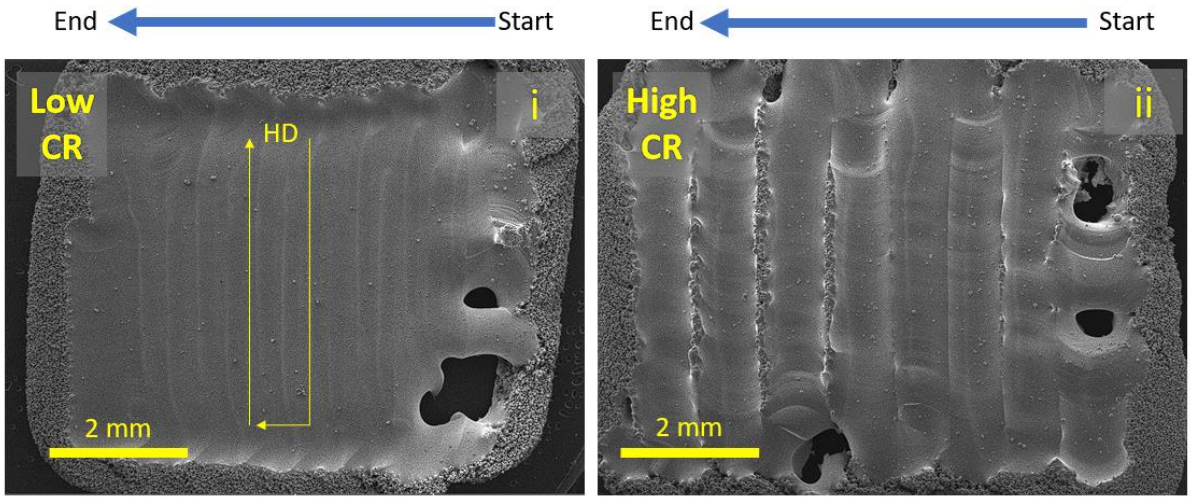

Figure 5.7 - Evaluation of Cooling Rate Impacts through Top Surface SEM Imaging: Parameter Samples (i) 50SS400HD100LH23E_0^* and (ii) 75SS800HD400LH2E_0^*

5.3.2 Single Track Studies

This section examines the impact of the number of diode lasers on melt pool width and depth. The goal is to understand how melt pool dimensions vary with consecutive active lasers and their parameters.

The study began by setting layer height at 1000 µm and scanning speed at 50 mm/min for a single-track length of 20 mm. The number of laser impacts on the melt pool was then

observed, following prior research [9][8] methodologies. Analysis of data from the beam profilometer revealed the FWHM beam dimensions for laser groups using 1, 3, 6, and 9 lasers to be 52 μm, 215 μm, 430 μm, and 659 μm, respectively. The results of these single-track studies showed that the melt pool width was approximately 75% greater than the irradiated area of the active lasers in these four distinct laser groups. Furthermore, Figure 5.8-a depicts that both the width and depth of the melt pool increased correspondingly. However, it is important to note that the depth of the melt pool appeared to have a limit to its penetration depth, even as the number of lasers increased (and therefore, the laser-irradiated width of the melt area increased). There was no significant change in the energy input per unit area on the powder bed, whether a single laser or a configuration using all nine lasers was used. This can be attributed to the fact that the energy input remained constant.

Figure 5.8-b shows the results of a parameter study conducted with nine 36W lasers to observe the effect of varying scanning speed on melt pool width and depth, using Table 5-3-1 and Table 5-3-2 data sets. The study shows an upward trend in melt pool width from 20 to 80 mm/min scanning speed, extending to 100 mm/min for melt pool depth. At lower scanning speeds (20 to 100 mm/min), excessive heat concentration at the focal point results in very high temperatures. Without preheating the powder bed, a temperature gradient forms, leading to rapid heat conduction and melting a larger area, thus creating larger melt pools. At higher speeds (300-500 mm/min), cross-sectional dimensions of the melt pools become more spherical. Measurements from the top of the solidified track to the last solidified section indicate that the peak point of the top surface is higher at slower speeds. Between 300-500 mm/min, sphericity increases due to balling phenomena, causing an increase in depth. Beyond 500 mm/min, melt pool dimensions decrease and tracks become discontinuous due to high sintering rates. Thus, both depth and width of the melt pool decrease as scanning speed increases past 100 mm/min. In single-track processing, physical characteristics such as the HAZ, cracks, spattering, balling phenomena, substrate penetration, and track continuity were assessed.

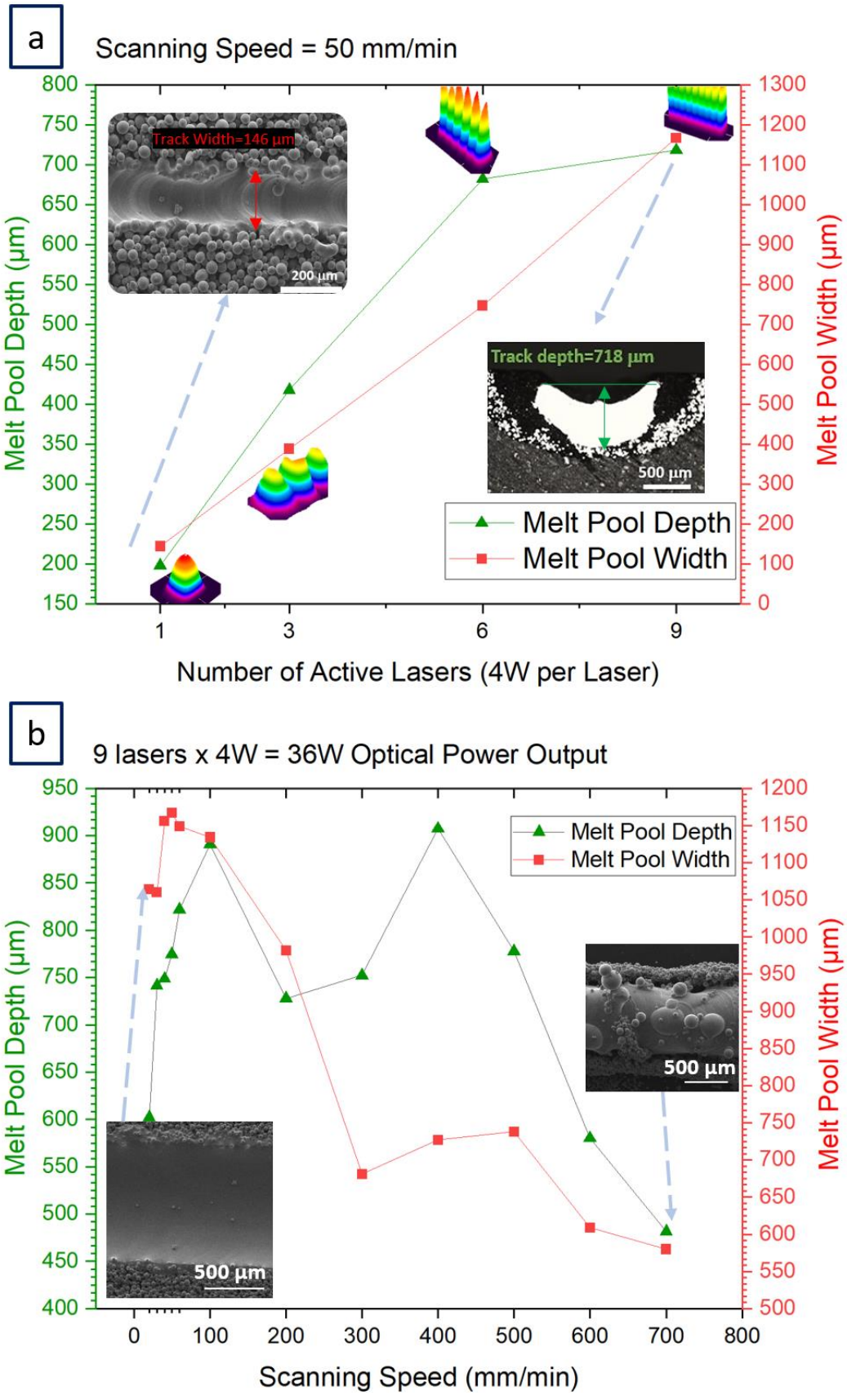

Figure 5.8 - Graphs of Single Tracks Illustrating Melt Pool Width and Depth: (a) Relationship with Number of Active Lasers, (b) Relationship with Scanning Speed

Table 5-4 provides a detailed compilation of information on the observed defects. Single tracks with a scanning speed between 40 and 80 mm/min produced the smoothest surface finish. Spattering was significantly reduced when scanning speed was below 80 mm/min compared to higher speeds. The powder can still be melted at speeds of 90 to 500 mm/min, but with defects. The HAZ is larger than that of single laser LPBF systems due to the inherently slow scanning speed [8]. The HAZ was measured from the last solidified section of the tracks towards the end of sintering until reaching the raw powder. The results showed that the HAZ decreased as the scanning speed increased. This was because the energy applied per unit area at a given time decreased. In practice, the HAZ remained relatively linear beyond a scanning speed of 300 mm/min. At scanning speed values above 600 mm/min, the powder only sintered, making it difficult to identify a clear reference point for measuring the HAZ. It is important to note that limiting the scanning speed to values as low as 20 or 50 mm/min results in minimal spattering or low amounts of spattering, typically involving fewer than five ejected particles per second. This phenomenon contrasts with industrial LPBF systems, where spattering tends to increase with higher speeds [195]. Cracks are likely to have occurred due to a high cooling rate. The degree of substrate penetration was determined by the ease with which the tracks could be removed from the substrate.

Table 5-4 - Results from Single-Track Parameter Experiments (S2S – Sticked to Substrate)

Parameters	Observations / Defects					
Speed (mm/min)	*HAZ (µm)*	*Cracks*	*Spatter (particle(s))*	*Balling*	*Substrate Penetration*	*Track Continuity*
20	≈2000	Major	0-2	No	S2S	Yes
30	≈1000	Minor	0-3	No	S2S	Yes
40	≈500	No	1-3	No	S2S	Yes
50	≈450	No	1-4	No	S2S	Yes
60	≈400	No	2-5	No	S2S	Yes
70	≈300	No	2-5	No	S2S	Yes
80-200	300-200	No	10-30	Yes	Half S2S	Yes
300-500	≈200	No	30+	Yes	Separated	Yes
600-1000	N/A	N/A	High (50+)	Yes	Separated	No

5.3.3 Single Layer Studies

The investigation aimed to determine the optimal overlap value to achieve the highest possible density while maintaining surface quality. Cross-sectional analysis and the average surface roughness (R_a) of the top surface were the three factors used to make this assessment. The powder was applied at a layer height of 400 µm, as outlined in the methodology. The percentage of overlap was calculated (Eq.15) using the average melt pool width (1078 µm) at 50 and 75 mm/min scanning speed. Negative values indicate no overlap and positive values indicate overlap (see Table 5-3-3). Figure 5.9 illustrates the effect of hatch distance on the sample. The top surface consistently exhibited nearly full density up to 800 µm hatch distance. However, on examination of the cross-section it is clear that full adhesion was only achieved at 400 µm and 500 µm hatch distance. At scanning speeds beyond 900 µm hatch distance, sintered powders accumulated between the tracks. 300 µm hatch distance samples consistently cracked or shattered during sectioning in all experiments, probably due to a significant thermal gradient caused by lack of substrate heating. Therefore, the study did not investigate 200 µm hatch distance and 100 µm hatch distance.

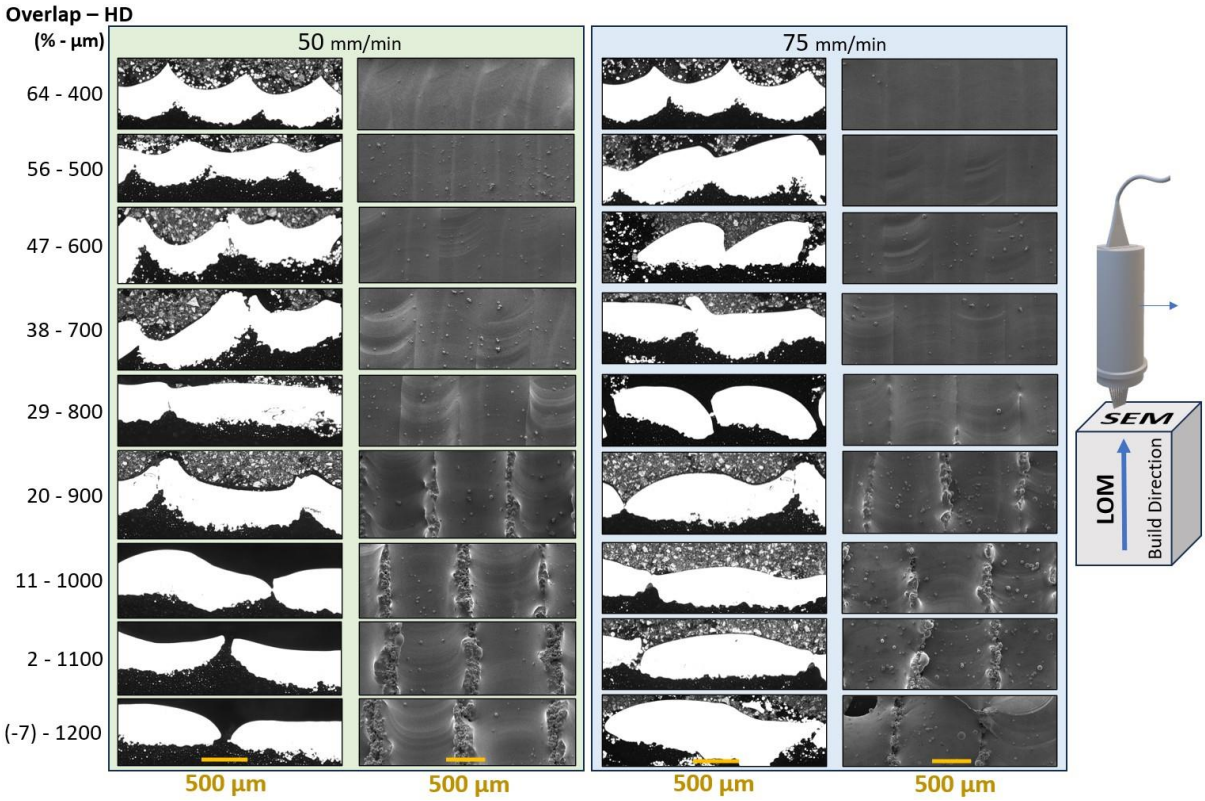

Figure 5.9 - Cross-Sectioned LOM and Top Surface SEM Photographs of Hatch Distance (HD) Study Specimens: 50 mm/min Column (Green) and 75 mm/min Column (Blue), with Yellow Bars Denoting 500 µm Scale for Each Column

The tracks had a crescent shape, with the curvature becoming more pronounced towards the edges as the hatch distance decreased. This was because the lasers were perpendicular to the scanning direction. This phenomenon may have implications for the density of multi-layered samples and is referred to as the 'crescent effect' (Figure 5.10 and Figure 5.13). The phenomenon could be attributed to Marangoni flow, heat transfer dynamics, and recoil pressure [114,181,183,237]. The temperature distribution of the wider melt pool resembles a crescent moon, with a hotter center and cooler edges. This is due to Marangoni flow, which occurs when surface tension differences caused by temperature variations pull the liquid towards the hotter center. Heat is also transferred to the cooler powder bed and substrate at the bottom of the melt pool near the first laser. The melt pool bottom of the fifth laser is surrounded by high temperatures and transfers its heat primarily towards the cooler substrate. The crescent shape is reinforced by the combined factors of the recoil pressure pushing molten metal downwards and concentrating heat at the center, potentially impeding downward heat flow near the center where the pressure is highest and sharpening the curvature at the edges.

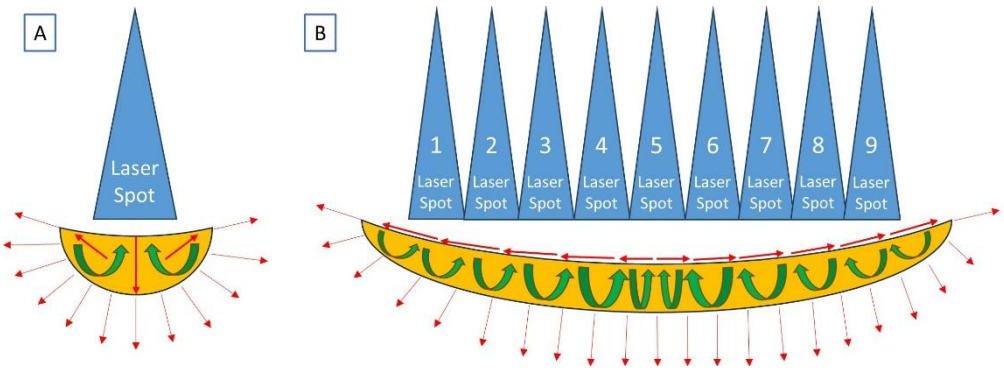

Figure 5.10 - Illustration of the Crescent Effect: Showcasing Marangoni Flow with Green Arrows and Heat Transfer with Red Arrows in (A) Single Laser and (B) Multi-Laser Processing

To improve uniformity in the multilayer fabrication process, it was investigated that the relationship between surface roughness (R_a) measurements and E_0^*, while limiting the influencing factors to only scanning speed and hatch distance (as shown in Figure 5.11-A). The analysis indicates that rough surfaces may result in uneven layer heights, leading to inconsistent energy density distribution within the layer due to variations caused by the crescent effect. Furthermore, the study found that decreasing the scanning speed led to a decrease in R_a and an increase in energy density. Additionally, a negative correlation between

hatch distance and scanning speed was observed with regards to surface roughness, which can be divided into two distinct sections. To categorize the sections for the study, it was divided two parts which the first section when hatch distance exceeded 800 µm and the second section when hatch distance fell below 800 µm. The first section related to the discontinuities observed between the tracks, which were mainly due to an insufficient number of lasers (or insufficient overlap) or a high cooling rate. This resulted in a reduced energy density, which promoted the sintering of the material rather than complete melting (see Figure 5.11-B). The second section became relevant when tracks merged with previous ones. In this case, using a shorter hatch distance reduced the cooling rate and mitigated the crescent effect in the area. It is possible that the edge of the previous track was partially re-melted and re-solidified, and therefore the height of the peaks was reduced (Figure 5.11-C).

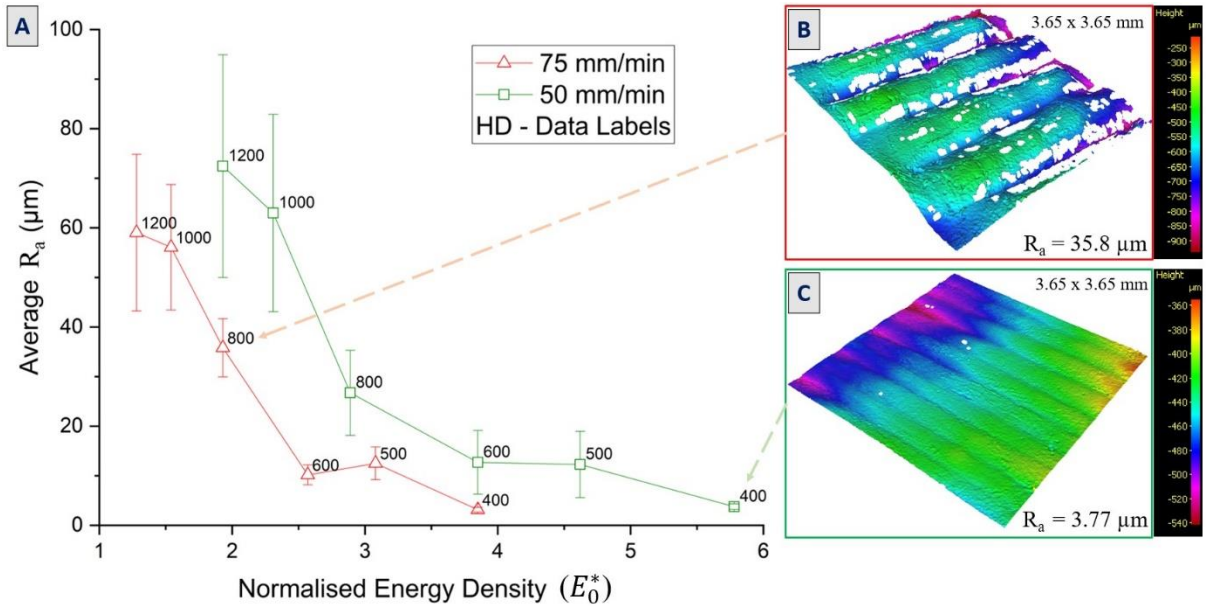

Figure 5.11 – (A) Chart Illustrating the Correlation Between Surface Roughness (Ra) and Normalised Energy Density (E_0^*) Utilising 3D Light Spectrometry Images with Hatch Distance (HD) Annotations at (B) 75SS800HD and (C) 50SS400HD

5.3.4 Multilayer Studies based on Normalised Energy Density

5.3.4.1 Densification studies

For single-layer fabrication, it is preferable to use hatch distance parameters below 800 µm. As shown in Figure 5.9 and the roughness study in Figure 5.11, this will result in a greater area of fusion between the tracks. The scanning speed should be set to either 50 mm/min or 75 mm/min, with 75 mm/min being the upper limit based on the results of the single-track study. To ensure similar E_0^* values, groups with related scanning speed and hatch

distance parameters should be selected. The study of layer height began at a depth of 800 µm and concentrated on the lower half of each group until 100 µm, as shown in Figure 5.12 of Table 5-3-4. Due to insufficient fusion, the layer height layer at 800 µm is not visible on the graph.

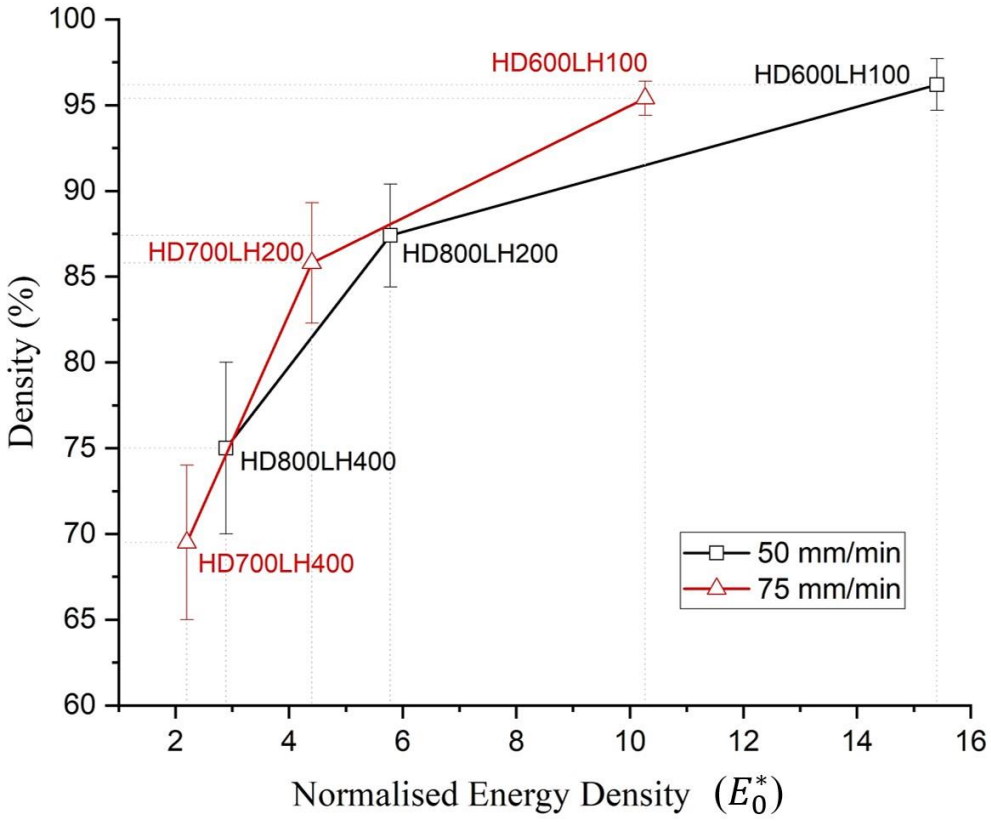

Figure 5.12 - Examination of the Relationship Between Sample Density and Normalised Energy Density (E_0^*) Across Diverse Parameter Sets

Figure 5.12 includes two samples, as shown in Figure 5.13. The modification of hatch distance values to 600 µm in Figure 5.12 was necessary due to inconsistent E_0^* values within a single layer (Figure 5.13-b-c-e-f), which was attributed to the crescent effect. Therefore, the hatch distance values were gradually reduced to ensure consistency, first to 700 µm and then to 600 µm. Figure 5.12 shows that when the hatch distance is 600 µm and the layer height is 100 µm, the samples can reach high-density regions (>95%) and connect with the solidified layer below. Additionally, decreasing the layer height to achieve a high E_0^* increases density.

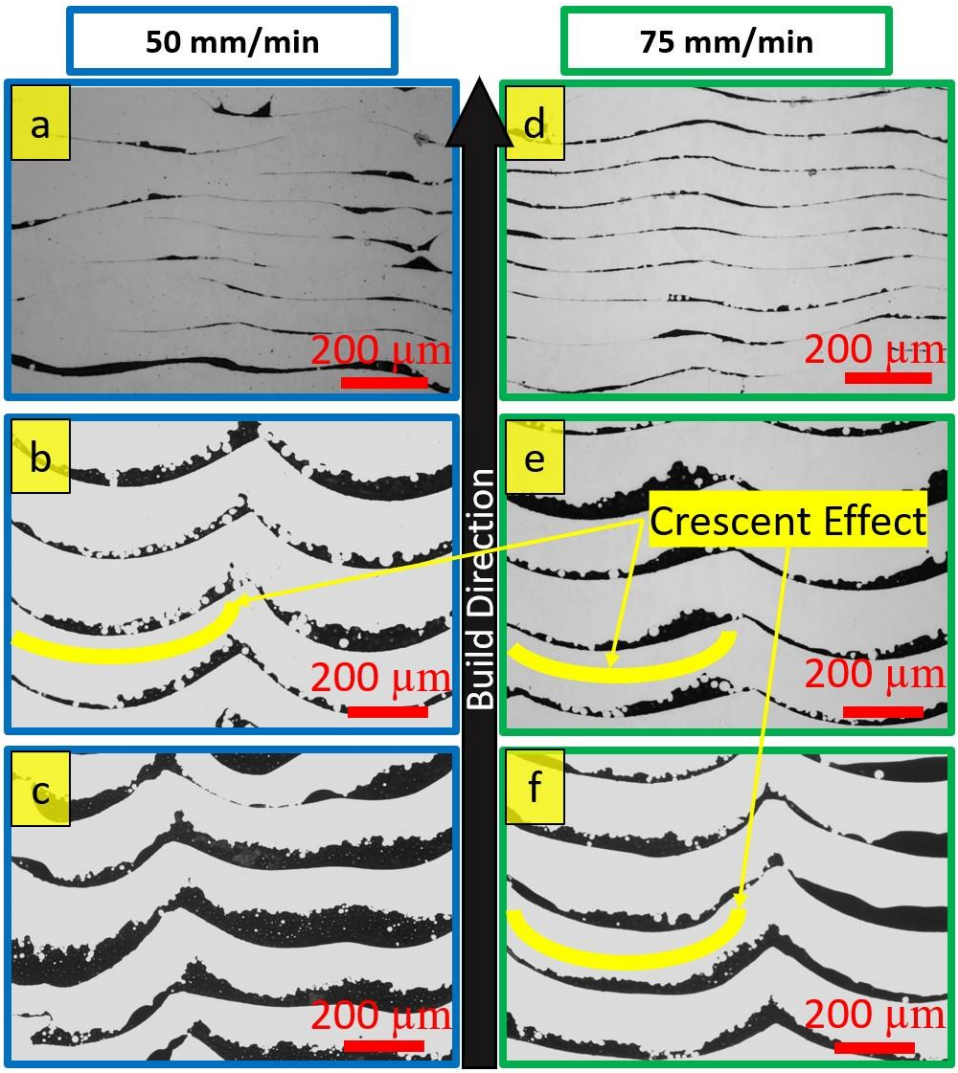

Figure 5.13 - LOM Cross-Sectioned Photographs Showing Different Parameter Sets, with Illustrations Demonstrating the 'Crescent Effect' (where (a) 600HD100LH, (b) 800HD200LH, (c) 800HD400LH, (d) 600HD100LH, (e) 800HD200LH, (f) 800HD400LH). (Black sections indicate porosity/air gap/lack of fusion)

Furthermore, the layer height was reduced to 70 µm, which is the optimal layer height reported in a previous study [8]. Additionally, four distinct parameters were selected in the E_0^* region, assumed to be within the upper and lower limits, to establish the boundary conditions of the high densification section for the multi-layer study only. This section ranges from E_0^*=4.4 to E_0^*=16.5 (derived from [9] and [8]). Figure 5.14 displays the cross-sectional images. Based on the images provided, it can be observed that density increases with E_0^* (from Figure 5.14-A to Figure 5.14-D). Additionally, Figure 5.14-A and 81-C exhibit comparable scanning speed values, as all other parameters were held constant. Therefore, a slower process speed leads to higher densification. It can be concluded that only Figure 5.14-D, which was above the E_0^*=16 region, has sufficient energy to produce parts with a density greater

than 95%. However, achieving near-full dense samples by reducing the layer height requires higher energy input. This is because some unmelted powders (Figure 5.14-D) were observed between the layers, resulting in porosity and lack of fusion defects. Therefore, a sample with nearly full density has not yet been obtained.

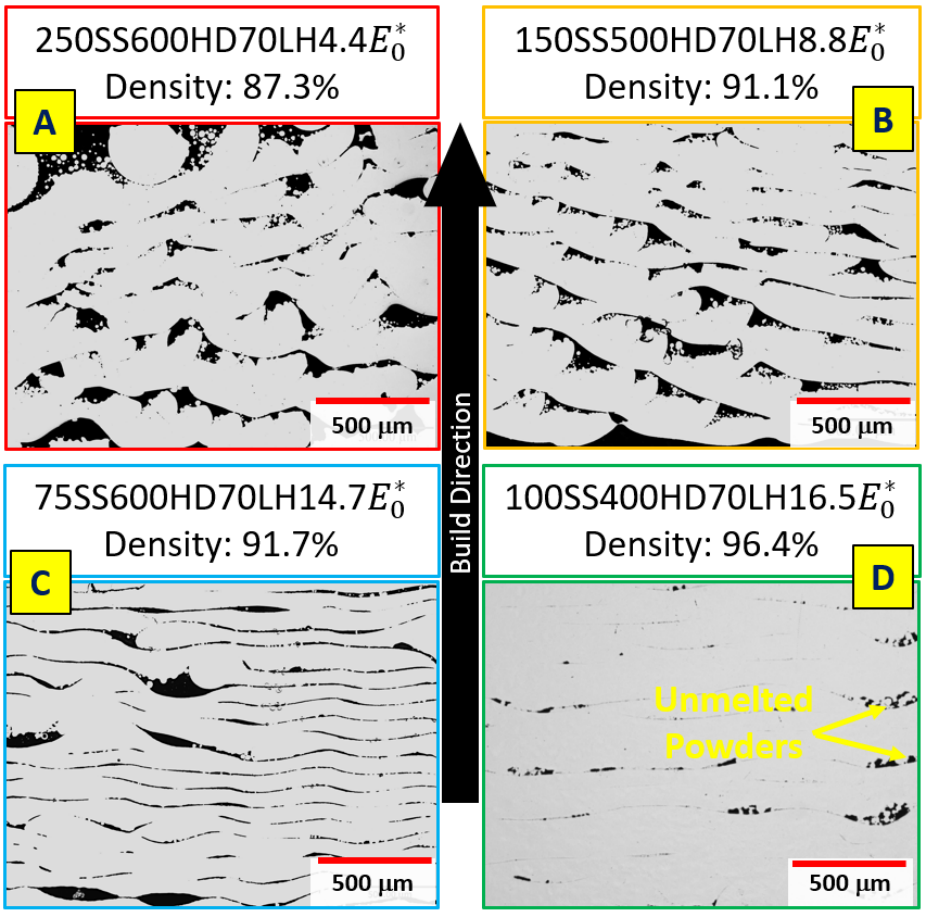

Figure 5.14 - Visual Examination of Densification through Cross-Sectioned Images in the Study of Normalised Energy Density (E_0^*). (Black areas represent porosity)

5.3.4.2 Offset and Rescanning Effect on Densification

In order to improve the density of the samples, it was crucial to reduce the crescent effect. The objective was to attain a uniform layer surface by ensuring a consistent layer height within each layer, which in turn would lead to a uniform NED. According to existing literature, utilising a rescanning strategy with low energy density can result in smoother top surfaces [145,233]. Hence, the sample with the code 100SS400HD70LH16.5E_0^* was selected to carry out the offset and rescanning experiments, as it exhibited the highest density among all other samples. The purpose of the offset scan was to align the crescent peak points on top of each other in order to investigate their influence on the melt pool and density. Conversely,

the rescanning began with the end of a sample followed by a change in direction after the completion of powder melting for the layer, and finally coming to a halt at the starting point. All of these actions were performed at a specific speed without disrupting the layer's processing. Figure 5.15-A illustrates the multi-laser head that was programmed for three offset configurations (0%, 25%, and 50%) based on spot size. This programming aimed to minimise the crescent effects and increase the density. Subsequently, the study proceeded with a 50% offset rescanning strategy.

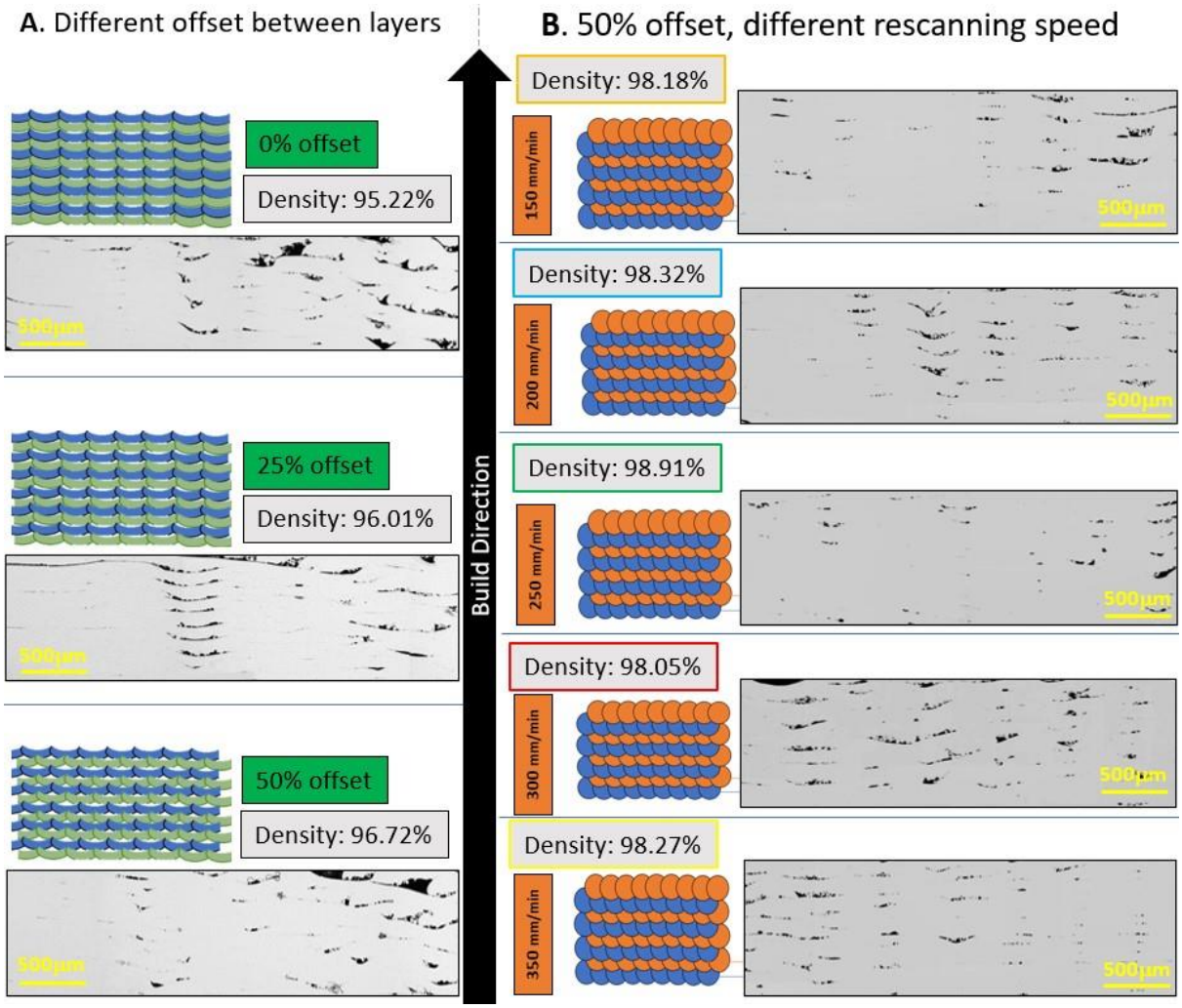

Figure 5.15 - Results of (A) Offset and (B) Offset+Rescanning Parameter Optimization: Illustrated with Optical Microscopy (LOM) Images

In Figure 5.15-B, the experiments ranged from 150 mm/min to 350 mm/min with increments of 50 mm/min. The density increased up to 250 mm/min but then decreased. This decrease was likely due to the fact that the lasers were only able to partially melt the surface up to 250 mm/min before the decreasing energy density, caused by increased speeds,

hindered further melting [147,233]. Among these, the 250 mm/min scanning speed yielded the lowest R_a. It's notable that a 100 mm/min was also tested but the samples slightly warped, often causing the wiper to dislodge them from the substrate in subsequent layers.

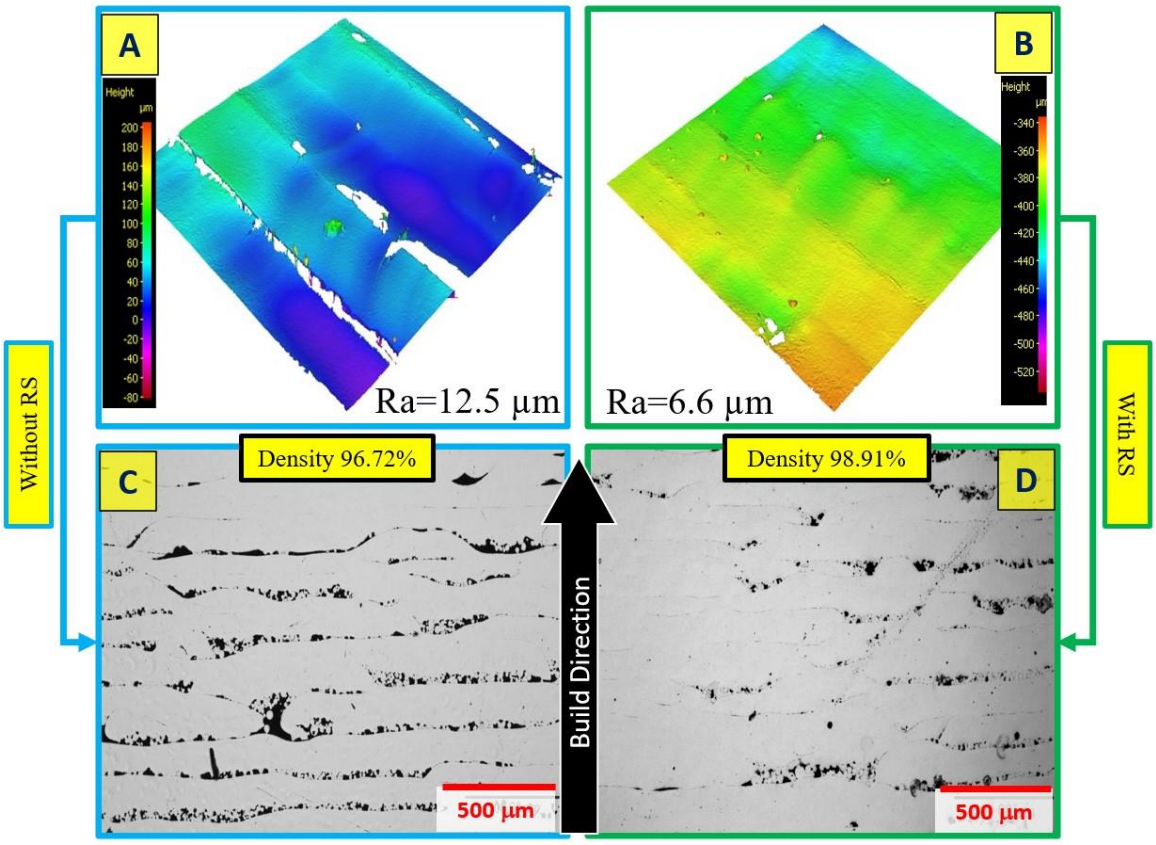

Figure 5.16 - Effect of Rescanning (RS) on Top Surface Roughness (Ra) and Density: (a) and (c) without RS Approach, (b) and (d) employing RS Approach, (a) and (b) denote Ra, (c) and (d) depict LOM Photographs. (Parameters: 100SS400HD70LH for both specimens, with or without RS250SS400HD)

Rescanning reduced surface roughness by almost 50% (Figure 5.16-A-B) and increased sample density by 2% (Figure 5.16-C-D). To achieve more significant densification, a higher E_0^* parameter was required. Therefore, in order to ensure comparability of the results with Figure 5.16, layer height was reduced to 60 µm while keeping the same parameters (100SS400HD60LH, E_0^*=19.3). Additionally, a slightly higher E_0^* parameter (E_0^*>20) was chosen. The scanning speed was reduced to 75 mm/min because it produces smooth and consistent tracks. The hatch distance was set at 500 µm, resulting in an E_0^* of 20.5 for 75SS500HD60LH. All samples were fabricated using rescanning strategy. Figure 5.17 shows that compared to the 70 µm layer height version, the reduction of the layer height to 60 µm resulted in an increase in density, fusion between layers and a reduction in porosity. The

highest density was achieved with E_0^*=20.5 parameters using the rescanning strategy (Figure 5.17-B).

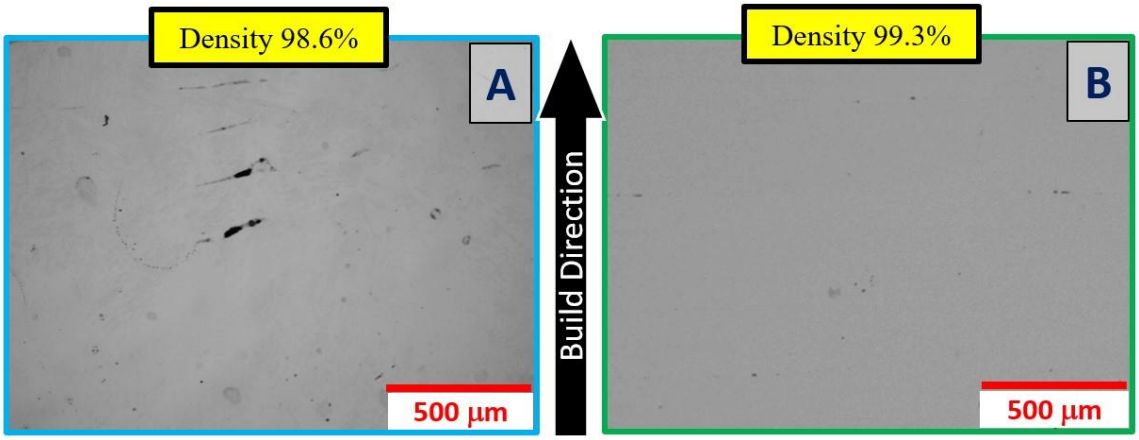

Figure 5.17 – LOM Photographs of 60 µm LH Specimens at Different E_0^* Adjustments: (A) Parameters 100SS400HD60LH19.3E_0^*, (B) 75SS500HD60LH20.5E_0^*. (Black areas indicate porosity)

To analyse the tested parameters visually, a density chart incorporating E_0^* is presented in Figure 5.18-A. Using the data from this chart, a corresponding E_0^* chart was generated, which colour-codes the E_0 regions based on sample density, as illustrated in Figure 5.18-B. These graphs are used to create a parameter map. This map shows the regions where the density exceeds 95%. The analysis outcomes suggest that high-density samples can be achieved in the DAM system by using nine 450 nm 4W diode lasers without preheating, provided that E_0^* >20.5. In contrast, [8] reported that part densities of 98% and above can be achieved by using ten 5W 808 nm diode lasers arranged in arrays, coupled with up to 300°C powder bed heating module [9]. Therefore, 450 nm diode lasers have the potential to be approximately 28% more efficient than their 808 nm counterparts in the DAM system, in terms of power required (50W in 808 nm [8] (higher than 95% density) versus 36W in 450 nm (99.3%)), when disregarding the energy consumed for the rescanning. Efficiency calculations require further scrutiny, particularly considering the different operational configurations. The 808 nm system operates in arrays, each comprising two arrays with five lasers. It is necessary to increase the number of lasers or to replace the power of a single laser with something greater than 4 W or to reduce the layer height to less than 60 µm in order to explore the region of excess energy on the parameter maps such as keyhole. As a result of these limitations, in comparison with [8], there is no excess energy region on the E_0^* parameter map.

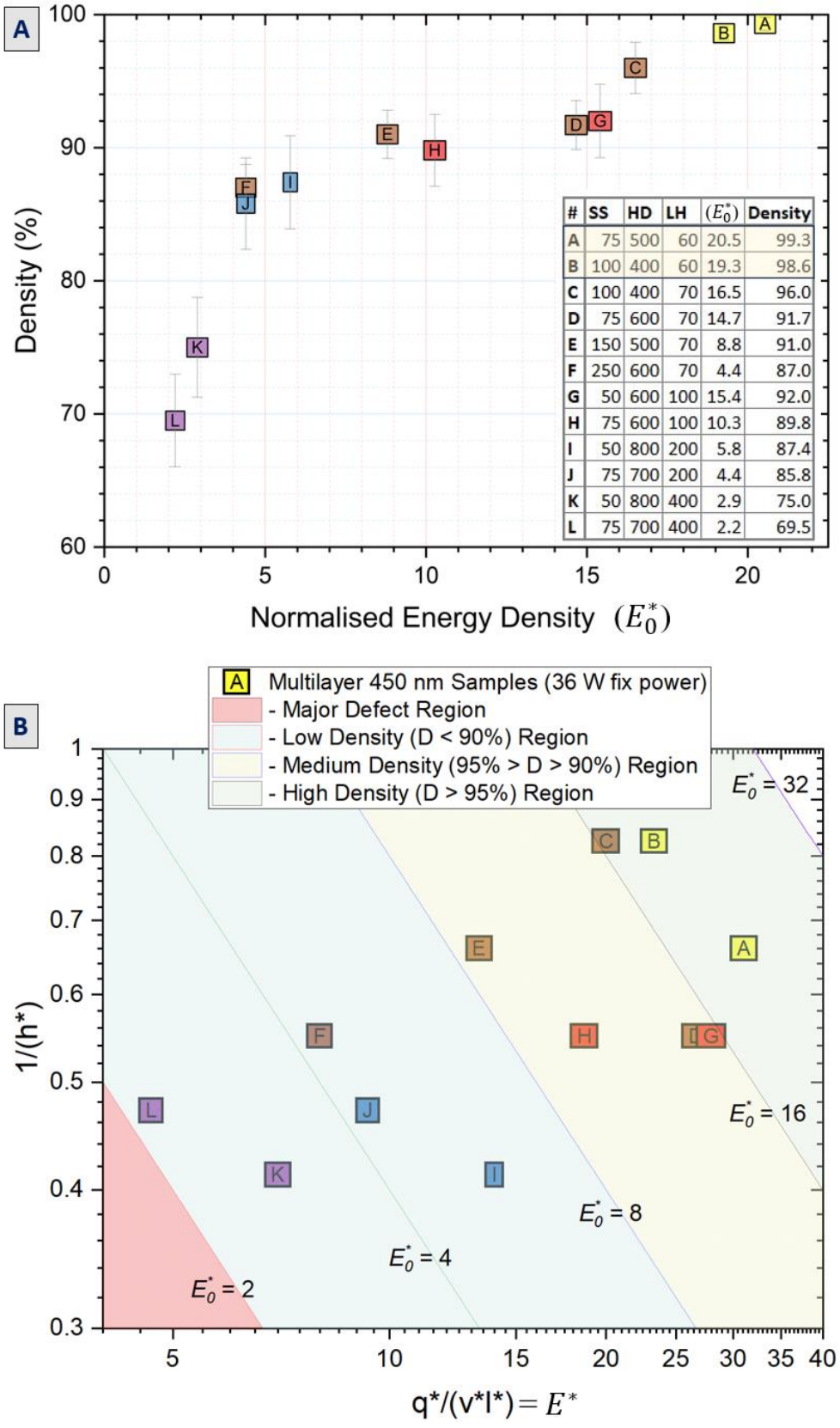

#	SS	HD	LH	(E_0^*)	Density
A	75	500	60	20.5	99.3
B	100	400	60	19.3	98.6
C	100	400	70	16.5	96.0
D	75	600	70	14.7	91.7
E	150	500	70	8.8	91.0
F	250	600	70	4.4	87.0
G	50	600	100	15.4	92.0
H	75	600	100	10.3	89.8
I	50	800	200	5.8	87.4
J	75	700	200	4.4	85.8
K	50	800	400	2.9	75.0
L	75	700	400	2.2	69.5

Figure 5.18 - (A) Summary of Densification Research, (B) Updated NED (E_0^*) Colour Chart Showcasing Research Outcomes (Table in A Outlines Parameters, E_0^*, and Sample Densities; Highlighted Rescanned Samples in Yellow)

5.3.5 Phase Determination

The purpose of XRD was the verification of the presence of α'/α and β phase structures, specifically [238] α and α' (HCP), and β phase (BCC) structures. Variable peak locations are observed during XRD analyses due to this reason [239]. To investigate the influence of different cooling rates on the phase formation based on E_0^*, XRD patterns (Figure 5.19) were obtained from 70 µm layer height (C, D, E, F) and the highest dense part (A with 60 µm layer height). For Ti6Al4V, if the cooling rate exceeds the critical martensitic transformation value (410°C/s), a complete transformation into the martensite phase (α/α') occurs, originating from the primary β grains (T_α = 595°C, T_β = 995°C) [210]. ICDD PDF4+ (Powder Diffraction File) maps 04-020-7055 [227] for α and 00-044-1294 [228] for β (as undetectable at room temperature [210]) were used for phase identification.

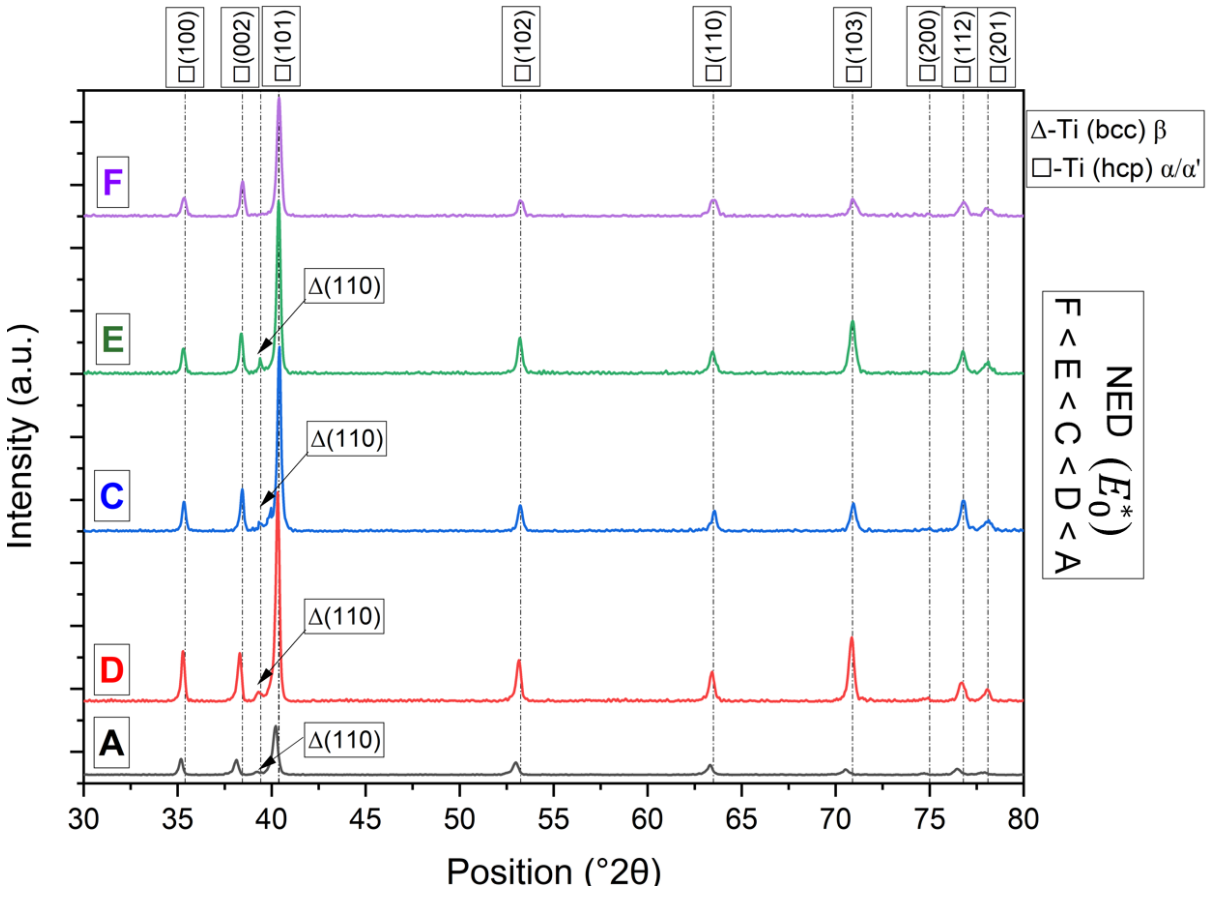

Figure 5.19- XRD Data Interpretation Aligned with Their Normalised Energy Density (NED) Values for sample F- 250SS600HD70LH, sample E- 150SS500HD70LH, sample C- 100SS400HD70LH, sample D- 75SS600HD70LH, sample A- 75SS500HD60LH Parameters

Figure 5.19 shows that the sample with the lowest E_0^* (F (E_0^*=4.4)) did not exhibit any β peaks due to its rapid cooling rate compared to other samples. This result is consistent with traditional LPBF results [167]. It can be concluded that for 450 nm DAM parts, only *α′/α* peaks are observed when E_0^* is lower than 8, while β peaks are observed when E_0^* is higher than 8. This finding is supported by [8], who reported the observation of β peaks with 600℃/s. Furthermore, sample A exhibited a shift in the graph that affected all peaks, indicating that the height of the sample was the issue during the XRD procedure. It should be noted that a small shift within a single peak may occur due to microstrain, temperature changes, compositional variations, or lattice imperfections, which can contribute to peak shifts in XRD patterns [239]. Figure 5.19 shows that as E_0^* increases (or cooling rates decreases from Sample F to Sample A), the peaks become less intense. This reduction in peak intensity may be due to microstrains from dislocations, which prevent the atoms of the alloy from dissolving sufficiently [145]. This leads to increased residual stress, resulting in peak broadening instead of sharpening, which is indicative of smaller crystal grains [239]. However, a more comprehensive study and analysis is required to fully comprehend residual stress, either through conventional measurement techniques or high-temperature methods, to determine the exact cause of the decrease in peak intensity following a specific cooling rate.

5.3.6 Microstructure Analyses

Sample A, which had a density of 99.3% and was rescanned at each layer (75SS500HD60LH), was used to examine the microstructure of 450 nm Ti6Al4V material. Other samples were excluded due to severe porosity and lack of fusion defects. Figure 5.19 showed the existence of *α* and β phases in Sample A. To contrast *α* and β, SEM image analyses were undertaken using BSE mode. The β phase in Ti6Al4V is stabilized by heavy elements such as Vanadium (V) and Iron (Fe), which appear as brighter lines and points under the BSE mode in SEM [240].

As shown in Figure 5.20-A1, A2, and A3, the microstructure along the vertical direction of the structure showed significant variation between sections. Rescanning may also affect the structure and grain length distribution due to additional heat energy applied to the material just after solidification, assuming it increases the solidification time. Section A3 showed coarser lamellar structures of the *α*+β and *α*′ type, resulting from slower cooling rates

which resulted in minimal temperature differences between adjacent layers. This suggests, particularly in the lower part of the specimen, a partially annealed state with fewer acicular α' structures. The occurrence of α+β can be attributed to the increase in temperature of the lower layer during the processing of the subsequent layers and the consequent decrease in cooling rate. On the other hand, section A1 showed finer grain sizes and more martensite α' sub-grains as they approached the build direction. Therefore, as one approaches the top surface, cooling rate increases, producing fewer needle-shaped α' structures [21]. Furthermore, the entire sample exhibited a basket-weave microstructure, which was especially noticeable in section A1. The processing conditions should be almost identical to ensure a valid comparison of microstructures between traditionally produced single laser LPBF Ti6Al4V and those produced by DAM.

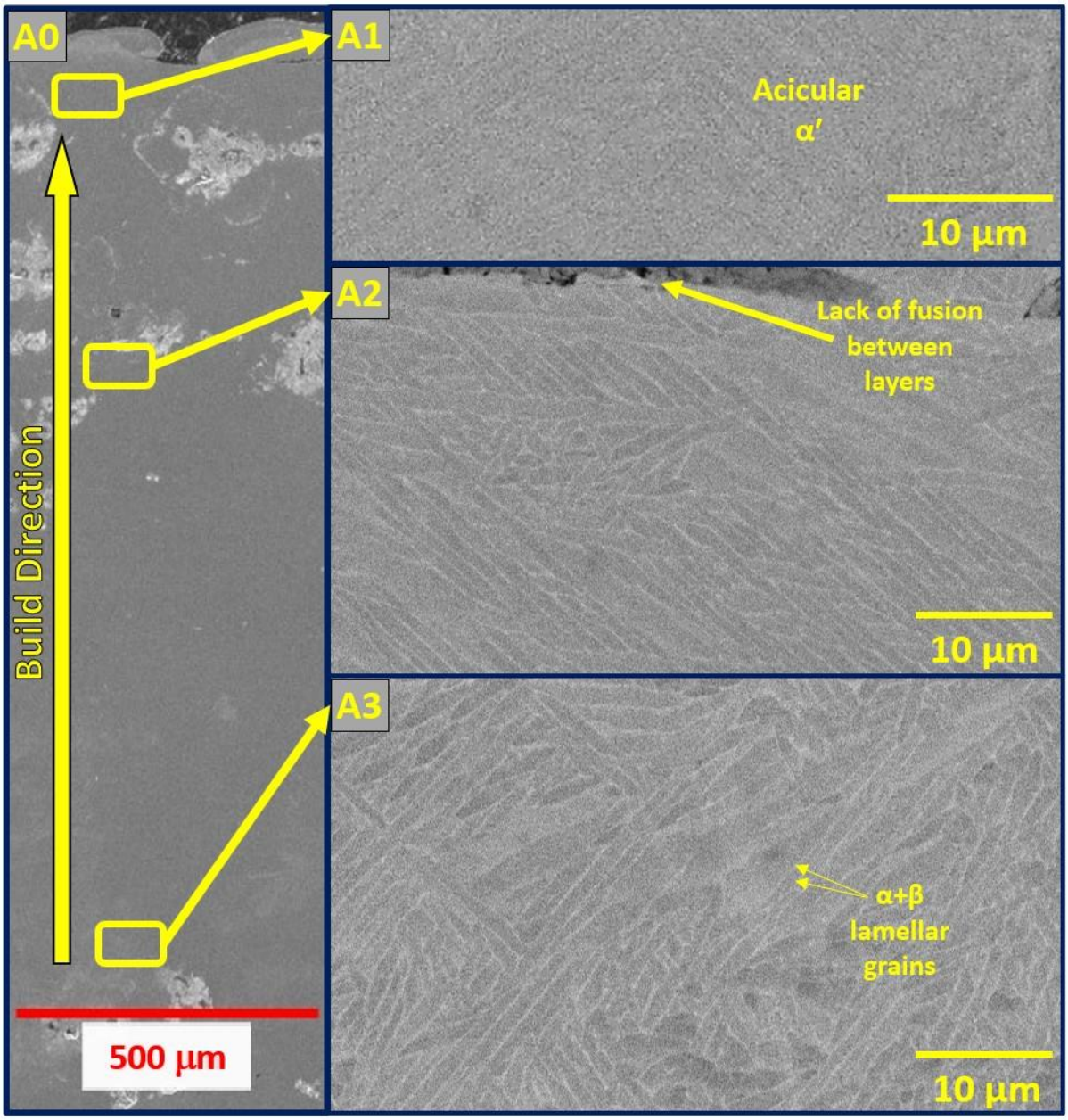

Figure 5.20 - SEM-BSE Microstructural Examination of Sample A: (A0) Overview at Lower Magnification, (A1) Detail of Top Surface, (A2) Central Section, (A3) Lower-Middle Section (No Etching Procedure Applied)

5.3.7 Hardness Tests

5.3.7.1 Vickers Micro-Hardness Tests

Figure 5.21 shows a significant drop in Vickers hardness values after implementing the rescanning strategy, which aims to increase density by reducing porosity. The hardness values decreased to below the 350-400 HV range. Before rescanning, the material had much higher hardness, typically in the 550-650 HV range (samples with condition E_0^*<17). An increase in

E_0^* generally corresponds to a slight decrease in hardness. Two different scenarios can be used to understand this situation.

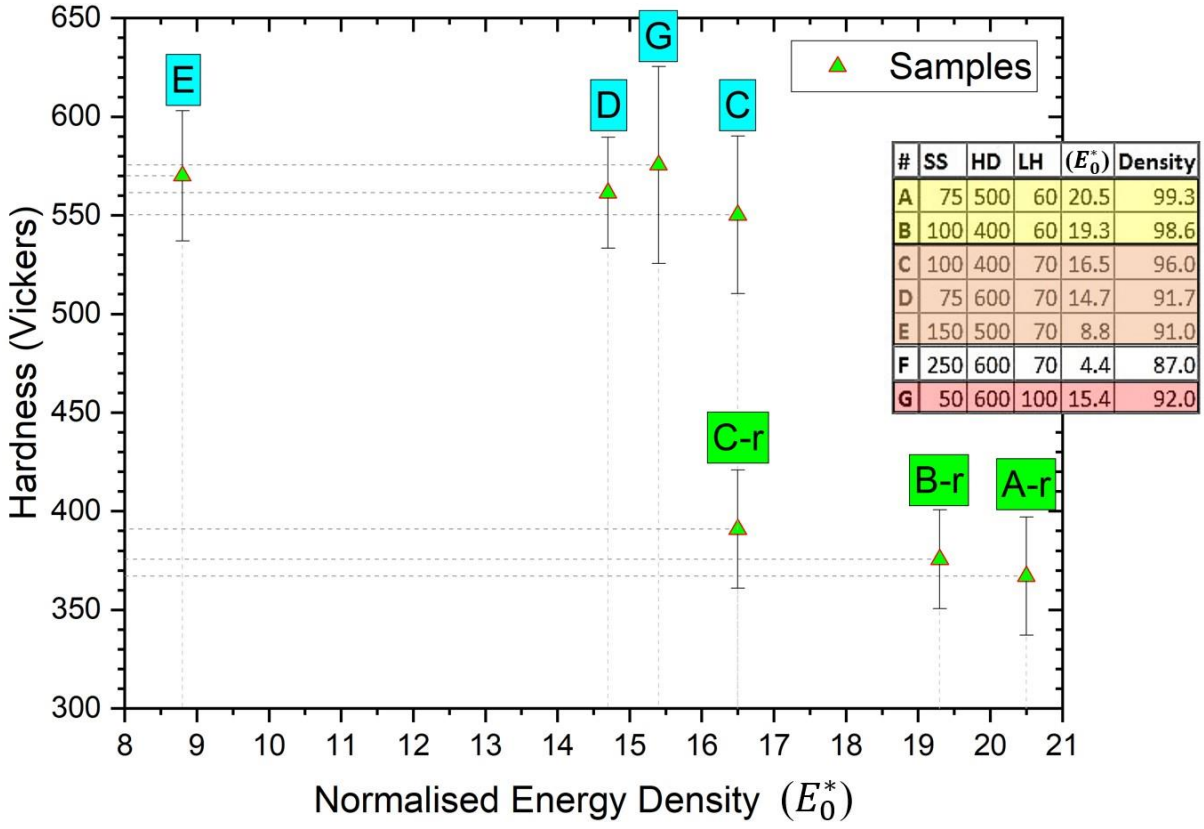

#	SS	HD	LH	(E_0^*)	Density
A	75	500	60	20.5	99.3
B	100	400	60	19.3	98.6
C	100	400	70	16.5	96.0
D	75	600	70	14.7	91.7
E	150	500	70	8.8	91.0
F	250	600	70	4.4	87.0
G	50	600	100	15.4	92.0

Figure 5.21 - Vickers Hardness Compared to Normalised Energy Density (E_0^*) in High-Density Specimens: Concentration on Specimens Above 90% Density, Incorporating Rescanned Specimens C-r, B-r, and A-r

These variations in hardness data may be used as evidence for a coarser microstructure which appears as hardness decreases in accordance with the Hall-Petch relationship [241]. In addition, the XRD section discusses the martensitic transformation caused by cooling rate. The α' phase of acicular shape martensite exhibits harder characteristics, especially on Ti6Al4V, compared to its β phase [209]. The α phase stabilizing alloying elements were assumed to be primarily present in α sub-grains. This results in an element-deficient α' phase in lamellar sections, which causes significant differences in hardness (fluctuations) and strength between the α+β lamellae [242]. Furthermore, metal oxidation can alter hardness, as O_2 affects α phase stabilizers [151]. Metals have a natural tendency to oxidise, which may explain unexpected increases in hardness values during fabrication. This is particularly relevant given that all processes were conducted with an argon re-circulation system. Large fluctuations in hardness values may also be caused by small

porosities located beneath or near the indent location, which absorb pressure. Therefore, a small indent area could lead to high hardness.

5.3.7.2 Nano Indentation

Figure 5.22 presents the results of nano-indentation for samples A, B, and C, exclusively focusing on their rescanned versions. The hardness values obtained from these results demonstrate a similar trend to those observed in the micro-hardness test (Figure 5.21) although with a slight variation. Notably, the nano-indentation results indicate significantly higher hardness values, ranging from 4.7 to 5.0 GPa, in comparison to the range of 3.6 to 4.0 GPa observed in the micro-hardness tests. Sample B exhibits a wide range of Young's modulus results, which can likely be attributed to the indenter contacting less dense regions, resulting in material elongation and influencing the overall graph. The discrepancy in hardness values between the alpha and beta structures is also evident, with the alpha phase typically displaying higher hardness [8,240]. Given the nine measurements encompassed in a matrix, the results may vary depending on whether the indenter interacts with the harder alpha phase or the softer beta phase.

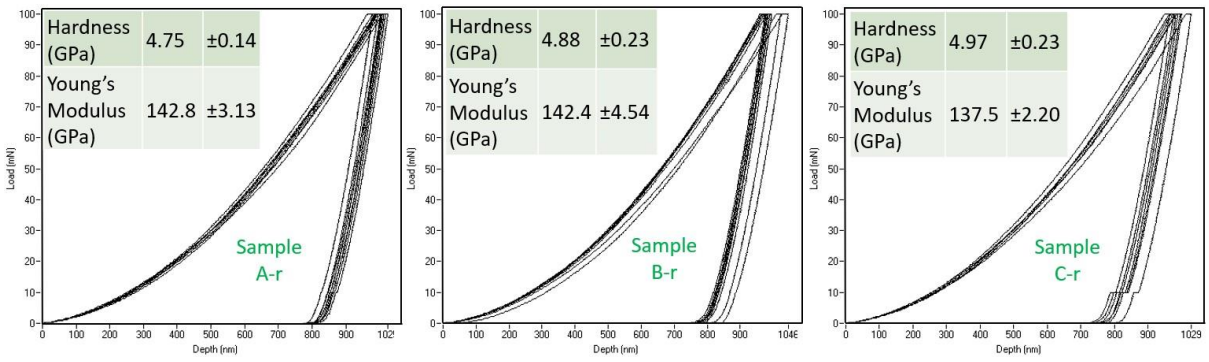

Figure 5.22 - Nano-indentation results of rescanned samples only, A, B and C respectively.

5.4 Chapter Conclusion

In this chapter, the effect of the 450 nm DAM system with a single array on Ti6Al4V powder bed was examined. the initial phase involved calibrating lasers to various power levels, with 4W chosen as the maximum effective power for melting Ti6Al4V powder over 2.8W. The study explored the impact of speed and track overlap on surface defects, material integrity, and wetting capabilities, finding that scanning speeds below 100 mm/min enhanced sample integrity. The research progressed to multi-layer studies, revealing that higher energy densities, primarily influenced by scanning speed, reduced void formation. However,

inconsistencies in hatch distance movement among individual tracks necessitated further investigation. The study also examined the critical role of cooling rates, the 'crescent effect' in melt pools, and the effect of rescanning strategies on sample density and surface roughness, ultimately finding that higher energy input was necessary to achieve near-full density in the samples. Key findings are:

- Delayed coolant activation and problematic feedback loops at maximum power led to void formation. Maximum power of 4W was effective for melting Ti6Al4V powder, with optimal scanning speeds below 100 mm/min for higher sample integrity.
- Higher energy densities reduced void formation, but inconsistencies in hatch distance movement complicated the results.
- Slow scanning speeds and thin layer heights influenced cooling rates, affecting adjacent powders similarly to hatch distance.
- Increased laser count led to wider (~1100 µm) and deeper melt pools. This phenomenon named as ‘Crescent Effect’ in the thesis which identified as in lower hatch distances due to perpendicular laser orientation, influenced by Marangoni flow, heat transfer, and recoil pressure.
- Rescanning strategies reduced surface roughness by 50% and increased sample density by 2%.
- Microstructural analysis varied significantly along the vertical build direction; slower cooling rates resulted in coarser structures at the bottom, finer martensitic structures at the top.
- Rescanning decreased Vickers hardness values, moreover, nanoindentation showed higher hardness due to microstructural changes.
- 4W system could not achieve part densities of 99.3% and above, likely due to insufficient powder bed heating and potential oxygen ingress.

6. Hybrid Laser Powder Bed Fusion (HLPBF) Processing

6.1 Introduction

This study introduces a novel HLPBF system that combines two distinct laser processing methods. Each laser in this system induces markedly different melt pool solidification rates within the same layer, allowing for enhanced control over microstructural outcomes compared to conventional LPBF systems employing a single laser type. The dual laser setup comprises a traversing DAM laser head, housing an array of nine 4W 450 nm diode lasers alongside a conventional 1064 nm LPBF 200W single fibre-laser and galvo-scanning head. Ti6Al4V feedstock underwent processing utilizing both laser types within a single sample for the first time. A specific scanning strategy delineated separate laser processing regions within the same sample, including an overlap where both lasers interacted to fuse the feedstock and bridge the two regions. The FLM regions experienced significantly higher cooling rates (~10^7 °C/s) compared to DAM regions (~600 °C/s), resulting in finer microstructures characterized by acicular α'/α phases. In contrast, DAM regions exhibited larger α+β grains with parent β grain sizes approximately 13 times larger than those in the FLM zone. Beyond its in-situ spatial microstructural tailoring capability, this investigation also sheds light on variations in the laser-induced heat-affected zone, surface roughness, and mechanical properties across DAM, FLM, and overlap regions within fabricated Ti6Al4V samples.

6.2 Methodology for Hybrid Laser Studies

FLM parameters were chosen from chapter 4 and DAM parameters selected were based on guidelines from chapter 5. These parameter sets showed the highest density for FLM and DAM parts. Parameters summarised in Table 6-1.

Table 6-1 – Hybrid Laser Parameter Dataset: Correlation of Normalised Energy Density with Cross-Sectional Densities.

Processing Technology	NED	Power (W)	Scanning Speed (mm/s)	Hatch Distance (µm)	Layer Height (µm)	Density (%)
FLM	2.56	140	900	40	60	99.88
DAM	20.5	36	1.25	500	60	99.30

6.3 Results and Discussion

6.3.1 Proof of Concept of the Hybrid Laser Studies via Multi-Layer Fabrication

6.3.1.1 Hybrid Laser Overlap Studies

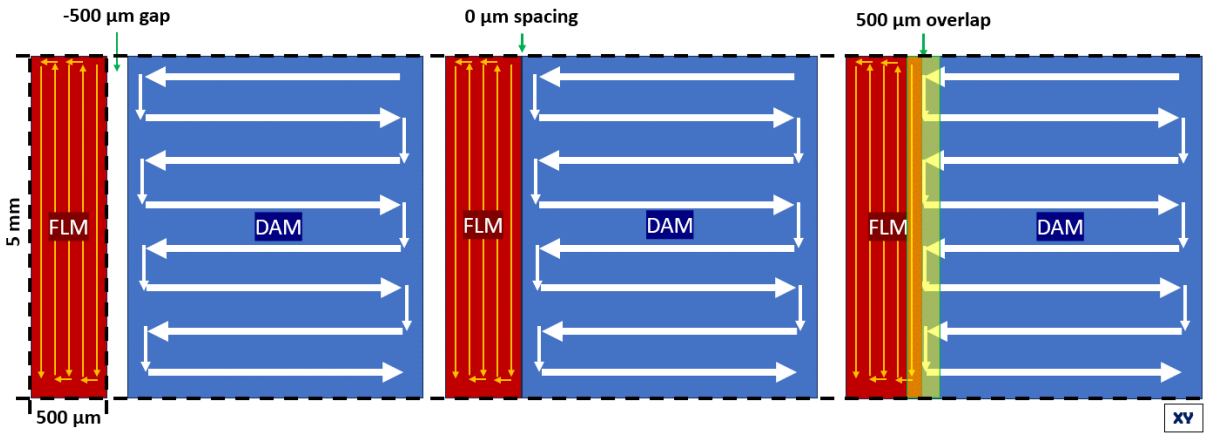

Figure 6.1 – Graphic Representation of Scanning Order in Hybrid Laser Overlap Experiments

In order to understand the intersection area of the lasers in terms of the percentage of sample overlap, several studies were carried out. Figure 6.1 showed the scanning strategy used for hybrid sample overlap studies. For FLM sample, the scanning area width was set to 500 µm, with a length of 5 mm. The scanning tracks followed the longer side of the shape (which was parallel to the 5 mm edge – see Figure 6.1) for each layer. This decision was made to avoid warping caused by tracks parallel to the 500 µm edge, which often resulted in delamination from the substrate or cracking at the connection points of the DAM part. These issues were caused by the higher temperature of the shorter tracks. Hence, a significant temperature gradient arises between the processed tracks and the unprocessed edge, resulting in distortion within the same layer [3,77]. DAM sample was processed first, then FLM sample produced afterwards. The reason for this is that FLM has higher power than that

of a DAM system, therefore, it was assumed that FLM has ability to remelt the solidified section of the layer [145,147,233].

To speed up the evaluation process, the layer height was doubled (120 µm) only for the overlap study to decrease the production time, since the primary aim was to determine the optimal spacing only. The FLM zone was moved in three stages, increasing 500 µm each time, to transition from a 500 µm gap to a 500 µm overlap with a completed DAM component (see Figure 6.1 and Figure 6.2). Figure 6.2 demonstrates that the overlap sample percentage experiment results. Figure 6.2-A-B-C showing the top surface spectrometry results to judge the loose powder and surface roughness of the samples. Figure 6.2-A1-B1-C1 shows the cross-sectional images of the hybrid overlap samples to understand the where the melt pool connection happens.

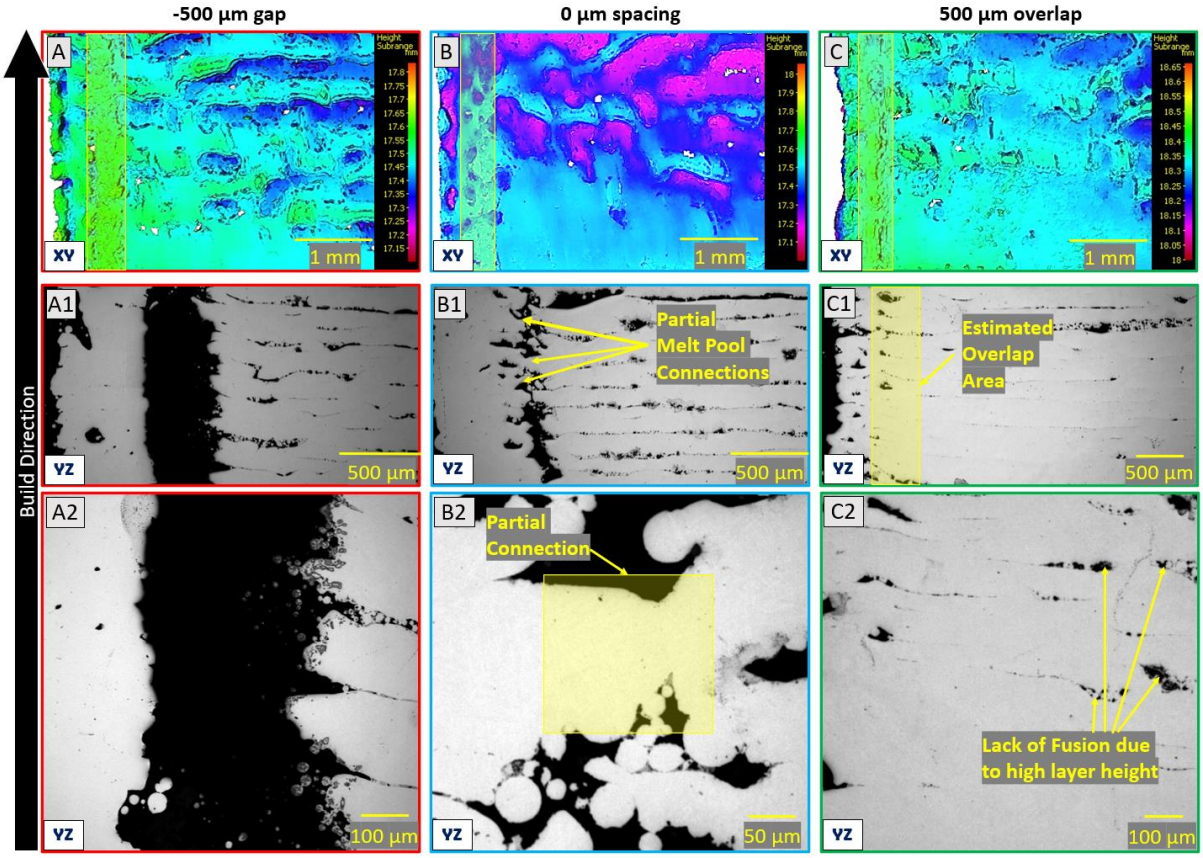

Figure 6.2 - HLPBF Overlap Experiments: Top Surface Roughness Measurements and Cross-Sectional LOM Images for 500 µm Gap, 0 µm Spacing, and 500 µm Overlap – showing on XY and XZ Plane

Results showed that 500 µm gap did not showed any sign of connections (Figure 6.2-A1-A2) but 0 µm spacing started to show partial melt pool connections between already

processed DAM sample and FLM sample (Figure 6.2-B1-B2). 500 µm overlapped sample is the most favourable setting to conduct further research (Figure 6.2-C1-C2). Moreover, 500 µm overlapped samples showed no loose powders detected on the top surface compared to other samples (Figure 6.2-A-B-C).

Figure 6.3 showed the 500 µm overlapped sample's top surface image via SEM. It can be clearly seen that the top surface of FLM processed section revealed much smoother surface finish compared to DAM processed section. Moreover, the connection between the FLM and DAM samples observed fully connected which can be examined in detail in Figure 6.2-C1-C2.

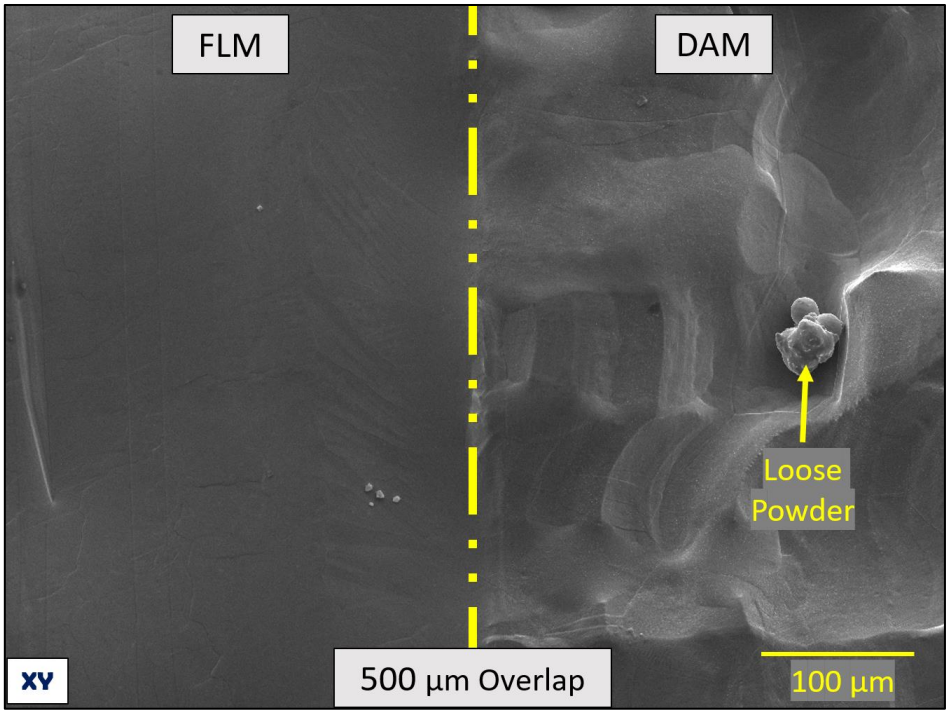

Figure 6.3 - Top surface Examination through SEM imaging of 500 µm overlapped sample with FLM and DAM sections

Further refinements may be necessary to achieve precise 0 µm spacing adjustments with improved system electronics. In-situ investigations, such as X-ray imaging, can be crucial to gain a thorough understanding of the connection between FLM and DAM components within the cross-sectional perspective.

6.3.1.2 Defining the Hybrid Laser Scanning Order

Due to the inherent processing capabilities of HLPBF system, the correct sequence of scanning strategies is critical. This sequence can be either FLM processing first, then DAM

processing (FLM+DAM), or DAM processing first, then FLM processing (DAM+FLM), as the DAM retracts to clear the area for the FLM process. To comprehend the influence of the laser activation order, a solitary specimen was utilized, and various orders were executed with a 500 µm overlap while creating 60 µm layer height in the hybrid same example to actually see the effect of the optimum parameters for both processing technologies (refer to Figure 6.4-A)). This technique allowed the observation of the effects on one sample. It is evident from Figure 6.4-(B) that the DAM+FLM strategy produces less porosity with a 98.52% intersection density, indicating a denser outcome compared to the FLM+DAM strategy with a 96.09% intersection density. On the other hand, the DAM+FLM approach corresponds with prevalent contour scanning techniques implemented in industrial LPBF systems. This variation is due to the significant spot size of the DAM system which measures around 650 µm in length, compared to the 100 µm of the FLM. As the DAM melts, many powders are assimilated by the >1000 µm wide melt pool as discussed in *6.4.1.Single Track Studies*. As a result, void sections arise after the HAZ portions around the edges of the geometry. However, it is assumed that void sections arise around the melt pool due to high recoil pressure when the FLM process commences [202]. Consequently, in the DAM+FLM sequence, FLM commences in the HAZ region of the DAM, resulting in less porosity.

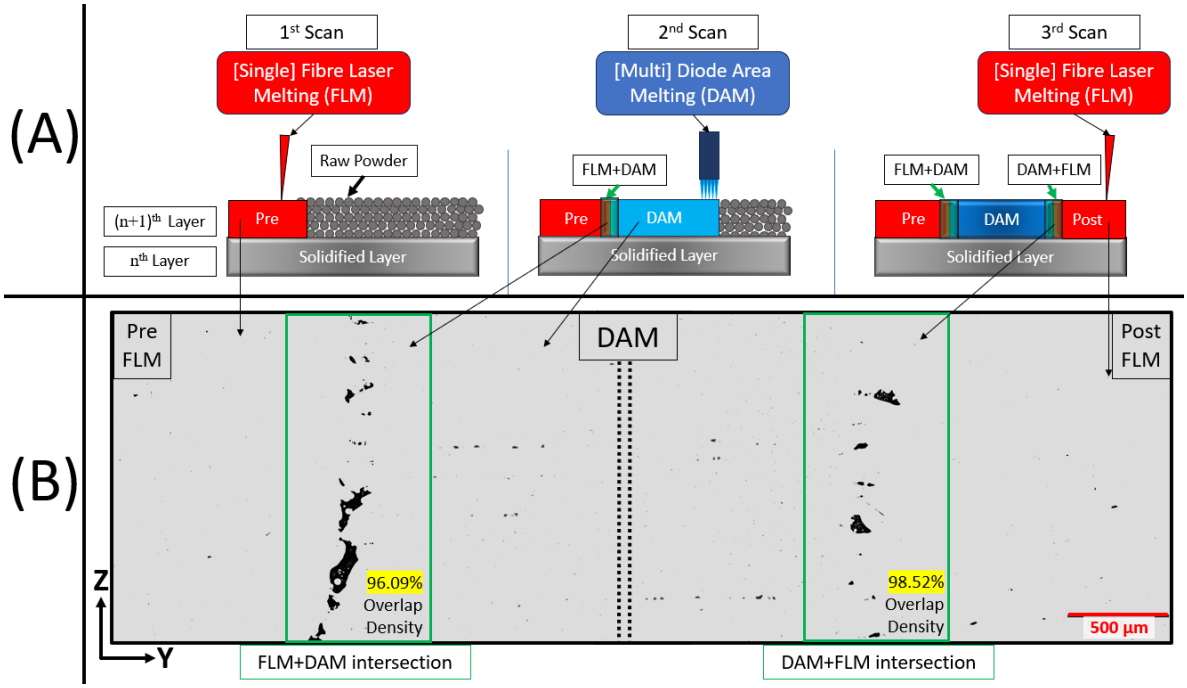

Figure 6.4 - Scanning Order Experiments: (A) Diagrammatic Representation of Experiment Setup, (B) Optical Microscopy Images Adjusted for Density Analysis with Intersection Densities (Black Points Represents Porosity).

It is noteworthy that almost all of the FLM+DAM sections showed cracking, occurring either during the melting phase or after melting was concluded. This phenomenon can be attributed to residual stresses caused by rapid solidification or, more simply put, the high cooling rate associated with FLM. Moreover, FLM exposes more part sections to high temperatures during the process, as compared to DAM which operates at a slower velocity. This process effectively imitates stress-relieving. DAM operates at a significantly higher speed per minute compared to the stress-relieving procedure per hour. As a result, when these sections are connected to the DAM component, it is presumed that the gradual expansions and contractions apply forces that cause delamination or cracking. Furthermore, the heat transfer occurring between the FLM+DAM and DAM+FLM methods will affect the microstructure of the junctions. While this issue can be alleviated through methods such as powder-bed heating or optical pre-heating, it is evident that further energy input is necessary to effectively tackle this challenge.

6.3.1.3 Side Surface Roughness of FLM and DAM samples

During the SSR analyses, the starting and ending points of FLM were measured for both to facilitate comparison with the DAM samples start and end as DAM's starting procedure was different than FLM in this study (Figure 3.16-B). In Figure 6.5, the DAM and post-FLM samples' start, and end side surface roughness data were shown. It can be said that the SSR in DAM samples has the potential to expand up to 100 times more than in FLM samples in different locations. Overall, it can be said that with an increase in SS, average SSR drops significantly especially comparing the DAM and FLM samples.

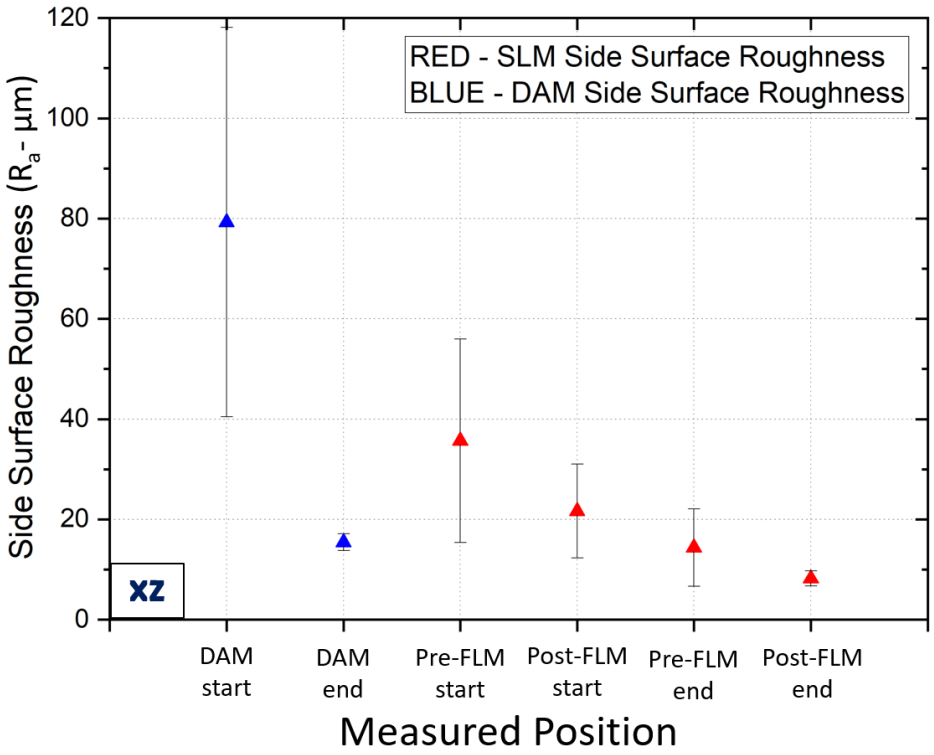

Figure 6.5 – Comparative Analysis of Heat-Affected Zone (HAZ) in DAM and FLM Samples with Side Surface Roughness (SSR-R_a) Values

Evaluating SSR in DAM parts poses difficulties as they are predominantly composed of sintered powders. Therefore, Figure 6.6 was shown to understand the HAZ and SSR analyses differences with different locations. It has been found in *Multi-laser PBF* with Ti6Al4V via Use of 450 nm Diode Area Melting System that increasing the speed in DAM systems resulted in a decrease in HAZ under the same power settings. This is demonstrated through comparing the start and end sides of the sample for DAM and for FLM (Figure 6.6-B1-D1) (with the end section being the starting point of rescanning with a 250 mm/min SS), and a comparable pattern was observed in samples fabricated through FLM as well with the different contour settings in literature [226,243,244]. The features of the FLM system establish it as a potentially effective method to address the elevated SSR issue encountered in DAM samples when both systems combined for hybrid sample processing. Consequently, the control of SSR can be done.

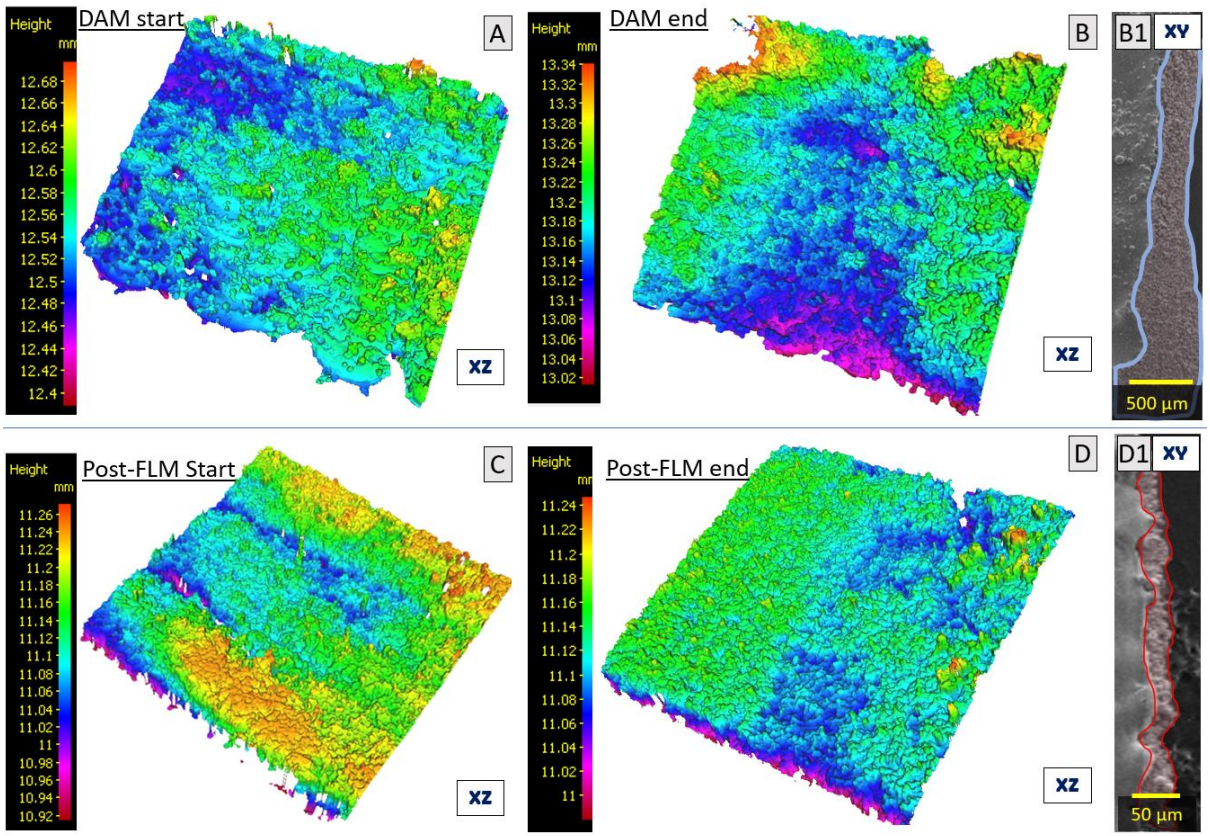

Figure 6.6 - Side Surface Roughness (SSR) Images: (A, B, B1) from DAM and (C, D, D1) Showing Post-FLM Start and End Positions

6.3.2 Characterization of HLPBF Samples

6.3.2.1 LOM, SEM/BSE and XRD Analyses

The structure of Ti6Al4V *α+*β appeared with slow cooling rate generally due to low in-situ thermal gradient [95]. Moreover, the LOM (Figure 6.7-A-B-C) and BSE (Figure 6.7-D-E-F) images show that DAM has high probability of a slower cooling rate in comparison to FLM. This is not only because of the existence of *α+*β structures but also because of non-determinability of the parent β grain boundaries in DAM (Figure 6.7-A). However, the parent β grain boundaries can be determined in FLM microstructure image (Figure 6.7-C). Moreover, it can be observed that the sub-grain size of DAM sample (Figure 6.7-D) is comparatively much larger than FLM sample (Figure 6.7-C-F). This cooling rate difference allows for the growth of larger sub-grains in DAM, which leads to the formation of *α+β* grains (Figure 6.7-A-D), contrasting with the acicular *α'/α* (basket-weave) structures observed in FLM (Figure 6.7-C-F) [46,240]. However, there is not clear indication for microstructure comments in the overlap region in Figure 6.7-B-E. This is one of the indications of why the EBSD analyses are necessary to understand what happens in the overlap region. From the Figure 6.7 it can be said that the

thermal footprint of the DAM, particularly in the build direction, exhibits distinctive characteristics compared to FLM. DAM, utilising multiple diode lasers with shorter wavelengths tends to create larger melt pools due to rapid heat conduction and a significant temperature gradient when the powder bed is not preheated. This results in broader and deeper melt pools at lower scanning speeds (20-100 mm/min), with substantial heat concentration at the focal point. As scanning speed increases, the thermal footprint changes, with melt pool dimensions decreasing and becoming discontinuous beyond 500 mm/min due to high sintering rates. In contrast, FLM typically produces finer and more focused thermal footprints, with the single fibre laser delivering a consistent and controlled heat input. This results in less variability in melt pool size and shape compared to DAM. Additionally, FLM's higher cooling rates lead to more rapid solidification, influencing the microstructural properties differently than DAM.

Overall, while DAM provides the potential for larger and deeper melt pools, it also introduces challenges related to controlling the thermal footprint, especially at higher scanning speeds. FLM offers a more stable and controlled thermal profile, which is crucial for achieving consistent microstructural properties and minimizing defects such as cracks and porosity.

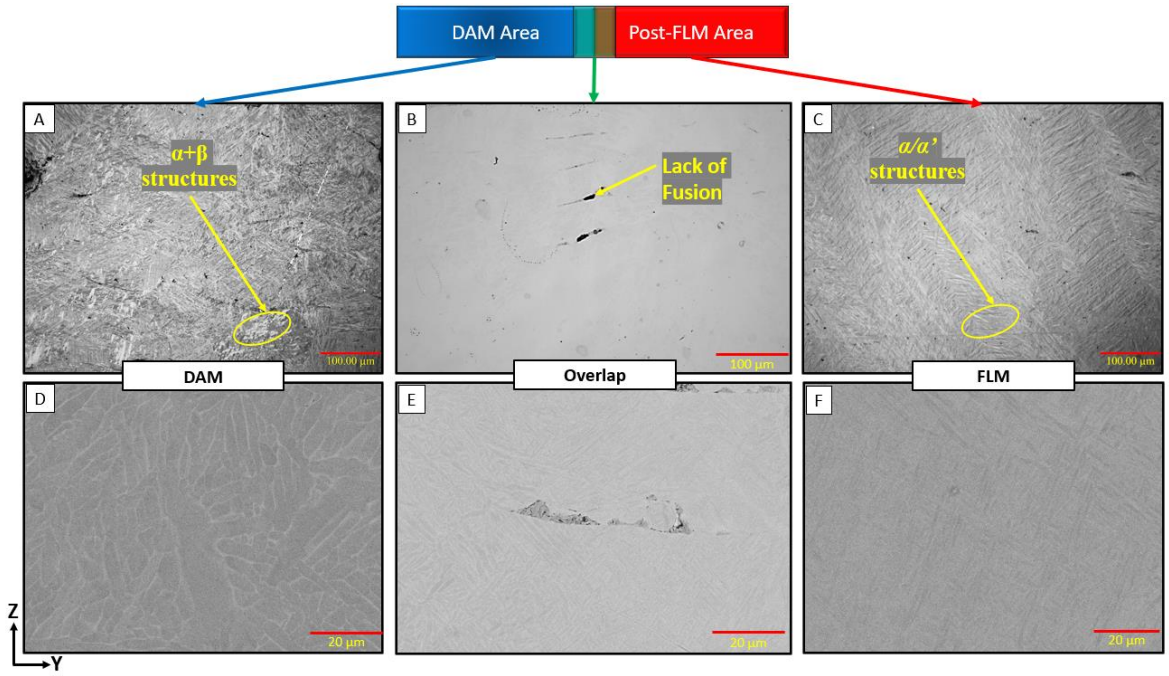

Figure 6.7 - Microstructure examination through microscopy images at YZ plane cross-section: LOM images of (A) DAM section, (B) overlap section, (C) FLM section, and SEM/BSE images of (D)DAM section, (E) overlap section, (F) FLM section

The International Centre for Diffraction Data (ICDD) Powder Diffraction File (PDF) cards were used again to match the structure of the material with the database. PDF 04-020-7055[227] card for *β* phase (as this phase cannot be clearly detected at room temperature [36]), and 00-044-1294[228] card for *α* for phase) were used to of the graph in Figure 6.8. It is evident that DAM generated higher *α* peaks than FLM in their as-built conditions. This correlation can be credited to the larger grain size in DAM, which enables it to reflect more incident beams in a consistent direction toward the collector [240,245]. Additionally, it has been associated that FLM primarily produces *α'* structures, characterized by acicular-shaped sub-grains, which may lead to incident beams being less likely to align in the same direction [239]. This phenomenon can be attributed to the slower cooling rate of the DAM process. Furthermore, in the FLM process, a noticeable decrease in peak intensity is observed. This reduction could be attributed to microstrains caused by dislocations inhibiting sufficient dissolution of the alloy atoms [145,151]. This XRD analysis data was used to set up the EBSD analysis.

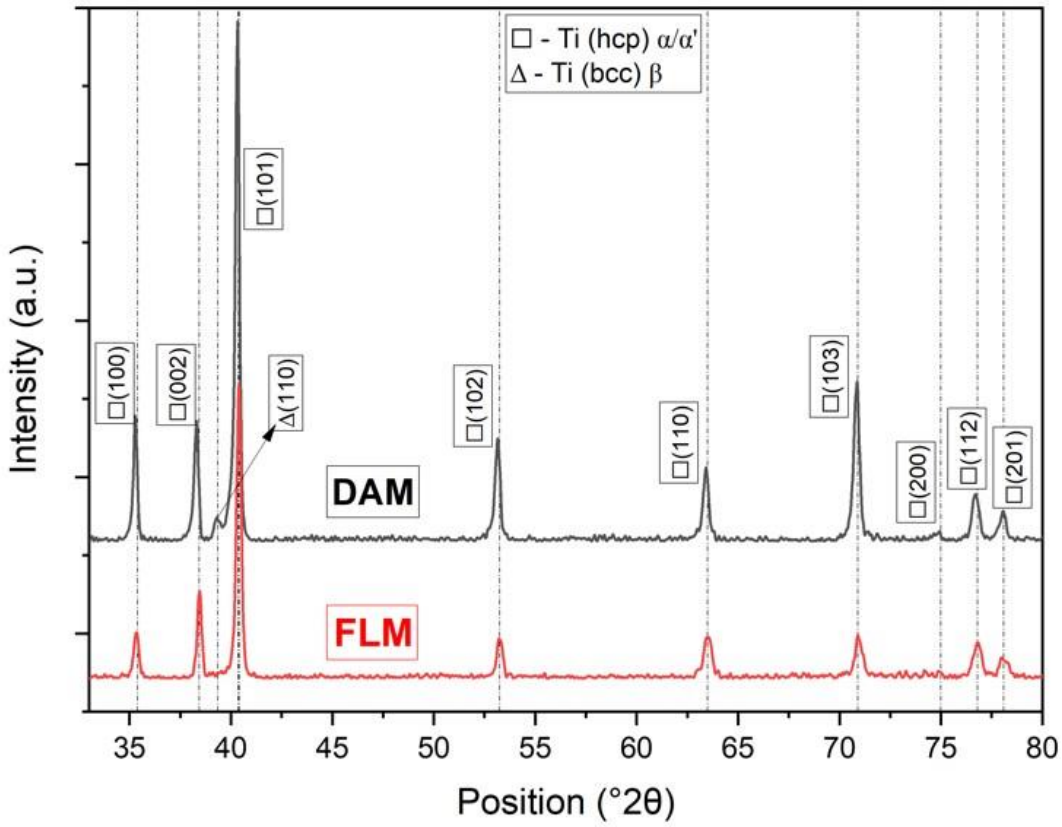

Figure 6.8 - X-Ray Diffraction Patterns of Separate DAM and FLM Parts: Distinct Analysis of Non-Hybrid Samples.

6.3.2.2 EDS Analysis

EDS analyses were conducted in several regions, including the pre and post FLM regions, middle DAM sections, and the intersection areas in the FLM+DAM+FLM samples. The aim of these analyses was to evaluate and compare the degree of elemental loss or vaporization in the various regions to determine if there were any significant differences. In Figure 6.9, the red, yellow, and blue areas represented the acceptable elemental weight percentage range according to the data sheet [213] and ASTM F1108-97a standard. Based on the data presented in the graph, it can be concluded that there was no observable elemental vaporization happened. In addition, the O_2 detected in these analyses was at negligible levels. This likely occurred after the samples were removed from the substrate, as the time prior to measurement could have resulted in surface oxidation.

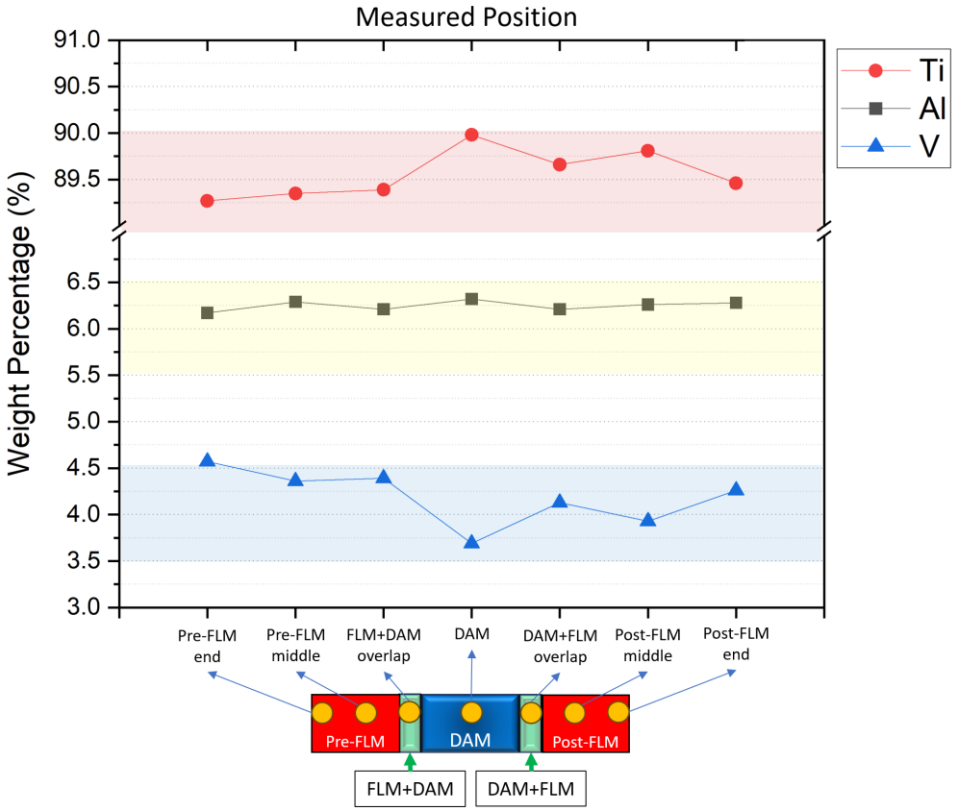

Figure 6.9 - Locations and Elemental Percentages in EDS Mapping: Averaged Area Values Indicated by Dots, Omitting Error Bars Due to Measurement Methodology.

6.3.2.3 Electron Backscatter Diffraction (EBSD) Analysis

EBSD analysis was focused on a sample section processed with DAM+FLM to reveal the crystallography and microstructural changes between DAM and FLM zones (Figure 6.10). This scan is divided into three zones to distinguish DAM (Zone I), overlap (DAM+FLM - Zone

II), and FLM (Zone III) region. Maximum feret diameter is used to evaluate the size of α/α' laths in different zones. The average maximum feret diameter for DAM, overlap, and FLM regions are calculated as 6.85 µm, 7.1 µm and 6.61 µm, respectively. This makes 7% larger α laths in overlapping region than FLM region whereas only 3% larger than DAM region. Despite the detection of the β phase in XRD analysis (Figure 6.8), the detected β amount by EBSD is less than 0.5% in volume in all three zones. IPF of parent β grains reconstructed from Figure 6.10-a according to Burgers orientation relationship is given in Figure 6.10-b. DAM, overlap, and FLM melted regions are showed with dashed rectangles as Zone I, Zone II and Zone III, respectively, in Figure 6.10-b. The grain area is used to evaluate parent β grain size as parent β grains are much larger than α laths. The average grain area was measured as 5940 μm^2 for DAM, 590 μm^2 for overlap, and 454 μm^2 for FLM regions. This means parent β grains in DAM zone are approximately 10 times larger than overlap zone and 13 times larger than FLM zone. None of the parent β grains imaged in DAM zone were scanned completely in EBSD imaging. This shows that DAM grains are even larger than calculated numbers.

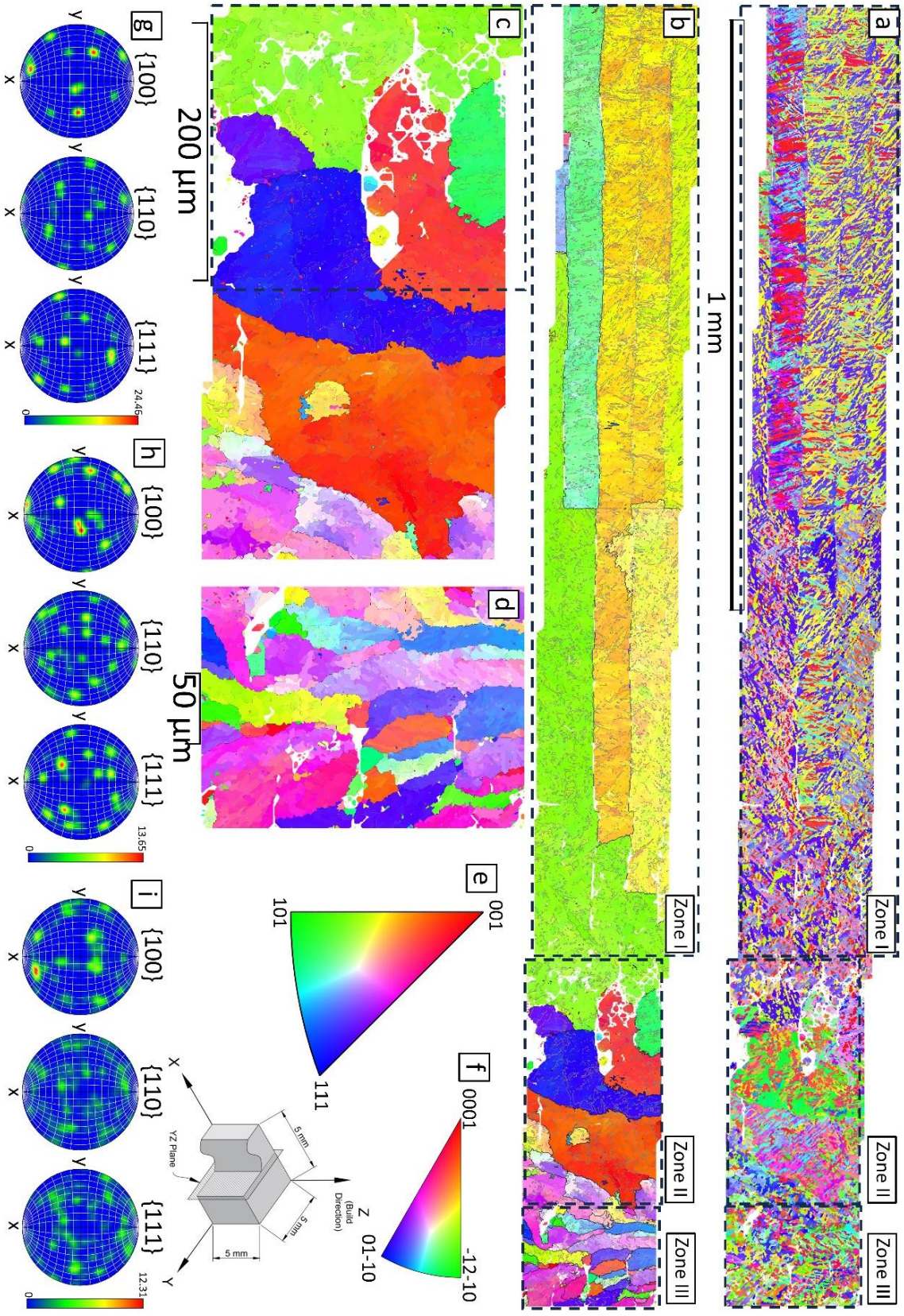

Figure 6.10 -Hybrid-laser processed sample (DAM+FLM section only) IPFs: (a) α phase, (b) reconstructed parent β grains and, DAM (Zone I), transition (Zone II) and FLM (Zone III) zones, magnified views of (c) transition (Zone II) and (d) FLM zones (Zone III), colour key for (e) α phase and (f) β phase, pole Figures of reconstructed parent β grains' from (g) DAM (Zone I), (h) overlap (Zone II) and (i) FLM (Zone III) zones. IPFs colours in (a)-(d) are represented according to Z axis.

Magnified views of Zone II and Zone III are given in Figure 6.10-c,d. Different parent β grain structures in different zones can be seen from Figure 6.10-b,c,d. DAM region has large and wide grains (Figure 6.10-b, Zone I) and all grains are larger than the EBSD imaging size despite millimetre scale image. On the other hand, overlapping and FLM region (Figure 6.10-c,d) has much smaller parent β grains. Parent β grains of the Zone II started to follow grains of the DAM zone (Figure 6.10-b, Zone I, and Figure 6.10-c, dashed rectangle) and transformed to columnar trains as the distance from DAM zone increases. In the FLM region (Figure 6.10-d), grains are totally transformed to columnar grains; however, these grains are noted as smaller than transition zone.

Pole figures for reconstructed grains in DAM, overlapping and FLM regions are given in Figure 6.10 (g,h,i), respectively. A texture is noted at certain regions for DAM region (Figure 6.10 (g)). However, these mostly arise due to large parent β grains. A weak texture on $\langle 100 \rangle_{\beta}$ direction is observed for Zone II (Figure 6.10 (h)). Two relatively large grains coloured in red in Zone II (Figure 6.10 (c)) caused this texture though other randomly distributed small grains caused a spread texture. The FLM zone (Figure 6.10(i)) does not have a strong texture and grains are mostly distributed in random directions relative to build direction.

Parent β grains are the first to solidify upon cooling down. Therefore, parent β grains potentially could give useful information about the solidification characteristics of DAM, overlap, and FLM zones. DAM provides a significantly larger melt pool compared to FLM laser. This provides larger liquid volume and cooling rate in DAM zone (~600°C/s [8]) is expected to be much slower than FLM cooling rate (~10^5-10^7°C/s [46,47]) due to this wide molten metal pool (>1000 µm). Hence, much larger parent β grains in millimetre scale were formed due to large molten volume and lower cooling rate. Upon cooling down further, parent β grain microstructure transformed to α+β microstructure.

Despite lower than FLM cooling rate, this cooling rate still may not be low enough for the formation of coarse β grains. Ahmed and Rack [36] suggested that the critical cooling rate for martensitic transformation is 410°C/s. The cooling rate for DAM measured by Alsaddah *et al.* [8,9] is 600°C/s while using 808 nm diode lasers. This is quite close to critical cooling rate for martensitic formation. This closeness probably caused formation of fine β grains

distributed within the α matrix. Considering the 400 nm step size of the EBSD scan, fine β probably was undetectable with the EBSD.

This overlapping can be confirmed from microstructural changes between DAM, FLM and overlap regions (Figure 6.10 (a,b)). DAM system scans and melts down the layer prior to FLM laser. Therefore, in the overlapping region, FLM melts down a solid layer rather than the powder layer. Columnar grains are formed in PBF process, and these columnar grains are growing through many layers [20,65]. Similar to this mechanism, grains in the overlapping region grow from previous solid DAM parent β grains (Figure 6.10 (c), dashed rectangle). As the parent grains are wide large grains in DAM zone, overlapping zone's grains follow their direction due to growing from these grains. However, these grains transform to vertical columnar grains as the distance increased from the DAM region due to the heat transfer through the base plate [65]. This creates different grain directions within the overlap zone.

FLM zone has the smallest parent β grains compared to two other zones (Figure 6.10 (d)). All these grains are columnar with a vertical growth direction. This is expected for single laser LPBF process [20,65] which typically uses fibre lasers similar to the one used in FLM zone of this study. Smaller melt pool and higher cooling rate in the FLM zone resulted in smaller parent β grains and the transformation from DAM zone's large wide parent grains to FLM zone's smaller vertical parent grains can be identified from overlap zone (Figure 6.10 (c)).

Overlapped region provided the largest α lath size compared to DAM and FLM zones. The FLM zone has the smallest α lath size, and it is expected to be due to high cooling rate. It is followed by DAM and overlapping regions' respectively. It is likely that, remelting of overlap region provided the highest energy input and this region had the highest α lath size. However, the α lath size difference between zones is not as considerable as the parent β grain size difference. This suggests that despite having low enough cooling rate to obtain a detectable β phase by XRD, the cooling rate was still not low enough to generate β grains large enough to be detected by EBSD with 400 nm step size. This could be another supporting reason why β volume fraction was below 0.5%.

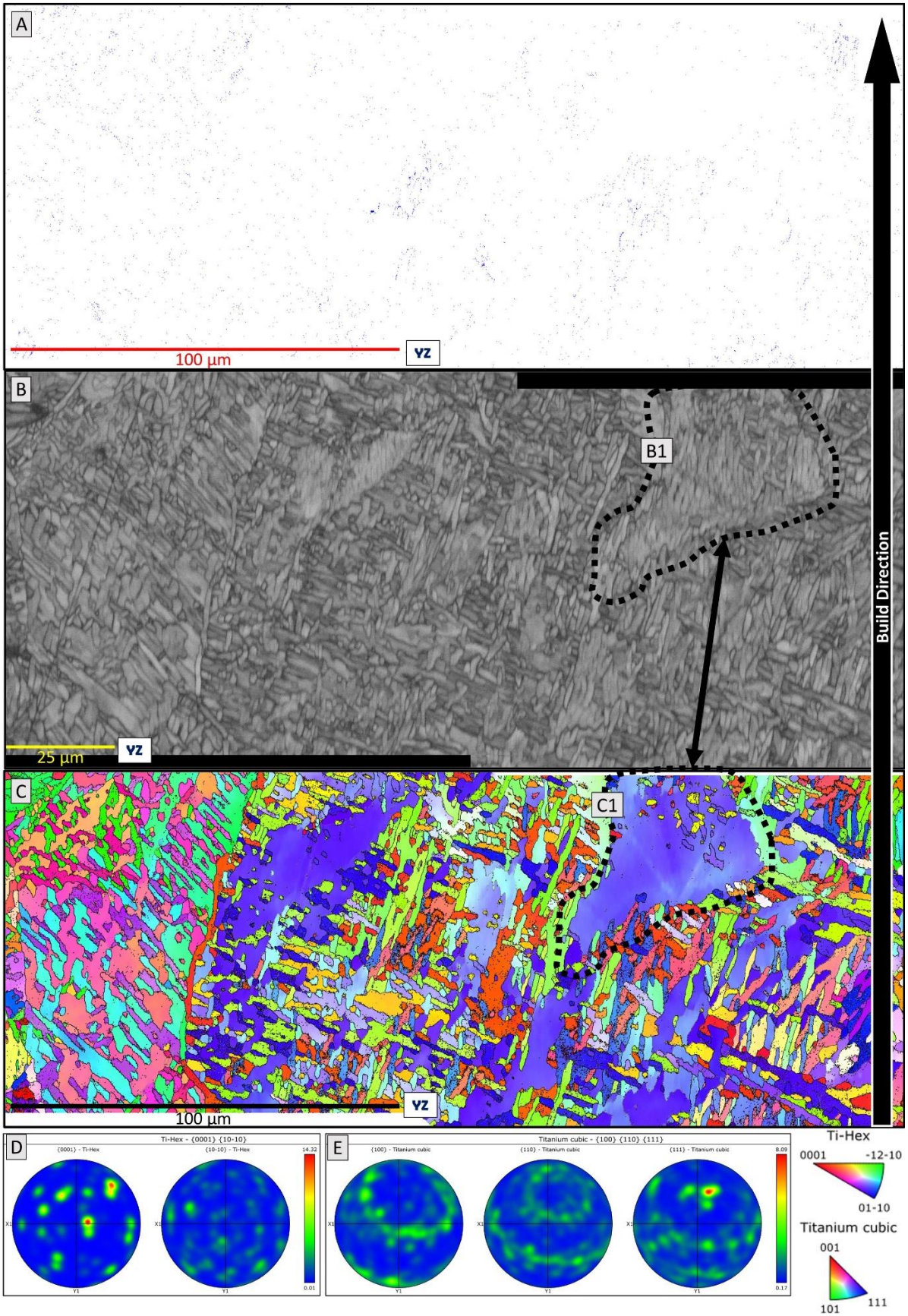

Figure 6.11 – (A) Phase Image that blue dots represents β phase, (B) SEM image taken from ENSD Analysis, (C) EBSD image of High magnification area, (D) is the pole figure for α phase, (E) is the pole figure for β phase

Figure 6.11 shows a high-magnification EBSD analysis of the DAM+FLM sample at the overlap area. This section was not included in Figure 6.10 because the area of interest is located slightly below the baseline of the overlap region. Figure 6.11-A depicts titanium cubic (β-phase) structures (blue) compared to hexagonal structures (white), with the β-phase accounting for 0.3% by volume. This indicates that although the cooling rate was low enough to detect β-phase by XRD, there was not low enough to form β-grains large enough for EBSD detection, even at a step size of 150 nm.

The EBSD analysis of sections B and C in Figure 6.11 indicates the existence of primary β grains at locations B1 and C1 at the overlap region when comparing two images together. Furthermore, the Figure 6.11 reveals the main characteristics of the sub-grains, which the Figure 6.11-C1 appeared less defined due to the grain boundary angle setting (2°-10°) in the analysis software, which highlighted grains with aligned crystallographic orientations. It is important to note that this setting only distinguishes boundaries exceeding 10° as distinct grain edges. The analysis revealed that 12.3% of the grain boundaries were low-angle (2°-10°) and 87.7% were high-angle (>10°), indicating a dominant 'basket-weave' texture. Additionally, approximately 12.3% of the sub-grains exhibited lamellar morphology and a preferred orientation along the build direction, as supported by Figure 6.11-D which showed a weak but evident texture of $\langle 0001 \rangle_{\alpha}$ and $\langle 01\text{-}10 \rangle_{\alpha}$ phases concentrated towards the build direction. Figure 6.11-E shows a similar weak texture of the $\langle 111 \rangle_{\beta}$ orientation for cubic phases, which tends towards the build direction. The basket-weave microstructure contains a prevalence of low-angle grain boundaries, which could cause fluctuations in nano-indentation results due to the homogeneity and close structural proximity of adjacent grains.

6.3.2.4 Micro and Nano-Indentation

The micro-hardness data presented in Figure 6.12 indicate that the material has softer characteristics during the DAM phase, with increasing hardness observed in the FLM phase. The Hall-Petch relationship suggests that a fine microstructure increases the hardness of the material, as reported in the literature [231,232]. Specifically, the FLM-processed material exhibits hardness values ranging from 3.0 to 3.4 GPa, in contrast to the 2.2 to 2.3 GPa range for the DAM-processed section. These findings align with the EBSD analysis, which shows that a coarser microstructure of Ti6Al4V contributes to reduced hardness. The data collected indicates that the pre-FLM section experienced lower levels of hardness relative to the post-

FLM section. The variance in hardness can be attributed to increased heat exposure (in FLM+DAM) resulting from the DAM process, with subsequent impacts on the microstructure. Conversely, the post-FLM section demonstrated higher Vickers hardness values potentially due to the rapid cooling rate inherent in this process. Moreover, the microstructure at the DAM intersection appears to undergo changes in the post-FLM section, leading to an increase in post-intersection hardness values when compared to pre-intersection values.

The alteration may be attributed to two potential factors; firstly, the DAM retraction from the powder-bed for FLM initiation is necessary and increases the temperature gradient, leading to a gradual structural cooling over time. Secondly, the FLM technique functions in a similar way to a re-scanning laser over the transition area, but at a much higher speed (almost 900 times faster). This accelerated process results in shorter microstructures compared to those found in the fully DAM processed area.

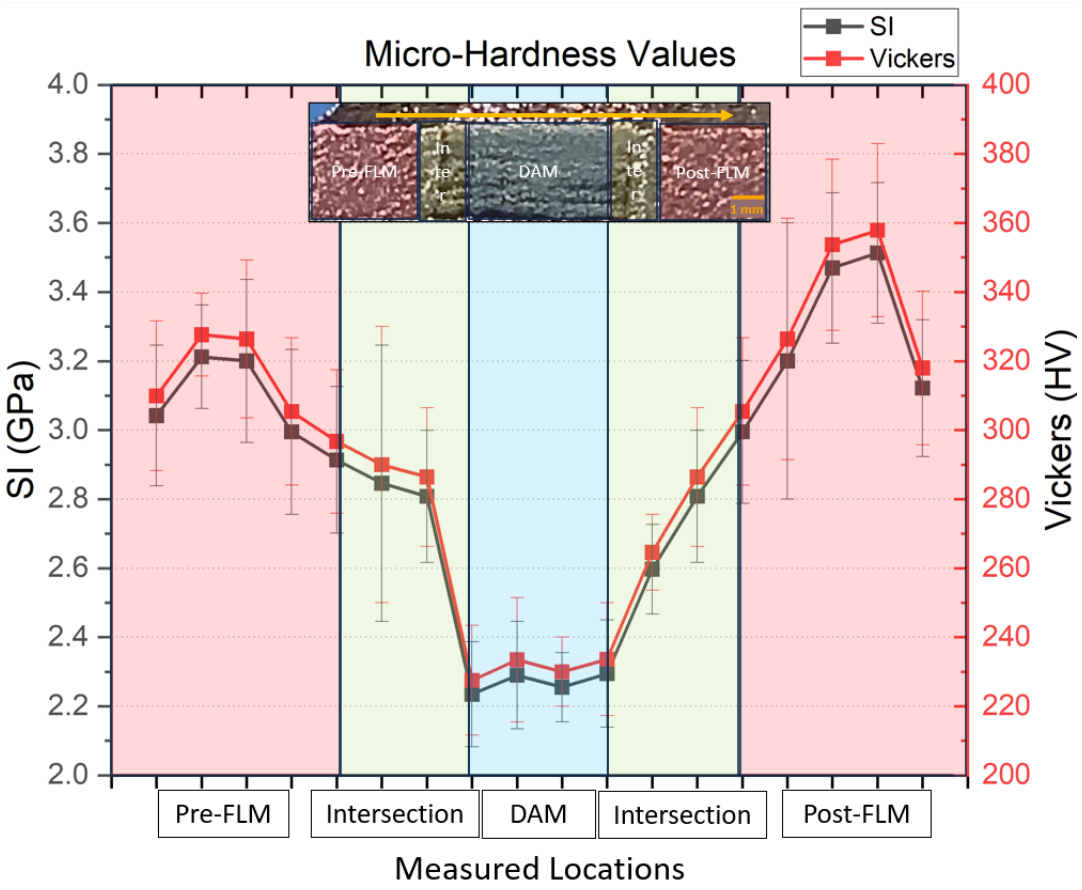

Figure 6.12 - Micro-Vickers Hardness Test Outcomes for the FLM+DAM+FLM Sample

Accurate micro-hardness measurement can be challenging due to the large indentation area. Any air gap between the specimen and the hot-mounted bakelite structure

can have a similar effect to that of a spring, reducing the measured hardness. A similar effect on the results can also be caused by a high level of porosity beneath the indentation surface (especially at the overlap region in this sample), as this will add springiness to the material. Nano-indentation has a much smaller indenter inherently, therefore, expected to provide more accurate hardness measurements due to the much smaller impact area of the indenter compared to micro-hardness. According to Figure 6.13 displays a load and depth graph under a maximal load of 100 mN of the results of the nano-indentation hardness analyses for the as-built Ti6Al4V specimens (FLM+DAM+FLM). It illustrates the reduced modulus of elasticity, calculated Young's modulus, and the hardness values across nine distinct matrix locations within the sample.

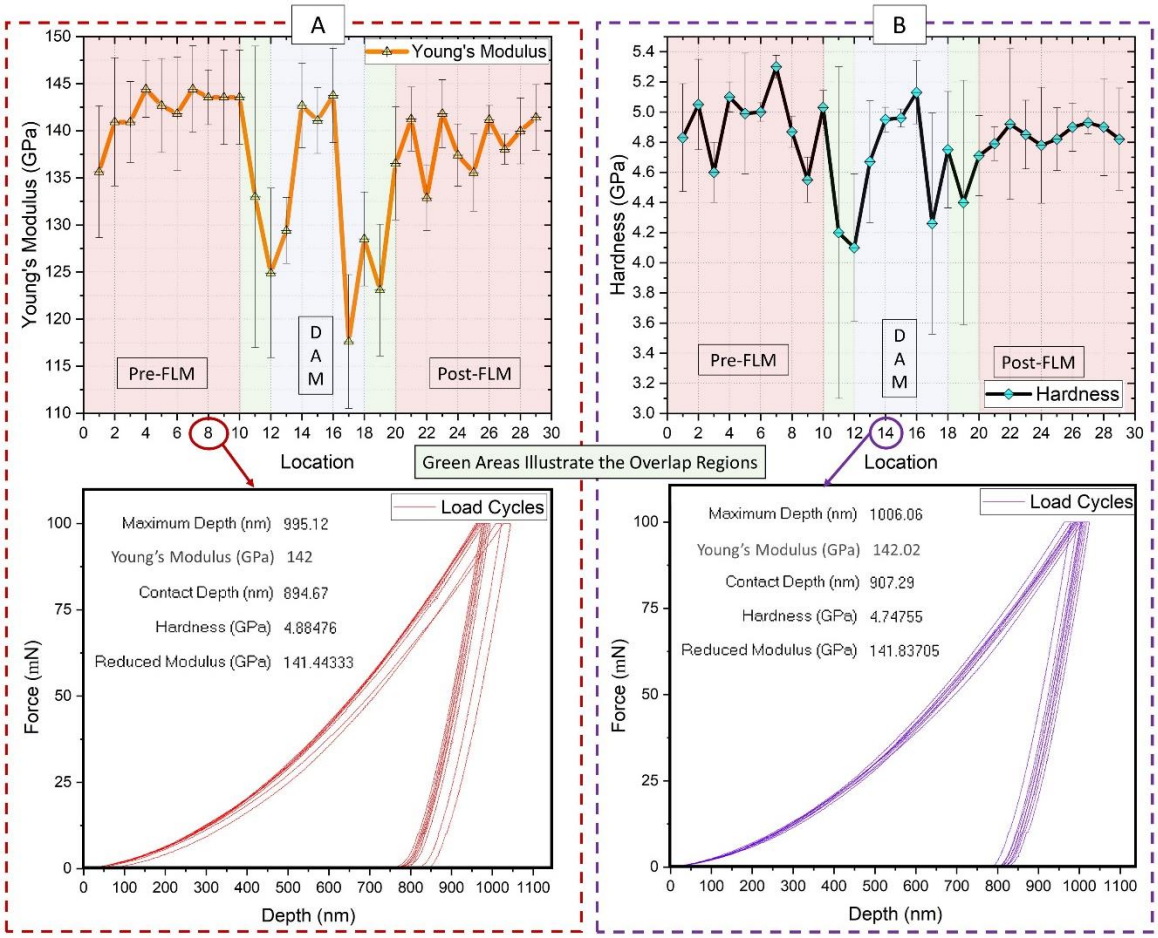

Figure 6.13 - Nano-Indentation Test Results for FLM+DAM+FLM Sample Spanning Pre-FLM to Post-FLM: (A) Young's Modulus Measurements, (B) Hardness Evaluations, Including Overlap and DAM-Only Regions

The results are consistent with the micro-indentation hardness data in most regions, apart from the section which was processed with DAM. The cause of the reduced hardness

seen in the DAM area might be the presence of porosity between the layers, or a lack of fusion between them, which could negatively impact the micro-hardness measurements and potentially result in lower hardness values. This explanation could also apply to the intersection area, where some degree of porosity has been documented. Hence, the occurrence of porosity in these regions could account for the discrepancies in the outcomes, as highlighted by the extensive error bars in the data.

Nano-indentation appears to provide a more accurate measure of the hardness of certain phase structures [8], as it is unaffected by potential sub-surface processing or material preparation defects, ensuring an accurate measurement of the hardness of, for instance, martensite α' structures. Variations in hardness can be accounted for by the indenter impacting different phases, such as α', α+β, *or* β, with α' exhibiting higher levels of hardness in most cases [95,209,240]. The EBSD data showed larger sub-grain sizes in the overlap regions compared to the post-FLM and DAM regions. According to the Hall-Petch relationship [145,210,241], this implies lower hardness at these interfaces, as observed in Figure 6.13. In addition, both Young's modulus and hardness appeared to increase as the cooling rate decreased. In this context, the scanning speed of DAM is significantly lower than that of FLM at 1.25 mm/s and 900 mm/s respectively, which affects the cooling dynamics and the resulting mechanical properties.

Generally, post-process heat treatment is required to achieve α+β structures or highly elevated in-situ powder-bed temperatures such as those experienced within the EBM process (above 600℃) [51]. Moreover, α+β structures generally exhibit a better ductility and more favourable total elongation failure in the industry [51,246]. These hardness results may indicate that the ductility of the DAM processed area (α+β) is higher than that of a FLM processed area (acicular α'), which can eliminate the necessity for post-heat treatment procedure (therefore cost reduction) [51,246].

6.4 Chapter Conclusion

In this chapter a hybrid PBF-LB system combining a closely packed linear array of 450 nm diode lasers together with a 1064 nm fiber laser was used to process Ti6Al4V feedstock. It was found that there was a variation in sample properties (microstructure, mechanical properties, and surface roughness) across the FLM, DAM, and laser overlap regions. First,

scanning order study was conducted. DAM samples were processed first, followed by FLM, to leverage the higher power of FLM for re-melting solidified layers. The overlap distance was found to be 500 µm. SEM images indicated that FLM sections had smoother surfaces than DAM sections of the top surface. Two scanning strategies—FLM followed by DAM (FLM+DAM) and DAM followed by FLM (DAM+FLM)—were compared, revealing that the DAM+FLM strategy resulted in significantly lower porosity and fewer cracks, whereas the FLM+DAM strategy often exhibited cracking due to high residual stresses.

The study highlighted significant differences in SSR, with DAM samples exhibiting much higher SSR than FLM samples due to higher HAZ. Microstructural analysis via SEM, XRD, and EBSD revealed that DAM samples had larger sub-grain sizes and α+β grains, while FLM samples showed finer acicular α/α' structures. EDS analysis confirmed that elemental composition remained within industry standards. The study identified limitations in aligning two LPBF systems and achieving precise overlap tolerances, suggesting potential improvements such as heating the powder bed using DAM lasers in a defocused position. Key findings summarised as:

- Optimal 500 µm overlap between DAM and FLM samples. Moreover, HLPBF produced high density hybrid samples using both laser types independently and sequentially.
- DAM+FLM scanning strategy reduced porosity and cracking.
- DAM samples exhibited higher SSR due to higher HAZ, therefore, FLM can be an improvement equipment for DAM samples for contouring.
- Different cooling rates led to microstructure control in DAM and FLM, which 13x larger parent β grains were found in DAM zone compared to FLM zone. Therefore, spatial microstructural tailoring can be done via HLPBF system.
- Elemental composition remained within industry standards for both processing technology. Furthermore, HLPBF showed a potential to reduce post-processing time, such as heat treatment, for LPBF specimens due to laser system capabilities.

This chapter concluded that precise control over scanning strategies and system refinements are essential for optimizing the HLPBF process and minimizing defects.

7. Conclusions

This research aimed to investigate the feasibility of integrating two distinct laser processing systems into a single LPBF setup (HLPBF) to address specific challenges associated with each individual system, such as side surface roughness observed in DAM and the effect of cooling rate differences on hybrid LPBF-produced parts, ultimately achieving spatial microstructure tailoring with Ti6Al4V feedstock. The study encompassed several key experimental setups and analyses to evaluate the performance and outcomes of the HLPBF system.

In the first major study, the reliability of the fibre laser equipment was assessed using Ti6Al4V powder in the bespoke HLPBF system. The second study focused on the effect of the 450 nm DAM system with a single array on the Ti6Al4V powder bed. It explored the impact of scanning speed and track overlap on surface defects, material integrity, and wetting capabilities. These investigations included single track studies to identify optimal parameters, followed by single and multi-layer studies, cross-sectional density, side surface roughness correlated with normalized energy density, XRD, microstructural examination, EDS, and micro and nano-indentation analyses.

The third study investigated a hybrid LPBF system combining 450 nm diode lasers with a 1064 nm fibre laser to process Ti6Al4V feedstock, DAM and FLM respectively. Variations in sample properties were observed across FLM, DAM, and laser overlap regions, with significant differences in microstructure and mechanical properties. The study identified optimal overlap distances and scanning strategies, emphasizing the importance of precise control over scanning sequences to reduce porosity and cracking and achieve spatial microstructural tailoring. Key findings of each chapter can be summarised as follows.

<u>Fibre Laser Equipment:</u>

- The custom fibre laser in the HLPBF could produce high-density Ti6Al4V specimens with minimal defects with 60 µm layer height, reaching peak densities of 99.88%.

- Reducing normalised energy density improved side surface roughness, and Basket-weave microstructures were dominant under all experimental conditions.
- Data from micro and nano-indentation suggest that increasing normalised energy density described as a decrease in cooling rate, therefore, affecting the microstructure and mechanical properties.

450 nm DAM System:

- Maximum power of 4W was effective for melting Ti6Al4V powder, with optimal scanning speeds below 100 mm/min for higher sample integrity.
- Increased laser count led to wider (~1100 µm) and deeper melt pools, identified as the 'Crescent Effect'. Higher energy densities reduced void formation, therefore, reduced the crescent effect.
- Rescanning strategies reduced top surface roughness by 50%, increased sample density by 2%, decreased Vickers hardness values, however, nanoindentation showed higher hardness due to microstructural changes.
- 36W system could not achieve part densities of 99.3% and above, likely due to insufficient powder bed heating and potential oxygen ingress.

Hybrid PBF-LB System:

- DAM samples exhibited higher SSR due to higher HAZ, suggesting FLM as an improvement tool for contouring DAM samples.
- Different cooling rates led to microstructure control, with 13x larger parent β grains found in the DAM zone compared to the FLM zone, allowing for spatial microstructural tailoring via HLPBF as proposed in the aim of the research.
- HLPBF showed potential to reduce post-processing time, such as heat treatment, for LPBF specimens due to laser system capabilities.

In summary, this research demonstrates the potential of the HLPBF system to effectively integrate distinct laser processing methods, achieving enhanced control over microstructure and mechanical properties in Ti6Al4V parts. The findings underscore the importance of optimizing scanning strategies, energy densities, and cooling rates to minimize

defects and maximize material performance, paving the way for advanced applications in additive manufacturing.

6.5 Future Research Suggestions

These recommendations could be pursued as part of a research project for a Master's degree, a post-doctoral research project or a PhD.

I. **Scalability of HLPBF for larger components:** Investigate the ability of HLPBF to produce larger components and its integration into production lines, focusing on system reliability and repeatability in an industrial environment, and conducting a case study to determine the suitability to the industry of varying hardness across different sections of a part. Limitation can be the power supply.

II. **Extending HLPBF with more lasers or wavelengths:** Investigating the addition of more diode lasers to the current limit of 50, focusing on the development of a suitable cooling module, and exploring the impact of different laser wavelengths on the control of microstructure and material properties. Limitation can be the laser mirror capability with different wavelengths.

III. **Microstructural investigation of vertical hybrid samples:** Perform detailed analysis of vertical hybrid samples, including all faces (top, sides, bottom) to understand the uniformity and consistency of the hybrid manufacturing process. Limitation can be remelting of DAM top of a FLM produced sample due to lack of penetration energy.

IV. **HLPBF with different materials:** Explore the potential of HLPBF with a wider range of challenging materials, including superalloys, metal matrix composites or precious metals, to understand the adaptability and effectiveness of the process. Limitation can be the absorptivity of the material may not be satisfactory.

V. **Effects of optical preheating:** Investigate the effects of optical preheating on the DAM, FLM or hybrid samples, focusing on how it affects the processing capabilities and resulting microstructures. Limitation can be build chamber space and heat transfer may damage the multi-laser head.

VI. **Functionally graded materials via HLPBF:** Investigate the creation of materials with graded properties in a single component using HLPBF, exploring the feasibility

of multi-material processing and how dual wavelength systems can aid the processing of different materials such as copper with titanium or nickel alloys. Limitation can be the material spreading equally inside the chamber.

VII. **Reduce post-processing time:** Conduct comparative studies of traditional and HLPBF processes, with a particular focus on the potential reduction in post-processing time and steps required in HLPBF. Limitation can be the software of the HLPBF due to unmatching capability of an industrial system.

VIII. **Modelling the multi-laser powder bed fusion approach via theoretical work:** A theory-based computational mechanics approach can be used to analyse the interaction of multi-laser systems with metal powder. This can be complemented by comparison with experimental results. This comprehensive approach can be integrated theoretical predictions with practical observations, providing a more robust understanding of the effectiveness and behaviour of multiple laser systems in metal powder processing. Limitation can be the processing power required for run a multi-laser simulation. HPC may require.

IX. **Melt Pool Interaction with Dual Laser Systems:** Investigate the interaction between melt pools produced by different laser systems, requiring system adjustments to start both laser systems simultaneously for a comprehensive analysis. Limitation can be the DAM system movement mechanism update.

X. **Environmental and economic impacts:** Evaluate the sustainability and economic feasibility of HLPBF, comparing its impact with traditional manufacturing processes to demonstrate its viability for industries prioritising sustainability. Limitation can be the incomparability of high prototyping cost.

XI. **Advanced software for HLPBF:** Develop and refine software solutions that can accurately predict and optimise HLPBF results based on various input parameters and material properties, improving the efficiency and reliability of the process. Limitation can be addressed as many communication modules integration into the single software.

8. References

[1] H. Shipley, D. McDonnell, M. Culleton, R. Coull, R. Lupoi, G. O'Donnell, D. Trimble, Optimisation of process parameters to address fundamental challenges during selective laser melting of Ti-6Al-4V: A review, International Journal of Machine Tools and Manufacture 128 (2018) 1–20. https://doi.org/10.1016/j.ijmachtools.2018.01.003.

[2] H.D. Nguyen, A. Pramanik, A.K. Basak, Y. Dong, C. Prakash, S. Debnath, S. Shankar, I.S. Jawahir, S. Dixit, D. Buddhi, A critical review on additive manufacturing of Ti-6Al-4V alloy: microstructure and mechanical properties, J. Mater. Res. Technol. 18 (2022) 4641–4661. https://doi.org/10.1016/j.jmrt.2022.04.055.

[3] W.S.W. Harun, M.S.I.N. Kamariah, N. Muhamad, S.A.C. Ghani, F. Ahmad, Z. Mohamed, A review of powder additive manufacturing processes for metallic biomaterials, Powder Technology 327 (2018) 128–151. https://doi.org/10.1016/j.powtec.2017.12.058.

[4] D. Sun, D. Gu, K. Lin, J. Ma, W. Chen, J. Huang, X. Sun, M. Chu, Selective laser melting of titanium parts: Influence of laser process parameters on macro- and microstructures and tensile property, Powder Technology 342 (2019) 371–379. https://doi.org/10.1016/j.powtec.2018.09.090.

[5] S. Sun, M. Brandt, M. Easton, Powder bed fusion processes: An overview, in: Laser Additive Manufacturing: Materials, Design, Technologies, and Applications, 2017: pp. 55–77. https://doi.org/10.1016/b978-0-08-100433-3.00002-6.

[6] D. Herzog, V. Seyda, E. Wycisk, C. Emmelmann, Additive manufacturing of metals, Acta Mater. 117 (2016) 371–392. https://doi.org/10.1016/j.actamat.2016.07.019.

[7] C. Emmelmann, D. Herzog, J. Kranz, Design for laser additive manufacturing, Laser Additive Manufacturing: Materials, Design, Technologies, and Applications (2017) 259–279. https://doi.org/10.1016/b978-0-08-100433-3.00010-5.

[8] M. Alsaddah, A. Khan, K. Groom, K. Mumtaz, Diode area melting of Ti6Al4V using 808 nm laser sources and variable multi-beam profiles, Materials & Design 215 (2022) 110518. https://doi.org/10.1016/j.matdes.2022.110518.

[9] M. Alsaddah, A. Khan, K. Groom, K. Mumtaz, Use of 450-808 nm diode lasers for efficient energy absorption during powder bed fusion of Ti6Al4V, The International Journal of Advanced Manufacturing Technology 113 (2021) 2461–2480. https://doi.org/10.1007/s00170-021-06774-4.

[10] H. Ali, H. Ghadbeigi, K. Mumtaz, Effect of scanning strategies on residual stress and mechanical properties of Selective Laser Melted Ti6Al4V, Materials Science and Engineering A 712 (2018) 175–187. https://doi.org/10.1016/j.msea.2017.11.103.

[11] J. Jhabvala, E. Boillat, T. Antignac, R. Glardon, On the effect of scanning strategies in the selective laser melting process, Virtual Phys. Prototyp. 5 (2010) 99–109. https://doi.org/10.1080/17452751003688368.

[12] A.K. Subramaniyan, A.S. Reddy, S. Mathias, A. Shrivastava, P. Raghupatruni, Influence of post-processing techniques on the microstructure, properties and surface integrity of AlSiMg alloy processed by laser powder bed fusion technique, Surf. Coat. Technol. 425 (2021) 127679. https://doi.org/10.1016/j.surfcoat.2021.127679.

[13] M.F. Sadali, M.Z. Hassan, F. Ahmad, H. Yahaya, Z.A. Rasid, Influence of selective laser melting scanning speed parameter on the surface morphology, surface roughness, and micropores for manufactured Ti6Al4V parts, J. Mater. Res. 35 (2020) 2025–2035. https://doi.org/10.1557/jmr.2020.84.

[14] M. Zavala-Arredondo, N. Boone, J. Willmott, D.T.D. Childs, P. Ivanov, K.M. Groom, K. Mumtaz, Laser diode area melting for high speed additive manufacturing of metallic components, Materials & Design 117 (2017) 305–315. https://doi.org/10.1016/j.matdes.2016.12.095.

[15] M. Zavala-Arredondo, K.M. Groom, K. Mumtaz, Diode area melting single-layer parametric analysis of 316L stainless steel powder, International Journal of Advanced Manufacturing Technology 94 (2018) 2563–2576. https://doi.org/10.1007/s00170-017-1040-4.

[16] M. Zavala-Arredondo, H. Ali, K.M. Groom, K. Mumtaz, Investigating the melt pool properties and thermal effects of multi-laser diode area melting, International Journal of Advanced Manufacturing Technology 97 (2018) 1383–1396. https://doi.org/10.1007/s00170-018-2038-2.

[17] H. Caglar, A. Liang, K. Groom, K. Mumtaz, Multi-laser powder bed fusion of Ti6Al4V: Diode area melting utilizing low-power 450 nm diode lasers, J. Mater. Process. Technol. 325 (2024) 118303. https://doi.org/10.1016/j.jmatprotec.2024.118303.

[18] W.E. Frazier, Metal Additive Manufacturing: A Review, J. Mater. Eng. Perform. 23 (2014) 1917–1928. https://doi.org/10.1007/s11665-014-0958-z.

[19] S.A.M. Tofail, E.P. Koumoulos, A. Bandyopadhyay, S. Bose, L. O'Donoghue, C. Charitidis, Additive manufacturing: scientific and technological challenges, market uptake and opportunities, Mater. Today 21 (2018) 22–37. https://doi.org/10.1016/j.mattod.2017.07.001.

[20] T. DebRoy, H.L. Wei, J.S. Zuback, T. Mukherjee, J.W. Elmer, J.O. Milewski, A.M. Beese, A. Wilson-Heid, A. De, W. Zhang, Additive manufacturing of metallic components – Process, structure and properties, Prog. Mater. Sci. 92 (2018) 112–224. https://doi.org/10.1016/j.pmatsci.2017.10.001.

[21] S. Chowdhury, N. Yadaiah, C. Prakash, S. Ramakrishna, S. Dixit, L.R. Gupta, D. Buddhi, Laser powder bed fusion: a state-of-the-art review of the technology, materials, properties & defects, and numerical modelling, J. Mater. Res. Technol. 20 (2022) 2109–2172. https://doi.org/10.1016/j.jmrt.2022.07.121.

[22] H. Zhang, C.K.P. Vallabh, X. Zhao, Influence of Spattering on In-process Layer Surface Roughness during Laser Powder Bed Fusion, ArXiv (2023). https://doi.org/10.48550/arxiv.2303.00272.

[23] E. Yasa, J. Deckers, T. Craeghs, M. Badrossamay, J.P. Kruth, Investigation on occurrence of elevated edges in selective laser melting, in: 2009: pp. 180–192.

[24] K. Mumtaz, N. Hopkinson, Top surface and side roughness of Inconel 625 parts processed using selective laser melting, Rapid Prototyping Journal 15 (2009) 96–103. https://doi.org/10.1108/13552540910943397.

[25] H. Yang, X. Tang, C. Hu, S. Liu, Y. Fan, Y. Xiao, G. Lu, Q. Wang, G. Chen, P. Xing, H. Tan, Z. Guo, Z. Niu, Study on laser welding of copper material by hybrid light source of blue diode laser and fiber laser, J. Laser Appl. 33 (2021) 032018. https://doi.org/10.2351/7.0000386.

[26] undefined I.S.O. (ISO)/ASTM International, ISO/ASTM 52910:2017(E). Standard Guidelines for Design for Additive Manufacturing., ISO/ASTM International 2017 (2017) 1–14. https://doi.org/10.1520/iso.

[27] M.M. Prabhakar, A.K. Saravanan, A.H. Lenin, I.J. leno, K. Mayandi, P.S. Ramalingam, A short review on 3D printing methods, process parameters and materials, Mater. Today: Proc. 45 (2021) 6108–6114. https://doi.org/10.1016/j.matpr.2020.10.225.

[28] A. 52900:2015, Standard Terminology for Additive Manufacturing – General Principles – Terminology, ASTM International i (2015) 1–9. https://doi.org/10.1520/f2792-12a.2.

[29] J. López-Barroso, C.G. Flores-Hernández, A.L. Martínez-Hernández, G. Martínez-Barrera, C. Velasco-Santos, Advanced Composites, Adv. Mater. Res. Technol. (2023) 121–186. https://doi.org/10.1007/978-3-031-42731-2_5.

[30] undefined ASTM, Standard for Additive Manufacturing – Post Processing Methods – Standard Specification for Thermal Post-Processing Metal Parts Made Via Powder Bed Fusion, ASTM Standards (2018) 4–6. https://doi.org/10.1520/f3301-18.

[31] undefined ASTM, Guide for Additive Manufacturing — Design — Directed Energy, International Standard F3413-2019 (2019) 1–24. https://doi.org/10.1520/f3413-19.design.

[32] A.F.− 14, Standard Guide for Characterizing Properties of Metal Powders Used for Additive Manufacturing Processes, 2014. file:///D:/Sorted Papers/ASTM - 2014 - Standard Guide for Characterizing Properties of Metal Powders Used for Additive Manufacturing Processes.pdf.

[33] undefined A. International, Standard Test Methods for Density of Compacted or Sintered Powder Metallurgy (PM) Products Using Archimedes' Principle, Astm B962-13 i (2013) 1–7. https://doi.org/10.1520/b0962-13.2.

[34] D.D. Gu, W. Meiners, K. Wissenbach, R. Poprawe, Laser additive manufacturing of metallic components: materials, processes and mechanisms, International Materials Reviews 57 (2012) 133–164. https://doi.org/10.1179/1743280411y.0000000014.

[35] L.E. Murr, S.M. Gaytan, D.A. Ramirez, E. Martinez, J. Hernandez, K.N. Amato, P.W. Shindo, F.R. Medina, R.B. Wicker, Metal Fabrication by Additive Manufacturing Using Laser and Electron Beam Melting Technologies, Journal of Materials Science and Technology 28 (2012) 1–14. https://doi.org/10.1016/s1005-0302(12)60016-4.

[36] T. Ahmed, H.J. Rack, Phase transformations during cooling in α+β titanium alloys, Mater. Sci. Eng.: A 243 (1998) 206–211. https://doi.org/10.1016/s0921-5093(97)00802-2.

[37] K. Dietrich, J. Diller, S.D.-L. Goff, D. Bauer, P. Forêt, G. Witt, The influence of oxygen on the chemical composition and mechanical properties of Ti-6Al-4V during laser powder bed fusion (L-PBF), Addit. Manuf. 32 (2020) 100980. https://doi.org/10.1016/j.addma.2019.100980.

[38] Dr.C. Leyens, Dr.M. Peters, Titanium and Titanium Alloys: Fundamentals and Applications, 2003. https://doi.org/10.1002/3527602119.

[39] R. Acharya, J.A. Sharon, A. Staroselsky, Prediction of microstructure in laser powder bed fusion process, Acta Mater. 124 (2017) 360–371. https://doi.org/10.1016/j.actamat.2016.11.018.

[40] Y. Yang, Y.J. liu, J. Chen, H.L. Wang, Z.Q. Zhang, Y.J. Lu, S.Q. Wu, J.X. Lin, Crystallographic features of α variants and β phase for Ti-6Al-4V alloy fabricated by selective laser melting, Mater. Sci. Eng.: A 707 (2017) 548–558. https://doi.org/10.1016/j.msea.2017.09.068.

[41] U.S. Bertoli, G. Guss, S. Wu, M.J. Matthews, J.M. Schoenung, In-situ characterization of laser-powder interaction and cooling rates through high-speed imaging of powder bed fusion additive manufacturing, Mater. Des. 135 (2017) 385–396. https://doi.org/10.1016/j.matdes.2017.09.044.

[42] R. Shi, S.A. Khairallah, T.T. Roehling, T.W. Heo, J.T. McKeown, M.J. Matthews, Microstructural control in metal laser powder bed fusion additive manufacturing using laser beam shaping strategy, Acta Materialia 184 (2020) 284–305. https://doi.org/10.1016/j.actamat.2019.11.053.

[43] F. Bartolomeu, M. Gasik, F.S. Silva, G. Miranda, Mechanical Properties of Ti6Al4V Fabricated by Laser Powder Bed Fusion: A Review Focused on the Processing and Microstructural Parameters Influence on the Final Properties, Metals 12 (2022) 986. https://doi.org/10.3390/met12060986.

[44] X. Tan, Y. Kok, Y.J. Tan, G. Vastola, Q.X. Pei, G. Zhang, Y.-W. Zhang, S.B. Tor, K.F. Leong, C.K. Chua, An experimental and simulation study on build thickness dependent microstructure for electron beam melted Ti–6Al–4V, J. Alloy. Compd. 646 (2015) 303–309. https://doi.org/10.1016/j.jallcom.2015.05.178.

[45] R. Shanmugam, D. Veeman, M.S. Mannan, G. Kalaiselvan, Effect of Heat Treatment on the Oxidation and High Temperature Wear Performance of Alloy Ti-6Al-4V Manufactured by Direct Metal Laser Sintering, Vol. 2B: Adv. Manuf. (2022). https://doi.org/10.1115/imece2022-95392.

[46] J. Yang, H. Yu, J. Yin, M. Gao, Z. Wang, X. Zeng, Formation and control of martensite in Ti-6Al-4V alloy produced by selective laser melting, Mater. Des. 108 (2016) 308–318. https://doi.org/10.1016/j.matdes.2016.06.117.

[47] P.A. Hooper, Melt pool temperature and cooling rates in laser powder bed fusion, Addit. Manuf. 22 (2018) 548–559. https://doi.org/10.1016/j.addma.2018.05.032.

[48] C. Zhong, J. Liu, T. Zhao, T. Schopphoven, J. Fu, A. Gasser, J.H. Schleifenbaum, Laser Metal Deposition of Ti6Al4V—A Brief Review, Appl. Sci. 10 (2020) 764. https://doi.org/10.3390/app10030764.

[49] W.M. Steen, J. Mazumder, Laser Material Processing, 4th ed., 2010. https://doi.org/10.1007/978-1-84996-062-5.

[50] W. Xu, M. Brandt, S. Sun, J. Elambasseril, Q. Liu, K. Latham, K. Xia, M. Qian, Additive manufacturing of strong and ductile Ti–6Al–4V by selective laser melting via in situ martensite decomposition, Acta Mater. 85 (2015) 74–84. https://doi.org/10.1016/j.actamat.2014.11.028.

[51] W. Xu, E.W. Lui, A. Pateras, M. Qian, M. Brandt, In situ tailoring microstructure in additively manufactured Ti-6Al-4V for superior mechanical performance, Acta Mater. 125 (2017) 390–400. https://doi.org/10.1016/j.actamat.2016.12.027.

[52] C.M. Cepeda-Jiménez, F. Potenza, E. Magalini, V. Luchin, A. Molinari, M.T. Pérez-Prado, Effect of energy density on the microstructure and texture evolution of Ti-6Al-4V manufactured by laser powder bed fusion, Mater. Charact. 163 (2020) 110238. https://doi.org/10.1016/j.matchar.2020.110238.

[53] R. Zhao, C. Chen, W. Wang, T. Cao, S. Shuai, S. Xu, T. Hu, H. Liao, J. Wang, Z. Ren, On the role of volumetric energy density in the microstructure and mechanical properties of laser powder bed fusion Ti-6Al-4V alloy, Addit. Manuf. 51 (2022) 102605. https://doi.org/10.1016/j.addma.2022.102605.

[54] M. Simonelli, Y.Y. Tse, C. Tuck, The formation of α + β microstructure in as-fabricated selective laser melting of Ti–6Al–4V, J. Mater. Res. 29 (2014) 2028–2035. https://doi.org/10.1557/jmr.2014.166.

[55] T. Larimian, M. Kannan, D. Grzesiak, B. AlMangour, T. Borkar, Effect of energy density and scanning strategy on densification, microstructure and mechanical properties of 316L stainless steel processed via selective laser melting, Materials Science and Engineering: A 770 (2020) 138455. https://doi.org/10.1016/j.msea.2019.138455.

[56] D.S. Watring, J.T. Benzing, N. Hrabe, A.D. Spear, Effects of laser-energy density and build orientation on the structure–property relationships in as-built Inconel 718 manufactured by laser powder bed fusion, Addit. Manuf. 36 (2020) 101425. https://doi.org/10.1016/j.addma.2020.101425.

[57] M. Thomas, G.J. Baxter, I. Todd, Normalised model-based processing diagrams for additive layer manufacture of engineering alloys, Acta Mater. 108 (2016) 26–35. https://doi.org/10.1016/j.actamat.2016.02.025.

[58] B. Fields, M. Amiri, J. Lim, J.T. Pürstl, M.R. Begley, D. Apelian, L. Valdevit, Microstructural Control of a Multi-Phase PH Steel Printed with Laser Powder Bed Fusion, Adv. Mater. Technol. (2024). https://doi.org/10.1002/admt.202301037.

[59] A. Safdar, L.-Y. Wei, A. Snis, Z. Lai, Evaluation of microstructural development in electron beam melted Ti-6Al-4V, Mater. Charact. 65 (2012) 8–15. https://doi.org/10.1016/j.matchar.2011.12.008.

[60] H. Galarraga, R.J. Warren, D.A. Lados, R.R. Dehoff, M.M. Kirka, Fatigue crack growth mechanisms at the microstructure scale in as-fabricated and heat treated Ti-6Al-4V ELI manufactured by electron beam melting (EBM), Eng. Fract. Mech. 176 (2017) 263–280. https://doi.org/10.1016/j.engfracmech.2017.03.024.

[61] B. Wysocki, P. Maj, R. Sitek, J. Buhagiar, K. Kurzydłowski, W. Święszkowski, Laser and Electron Beam Additive Manufacturing Methods of Fabricating Titanium Bone Implants, Appl. Sci. 7 (2017) 657. https://doi.org/10.3390/app7070657.

[62] M. Hao, L. Zhang, B. Zhou, H. Li, M. Li, F. Lin, Performance of Ti6Al4V fabricated by electron beam and laser hybrid preheating and selective melting strategy, China Foundry 18 (2021) 351–359. https://doi.org/10.1007/s41230-021-1039-1.

[63] E. Santecchia, S. Spigarelli, M. Cabibbo, Material Reuse in Laser Powder Bed Fusion: Side Effects of the Laser—Metal Powder Interaction, Metals 10 (2020) 341. https://doi.org/10.3390/met10030341.

[64] Y. Zhang, L. Wu, X. Guo, S. Kane, Y. Deng, Y.G. Jung, J.H. Lee, J. Zhang, Additive Manufacturing of Metallic Materials: A Review, Journal of Materials Engineering and Performance 27 (2018). https://doi.org/10.1007/s11665-017-2747-y.

[65] S. Liu, Y.C. Shin, Additive manufacturing of Ti6Al4V alloy: A review, Materials & Design 164 (2019) 107552. https://doi.org/10.1016/j.matdes.2018.107552.

[66] S.-K. Rittinghaus, V.R.M. Ramirez, A. Vogelpoth, U. Hecht, J. Schmelzer, Laser based manufacturing of titanium aluminides, MATEC Web of Conferences 321 (2020) 08001. https://doi.org/10.1051/matecconf/202032108001.

[67] P. Ibrahim, R. Garrard, M.M. Attallah, Laser Powder Bed Fusion of a β Titanium Alloy: Microstructural Development, Post-Processing, and Mechanical Behaviour, Mater. Sci. Eng.: A (2024) 146617. https://doi.org/10.1016/j.msea.2024.146617.

[68] S. Cao, Y. Zou, C.V.S. Lim, X. Wu, Review of laser powder bed fusion (LPBF) fabricated Ti-6Al-4V: process, post-process treatment, microstructure, and property, Light: Adv. Manuf. 2 (2021) 1. https://doi.org/10.37188/lam.2021.020.

[69] H.M. Khan, Y. Karabulut, O. Kitay, Y. Kaynak, I.S. Jawahir, Influence of the post-processing operations on surface integrity of metal components produced by laser powder bed fusion additive manufacturing: a review, Mach. Sci. Technol. 25 (2020) 118–176. https://doi.org/10.1080/10910344.2020.1855649.

[70] A.M. Khorasani, I. Gibson, A. Ghasemi, A. Ghaderi, Modelling of laser powder bed fusion process and analysing the effective parameters on surface characteristics of Ti-6Al-4V, Int. J. Mech. Sci. 168 (2020) 105299. https://doi.org/10.1016/j.ijmecsci.2019.105299.

[71] F. Ahmed, U. Ali, D. Sarker, E. Marzbanrad, K. Choi, Y. Mahmoodkhani, E. Toyserkani, Study of powder recycling and its effect on printed parts during laser powder-bed fusion of 17-4 PH stainless steel, J. Mater. Process. Technol. 278 (2020) 116522. https://doi.org/10.1016/j.jmatprotec.2019.116522.

[72] Q. Wu, C. Qiao, Y. Wu, Z. Liu, X. Li, J. Wang, X. An, A. Huang, C.V.S. Lim, Numerical investigation on the reuse of recycled powders in powder bed fusion additive manufacturing, Addit. Manuf. 77 (2023) 103821. https://doi.org/10.1016/j.addma.2023.103821.

[73] G. Rasiya, A. Shukla, K. Saran, Additive Manufacturing-A Review, Mater. Today: Proc. 47 (2021) 6896–6901. https://doi.org/10.1016/j.matpr.2021.05.181.

[74] J. Nandy, H. Sarangi, S. Sahoo, A Review on Direct Metal Laser Sintering: Process Features and Microstructure Modeling, Lasers Manuf. Mater. Process. 6 (2019) 280–316. https://doi.org/10.1007/s40516-019-00094-y.

[75] C. Zhang, F. Chen, Z. Huang, M. Jia, G. Chen, Y. Ye, Y. Lin, W. Liu, B. Chen, Q. Shen, L. Zhang, E.J. Lavernia, Additive manufacturing of functionally graded materials: A review, Mater. Sci. Eng.: A 764 (2019) 138209. https://doi.org/10.1016/j.msea.2019.138209.

[76] A. Gisario, M. Kazarian, F. Martina, M. Mehrpouya, Metal additive manufacturing in the commercial aviation industry: A review, Journal of Manufacturing Systems 53 (2019) 124–149. https://doi.org/10.1016/j.jmsy.2019.08.005.

[77] J.L. Bartlett, X. Li, An overview of residual stresses in metal powder bed fusion, Addit. Manuf. 27 (2019) 131–149. https://doi.org/10.1016/j.addma.2019.02.020.

[78] Y. Liu, Y. Yang, D. Wang, A study on the residual stress during selective laser melting (SLM) of metallic powder, The International Journal of Advanced Manufacturing Technology 87 (2016) 647–656. https://doi.org/10.1007/s00170-016-8466-y.

[79] E. Yasa, J. Deckers, J.-P. Kruth, M. Rombouts, J. Luyten, Part and material properties in selective laser melting of metals, 2010. https://www.researchgate.net/publication/266036449.

[80] M.J. Matthews, T.T. Roehling, S.A. Khairallah, T.U. Tumkur, G. Guss, R. Shi, J.D. Roehling, W.L. Smith, B.K. Vrancken, R.K. Ganeriwala, J.T. McKeown, Controlling melt pool shape, microstructure and residual stress in additively manufactured metals using modified laser beam profiles, Procedia CIRP 94 (2020) 200–204. https://doi.org/10.1016/j.procir.2020.09.038.

[81] I. Gibson, D. Rosen, B. Stucker, M. Khorasani, Additive Manufacturing Technologies, (2020) 555–607. https://doi.org/10.1007/978-3-030-56127-7_19.

[82] T. Maconachie, M. Leary, B. Lozanovski, X. Zhang, M. Qian, O. Faruque, M. Brandt, SLM lattice structures: Properties, performance, applications and challenges, Materials and Design 183 (2019). https://doi.org/10.1016/j.matdes.2019.108137.

[83] N. Shahrubudin, T.C. Lee, R. Ramlan, An Overview on 3D Printing Technology: Technological, Materials, and Applications, Procedia Manuf. 35 (2019) 1286–1296. https://doi.org/10.1016/j.promfg.2019.06.089.

[84] T. Hanemann, L.N. Carter, M. Habschied, N.J.E. Adkins, M.M. Attallah, M. Heilmaier, In-situ alloying of AlSi10Mg+Si using Selective Laser Melting to control the coefficient of thermal expansion, Journal of Alloys and Compounds 795 (2019) 8–18. https://doi.org/10.1016/j.jallcom.2019.04.260.

[85] K. SHAH, LASER DIRECT METAL DEPOSITION OF DISSIMILAR AND FUNCTIONALLY GRADED ALLOYS, The University of Manchester, 2011.

[86] F. Silze, M. Schnick, I. Sizova, M. Bambach, Laser Metal Deposition of Ti-6Al-4V with a Direct Diode Laser Set-up and Coaxial Material Feed, Procedia Manufacturing 47 (2020) 1154–1158. https://doi.org/10.1016/j.promfg.2020.04.156.

[87] E.O. Olakanmi, R.F. Cochrane, K.W. Dalgarno, A review on selective laser sintering/melting (SLS/SLM) of aluminium alloy powders: Processing, microstructure, and properties, Progress in Materials Science 74 (2015) 401–477. https://doi.org/10.1016/j.pmatsci.2015.03.002.

[88] L.C. Capozzi, A. Sivo, E. Bassini, Powder spreading and spreadability in the additive manufacturing of metallic materials: A critical review, J. Mater. Process. Technol. 308 (2022) 117706. https://doi.org/10.1016/j.jmatprotec.2022.117706.

[89] Selective laser melting (SLM) 3D Printing Service, SLM Diagram, (n.d.). https://www.pcbway.com/rapid-prototyping/3D-Printing/3D-Printing-SLM.html (accessed January 22, 2024).

[90] H. Jia, H. Sun, H. Wang, Y. Wu, H. Wang, Scanning strategy in selective laser melting (SLM): a review, Int. J. Adv. Manuf. Technol. 113 (2021) 2413–2435. https://doi.org/10.1007/s00170-021-06810-3.

[91] A.J. Pinkerton, [INVITED] Lasers in additive manufacturing, Opt. Laser Technol. 78 (2016) 25–32. https://doi.org/10.1016/j.optlastec.2015.09.025.

[92] X. Ni, D. Kong, W. Wu, L. Zhang, C. Dong, B. He, L. Lu, K. Wu, D. Zhu, Corrosion Behavior of 316L Stainless Steel Fabricated by Selective Laser Melting Under Different Scanning Speeds, J. Mater. Eng. Perform. 27 (2018) 3667–3677. https://doi.org/10.1007/s11665-018-3446-z.

[93] D. Wang, L. Liu, G. Deng, C. Deng, Y. Bai, Y. Yang, W. Wu, J. Chen, Y. Liu, Y. Wang, X. Lin, C. Han, Recent progress on additive manufacturing of multi-material structures with laser powder bed fusion, Virtual Phys. Prototyp. 17 (2022) 329–365. https://doi.org/10.1080/17452759.2022.2028343.

[94] G. Gong, J. Ye, Y. Chi, Z. Zhao, Z. Wang, G. Xia, X. Du, H. Tian, H. Yu, C. Chen, Research status of laser additive manufacturing for metal: a review, J. Mater. Res. Technol. 15 (2021) 855–884. https://doi.org/10.1016/j.jmrt.2021.08.050.

[95] J. Gong, K. Wei, M. Liu, W. Song, X. Li, X. Zeng, Microstructure and mechanical properties of AlSi10Mg alloy built by laser powder bed fusion/direct energy deposition hybrid laser additive manufacturing, Addit. Manuf. 59 (2022) 103160. https://doi.org/10.1016/j.addma.2022.103160.

[96] A. Jiménez, P. Bidare, H. Hassanin, F. Tarlochan, S. Dimov, K. Essa, Powder-based laser hybrid additive manufacturing of metals: a review, The International Journal of Advanced Manufacturing Technology 114 (2021) 63–96. https://doi.org/10.1007/s00170-021-06855-4.

[97] J. Yan, Y. Zhou, R. Gu, X. Zhang, W.-M. Quach, M. Yan, A Comprehensive Study of Steel Powders (316L, H13, P20 and 18Ni300) for Their Selective Laser Melting Additive Manufacturing, Metals 9 (2019) 86. https://doi.org/10.3390/met9010086.

[98] H.K. Rafi, T.L. Starr, B.E. Stucker, A comparison of the tensile, fatigue, and fracture behavior of Ti–6Al–4V and 15-5 PH stainless steel parts made by selective laser melting, Int. J. Adv. Manuf. Technol. 69 (2013) 1299–1309. https://doi.org/10.1007/s00170-013-5106-7.

[99] J. Zhang, B. Song, Q. Wei, D. Bourell, Y. Shi, A review of selective laser melting of aluminum alloys: Processing, microstructure, property and developing trends, Journal of Materials Science and Technology 35 (2019) 270–284. https://doi.org/10.1016/j.jmst.2018.09.004.

[100] J. Metelkova, D. Ordnung, Y. Kinds, A. Witvrouw, B.V. Hooreweder, Improving the quality of up-facing inclined surfaces in laser powder bed fusion of metals using a dual laser setup, Procedia CIRP 94 (2020) 266–269. https://doi.org/10.1016/j.procir.2020.09.050.

[101] T. Heeling, K. Wegener, The effect of multi-beam strategies on selective laser melting of stainless steel 316L, Addit. Manuf. 22 (2018) 334–342. https://doi.org/10.1016/j.addma.2018.05.026.

[102] C.-Y. Tsai, C.-W. Cheng, A.-C. Lee, M.-C. Tsai, Synchronized multi-spot scanning strategies for the laser powder bed fusion process, Addit. Manuf. 27 (2019) 1–7. https://doi.org/10.1016/j.addma.2019.02.009.

[103] C. Zhang, H. Zhu, Z. Hu, L. Zhang, X. Zeng, A comparative study on single-laser and multi-laser selective laser melting AlSi10Mg: defects, microstructure and mechanical properties, Mater. Sci. Eng.: A 746 (2019) 416–423. https://doi.org/10.1016/j.msea.2019.01.024.

[104] K. Wei, F. Li, G. Huang, M. Liu, J. Deng, C. He, X. Zeng, Multi-laser powder bed fusion of Ti–6Al–4V alloy: Defect, microstructure, and mechanical property of overlap region, Mater. Sci. Eng.: A 802 (2021) 140644. https://doi.org/10.1016/j.msea.2020.140644.

[105] J. Yin, D. Wang, H. Wei, L. Yang, L. Ke, M. Hu, W. Xiong, G. Wang, H. Zhu, X. Zeng, Dual-beam laser-matter interaction at overlap region during multi-laser powder bed

fusion manufacturing, (2021). https://reader.elsevier.com/reader/sd/pii/S2214860421003419?token=1A9298B79CE6E0134BC4F7C7C79B6C5FC7EF559DB49FD25ECFB29C7A03BB0E6AC8EC7D6A1E08E78DC60E6D28B56C163A&originRegion=eu-west-1&originCreation=20210714131811.

[106] F. Li, Z. Wang, X. Zeng, Microstructures and mechanical properties of Ti6Al4V alloy fabricated by multi-laser beam selective laser melting, Mater. Lett. 199 (2017) 79–83. https://doi.org/10.1016/j.matlet.2017.04.050.

[107] W. Zhang, M. Tong, N.M. Harrison, Scanning strategies effect on temperature, residual stress and deformation by multi-laser beam powder bed fusion manufacturing, Addit. Manuf. 36 (2020) 101507. https://doi.org/10.1016/j.addma.2020.101507.

[108] Z. Liu, Y. Yang, C. Song, H. Zhou, Z. Chen, Z. Liu, R. Jiang, Z. Zhou, D. Wang, The surface quality, microstructure and properties of SS316L using a variable area scan strategy during quad-laser large-scale powder bed fusion, Mater. Sci. Eng.: A 871 (2023) 144450. https://doi.org/10.1016/j.msea.2022.144450.

[109] P. Mishra, T. Ilar, F. Brueckner, A. Kaplan, Energy efficiency contributions and losses during selective laser melting, J. Laser Appl. 30 (2018) 032304. https://doi.org/10.2351/1.5040603.

[110] N.H. Paulson, B. Gould, S.J. Wolff, M. Stan, A.C. Greco, Correlations between thermal history and keyhole porosity in laser powder bed fusion, Additive Manufacturing 34 (2020). https://doi.org/10.1016/j.addma.2020.101213.

[111] R. Li, J. Liu, Y. Shi, L. Wang, W. Jiang, Balling behavior of stainless steel and nickel powder during selective laser melting process, The International Journal of Advanced Manufacturing Technology 59 (2012) 1025–1035. https://doi.org/10.1007/s00170-011-3566-1.

[112] L. Nastac, 3D Modeling of the Solidification Structure Evolution and of the Inter Layer/Track Voids Formation in Metallic Alloys Processed by Powder Bed Fusion Additive Manufacturing, Materials 15 (2022) 8885. https://doi.org/10.3390/ma15248885.

[113] J. Volpp, Behavior of powder particles on melt pool surfaces, International Journal of Advanced Manufacturing Technology 102 (2019) 2201–2210. https://doi.org/10.1007/s00170-018-03261-1.

[114] T. Zhang, H. Li, S. Liu, S. Shen, H. Xie, W. Shi, G. Zhang, B. Shen, L. Chen, B. Xiao, M. Wei, Evolution of molten pool during selective laser melting of Ti–6Al–4V, J. Phys. D: Appl. Phys. 52 (2018) 055302. https://doi.org/10.1088/1361-6463/aaee04.

[115] R.W. McVey, R.M. Melnychuk, J.A. Todd, R.P. Martukanitz, Absorption of laser irradiation in a porous powder layer, J. Laser Appl. 19 (2007) 214–224. https://doi.org/10.2351/1.2756854.

[116] M. Alsaddah, Multi-laser powder bed fusion using 808 nm sources, The University of Sheffield, 2018.

[117] J.H. Karp, V. Ostroverkhov, D. Bogdan, M. Graham, B. Mccarthy, W. Carter, Area melting with multi-laser arrays to increase build rate for metal powder bed fusion additive manufacturing, in: SPIE, 2019: p. 8. https://doi.org/10.1117/12.2513892.

[118] A.T. Payne, Multiple beam laser diode additive manufacturing for metal parts, University of Cambridge, 2017.

[119] Y. Nakatsu, Y. Nagao, T. Hirao, K. Kozuru, T. Kanazawa, S. Masui, E. Okahisa, T. Yanamoto, S. Nagahama, Edge-emitting blue laser diode with high CW wall-plug efficiency of 50 %, Gallium Nitride Mater. Devices XVII 12001 (2022) 1200109-1200109–6. https://doi.org/10.1117/12.2601154.

[120] M. Baumann, A. Balck, J. Malchus, R.V. Chacko, S. Marfels, U. Witte, D. Dinakaran, S. Ocylok, M. Weinbach, C. Bachert, A. Kösters, V. Krause, H. König, A. Lell, B. Stojetz, M. Ali, U. Strauss, 1000 W blue fiber-coupled diode-laser emitting at 450 nm, in: SPIE, 2019: p. 3. https://doi.org/10.1117/12.2511255.

[121] K. Kellens, E. Yasa, Renaldi, W. Dewulf, J.P. Kruth, J.R. Duflou, Energy and Resource Efficiency of SLS/SLM Processes, in: University of Texas at Austin, 2017. https://doi.org/10.26153/tsw/15272.

[122] E. Yasa, T. Craeghs, J. Kruth, SELECTIVE LASER SINTERING/MELTING AND SELECTIVE LASER EROSION WITH ND:YAG LASERS, Journal of Optics Research 14 (2005) 211–273. https://www.proquest.com/scholarly-journals/selective-laser-sintering-melting-erosion-with-nd/docview/1701611326/se-2.

[123] S.N. Grigoriev, A.V. Gusarov, A.S. Metel, T.V. Tarasova, M.A. Volosova, A.A. Okunkova, A.S. Gusev, Beam Shaping in Laser Powder Bed Fusion: Péclet Number and Dynamic Simulation, Metals 12 (2022) 722. https://doi.org/10.3390/met12050722.

[124] L. Caprio, A.G. Demir, B. Previtali, Comparative study between CW and PW emissions in selective laser melting, J. Laser Appl. 30 (2018) 032305. https://doi.org/10.2351/1.5040631.

[125] K. Karami, A. Blok, L. Weber, S.M. Ahmadi, R. Petrov, K. Nikolic, E.V. Borisov, S. Leeflang, C. Ayas, A.A. Zadpoor, M. Mehdipour, E. Reinton, V.A. Popovich, Continuous and pulsed selective laser melting of Ti6Al4V lattice structures: Effect of post-processing on microstructural anisotropy and fatigue behaviour, Addit. Manuf. 36 (2020) 101433. https://doi.org/10.1016/j.addma.2020.101433.

[126] P.S. Cook, D.J. Ritchie, Determining the laser absorptivity of Ti-6Al-4V during laser powder bed fusion by calibrated melt pool simulation, Opt. Laser Technol. 162 (2023) 109247. https://doi.org/10.1016/j.optlastec.2023.109247.

[127] L. für Lasertechnik, Beam parameter product and beam quality, (2016). https://www.youtube.com/watch?v=WB6S5qqhSUc (accessed January 23, 2024).

[128] R. Paschotta, Beam Quality Factor, (n.d.). https://doi.org/10.61835/zxz.

[129] P.J. Shayler, Laser beam distribution in the focal region, Appl. Opt. 17 (1978) 2673. https://doi.org/10.1364/ao.17.002673.

[130] Laser Beam Profiles | Laserglow, (n.d.). https://www.laserglow.com/content/Laser-Beam-Profiles (accessed January 23, 2024).

[131] J. Niu, J. Xu, Coupling efficiency of laser beam to multimode fiber, Opt. Commun. 274 (2007) 315–319. https://doi.org/10.1016/j.optcom.2007.02.027.

[132] The beginner's guide on spot size of laser beam, (n.d.). https://www.gentec-eo.com/blog/spot-size-of-laser-beam (accessed January 23, 2024).

[133] H. Lee, C.H.J. Lim, M.J. Low, N. Tham, V.M. Murukeshan, Y.J. Kim, Lasers in additive manufacturing: A review, International Journal of Precision Engineering and Manufacturing - Green Technology 4 (2017) 307–322. https://doi.org/10.1007/s40684-017-0037-7.

[134] G. Shen, M.L. Rivers, Y. Wang, S.R. Sutton, Laser heated diamond cell system at the Advanced Photon Source for in situ x-ray measurements at high pressure and temperature, Rev. Sci. Instrum. 72 (2001) 1273–1282. https://doi.org/10.1063/1.1343867.

[135] J.D. Majumdar, I. Manna, Laser material processing, Int. Mater. Rev. 56 (2011) 341–388. https://doi.org/10.1179/1743280411y.0000000003.

[136] L. Mugwagwa, D. Dimitrov, S. Matope, I. Yadroitsev, Evaluation of the impact of scanning strategies on residual stresses in selective laser melting, Int. J. Adv. Manuf. Technol. 102 (2019) 2441–2450. https://doi.org/10.1007/s00170-019-03396-9.

[137] P.A. Bélanger, Beam propagation and the ABCD ray matrices, Opt. Lett. 16 (1991) 196. https://doi.org/10.1364/ol.16.000196.

[138] Beam radius, explained by RP; laser beam, diameter, second moment, ISO Standard 11146, (n.d.). https://www.rp-photonics.com/beam_radius.html (accessed January 23, 2024).

[139] J. Bi, L. Wu, S. Li, Z. Yang, X. Jia, M.D. Starostenkov, G. Dong, Beam shaping technology and its application in metal laser additive manufacturing: A review, J. Mater. Res. Technol. 26 (2023) 4606–4628. https://doi.org/10.1016/j.jmrt.2023.08.037.

[140] L. Parry, I.A. Ashcroft, R.D. Wildman, Understanding the effect of laser scan strategy on residual stress in selective laser melting through thermo-mechanical simulation, Addit. Manuf. 12 (2016) 1–15. https://doi.org/10.1016/j.addma.2016.05.014.

[141] B. Cheng, S. Shrestha, K. Chou, Stress and deformation evaluations of scanning strategy effect in selective laser melting, Additive Manufacturing 12 (2016) 240–251. https://doi.org/10.1016/j.addma.2016.05.007.

[142] J. Han, M. Wu, Y. Ge, J. Wu, Optimizing the structure accuracy by changing the scanning strategy using selective laser melting, Int. J. Adv. Manuf. Technol. 95 (2018) 4439–4447. https://doi.org/10.1007/s00170-017-1503-7.

[143] R. Stamp, P. Fox, W. O'Neill, E. Jones, C. Sutcliffe, The development of a scanning strategy for the manufacture of porous biomaterials by selective laser melting, J. Mater. Sci.: Mater. Med. 20 (2009) 1839. https://doi.org/10.1007/s10856-009-3763-8.

[144] S. Waqar, K. Guo, J. Sun, Evolution of residual stress behavior in selective laser melting (SLM) of 316L stainless steel through preheating and in-situ re-scanning techniques, Opt. Laser Technol. 149 (2022) 107806. https://doi.org/10.1016/j.optlastec.2021.107806.

[145] Z. Xiao, C. Chen, Z. Hu, H. Zhu, X. Zeng, Effect of rescanning cycles on the characteristics of selective laser melting of Ti6Al4V, Opt. Laser Technol. 122 (2020) 105890. https://doi.org/10.1016/j.optlastec.2019.105890.

[146] S. Zou, H. Xiao, F. Ye, Z. Li, W. Tang, F. Zhu, C. Chen, C. Zhu, Numerical analysis of the effect of the scan strategy on the residual stress in the multi-laser selective laser melting, Results in Physics 16 (2020) 103005. https://doi.org/10.1016/j.rinp.2020.103005.

[147] A. Liang, K.S. Pey, T. Polcar, A.R. Hamilton, Effects of rescanning parameters on densification and microstructural refinement of 316L stainless steel fabricated by laser powder bed fusion, J. Mater. Process. Technol. 302 (2022) 117493. https://doi.org/10.1016/j.jmatprotec.2022.117493.

[148] E. Malekipour, H. El-Mounayri, Scanning Strategies in the PBF Process: A Critical Review, Vol. 2A: Adv. Manuf. (2020). https://doi.org/10.1115/imece2020-24589.

[149] S. Griffiths, M.D. Rossell, J. Croteau, N.Q. Vo, D.C. Dunand, C. Leinenbach, Effect of laser rescanning on the grain microstructure of a selective laser melted Al-Mg-Zr alloy, Mater. Charact. 143 (2018) 34–42. https://doi.org/10.1016/j.matchar.2018.03.033.

[150] H. Sheng, Y. Yee Wai, Laser re-scanning strategy in selective laser melting for part quality enhancement : a review, (2018). https://doi.org/10.25341/d4gp4j.

[151] X.-J. Shen, C. Zhang, Y.-G. Yang, L. Liu, On the microstructure, mechanical properties and wear resistance of an additively manufactured Ti64/metallic glass composite, Addit. Manuf. 25 (2019) 499–510. https://doi.org/10.1016/j.addma.2018.12.006.

[152] M. Arredondo, Diode Area Melting Use of High Power Diode Lasers in Additive Manufacturing of Metallic Components, The University of Sheffield, 2017.

[153] S. Vock, B. Klöden, A. Kirchner, T. Weißgärber, B. Kieback, Powders for powder bed fusion: a review, Progress in Additive Manufacturing 4 (2019) 383–397. https://doi.org/10.1007/s40964-019-00078-6.

[154] A. Nouri, A. Sola, Metal particle shape: A practical perspective, Met. Powder Rep. 73 (2018) 276–282. https://doi.org/10.1016/j.mprp.2018.04.001.

[155] C. Vakifahmetoglu, B. Hasdemir, L. Biasetto, Spreadability of Metal Powders for Laser-Powder Bed Fusion via Simple Image Processing Steps, Materials 15 (2021) 205. https://doi.org/10.3390/ma15010205.

[156] L. Cordova, T. Bor, M. de Smit, M. Campos, T. Tinga, Measuring the spreadability of pre-treated and moisturized powders for laser powder bed fusion, Addit. Manuf. 32 (2020) 101082. https://doi.org/10.1016/j.addma.2020.101082.

[157] C.N. Hulme, P. Mellin, L. Marchetti, V. Hari, M. Uhlirsch, E. Strandh, K. Saeidi, S.D.-L. Goff, S. Saleem, V. Pettersson, A. Memarpour, K. Jakobsson, F. Meurling, A practicable and reliable test for metal powder spreadability: development of test and analysis technique, Prog. Addit. Manuf. 8 (2023) 505–517. https://doi.org/10.1007/s40964-022-00341-3.

[158] A. Mussatto, R. Groarke, A. O'Neill, M.A. Obeidi, Y. Delaure, D. Brabazon, Influences of powder morphology and spreading parameters on the powder bed topography uniformity in powder bed fusion metal additive manufacturing, Addit. Manuf. 38 (2021) 101807. https://doi.org/10.1016/j.addma.2020.101807.

[159] A.Y.M. Alfaify, The Effect of Changing Particle Size Distribution and Layer Thickness on the Density of Parts Manufactured Using the Laser Powder Bed Fusion Process, 2019.

[160] L. Avramović, V.M. Maksimović, Z. Baščarević, N. Ignjatović, M. Bugarin, R. Marković, N.D. Nikolić, Influence of the Shape of Copper Powder Particles on the Crystal Structure and Some Decisive Characteristics of the Metal Powders, Metals 9 (2019) 56. https://doi.org/10.3390/met9010056.

[161] B. Lane, E. Whitenton, S. Moylan, Multiple sensor detection of process phenomena in laser powder bed fusion, Thermosense: Therm. Infrared Appl. XXXVIII 986104 (2016) 986104-986104–9. https://doi.org/10.1117/12.2224390.

[162] M.A. Balbaa, A. Ghasemi, E. Fereiduni, M.A. Elbestawi, S.D. Jadhav, J.-P. Kruth, Role of powder particle size on laser powder bed fusion processability of AlSi10mg alloy, Addit. Manuf. 37 (2021) 101630. https://doi.org/10.1016/j.addma.2020.101630.

[163] M.J. Heiden, L.A. Deibler, J.M. Rodelas, J.R. Koepke, D.J. Tung, D.J. Saiz, B.H. Jared, Evolution of 316L stainless steel feedstock due to laser powder bed fusion process, Addit. Manuf. 25 (2019) 84–103. https://doi.org/10.1016/j.addma.2018.10.019.

[164] S.E. Brika, M. Letenneur, C.A. Dion, V. Brailovski, Influence of particle morphology and size distribution on the powder flowability and laser powder bed fusion manufacturability of Ti-6Al-4V alloy, Addit. Manuf. 31 (2020) 100929. https://doi.org/10.1016/j.addma.2019.100929.

[165] J.D. Roehling, W.L. Smith, T.T. Roehling, B. Vrancken, G.M. Guss, J.T. McKeown, M.R. Hill, M.J. Matthews, Reducing residual stress by selective large-area diode surface heating during laser powder bed fusion additive manufacturing, Additive Manufacturing 28 (2019) 228–235. https://doi.org/10.1016/j.addma.2019.05.009.

[166] Y. Tang, Y.F. Zhao, A survey of the design methods for additive manufacturing to improve functional performance, Rapid Prototyping Journal 22 (2016) 569–590. https://doi.org/10.1108/rpj-01-2015-0011.

[167] A. Pathania, A.K. Subramaniyan, B.K. Nagesha, Influence of post-heat treatments on microstructural and mechanical properties of LPBF-processed Ti6Al4V alloy, Prog. Addit. Manuf. 7 (2022) 1323–1343. https://doi.org/10.1007/s40964-022-00306-6.

[168] B. Song, S. Dong, B. Zhang, H. Liao, C. Coddet, Effects of processing parameters on microstructure and mechanical property of selective laser melted Ti6Al4V, Mater. Des. 35 (2012) 120–125. https://doi.org/10.1016/j.matdes.2011.09.051.

[169] O. Homburg, T. Mitra, Gaussian-to-top-hat beam shaping: an overview of parameters, methods, and applications, in: 2012: p. 82360A. https://doi.org/10.1117/12.907914.

[170] A. du Plessis, Effects of process parameters on porosity in laser powder bed fusion revealed by X-ray tomography, Addit. Manuf. 30 (2019) 100871. https://doi.org/10.1016/j.addma.2019.100871.

[171] Q. Guo, C. Zhao, M. Qu, L. Xiong, L.I. Escano, S.M.H. Hojjatzadeh, N.D. Parab, K. Fezzaa, W. Everhart, T. Sun, L. Chen, In-situ characterization and quantification of melt pool variation under constant input energy density in laser powder bed fusion additive manufacturing process, Addit. Manuf. 28 (2019) 600–609. https://doi.org/10.1016/j.addma.2019.04.021.

[172] L. Tonelli, A. Fortunato, L. Ceschini, CoCr alloy processed by Selective Laser Melting (SLM): effect of Laser Energy Density on microstructure, surface morphology, and hardness, Journal of Manufacturing Processes 52 (2020) 106–119. https://doi.org/10.1016/j.jmapro.2020.01.052.

[173] U.S. Bertoli, A.J. Wolfer, M.J. Matthews, J.-P.R. Delplanque, J.M. Schoenung, On the limitations of Volumetric Energy Density as a design parameter for Selective Laser Melting, Mater. Des. 113 (2017) 331–340. https://doi.org/10.1016/j.matdes.2016.10.037.

[174] M.A. Buhairi, F.M. Foudzi, F.I. Jamhari, A.B. Sulong, N.A.M. Radzuan, N. Muhamad, I.F. Mohamed, A.H. Azman, W.S.W. Harun, M.S.H. Al-Furjan, Review on volumetric energy density: influence on morphology and mechanical properties of Ti6Al4V manufactured via laser powder bed fusion, Prog. Addit. Manuf. 8 (2023) 265–283. https://doi.org/10.1007/s40964-022-00328-0.

[175] C. Körner, E. Attar, P. Heinl, Mesoscopic simulation of selective beam melting processes, Journal of Materials Processing Technology 211 (2011) 978–987. https://doi.org/10.1016/j.jmatprotec.2010.12.016.

[176] A. Rubenchik, S. Wu, S. Mitchell, I. Golosker, M. LeBlanc, N. Peterson, Direct measurements of temperature-dependent laser absorptivity of metal powders, Appl. Opt. 54 (2015) 7230. https://doi.org/10.1364/ao.54.007230.

[177] R. Indhu, V. Vivek, L. Sarathkumar, A. Bharatish, S. Soundarapandian, Overview of Laser Absorptivity Measurement Techniques for Material Processing, Lasers Manuf. Mater. Process. 5 (2018) 458–481. https://doi.org/10.1007/s40516-018-0075-1.

[178] M.L. Bortz, R.H. French, Optical reflectivity measurements using a laser plasma light source, Appl. Phys. Lett. 55 (1989) 1955–1957. https://doi.org/10.1063/1.102335.

[179] J. Trapp, A.M. Rubenchik, G. Guss, M.J. Matthews, In situ absorptivity measurements of metallic powders during laser powder-bed fusion additive manufacturing, Appl. Mater. Today 9 (2017) 341–349. https://doi.org/10.1016/j.apmt.2017.08.006.

[180] L. Lazov, N. Angelov, PHYSICAL MODEL ABOUT LASER IMPACT ON METALS AND ALLOYS, Contemp. Mater. 1 (2010) 124–128. https://doi.org/10.5767/anurs.cmat.100102.en.124l.

[181] A.D. Nikolov, D.T. Wasan, A. Chengara, K. Koczo, G.A. Policello, I. Kolossvary, Superspreading driven by Marangoni flow, Adv. Colloid Interface Sci. 96 (2002) 325–338. https://doi.org/10.1016/s0001-8686(01)00087-2.

[182] F. Wirth, T. Tonn, M. Schöberl, S. Hermann, H. Birkhofer, V. Ploshikhin, Implementation of the Marangoni effect in an open-source software environment and the influence of surface tension modeling in the mushy region in laser powder bed fusion (LPBF), Model. Simul. Mater. Sci. Eng. 30 (2022) 034001. https://doi.org/10.1088/1361-651x/ac4a26.

[183] H. Yin, T. Emi, Marangoni flow at the gas/melt interface of steel, Met. Mater. Trans. B 34 (2003) 483–493. https://doi.org/10.1007/s11663-003-0015-z.

[184] C. Qiu, C. Panwisawas, M. Ward, H.C. Basoalto, J.W. Brooks, M.M. Attallah, On the role of melt flow into the surface structure and porosity development during selective laser melting, Acta Mater. 96 (2015) 72–79. https://doi.org/10.1016/j.actamat.2015.06.004.

[185] Q. Guo, C. Zhao, M. Qu, L. Xiong, S.M.H. Hojjatzadeh, L.I. Escano, N.D. Parab, K. Fezzaa, T. Sun, L. Chen, In-situ full-field mapping of melt flow dynamics in laser metal additive manufacturing, Additive Manufacturing 31 (2020) 100939. https://doi.org/10.1016/j.addma.2019.100939.

[186] D. Gu, Y. Shen, Balling phenomena in direct laser sintering of stainless steel powder: Metallurgical mechanisms and control methods, Mater. Des. 30 (2009) 2903–2910. https://doi.org/10.1016/j.matdes.2009.01.013.

[187] X. Zhou, X. Liu, D. Zhang, Z. Shen, W. Liu, Balling phenomena in selective laser melted tungsten, J. Mater. Process. Technol. 222 (2015) 33–42. https://doi.org/10.1016/j.jmatprotec.2015.02.032.

[188] C. Qiu, N.J.E. Adkins, M.M. Attallah, Microstructure and tensile properties of selectively laser-melted and of HIPed laser-melted Ti–6Al–4V, Mater. Sci. Eng.: A 578 (2013) 230–239. https://doi.org/10.1016/j.msea.2013.04.099.

[189] Y. Yuan, T.R. Lee, Contact Angle and Wetting Properties, in: Springer Series in Surface Sciences, Springer, Berlin, Heidelberg, 2013: pp. 3–34. https://doi.org/10.1007/978-3-642-34243-1_1.

[190] W.T. Carter, M.G. Jones, L. Yuan, N. Zhou, S.J. Duclos, Control of Solidification in Laser Powder Bed Fusion Additive Manufacturing Using a Diode Laser Fiber Array, 1 (2020) 1–17.

[191] H. Chen, W. Yan, Spattering and denudation in laser powder bed fusion process: Multiphase flow modelling, Acta Mater. 196 (2020) 154–167. https://doi.org/10.1016/j.actamat.2020.06.033.

[192] C. Zhao, Q. Guo, X. Li, N. Parab, K. Fezzaa, W. Tan, L. Chen, T. Sun, Bulk-Explosion-Induced Metal Spattering During Laser Processing, Phys. Rev. X 9 (2019) 021052. https://doi.org/10.1103/physrevx.9.021052.

[193] J. Liu, P. Wen, Metal vaporization and its influence during laser powder bed fusion process, Mater. Des. 215 (2022) 110505. https://doi.org/10.1016/j.matdes.2022.110505.

[194] Q. Guo, C. Zhao, L.I. Escano, Z. Young, L. Xiong, K. Fezzaa, W. Everhart, B. Brown, T. Sun, L. Chen, Transient dynamics of powder spattering in laser powder bed fusion additive manufacturing process revealed by in-situ high-speed high-energy x-ray imaging, Acta Mater. 151 (2018) 169–180. https://doi.org/10.1016/j.actamat.2018.03.036.

[195] Z.A. Young, Q. Guo, N.D. Parab, C. Zhao, M. Qu, L.I. Escano, K. Fezzaa, W. Everhart, T. Sun, L. Chen, Types of spatter and their features and formation mechanisms in laser powder bed fusion additive manufacturing process, Addit. Manuf. 36 (2020) 101438. https://doi.org/10.1016/j.addma.2020.101438.

[196] D. Wang, S. Wu, F. Fu, S. Mai, Y. Yang, Y. Liu, C. Song, Mechanisms and characteristics of spatter generation in SLM processing and its effect on the properties, Materials & Design 117 (2017) 121–130. https://doi.org/10.1016/j.matdes.2016.12.060.

[197] T. Fedina, J. Sundqvist, A.F.H. Kaplan, Spattering and oxidation phenomena during recycling of low alloy steel powder in Laser Powder Bed Fusion, Mater. Today Commun. 27 (2021) 102241. https://doi.org/10.1016/j.mtcomm.2021.102241.

[198] S. Ly, A.M. Rubenchik, S.A. Khairallah, G. Guss, M.J. Matthews, Metal vapor micro-jet controls material redistribution in laser powder bed fusion additive manufacturing, Sci. Rep. 7 (2017) 4085. https://doi.org/10.1038/s41598-017-04237-z.

[199] Y. Huang, T.G. Fleming, S.J. Clark, S. Marussi, K. Fezzaa, J. Thiyagalingam, C.L.A. Leung, P.D. Lee, Keyhole fluctuation and pore formation mechanisms during laser powder bed fusion additive manufacturing, Nat. Commun. 13 (2022) 1170. https://doi.org/10.1038/s41467-022-28694-x.

[200] M. Bayat, A. Thanki, S. Mohanty, A. Witvrouw, S. Yang, J. Thorborg, N.S. Tiedje, J.H. Hattel, Keyhole-induced porosities in Laser-based Powder Bed Fusion (L-PBF) of Ti6Al4V: High-fidelity modelling and experimental validation, Addit. Manuf. 30 (2019) 100835. https://doi.org/10.1016/j.addma.2019.100835.

[201] W.E. King, H.D. Barth, V.M. Castillo, G.F. Gallegos, J.W. Gibbs, D.E. Hahn, C. Kamath, A.M. Rubenchik, Observation of keyhole-mode laser melting in laser powder-bed fusion additive manufacturing, J. Mater. Process. Technol. 214 (2014) 2915–2925. https://doi.org/10.1016/j.jmatprotec.2014.06.005.

[202] S. Pal, N. Gubeljak, R. Hudák, G. Lojen, V. Rajťúková, T. Brajlih, I. Drstvenšek, Evolution of the metallurgical properties of Ti-6Al-4V, produced with different laser

processing parameters, at constant energy density in selective laser melting, Results in Physics 17 (2020). https://doi.org/10.1016/j.rinp.2020.103186.

[203] C. Desrosiers, M. Letenneur, F. Bernier, N. Piché, B. Provencher, F. Cheriet, F. Guibault, V. Brailovski, Automated porosity segmentation in laser powder bed fusion part using computed tomography: a validity study, J. Intell. Manuf. (2024) 1–21. https://doi.org/10.1007/s10845-023-02296-w.

[204] C. Pleass, S. Jothi, Influence of powder characteristics and additive manufacturing process parameters on the microstructure and mechanical behaviour of Inconel 625 fabricated by Selective Laser Melting, Additive Manufacturing 24 (2018) 419–431. https://doi.org/10.1016/j.addma.2018.09.023.

[205] A. Sola, A. Nouri, Microstructural porosity in additive manufacturing: The formation and detection of pores in metal parts fabricated by powder bed fusion, J. Adv. Manuf. Process. 1 (2019). https://doi.org/10.1002/amp2.10021.

[206] M. Tang, P.C. Pistorius, J.L. Beuth, Prediction of lack-of-fusion porosity for powder bed fusion, Addit. Manuf. 14 (2017) 39–48. https://doi.org/10.1016/j.addma.2016.12.001.

[207] H. Gong, K. Rafi, H. Gu, T. Starr, B. Stucker, Analysis of defect generation in Ti–6Al–4V parts made using powder bed fusion additive manufacturing processes, Addit. Manuf. 1 (2014) 87–98. https://doi.org/10.1016/j.addma.2014.08.002.

[208] C. Chen, J. Yin, H. Zhu, Z. Xiao, L. Zhang, X. Zeng, Effect of overlap rate and pattern on residual stress in selective laser melting, Int. J. Mach. Tools Manuf. 145 (2019) 103433. https://doi.org/10.1016/j.ijmachtools.2019.103433.

[209] B. Vrancken, L. Thijs, J.-P. Kruth, J.V. Humbeeck, Heat treatment of Ti6Al4V produced by Selective Laser Melting: Microstructure and mechanical properties, J. Alloy. Compd. 541 (2012) 177–185. https://doi.org/10.1016/j.jallcom.2012.07.022.

[210] S.Q. Wu, Y.J. Lu, Y.L. Gan, T.T. Huang, C.Q. Zhao, J.J. Lin, S. Guo, J.X. Lin, Microstructural evolution and microhardness of a selective-laser-melted Ti–6Al–4V alloy after post heat treatments, J. Alloy. Compd. 672 (2016) 643–652. https://doi.org/10.1016/j.jallcom.2016.02.183.

[211] J.P. Kruth, L. Froyen, J.V. Vaerenbergh, P. Mercelis, M. Rombouts, B. Lauwers, Selective laser melting of iron-based powder, Journal of Materials Processing Technology 149 (2004) 616–622. https://doi.org/10.1016/j.jmatprotec.2003.11.051.

[212] M. Yakout, I. Phillips, M.A. Elbestawi, Q. Fang, In-situ monitoring and detection of spatter agglomeration and delamination during laser-based powder bed fusion of Invar 36, Opt. Laser Technol. 136 (2021) 106741. https://doi.org/10.1016/j.optlastec.2020.106741.

[213] Data Sheet - Ti6al4v carpenter grade 23 powder, (n.d.). https://www.carpenteradditive.com/hubfs/Resources/Data%20Sheets/PowderRange_TI64_Datasheet.pdf (accessed August 3, 2023).

[214] M. Thomas, G.J. Baxter, I. Todd, Normalised model-based processing diagrams for additive layer manufacture of engineering alloys, Acta Mater. 108 (2016) 26–35. https://doi.org/10.1016/j.actamat.2016.02.025.

[215] C. Additive, PowderRange Ti64 Datasheet, (2020). https://www.carpentertechnology.com/alloy-finder/powderrange-ti64 (accessed January 20, 2024).

[216] C. Lestrange, Effect of surface roughness on quality perception of Laser Sintered (LS) parts, 2016.

[217] A.K. Singla, M. Banerjee, A. Sharma, J. Singh, A. Bansal, M.K. Gupta, N. Khanna, A.S. Shahi, D.K. Goyal, Selective laser melting of Ti6Al4V alloy: Process parameters, defects and post-treatments, Journal of Manufacturing Processes 64 (2021) 161–187. https://doi.org/10.1016/j.jmapro.2021.01.009.

[218] Y. Zhu, J. Zou, H. Yang, Wear performance of metal parts fabricated by selective laser melting: a literature review, J. Zhejiang Univ.-Sci. A 19 (2018) 95–110. https://doi.org/10.1631/jzus.a1700328.

[219] B. Song, S. Dong, B. Zhang, H. Liao, C. Coddet, Effects of processing parameters on microstructure and mechanical property of selective laser melted Ti6Al4V, Mater. Des. 35 (2012) 120–125. https://doi.org/10.1016/j.matdes.2011.09.051.

[220] H. Gong*, K. Rafi*, T. Starr†, B. Stucker*, EFFECT OF DEFECTS ON FATIGUE TESTS OF AS-BUILT TI-6AL-4V PARTS FABRICATED BY SELECTIVE LASER MELTING, (n.d.). https://doi.org/10.26153/tsw/15369.

[221] E. Wycisk, C. Emmelmann, S. Siddique, F. Walther, High Cycle Fatigue (HCF) Performance of Ti-6Al-4V Alloy Processed by Selective Laser Melting, Adv. Mater. Res. 816–817 (2013) 134–139. https://doi.org/10.4028/www.scientific.net/amr.816-817.134.

[222] S.Q. Wu, Y.J. Lu, Y.L. Gan, T.T. Huang, C.Q. Zhao, J.J. Lin, S. Guo, J.X. Lin, Microstructural evolution and microhardness of a selective-laser-melted Ti–6Al–4V alloy after post heat treatments, J. Alloy. Compd. 672 (2016) 643–652. https://doi.org/10.1016/j.jallcom.2016.02.183.

[223] W.W. Wits, S. Carmignato, F. Zanini, T.H.J. Vaneker, Porosity testing methods for the quality assessment of selective laser melted parts, CIRP Ann. - Manuf. Technol. 65 (2016) 201–204. https://doi.org/10.1016/j.cirp.2016.04.054.

[224] X. Wang, S. Xu, S. Zhou, W. Xu, M. Leary, P. Choong, M. Qian, M. Brandt, Y.M. Xie, Topological design and additive manufacturing of porous metals for bone scaffolds and orthopaedic implants: A review, Biomaterials 83 (2016) 127–141. https://doi.org/10.1016/j.biomaterials.2016.01.012.

[225] V. Semak, A. Matsunawa, The role of recoil pressure in energy balance during laser materials processing, Journal of Physics D: Applied Physics 30 (1997) 2541–2552. https://doi.org/10.1088/0022-3727/30/18/008.

[226] Z. Chen, X. Wu, D. Tomus, C.H.J. Davies, Surface roughness of Selective Laser Melted Ti-6Al-4V alloy components, Addit. Manuf. 21 (2018) 91–103. https://doi.org/10.1016/j.addma.2018.02.009.

[227] Gates-Rector, B. T., 04-020-7055, The Powder Diffraction File: A Quality Materials Characterization Database, Powder Diffr. (2019) 352–360. https://doi.org/10.1017/s0885715619000812.

[228] Gates-Rector, S.; Blanton, 00-044-1294, The Powder Diffraction File: A Quality Materials Characterization Database, Powder Diffr. (2019) 352–360. https://doi.org/10.1017/s0885715619000812.

[229] D. Chioibasu, A. Achim, C. Popescu, G.E. Stan, I. Pasuk, M. Enculescu, S. Iosub, L. Duta, A. Popescu, Prototype Orthopedic Bone Plates 3D Printed by Laser Melting Deposition, Materials 12 (2019) 906. https://doi.org/10.3390/ma12060906.

[230] G. Zhang, J. Chen, M. Zheng, Z. Yan, X. Lu, X. Lin, W. Huang, Element Vaporization of Ti-6Al-4V Alloy during Selective Laser Melting, Metals 10 (2020) 435. https://doi.org/10.3390/met10040435.

[231] D.A. Porter, K.E. Easterling, K.E. Easterling, Phase Transformations in Metals and Alloys (Revised Reprint), 2009. https://doi.org/10.1201/9781439883570.

[232] S. Megahed, V. Aniko, J.H. Schleifenbaum, Electron Beam-Melting and Laser Powder Bed Fusion of Ti6Al4V: Transferability of Process Parameters, Metals 12 (2022) 1332. https://doi.org/10.3390/met12081332.

[233] X. Miao, M. Wu, J. Han, H. Li, X. Ye, Effect of Laser Rescanning on the Characteristics and Residual Stress of Selective Laser Melted Titanium Ti6Al4V Alloy, Materials 13 (2020) 3940. https://doi.org/10.3390/ma13183940.

[234] P. Tarín, A. Gualo, A.G. Simón, N.M. Piris, J.M. Badía, Study of Alpha-Beta Transformation in Ti-6Al-4V-ELI. Mechanical and Microstructural Characteristics, Mater. Sci. Forum 638–642 (2010) 712–717. https://doi.org/10.4028/www.scientific.net/msf.638-642.712.

[235] I. Yadroitsev, P. Krakhmalev, I. Yadroitsava, Hierarchical design principles of selective laser melting for high quality metallic objects, Addit. Manuf. 7 (2015) 45–56. https://doi.org/10.1016/j.addma.2014.12.007.

[236] T. Mukherjee, H.L. Wei, A. De, T. DebRoy, Heat and fluid flow in additive manufacturing – Part II: Powder bed fusion of stainless steel, and titanium, nickel and aluminum base alloys, Comput. Mater. Sci. 150 (2018) 369–380. https://doi.org/10.1016/j.commatsci.2018.04.027.

[237] S.A. Khairallah, A.T. Anderson, A. Rubenchik, W.E. King, Laser powder-bed fusion additive manufacturing: Physics of complex melt flow and formation mechanisms of pores, spatter, and denudation zones, Acta Mater. 108 (2016) 36–45. https://doi.org/10.1016/j.actamat.2016.02.014.

[238] L. Thijs, F. Verhaeghe, T. Craeghs, J.V. Humbeeck, J.-P. Kruth, A study of the microstructural evolution during selective laser melting of Ti–6Al–4V, Acta Materialia 58 (2010) 3303–3312. https://doi.org/10.1016/j.actamat.2010.02.004.

[239] L. Owen, Powder Refinement - opening the black box, in: Proc. 5th Int. Work. OpenCL, The University of Sheffield, 2022: pp. 1–20.

[240] Q. Gaillard, X. Boulnat, S. Cazottes, S. Dancette, C. Desrayaud, Strength/ductility trade-off of Laser Powder Bed Fusion Ti-6Al-4V: Synergetic effect of alpha-case formation and microstructure evolution upon heat treatments, Addit. Manuf. 76 (2023) 103772. https://doi.org/10.1016/j.addma.2023.103772.

[241] R.W. Armstrong, The influence of polycrystal grain size on several mechanical properties of materials, Met. Mater. Trans. B 1 (1970) 1169–1176. https://doi.org/10.1007/bf02900227.

[242] G. Lütjering, Influence of processing on microstructure and mechanical properties of (α+β) titanium alloys, Mater. Sci. Eng.: A 243 (1998) 32–45. https://doi.org/10.1016/s0921-5093(97)00778-8.

[243] A.E. Hassanin, F. Napolitano, C. Trimarco, E. Manco, F. Scherillo, D. Borrelli, A. Caraviello, A. Squillace, A. Astarita, Laser-Powder Bed Fusion of Inconel 718 Alloy: Effect of the Contour Strategy on Surface Quality and Sub-Surface Density, Key Eng. Mater. 926 (2022) 280–287. https://doi.org/10.4028/p-u9ydck.

[244] S. Dai, H. Liao, H. Zhu, X. Zeng, The mechanism of process parameters influencing the AlSi10Mg side surface quality fabricated via laser powder bed fusion, Rapid Prototyp. J. 28 (2022) 514–524. https://doi.org/10.1108/rpj-11-2020-0266.

[245] A. Borbély, A. Aoufi, D. Becht, X-ray methods for strain energy evaluation of dislocated crystals, J. Appl. Crystallogr. 56 (2023) 254–262. https://doi.org/10.1107/s1600576722012262.

[246] W. Xu, M. Brandt, S. Sun, J. Elambasseril, Q. Liu, K. Latham, K. Xia, M. Qian, Additive manufacturing of strong and ductile Ti–6Al–4V by selective laser melting via in situ martensite decomposition, Acta Mater. 85 (2015) 74–84. https://doi.org/10.1016/j.actamat.2014.11.028.